

**SURFACE MODIFICATIONS OF STEELS TO IMPROVE CORROSION
RESISTANCE IN SULFIDIZING-OXIDIZING ENVIRONMENTS**

A Dissertation
Submitted to
The Academic Faculty

By

Vikas Behrani

In Partial Fulfillment
Of the Requirement for the Degree
Doctor of Philosophy in Materials Science and Engineering

Georgia Institute of Technology
Atlanta, GA

December 2007

**SURFACE MODIFICATIONS OF STEELS TO IMPROVE CORROSION
RESISTANCE IN SULFIDIZING-OXIDIZING ENVIRONMENTS**

Approved by:

Dr. Preet M. Singh, Advisor
School of Materials Science and
Engineering
Georgia Institute of Technology

Dr. Naresh N. Thadhani
School of Materials Science and
Engineering
Georgia Institute of Technology

Dr. Meilin Liu
School of Materials Science and
Engineering
Georgia Institute of Technology

Dr. Thomas H. Sanders Jr.
School of Materials Science and
Engineering
Georgia Institute of Technology

Dr. William J. Frederick, Jr.
School of Chemical and Biomolecular
Engineering
Georgia Institute of Technology

Date approved:
September 24, 2007

To
Sai Baba

ACKNOWLEDGEMENTS

I would like to thank my advisor, Dr. Preet Singh, for being a wonderful mentor and a friend. I have learnt a great deal from him both academically and personally. I would like to thank my committee members Dr. Thomas H. Sanders, Jr., Dr. Meilin Liu, Dr. Naresh N. Thadhani and William J. Frederick, Jr. for their suggestions and comments to improve this study. Thanks to Jamshad Mahmood for always being there to help in laboratory and lighten the environment with his jokes.

I would like to thank Dr. Matthew D. Trexler for his help with EBSD studies, Dr. Dongsheng Li for help with texture discussions and Arun Sreeranganathan for help with nano-indentation measurements. I would also like to acknowledge my fellow group members, Dr. Patrick Hazelwood, Dong Yang, Stefanie Asher, Ananya Bhattacharya, Andrew Weeks and Theo Sanches for their support throughout the work.

This research was funded by the PSE Foundation Fellowship Program at Institute of Paper Science and Technology at Georgia Tech, State of Georgia-TIP₃ Program, DOE-(DE-AC05-00OR22725), and ORNL (6400004405).

Finally, I would like to thank my Parents, Ramesh and Rajkumari Behrani, brother, Amit Behrani, sister, Ritu Behrani, fiancée Neelam Udernani and Poonam Parwani for their love, support and understanding throughout the work.

TABLE OF CONTENTS

ACKNOWLEDGEMENTS	iv
LIST OF TABLES	ix
LIST OF FIGURES	xi
SUMMARY	xxiv
CHAPTER I: INTRODUCTION	1
Motivation	1
Background and Literature Review	3
1.1 Oxidation and Sulfidation of Metals and Alloys	3
1.1.1 Thermodynamics Considerations	4
1.1.2 Corrosion Products	7
1.1.3 Electrochemistry and Corrosion Reactions	7
1.2 Kinetics of Corrosion	9
1.2.1 Parabolic Law	9
1.2.2 Linear Rate Law	12
1.3 Fluctuating Temperatures and Gaseous Environments	13
1.4 Protective Coatings	24
1.5 Pack Cementation	26
1.5.1 Pack	27
1.5.2 Pack Reactions	27
1.5.3 Kinetics of Pack Cementation	30
1.6 Modification of Coatings	33
1.6.1 Hf and Y Modified Coatings	35

1.7 Stresses in Protective Scales	37
1.8 Piezospectroscopy (Laser Fluorescence)	38
1.8.1 Theoretical Background	38
1.8.2 Effects of Chromium Concentration on R1 and R2	46
1.8.3 Effects of Temperature on R1 and R2	46
CHAPTER II: EXPERIMENTAL PROCEDURES	47
2.1 Boiler Environment Characterization	47
2.2 Pack Cementation	51
2.3 High Temperature Corrosion Kinetics	54
2.4 Mechanical Properties	57
2.5 Luminescence Piezospectroscopy for Stress Measurements	58
2.5.1 Spectrometer	60
2.5.2 Stress mapping	60
CHAPTER III: FLUCTUATING SULFIDIZING-OXIDIZING ENVIRONMENTS AND ITS EFFECT ON PHASE STABILITY OF PROTECTIVE SCALE ON SA210 CARBON STEEL	62
Introduction	62
3.1 Boiler Environment Characterization at Tube Surface	64
3.2 Effect of Gas Composition on Corrosion Product	73
3.3 Effect of Cyclic Sulfidizing-Oxidizing Environments	75
3.3.1 Cycling between Sulfidizing $p_{S_2}=10^{-14}$ atm and Oxidizing $p_{O_2}=10^{-2}$ atm.	77
3.3.2 Cycling between $p_{S_2}=10^{-14}$ atm and ($p_{SO_2}=10^{-1}$ atm) at 300 °C	85
Summary	96

CHAPTER IV: CHROMIZED AND ALUMINIDE DIFFUSION COATINGS	97
Introduction	97
4.1 Chromized SA210	98
4.1.1 Microstructure	98
4.1.2 Corrosion Behavior	102
4.1.2.1 Tests in Static Sulfidizing Environments	104
4.1.2.2 Tests in Cyclic Sulfidizing-Oxidizing Environments	109
4.2 Aluminide Coatings on Carbon Steels	115
4.2.1 Aluminide Coating Growth Kinetics	115
4.2.1.1 Effect of Temperature on Aluminizing of Carbon Steel	120
4.2.1.2 Effect of Time on Aluminizing of Carbon Steel	123
4.2.2 Texture Analysis by EBSD	125
4.2.3 Mechanical Properties of Aluminide Coatings and Interface	132
4.2.4 Corrosion Behavior	139
4.2.4.1 Performance of Aluminide Coatings in Sulfidizing Environment	139
4.2.4.2 Oxidation	145
4.2.4.3 Cyclic Sulfidation-Oxidation	148
Summary	152
CHAPTER V: REACTIVE ELEMENT (Hf AND Y) MODIFIED Fe-Al INTERMETALLIC COATINGS	154
Introduction	154
5.1 Hf -modified Iron Aluminide Coatings	156
5.1.1 Thermodynamic Considerations	156
5.1.2 Microstructure of RE modified Iron Aluminide Coatings	161

5.2 Y-modified Iron Aluminide Coating	176
5.3 Oxidation/Sulfidation Behavior	184
5.3.1 Corrosion Behavior of Unmodified Fe-Al Coatings	186
5.3.2 Corrosion Performance of Aluminide Coatings with >1 at% RE Addition	189
5.3.2.1 Corrosion Mechanism of RE-modified Fe-Al Coatings in Cyclic Gaseous Environment	203
5.3.3 Corrosion Performance of Aluminide coatings with <0.5 at% RE Addition	207
Summary	220
CHAPTER VI: EFFECTS OF REACTIVE ELEMENTS (Hf and Y) ON STRESS DISTRIBUTION AND SPALLATION RESISTANCE OF PROTECTIVE Al₂O₃ SCALES	221
Introduction	221
5.1 Stress Mapping	223
6.1.1 Spectra Processing	223
6.1.2 Procedure used for Peak Fitting	224
6.2 Cyclic Oxidation at 1000°C	226
6.3 Stress Distribution in Scales	236
Summary	256
CHAPTER VII: GENERAL CONCLUSION	257
Scientific Accomplishments	260
APPENDIX A	262
APPENDIX B	267
APPENDIX C	271
REFERENCES	278

LIST OF TABLES

Table 1.1: Black liquor chemical analysis and calculated solid content. Also shown is the gaseous environment generated during combustion of black liquor.	15
Table 1.2: Gaseous environments generated due to combustion of black liquor in power generation equipments in pulp and paper industry.	16
Table 1.3: Experimentally determined piezpspectroscopic coefficients for R1 and R2 lines in Cr^{+3} spectrum.	45
Table 2.1: Chemical composition (in weight %) of carbon steel tube (SA210) used in this study.	52
Table 3.1: Corrosion kinetics parameters for different stages in Test-1, where S indicates $p_{\text{S}_2} = 10^{-14}$ atm and O indicates $p_{\text{O}_2} = 10^{-2}$ atm.	84
Table 3.2: Corrosion kinetics parameters for different stages in Test-2, where S indicates $p_{\text{S}_2} = 10^{-14}$ atm and O indicates $p_{\text{SO}_2} = 10^{-1}$ atm. Note that test started under oxidizing environment.	90
Table 3.3: Corrosion kinetics parameters for different stages in Test-3, where S indicate $p_{\text{S}_2} = 10^{-14}$ atm and O indicates $p_{\text{SO}_2} = 10^{-1}$ atm. Note that test started under sulfidizing environment.	94
Table 4.1: Corrosion rates of uncoated as compared to chromized SA210 in the temperature range of 300-800°C.	106
Table 4.2: Pack composition, process parameters and results for pack-aluminizing of SA-210 low carbon steel investigated in this study.	116
Table 4.3: Effect of aluminum concentration on coating average hardness and elastic modulus.	138
Table 4.4: Corrosion rates of samples exposed to different environments. k_l denotes linear rate and k_p denotes parabolic rate. S shows sulfidizing environment and O shows oxidizing environment.	147
Table 5.1: Pack cementation process parameters used for synthesis of Hf-modified iron aluminide coatings.	157
Table 5.2: Surface concentration of Al, Fe and Ff at spots shown in Figure 5.10.	170
Table 5.3: Spot EDS analysis of HfFeAl coating shown in Figure 5.12.	173

Table 5.4: Summary of HfFeAl coatings prepared with respective process parameters, Hf content and phases.	175
Table 5.5: Pack cementation conditions chosen to form yttrium-modified iron aluminide coatings on SA210 carbon steel.	178
Table 5.6: Fe, Al and Y concentration in YFeAl coating shown in Figure 5.15.	181
Table 5.7: Al, Fe and Y concentration in YFeAl coating prepared by pack-2 condition as shown in Figure 5.17.	183
Table 5.8: RE modified coatings chosen for corrosion kinetics study.	184
Table 5.9: Parabolic corrosion rates for each cycle as shown in Figure 5.20 for modified coating as compared to unmodified coatings in cyclic gaseous environments:(O) $p_{O_2}=0.21$ atm, (S) $p_{S_2} = 10^{-8}$ atm.	188
Table 5.10: Parabolic corrosion rates for each cycle as shown in Figure 5.22 for yttrium-modified coating as compared to unmodified coatings in cyclic gaseous environments: (O) $p_{O_2}=0.21$ atm, (S) $p_{S_2} = 10^{-8}$ atm.	192
Table 5.11: Fe, O, S, Al, and Y concentrations in scale after exposure to cyclic environments at 800°C for 100 hours as shown in Figure 5.10.	196
Table 5.12: Parabolic corrosion rates for each cycle as shown in Figure 5.26 for hafnium modified coating as compared to unmodified coatings in cyclic gaseous environments:(O) $p_{O_2}=0.21$ atm, (S) $p_{S_2} = 10^{-8}$ atm.	200
Table 5.13: Parabolic corrosion rates for each cycle as shown in Figure for modified coating as compared to unmodified coatings in cyclic gaseous environments:(O) $p_{O_2}=0.21$ atm, (S) $p_{S_2} = 10^{-8}$ atm.	202
Table 5.14: Parabolic corrosion rates for each cycle as shown in Figure for modified coating as compared to unmodified coatings in cyclic gaseous environments:(O) $p_{O_2} = 0.21$ atm, (S) $p_{S_2} = 10^{-8}$ atm.	212
Table 5.15: EDS elemental analysis for spots shown on Figure 5.35.	214
Table 5.16: Summary of effects of reactive element modifications on corrosion behavior of iron aluminide coatings in fluctuating sulfidizing-oxidizing environments at 800°C.	219
Table 6.1: Parabolic rate constants for oxidation of uncoated and coated samples under thermal cyclic conditions from 1000°C to room temperature every 24 hours.	231

LIST OF FIGURES

Figure 1.1: Ellingham diagram: Standard Gibbs free energy of formation for selected oxides.	5
Figure 1.2: Ellingham diagram: Standard Gibbs free energy of formation for selected sulfides.	6
Figure 1.3: Scale formation by (a) outward diffusion of metal ion, (b) inward diffusion of gaseous species (S^{2-} or O^{2-}). Black dots show the location of scale growth.	9
Figure 1.4: Scale formation mechanism in oxidative environment.	10
Figure 1.5: Diffusion controlled high temperature gaseous corrosion.	12
Figure 1.6: Schematic of typical Kraft Recovery Boiler used in pulp and paper industry for power generation.	14
Figure 1.7: Changes in H_2S concentration by decreasing the droplet size of black liquor feed in Kraft recovery boiler.	19
Figure 1.8: Changes in H_2S concentration by increasing the tertiary air flow by 10 volume % in Kraft recovery boiler.	20
Figure 1.9: Changes in temperature in Kraft recovery boiler by increasing the tertiary air flow by 10 volume %	21
Figure 1.10: H_2S iso-surface with different tertiary air ratios and openings.	22
Figure 1.11: Fe-Al Binary Phase Diagram Showing Ordered Intermetallic Phases in the Area of Interest (>50% Al).	30
Figure 1.12: Kinetics of pack cementation coating process. (1) Gas phase diffusion of aluminum halide molecules from the pack to the coating surface across the Al depleted zone of the pack. (2) Deposition of the masteralloy element from the halide gas at the gas/coating interface. (3) Solid state diffusion of the iron through the coating towards the coating/gas interface. (4) Growth of the coating phase at the coating/gas interface. (5) Desorption of the halogen species from the gas/coating interface. (6) Gas phase diffusion of the halogen back into the pack	32
Figure 1.13: Reactive element effect: change in scale growth mechanism.	36
Figure 1.14: Cr^{+3} substitution for Al^{+3} in Al_2O_3 crystal structure.	40

Figure 1.15: Electronic levels of Cr^{+3} in Al_2O_3 . Transitions resulting in characteristic R1 and R2 lines are labeled.	41
Figure 1.16: Cr^{+3} luminescence spectrum showing characteristic doublet of R1 and R2.	42
Figure 1.17: Effect of stress on R1 and R2 lines of Cr^{+3} spectrum. Shift towards left signifies compressive stresses in Al_2O_3 crystal.	43
Figure 2.1: Schematic of Boiler showing corrosion patterns and port locations on the waterwall surface in mid-furnace area (above the cut-line). Notice that the boiler had two air levels and higher corrosion rates were experienced till higher elevations in middle of side walls compared to the corners.	48
Figure 2.2: Schematic of boiler showing corrosion patterns and port location on the waterwall surface in mid-furnace area (above the cut-line).	50
Figure 2.3: Gas-sampling port installed in recovery boiler to collect samples from the tube surface.	50
Figure 2.4: Picture of a port installed in recovery boiler waterwalls to collect samples from the tube surface.	51
Figure 2.5: Experimental setup for pack cementation coatings.	53
Figure 2.6: TGA setup for corrosion kinetics studies in sulfidizing-oxidizing environments.	54
Figure 2.7: Stability diagram for (Fe,Al,Cr)-O-S system with superimposed measured boiler conditions (circular dots) and simulated conditions in laboratory (square dots) using mixture of N_2 , O_2 and H_2S .	56
Figure 2.8: Experimental setup for acquiring luminescence spectra from oxidized aluminized SA210 samples.	59
Figure 2.9: Spectrum collected for oxidized aluminide coating at 1000°C and corresponding deconvolution of R1 and R2 peaks.	61
Figure 3.1: (A) areas of high corrosion in kraft recovery boiler 6 feet above cut line, (B) areas of low corrosion at the same elevation as (A).	63
Figure 3.2: Schematic of kraft recover boiler showing corrosion patterns and port locations on the tube surface in mid-furnace area. Notice that the boiler had two air levels and higher corrosion rates were experienced till higher elevations in middle of side walls compared to the corners as shown in Figure 3.1.	65

- Figure 3.3: Concentration of H₂S in gas samples collected at the waterwall surface of Kraft Recovery Boiler on 8 different days under normal operating conditions. Gas-sampling port positions are shown in Figure 3.2. 66
- Figure 3.4: Variation in the partial pressure of sulfur in gas samples taken from different ports in the mid-furnace, shown in Figure 3.1 calculated from assuming equilibrium in all sulfur bearing species. 67
- Figure 3.5: Concentration of O₂ in gas samples collected at the waterwall surface of Kraft Recovery Boiler on 8 different days over a-year period under normal operating conditions. Port positions are shown in Figure 3.1. 68
- Figure 3.6: Variation in the partial pressure of oxygen in samples taken from different ports in the mid-furnace, shown in Figure 3.1. Partial pressures were calculated from oxidizing species. 69
- Figure 3.7: Fluctuations in gas composition measured in Kraft Recovery Boiler. Significant cycling between oxidizing and sulfidizing environments was observed. Partial pressures of oxygen and sulfur were calculated from measured gas composition. 71
- Figure 3.8: Ranges of gas fluctuations measured in boiler extrapolated to the gasification temperatures. Solid line represents pS₂ and dashed line represents pO₂. 72
- Figure 3.9: Phase Stability diagram for Fe-O-S system at 320°C. Diagram shows partial stability regions for different possible scale compositions as a function of oxygen and sulfur partial pressure in contact with iron. Round symbols show measured partial pressures in gases sampled from the port #1 on different days and the square symbols show simulated cyclic environments used in laboratory tests. 74
- Figure 3.10: Effect of fluctuating sulfidizing/oxidizing atmosphere on corrosion behavior of SA210 at 300°C. A and B denotes gas atmosphere as: Test-1: (A) pS₂ = 10⁻¹⁴ atm, (B) pO₂ = 10⁻² atm; Test-2: (A) pSO₂ = 10⁻¹ atm, (B) pS₂ = 10⁻¹⁴ atm; Test-3: (A) pS₂ = 10⁻¹⁴ atm, (B) pSO₂ = 10⁻¹ atm sulfidation, (b) Kinetic changes on environmental cycling shows extensive spallation. 76
- Figure 3.11: (a) Corrosion kinetics of SA210 in test-1 conditions as compared to static sulfidation, (b) Kinetic changes on environmental cycling shows extensive spallation. 78
- Figure 3.12: SE micrographs of laminated scale after test # 1. (A) Alternative oxide/sulfide scale corresponding to each cycle, (B) Extensive cracking in scale. Oxide scale is relatively continuous and free from cracking. 79

- Figure 3.13: Layered microstructure of scale on carbon steel sample after Test-1 with Sulfur-X-Ray maps showing presence of alternate oxide/sulfide layers of the scale. A layer with absence of sulfur in EDS maps was assumed to be an oxide. 80
- Figure 3.14: (a) rumpling in scale at scale scale/alloy interface due to CTE mismatch of scale and alloy, (b) highly porous sulfide scale and dense oxide microstructure. 82
- Figure 3.14: (c) Cracking between oxide-sulfide layered scales. EDS maps shows that some cracking was observed in oxide too. 83
- Figure 3.15: Corrosion kinetics of SA210 in test-2 conditions as compared to exposure to static sulfidizing environment. 85
- Figure 3.16: Change in corrosion kinetics of SA210 on environmental cycling in test-2 conditions. 86
- Figure 3.17: Cross-sectional SE micrographs of scale after Test # 2 (cycling between $p\text{SO}_2 = 10^{-1}$ atm and $p\text{S}_2 = 10^{-14}$ atm starting with oxidizing). Laminated structure is evident due to cycling of gaseous atmosphere between oxidizing and sulfidizing. 88
- Figure 3.18: Sulfur-X-Ray map of scale after Test-2. Unlike Test-1, oxide was observed at the scale-alloy interface. 89
- Figure 3.19: Scale/alloy interface showing good adherence of oxide for test-2. 90
- Figure 3.20: Physical appearance of samples after 100 hour exposure at 300°C. (A) Test-1: cycling between $p\text{S}_2 = 10^{-14}$ atm and $p\text{O}_2 = 10^{-2}$ atm, (B) Test-2: cycling between $p\text{SO}_2 = 10^{-1}$ atm and $p\text{S}_2 = 10^{-14}$ atm. 91
- Figure 3.21: Corrosion kinetics of SA210 in Test-3 conditions. Note that the conditions are similar to Test-2 with the first environment being oxidizing. 92
- Figure 3.22: Kinetic change of environmental cycling in Test-3 conditions. 93
- Figure 3.23: Cross-sectional SE micrographs of scale after Test – 3 with sulfur x-ray map. (Cycling between $p\text{SO}_2 = 10^{-1}$ atm and $p\text{S}_2 = 10^{-14}$ atm starting with mixed sulfidizing-oxidizing environments). 95
- Figure 4.1: XRD pattern of SA210 chromized at 800°C for 6 hrs showing formation of carbides and nitrides. 99

- Figure 4.2: Surface microstructure of chromized SA210 at 800°C for 6 hours. Network like granular structure is evident. 100
- Figure 4.3: (a) Cross-section micrograph of chromized SA210 at 800°C for 6 hours. Chromized induced ferrite is evident in carbon-deficient regions, (b) EDS concentration profile of Cr and Fe. 101
- Figure 4.4: (Fe,Cr)-O-S stability diagram at 300°C with points showing measured partial pressures of oxygen and sulphur. Circular dots show measured values and square dots show simulated values. 102
- Figure 4.5: (Fe,Cr)-O-S stability diagram at (a) 600°C, (b) 800°C. 103
- Figure 4.6: Corrosion behavior of chromized SA210 as compared to uncoated SA210 in static sulfidizing environments with $p_{S_2} = 10^{-15}$ atm . 104
- Figure 4.7: Magnified view of sulfidation behavior of chromized SA210 showing excellent behavior at 300°C and catastrophic failure at 600 and 800°C. Corrosion rates are listed in Table 1. 105
- Figure 4.8: XRD pattern of scale on chromized SA210 after exposure to $p_{S_2}=10^{-15}$ atm for 100 hrs at 600°C showing formation of chromium sulfides. 107
- Figure 4.9: (A) Cross-section of chromized SA210 after exposure to sulfidizing environment ($p_{S_2} = 10^{-15}$ atm) at 600°C. Thick and porous chromium sulfide scale was observed with significant spallation on removal from the TGA, (B) porous microstructure of Cr-sulfide scale. 108
- Figure 4.10: (a) Comparison of mass change behavior of chromized SA210 in cyclic and non cyclic environments at 300°C, (b) kinetics at environment change from sulfidizing to oxidizing. 110
- Figure 4.11: XRD patterns of chromized SA210 after 100 hours exposure to cyclic and noncyclic environments at 300°C. 112
- Figure 4.12: Surface microstructure of Cr-diffusion coated SA210 after 100 hours exposure to cyclic sulfidizing-oxidizing environments at 300°C with X-Ray maps of Sulfur, Oxygen and, Chromium. Mass change with time is shown in Figure 4.10. 113
- Figure 4.13: Cross-section micrograph of chromized SA210 after 100 hours exposure to cyclic sulfidizing-oxidizing atmosphere at 300°C with X-Ray maps of oxygen, chromium and iron. 114

Figure 4.14: (a) Fe ₂ Al ₅ pack cementation coating formed by high activity pack. (b) EDS map shows the Al (red) and Fe(green) elemental profiles, (c) surface microstructure of coating showing entrapped pack particles.	117
Figure 4.15: EDS line profile for samples coated at (a) varying temperatures, (b) varying deposition time.	119
Figure 4.16: Mass gain of coated sample as a function of thickness. Calculated density of Fe ₂ Al ₅ was 4.36 gm/cm ³	120
Figure 4.17: Activation energies of coating formation for 5 and 10 wt% Al packs.	121
Figure 4.18: Effect of time on coating thickness. Parabolic fit suggests that coating growth follows diffusion kinetics.	124
Figure 4.19: (a) Orthorhombic unit cell of Fe ₂ Al ₅ , (b) superlattice structure.	125
Figure 4.20: XRD pattern of Fe ₂ Al ₅ coating showing {002} preferred orientation.	126
Figure 4.21: Typical kikuchi pattern obtained for Fe ₂ Al ₅ phase and calculated indexing using lattice parameters from the literature.	127
Figure 4.22: EBSD phase map and Euler map for coating and interdiffusion zone. Phase map clearly distinguishes Fe ₂ Al ₅ .	128
Figure 4.23: {002}, {020}, and {200} pole figures for Fe ₂ Al ₅ phase.	130
Figure 4.24: (a) Fracture cross-section of coating showing columnar grains growing perpendicular to the substrate surface, (b) Kirkendall voids formed due to outward diffusion of Fe ⁺³ ions and coalescence of vacancies left behind.	131
Figure 4.25: Nanoindentation matrix chosen to study the mechanical properties of coating, substrate and interdiffusion zone. (a)100mN load, (b) 200mN load.	133
Figure 4.26: Load displacement curve for matrix chosen in figure 4.25(a) for 100mN maximum load.	134
Figure 4.27: Load displacement curve for matrix chosen in figure 4.25(b) for 200mN maximum load.	135
Figure 4.28: Effect of Al content on mechanical properties (hardness and elastic modulus). Al content was measured by EDS after indentation experiments. Results are listed in Table IV, (a) Average over the range	

from continuous stiffness measurements. (b) Calculated from method by Pharr method.	137
Figure 4.29: Sulfidation behavior of Fe-Al coating. Parabolic rate constants are listed in Table 4.4.	140
Figure 4.30 : XRD pattern of scale after sulfidation at 800°C.	141
Figure 4.31: (a) Surface SE micrograph of sulfidized Fe-Al coating. Two different morphologies were observed. The compositions were characterized by EDS and XRD: (b) whiskers of Al_2S_3 , (c) adherent $\Theta\text{-Al}_2\text{O}_3$	142
Figure 4.32: SE micrograph and EDS sulfur and oxygen maps of whiskers showing whiskers are rich and sulfur and oxygen	143
Figure 4.33: SE micrograph of adherent scale. EDS maps shows high oxygen content and negligible sulfur confirming Al_2O_3 phase.	144
Figure 4.34: Mass change behavior of Fe-Al coating in air at 800 and 1000°C. Parabolic rate are listed in Table 4.4.	145
Figure 4.35: Surface morphology of oxidized coating in air at 1000°C shows formation of $\Theta\text{-Al}_2\text{O}_3$ whiskers.	146
Figure 4.36: Alumina scale on aluminized SA210 after 100 hours of oxidation at 1000°C.	147
Figure 4.37: (a) Behavior of aluminide coatings in cyclic and noncyclic environments at 800°C, (b) spallation as environment changes from sulfidizing to oxidizing.	149
Figure 4.38: XRD pattern of aluminized SA210 after 100 hour exposure to cyclic and noncyclic environments at 800°C.	150
Figure 4.39: (A) Surface microstructure of scale formed on iron aluminide diffusion coating after 100 hours exposure to cyclic sulfidizing-oxidizing environments at 800°C. Alumina whisker network is covering the surface with minor amount of Al_2S_3 . Significant cracking is evident, (B) alumina whisker network.	151
Figure 5.1: Calculated partial pressure of $\text{AlCl}(\text{g})$ for the pack compositions listed in Table 5.1. Note that pack-1 has no Al.	158
Figure 5.2: Calculated partial pressure of $\text{HfCl}_4(\text{g})$ for the pack compositions listed in Table 1.	159

Figure 5.3: Cross-section of Hf-modified iron aluminide coating coated with pack-1 condition listed in Table 5.1 and corresponding EDS maps for aluminum, iron and hafnium.	162
Figure 5.4: EDS line profile of Hf-modified aluminide coating for pack condition 1.	163
Figure 5.5: XRD pattern of Hf-modified aluminide coating for pack-1 condition.	164
Figure 5.6: Cross-section of HfFeAl coating for pack-2 condition listed in Table 5.1.	165
Figure 5.7: XRD pattern of HfFeAl coating prepared using pack-2 condition. FeAl, HfC and HfN peaks were observed as primary phases.	166
Figure 5.8: Surface micrograph of HfFeAl coating prepared using pack-3 condition listed in Table 1. Fe, Hf and Al EDS maps confirming co-deposition of Al and Hf.	167
Figure 5.9: XRD pattern of HfFeAl coating prepared using pack-3 condition. Major phases detected were FeAl and HfN.	168
Figure 5.10: Surface micrograph of HfFeAl coating prepared using pack-4 condition listed in Table 1. Fe, Hf and Al EDS spot analysis confirming co-deposition of Al and Hf as shown in Table 2.	170
Figure 5.11: XRD pattern of HfFeAl coating prepared using pack-4 condition. Major phases detected were FeAl, and HfN.	171
Figure 5.12: Surface micrograph of HfFeAl coating prepared using pack-5 condition listed in Table 1. Fe, Hf and Al EDS maps and spot analysis confirming co-deposition of Al and Hf as shown in Table 3.	172
Figure 5.13: XRD pattern of HfFeAl coating prepared using pack-5 condition. Major phase detected was Fe ₂ Al ₅ .	173
Figure 5.14: Calculated partial pressures of AlCl(g) and YCl ₃ (g) for the pack composition listed in Table for YFeAl coatings.	179
Figure 5.15: Surface SE micrograph of YFeAl coating formed by pack-1 condition listed in Table . EDS maps of Fe, Y and Al confirms co-deposition with spot analysis showing yttrium deposition in 1-2 at% range as shown in Table 5.6.	180
Figure 5.16: XRD pattern of YFeAl coating formed using pack condition-1 listed in Table 5.5. Major phase detected was FeAl.	181

- Figure 5.17: Surface SE micrograph of YFeAl coating formed by pack-2 condition listed in Table . EDS maps of Fe, Y and Al confirms co-deposition with spot analysis showing yttrium deposition in 0.08-0.2 at% range as shown in Table 5.7. 182
- Figure 5.18: XRD pattern of YFeAl coating formed using pack condition-2 listed in Table. Major phase detected was Fe_2Al_5 183
- Figure 5.19: Fe-O-S, Al-O-S, Hf-O-S and Y-O-S stability diagram at 800°C. Square symbols show the simulated laboratory environments. 185
- Figure 5.20: Corrosion kinetics of unmodified coatings in cycling sulfidizing – oxidizing environments: $p\text{O}_2 = 0.21$ atm, (S) $p\text{S}_2 = 10^{-8}$ atm. Fe-Al coating behavior in static sulfidizing environment has been shown to compare the effects of cyclic environments. 187
- Figure 5.21: Spallation observed environmental cycling from sulfidizing-to oxidizing as shown in Figure 20(a). 188
- Figure 5.22: Corrosion kinetics of YFeAl coatings as compared to unmodified-Fe-Al coatings in cycling sulfidizing –oxidizing environments: (O) $p\text{O}_2 = 0.21$ atm, (S) $p\text{S}_2 = 10^{-8}$ atm. 190
- Figure 5.23: Kinetics of YFeAl coating in cyclic environments from (a)-(c) oxidizing-to-sulfidizing, (d)-(f) sulfidizing-to-oxidizing. 191
- Figure 5.24: (a) Surface micrographs of scale on YFeAl coating with Y=1.5 at%. TGA curves are shown in Figures 5.22-5.23, (b) surface XRD pattern. 194
- Figure 5.25: Cross-section of HfFeAl coating after exposure to cyclic sulfidizing-oxidizing environments at 800°C and EDS maps of Fe, Al, Fe, S, and O. 195
- Figure 5.26: Corrosion kinetics of HfFeAl coatings as compared to unmodified-Fe-Al coatings in cycling sulfidizing –oxidizing environments: (O) $p\text{O}_2 = 0.21$ atm, (S) $p\text{S}_2 = 10^{-8}$ atm. 198
- Figure 5.27: Kinetics of HfFeAl coating in cyclic environments from (a)-(c) oxidizing-to-sulfidizing, (d)-(f) sulfidizing-to-oxidizing. 199
- Figure 5.28: Corrosion kinetics of HfFeAl and YFeAl coatings as compared to unmodified-Fe-Al coatings in cycling sulfidizing –oxidizing environments: (O) $p\text{O}_2 = 0.21$ atm, (S) $p\text{S}_2 = 10^{-8}$ atm. Fe-Al coating behavior in static sulfidizing environment has been shown to compare the effects of cyclic environments. 201

- Figure 5.29: Corrosion mechanism for RE-modified Fe-Al coatings in cyclic oxidizing-sulfidizing environments. 206
- Figure 5.30: Corrosion kinetics of YFeAl coatings as compared to unmodified-Fe-Al coatings in cycling sulfidizing –oxidizing environments: (O) $p_{O_2} = 0.21$ atm, (S) $p_{S_2} = 10^{-8}$ atm. 208
- Figure 5.31: Kinetics of YFeAl coating in cyclic environments from (a)-(c) oxidizing-to-sulfidizing, (d)-(f) sulfidizing-to-oxidizing. 209
- Figure 5.32: Corrosion kinetics of YFeAl coatings as compared to unmodified-Fe-Al coatings in cycling sulfidizing –oxidizing environments: (O) $p_{O_2} = 0.21$ atm, (S) $p_{S_2} = 10^{-8}$ atm. 210
- Figure 5.33: Kinetics of HfFeAl coating in cyclic environments from (a)-(c) oxidizing-to-sulfidizing, (d)-(f) sulfidizing-to-oxidizing. 211
- Figure 5.34: Y, Al, O, Fe and S x-ray maps of scale developed on YFeAl coating (Y~0.3 at%) after exposure to cyclic gaseous environment at 800°C for 100 hours. 213
- Figure 5.35: Surface micrograph of HfFeAl coating (Hf~0.4 at%) after exposure to cyclic gaseous environment at 800°C for 100 hours. 214
- Figure 5.36: Hf, O, Al, Fe and S x-ray maps of scale developed on HfFeAl coating (Hf~0.4 at%) after exposure to cyclic gaseous environment at 800°C for 100 hours. 215
- Figure 5.37: Corrosion kinetics of HfFeAl and YFeAl coatings as compared to unmodified-Fe-Al coatings in cycling sulfidizing –oxidizing environments: (O) $p_{O_2} = 0.21$ atm, (S) $p_{S_2} = 10^{-8}$ atm. Fe-Al coating behavior in static sulfidizing environment has been shown to compare the effects of cyclic environments. 216
- Figure 6.1: Typical luminescence spectra obtained from Al_2O_3 scales on oxidized aluminide coatings. Deconvolution of peaks was carried out as described in section 6.1.2 225
- Figure 6.2: Thermal cycling expected from removing from and reinserting the samples into the heating zone. High cooling/heating rates can create tensile stresses. 226
- Figure 6.3: (a) Thermal cycling at 1000°C for uncoated, aluminized, Hf-modified, and Y-modified aluminide coatings in air, (b) magnified view of aluminide coatings 227

- Figure 6.4: SA210 after first thermal cycle at 1000°C, (a) Spallation and detachment of Fe₃O₄ scale at edges, (b) heave cracking at the planer surface. 229
- Figure 6.5: (a) Surface micrograph of unmodified Fe-Al coating after 10 one day thermal cycles from 1000°C to room temperature. (b) spalled region of scale. 230
- Figure 6.6: Rumpling or wavy morphology of alumina scale developed on Fe-Al coating after 240 hours of thermal cycling at 1000°C. 232
- Figure 6.7: Surface morphology of scale developed after 240 hours of thermal cycling on (a) YFeAl , (b) HfFeAl. 233
- Figure 6.8: Cross-section after 10 one day thermal cycles for scale on Fe-Al coating. 234
- Figure 6.9: Cross-section after 10 one day thermal cycles for scale on YFeAl coating showing smaller mean grain size as compared to unmodified coating in Figure 6.8. 234
- Figure 6.10: Cross-section after 10 one day thermal cycles for scale on HfFeAl coating with magnified view showing smaller grain size as compared to unmodified coating and Y-modified coating (see Figures 6.8 and 6.9). 235
- Figure 6.11: Surface and contour plots of stress maps of Fe-Al coating at sample edge after 72 hours of cyclic oxidation at 1000°C. 238
- Figure 6.12: Surface and contour plots of stress maps of Fe-Al coating at center of sample after 72 hours (3 cycles) of cyclic oxidation at 1000°C. 239
- Figure 6.13: Surface and contour plots of stress maps of Fe-Al coating at edge of sample after 168 hours (7 cycles) of cyclic oxidation at 1000°C. 241
- Figure 6.14: Surface and contour plots of stress maps of Fe-Al coating at center of sample after 168 hours (7 cycles) of cyclic oxidation at 1000°C. 242
- Figure 6.15: Surface and contour plots of stress maps of Fe-Al coating at edge of sample after 240 hours (10 cycles) of cyclic oxidation at 1000°C. 243
- Figure 6.16: Surface and contour plots of stress maps of Fe-Al coating at center of sample after 240 hours (10 cycles) of cyclic oxidation at 1000°C. 244
- Figure 6.17: Surface and contour plots of stress maps of Hf-Fe-Al coating at edge after 72 hours (3 cycles) of cyclic oxidation at 1000°C. 246
- Figure 6.18: Surface and contour plots of stress maps of Hf-Fe-Al coating at center of sample after 72 hours (3 cycles) of cyclic oxidation at 1000°C. 247

Figure 6.19: Surface and contour plots of stress maps of Hf-Fe-Al coating at edge of sample after 168 hours (7 cycles) of cyclic oxidation at 1000°C.	248
Figure 6.20: Surface and contour plots of stress maps of Hf-Fe-Al coating at center of sample after 168 hours (7 cycles) of cyclic oxidation at 1000°C.	249
Figure 6.21: Surface and contour plots of stress maps of Hf-Fe-Al coating at edge of sample after 240 hours (10 cycles) of cyclic oxidation at 1000°C.	250
Figure 6.22: Surface and contour plots of stress maps of Hf-Fe-Al coating at center of sample after 240 hours (10 cycles) of cyclic oxidation at 1000°C.	251
Figure 6.23: Stress distribution for Fe-Al, HfFeAl and YFeAl at corner grid after cyclic oxidation at 1000°C for (a) –(c) 72 hours, (d)-(f) 240 hours, respectively. Reactive element addition improves ability of scale to accommodate stresses.	254
Figure 6.24: Effect of reactive element doping on average stress in alumina scales during cyclic oxidation at 1000°C: (a) at edge of sample, (b) at middle of sample.	255
Figure A-1: Concentration of O ₂ measured in kraft recovery boiler.	263
Figure A-2: Concentration of CO ₂ measured in kraft recovery boiler.	263
Figure A-3: Concentration of COS measured in kraft recovery boiler.	264
Figure A-4: Concentration of CH ₃ S measured in kraft recovery boiler.	264
Figure A-5: Concentration of CH ₄ measured in kraft recovery boiler.	265
Figure A-6: Concentration of H ₂ measured in kraft recovery boiler.	265
Figure A-7: Concentration of H ₂ S measured in kraft recovery boiler.	266
Figure A-8: Concentration of CO measured in kraft recovery boiler.	266
Figure C-1: Surface and contour plots of stress maps of Y-Fe-Al coating at edge of sample after 72 hours (3 cycles) of cyclic oxidation at 1000°C.	272
Figure C-2: Surface and contour plots of stress maps of Y-Fe-Al coating at center of sample after 72 hours (3 cycles) of cyclic oxidation at 1000°C.	273
Figure C-3: Surface and contour plots of stress maps of Y-Fe-Al coating at edge of sample after 168 hours (7 cycles) of cyclic oxidation at 1000°C.	274

- Figure C-4: Surface and contour plots of stress maps of Y-Fe-Al coating at center of sample after 168 hours (7 cycles) of cyclic oxidation at 1000°C. 275
- Figure C-5: Surface and contour plots of stress maps of Y-Fe-Al coating at edge of sample after 240 hours (10 cycles) of cyclic oxidation at 1000°C. 276
- Figure C-6: Surface and contour plots of stress maps of Y-Fe-Al coating at center of sample after 240 hours (10 cycles) of cyclic oxidation at 1000°C. 277

SUMMARY

Industrial and power generation processes employ units like boilers and gasifiers to burn sulfur containing fuels such as coal or industrial waste to produce steam and syn gas (H_2 and CO), which can be used to generate electricity using turbines and fuel cells. These units often operate under environments containing gases such as H_2S , SO_2 , O_2 etc, which can attack the metallic structure and impose serious problems of corrosion. The shutdown of units and replacements of corroded material can in turn limit the cost effective operation of industrial processes. Corrosion control in high temperature sulfur bearing environments is a challenging problem requiring information on local gaseous species at the surface of alloy components and mechanisms of degradation (sulfidation or erosion corrosion) in these environments. Coatings have proved to be a better alternative for improving corrosion resistance of alloys without compromising their bulk mechanical properties.

Changes in process conditions may result in thermal cycling and/or environment cycling between oxidizing and sulfidizing environments at the alloy surface. Thermal or environmental cycling can damage the protective scale formed on the alloy surface, leading to a significant increase in the rate of corrosion. Objective of this study was to understand the effect of fluctuating environments on corrosion kinetics of carbon steels and develop diffusion based coatings to mitigate the high temperatures corrosion under these conditions. More specifically, the focus was : (1) to characterize the local gaseous environments at the surface of alloys in boilers; (2) optimizing diffusion coatings

parameters for carbon steel; (3) understand the underlying failure mechanisms in cyclic environments; (4) to improve aluminide coating behavior by co-deposition of reactive elements (RE) such as Yttrium and Hafnium; (5) to formulate a plausible mechanism of coating growth and effects of alloying elements on corrosion; and (6) to understand the spallation behavior of scale by measuring stresses in the scales.

The understanding of coating mechanism and effects of fluctuating gaseous environments provides information for designing materials with more reliable performance. The study also investigates the mechanism behind the effect of reactive elements on scale adhesion and sulfidation behavior. Thus, the present work will have a broad impact on the field of materials and coatings selection for high temperature industrial environments such as boilers and gasifiers, and provides information on RE-modified aluminized coatings on carbon steel as an alternative for the use of bulk superalloys under high temperature sulfur bearing environments.

CHAPTER I

INTRODUCTION

MOTIVATION

The ability of a material to reliably perform under high temperature aggressive environments, without degradation of the bulk mechanical properties, is one of the most important requirements for its selection for the power generation equipment. Addition of elements in alloys that can form thermodynamically stable protective layers is the fundamental aspect of any corrosion prevention methodology. One effective way is by enriching these elements at the surface through coatings, without compromising the bulk properties of the base alloy. There have been numerous studies on the development of aluminum and chromium rich coatings for the oxidizing environments. Tremendous progress has been made to increase the component-life in high oxygen containing environments. For clean and efficient power generation, new processes to produce energy from a variety of fuels continue to be developed. One such technology is gasification, which may be used for high sulfur containing fuels such as coal, black liquor, etc. Pyrolysis of high sulfur fuels creates reducing environments containing H_2S , which may accelerate degradation and failure of alloys. Thermal fluctuations, frequently experienced in boilers and gasifiers, can also be detrimental factor as sudden temperature changes may affect the scale stability causing it to spall, exposing the alloy to aggressive environments. Recent study^[1,2,3,4,5] showed that local gaseous compositions may also be unstable and fluctuate between oxidizing and sulfidizing. This necessitates development of high temperature sulfidation/oxidation resistant alloys and coatings. Published literature presents vast number of studies on coatings for nickel based alloys, developed

for oxidizing environments, which fail catastrophically in sulfur containing environments. The alternative to nickel based alloys is iron based alloys with superior sulfidation resistant coatings. Another criteria for some of combustion and gasification equipment is that the corrosion resistant coatings should also be hard enough to withstand the erosion due to flying ash particles (solid particulate erosion). The motivation of the present work was to better understand and develop coatings for iron based alloys (i.e. steels) that are resistant to high temperature fluctuating gaseous environments, and erosion corrosion. These include, but are not limited to:

1. Characterization of fluctuating environments (sulfidizing-oxidizing) in industrial boilers.
2. Stability of protective scales and mechanism of failure modes in simulated fluctuating environments.
3. Optimum parameters to develop Al and/or Cr based diffusion coatings for steels to withstand cyclic gaseous/thermal conditions and understand the kinetics of coating growth.
4. Investigate effects of alloying elements (Y and Hf) in diffusion coatings on their sulfidation/oxidation behavior.
5. Understand mechanism of protective scale stability under cyclic gaseous and thermal environments for Fe-Al, HfFeAl and YFeAl coatings.

BACKGROUND AND LITERATURE REVIEW

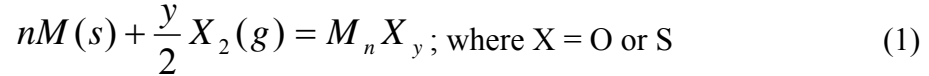
Reliable and cost effective operation of current and future power generation processes like gasification rely upon the performance of high temperature alloys in corrosive environments containing oxygen, sulfur, carbon species and solid particulates. These environments can cause chemical degradation such as oxidation, sulfidation and carburization, and mechanical corrosion such as particulate erosion. Corrosion prevention in these environments can be achieved if the alloy forms continuous, thermodynamically stable and self-healing protective oxide scale, such as alumina (Al_2O_3) and chromia (Cr_2O_3), on its surface. However, bulk addition of relevant alloying elements (aluminum, chromium) in quantities needed to form protective scale can compromise mechanical properties and cost. The optimum solution for these systems is to use a cost-effective material, with desired mechanical properties, as a base metal and modify its surface to provide protection against corrosive environments. Thus, high temperature alloys employ aluminide or chromized diffusion coatings to enrich the surface with the desired protective oxide scale-forming element(s).

1.1 OXIDATION AND SULFIDATION OF METALS AND ALLOYS

The high temperature oxidation and sulfidation of metals and alloys is a metal consuming process. The rate of corrosion depends on the reaction temperature and the reactive gas composition or partial pressure of reactive gases in the environment. In this section the mechanism and kinetics of metal corrosion by gaseous species such as oxygen and sulfur are reviewed.

1.1.1 Thermodynamics Considerations

When a metal is exposed to a gaseous species, such as oxygen or sulfur at high temperature, the corrosion product will be formed:



The second law of thermodynamics suggests that the driving force of the reaction can be given by:

$$\Delta G = \Delta G^\circ + RT \ln\left(\frac{a_{M_n X_y}}{a_M^n p_{X_2}^{\frac{y}{2}}}\right) \quad (2)$$

Where ΔG and ΔG° are the Gibbs free energy change and the standard free energy of formation, respectively, R is the universal gas constant, T is the absolute temperature, $a_{M_n X_y}$ and a_M are the activities of corrosion product and metal respectively, and p_{X_2} is the partial pressure of gaseous species. $\Delta G < 0$ will show the favorable reaction at temperature T . Activities of metal and corrosion product can be assumed as unity and thus equation can be rearranged to calculate the dissociation partial pressure of corrosion product at equilibrium ($\Delta G = 0$) as:

$$p_{X_2}^\circ = \exp\left(\frac{2\Delta G^\circ}{yRT}\right) \quad (3)$$

For $p_{X_2}^\circ > p_{X_2}$, the corrosion of the metal will occur. In the Ellingham diagram, straight lines are drawn to show the standard free energy of formation of oxides and sulfides as function of temperatures. Figure 1.1 and 1.2 shows the Ellingham diagrams for oxides

and sulfides respectively^[6]. Lower is the reaction line in the Ellingham diagram, more stable will the oxide/sulfide, for example Al_2O_3 and Cr_2O_3 are more stable than Fe_2O_3 .

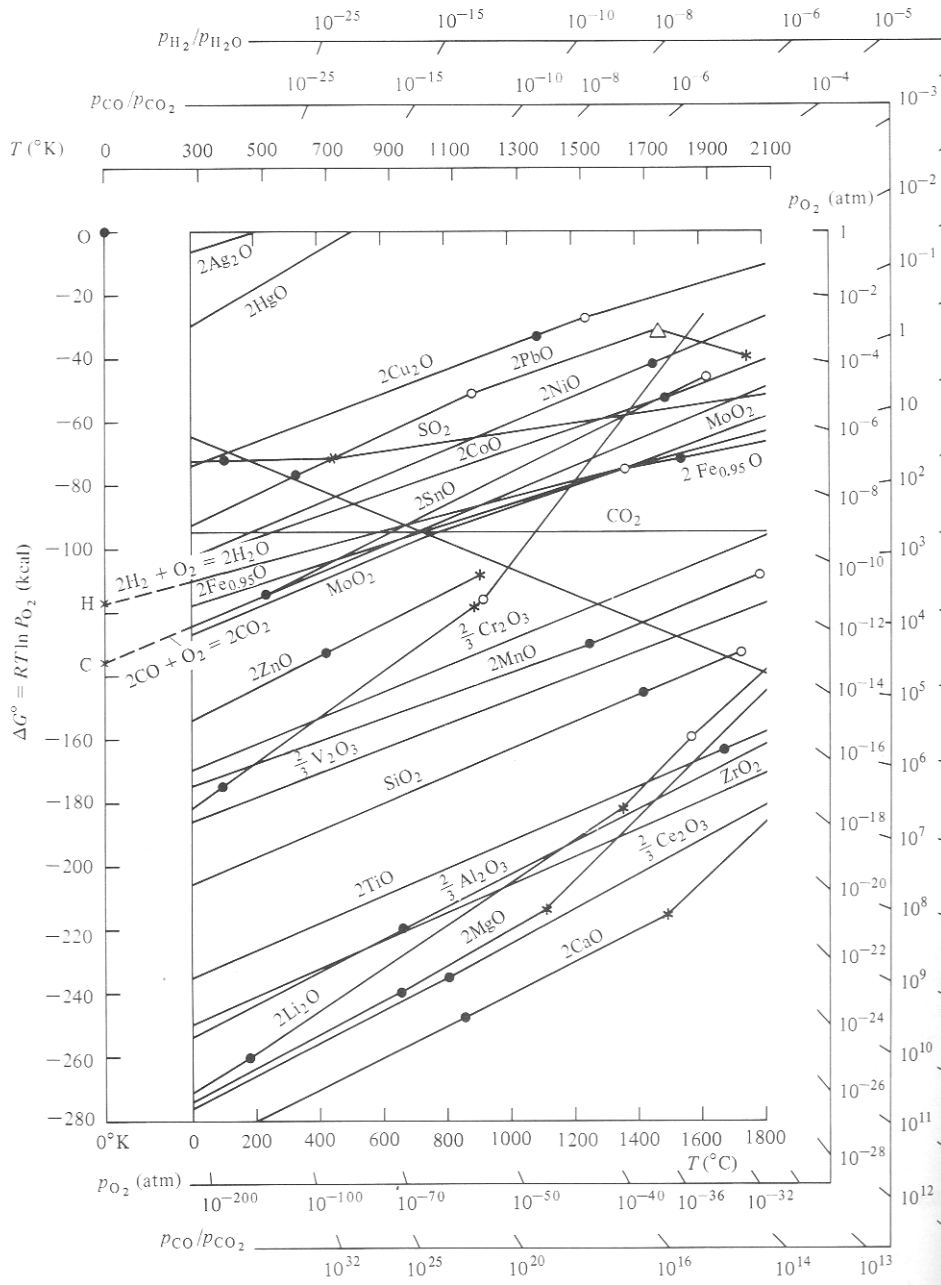


Figure 1.1: Ellingham diagram: Standard Gibbs free energy of formation for selected oxides ^[6].

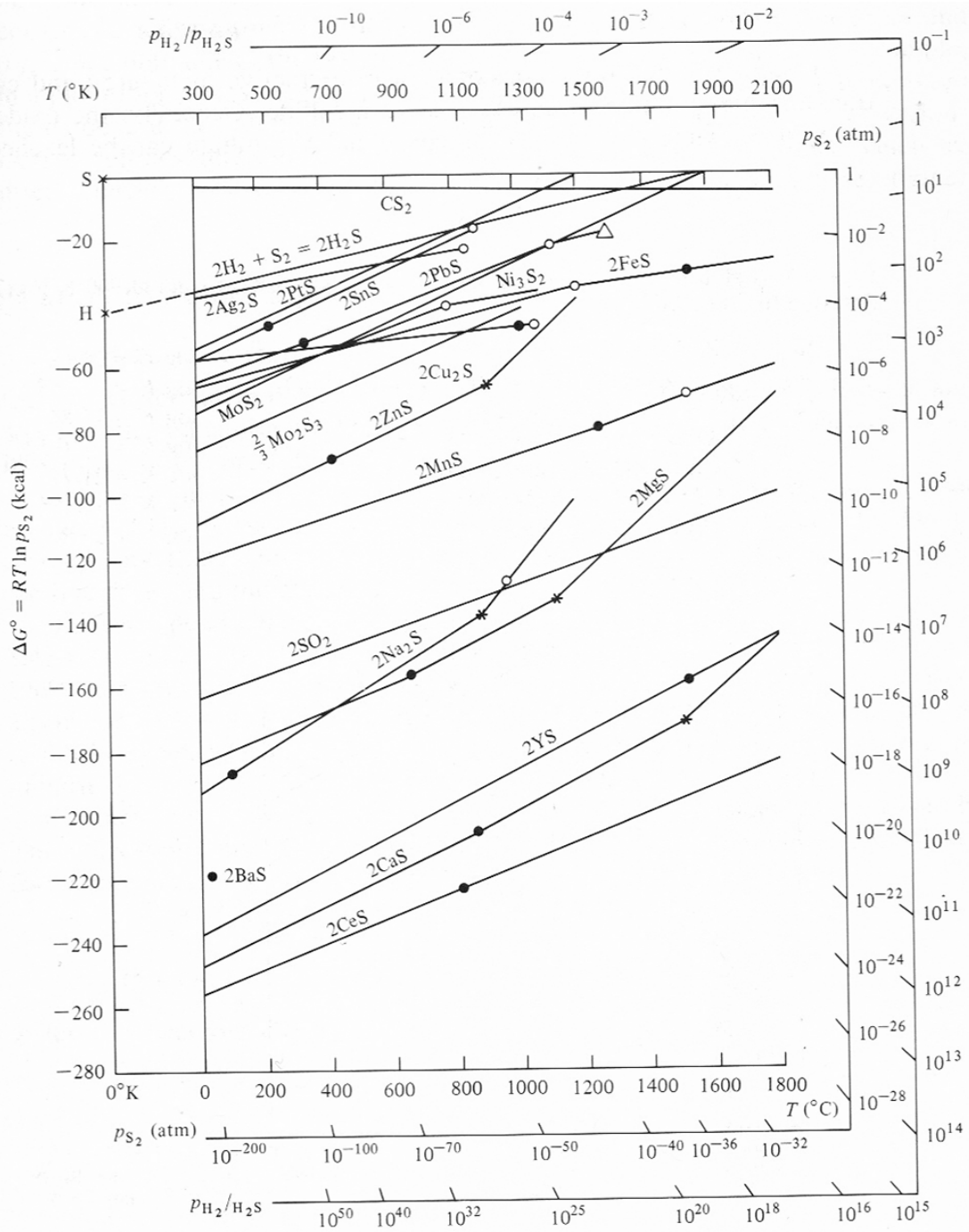


Figure 1.2: Ellingham diagram: Standard Gibbs free energy of formation for selected sulfides^[6].

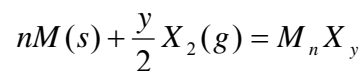
1.1.2 Corrosion products

On the submolecular level, the composition of corrosion products may deviate from their ideal stoichiometric chemical formulas. This results into defects in the corrosion product film. These defects in turn control the electrochemical behavior of the scale. By nature of the defects found in their lattices, they can be categorized as:

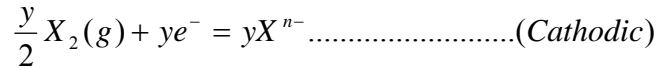
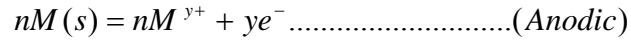
- i. *p-type metal-deficit product*, which contains metal cation vacancies. Cations diffuse in the corrosion product lattice by exchange with these vacancies. Charge neutrality in the lattice is maintained by the presence of electron holes or metal cations of higher than average positive charge. Current is passed by positively charged electron holes. For example Fe_{1-x}S is a iron deficit sulfide.
- ii. *n-type cation interstitial metal-excess product*, which contains interstitial cations, in addition to the cations in the crystal lattice. Charge neutrality is established through an excess of negative conduction electrons, which provide electrical conductivity in these scales.
- iii. *n-type anion vacancy containing scale*, which contains anion vacancies in the crystal lattice. Current is carried by electrons, excess of which is present in these scales to establish charge neutrality.

1.1.3 Electrochemistry and corrosion reactions

High-temperature gaseous corrosion reactions proceed by an electrochemical mechanism, with some similarities to the aqueous corrosion. For example, the reaction,



is a combination of two separate reactions:



The growth of an *n*-type cation interstitial product at the scale-gas interface is illustrated in Figure 1.3a. Interstitial metal cations are liberated at the metal-scale interface and migrate through the interstices of the scale to the scale-gas interface. Conduction band electrons also migrate to the scale-gas interface, where the fresh product is formed and the scale growth takes place.

For the *n*-type anion vacancy products, film growth tends to occur at the metal-scale interface, as shown in Figure 1.3b. Conduction band electrons migrate to the scale-gas interface, where the cathodic reaction occurs. The X^{n-} anions produced at this interface migrate through the scale lattice by exchange with anion vacancies. The metal cations are produced by the anodic reaction at the metal-scale interface. Final reaction product is formed and the growth of scale takes place at the metal/scale interface.

In the case of the *p*-type metal deficit oxides, metal cations produced by the anodic reaction at the metal-scale interface migrate to the scale-gas interface by exchange with cation vacancies. Electron charge is effectively transferred to the scale-gas interface by the movement of electron holes in the opposite direction (toward the metal-scale interface). The cathodic reaction and the scale growth by the formation of final product occur at the scale-gas interface (Figure 1.3a). Diffusion of defects (excess cations, cation vacancies, or anion vacancies) through the scale has very significant effect on the kinetics of corrosion at high temperatures.

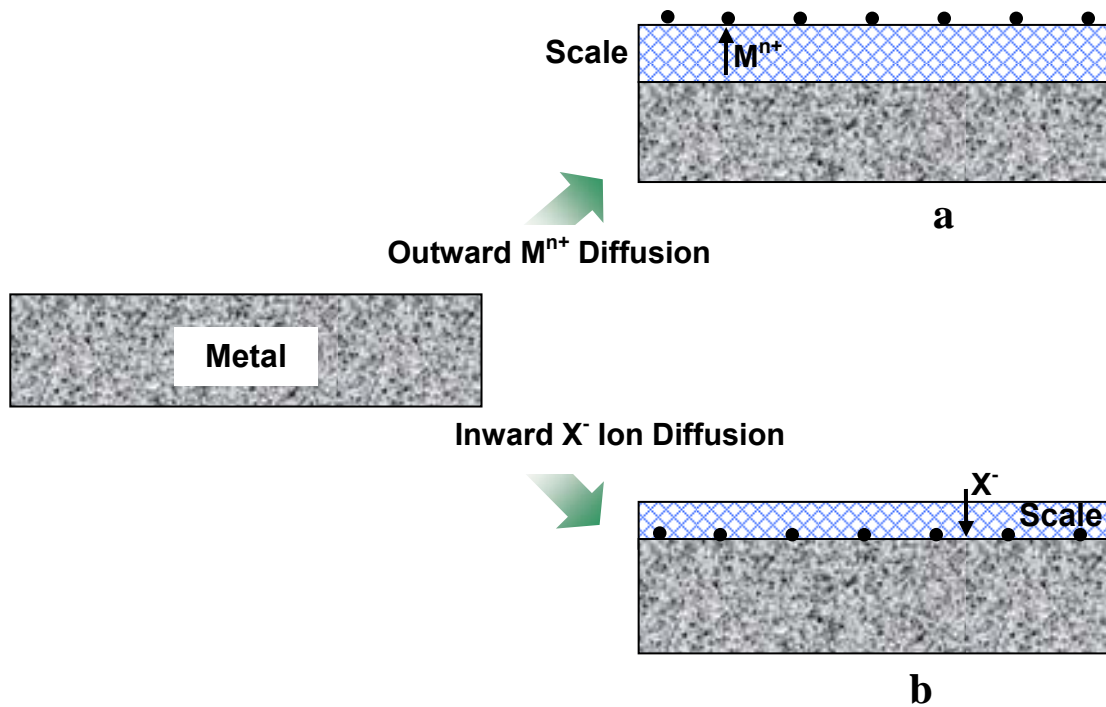


Figure 1.3: Scale formation by (a) outward diffusion of metal ion, (b) inward diffusion of gaseous species (S^{2-} or O^{2-}). Black dots show the location of scale growth.

1.2 KINETICS OF CORROSION

1.2.1 Parabolic Law:

The scale formation process for a metal M exposed to a reactant, such as O_2 , includes several stages such as: the adsorption of oxygen molecules on the metal surface, dissociation of O_2 into atoms, diffusion of reactants through the scale, final reaction and the formation of an oxide (Figure 1.4). The initial oxide nuclei will form at specific locations on the metal surface. Continuous oxide layer will be formed by their subsequent growth. When reactants are separated by a scale without physical discontinuities, such as cracks and pores, the diffusion of one or both reactants through the lattice and along grain boundaries will occur to support the further reaction.

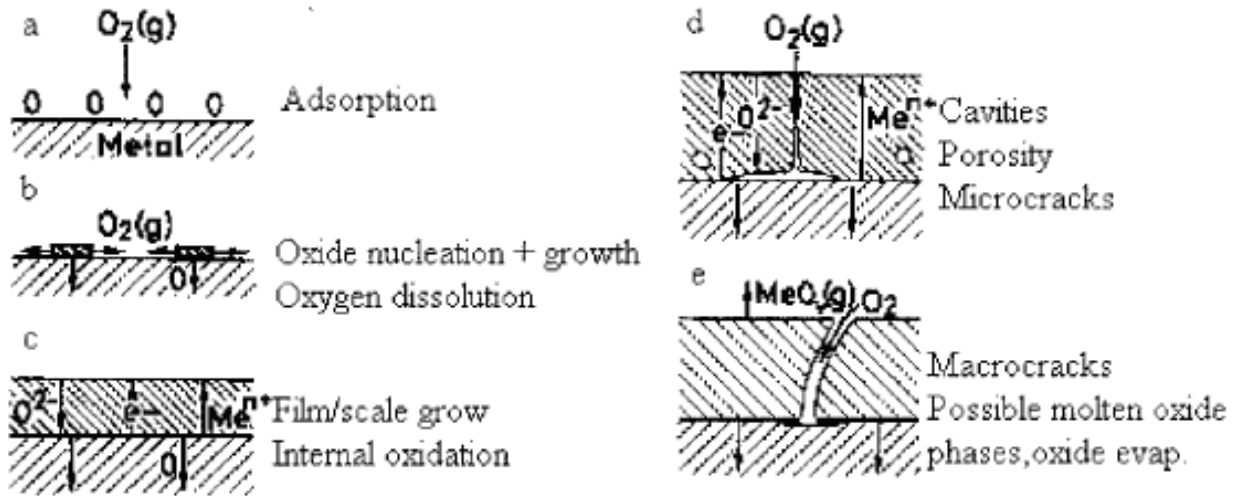


Figure 1.4: Scale formation mechanism in oxidative environment.

Both the chemical and electrical potential gradients provide the driving force for solid-state diffusion. If the ionic transport across the developing oxide layer controls the scaling rate, and thermodynamic equilibrium is established at all interfaces, then the outward cation flux, $j_{M^{n+}}$ is equal and opposite to the inward cation vacancy flux, j_{V_M} , Figure 1.5 shows a simplified model for diffusion-controlled oxidation. In mathematical terms,

$$j_{M^{n+}} = -j_{V_M} = D_{V_M} \frac{C_{V_M}'' - C_{V_M}'}{X} \quad (4)$$

Where, X is the thickness of oxide, D_{V_M} is the diffusion coefficient for cation vacancies, and C_{V_M}'' and C_{V_M}' are the vacancy concentration at the scale-gas and scale-metal interface

respectively. In the view of thermodynamic equilibrium established at each interface, $C_{V_M}'' - C_{V_M}'$ is constant, thus,

$$\frac{dX}{dt} = VJ_{V_M} = VD_{V_M} \frac{C_{V_M}'' - C_{V_M}'}{X} \quad (5)$$

Where V is the volume of oxide formed per unit of flux, and t is time. The equation can be reduced to

$$\frac{dX}{dt} = \frac{k'}{X} \quad \text{where, } k' = D_{V_M} \frac{C_{V_M}'' - C_{V_M}'}{\text{const.}} \quad (6)$$

Upon integration,

$$X^2 = k_p' t + C \quad (7)$$

where k_p' is parabolic rate constant in $\text{cm}^2 \cdot \text{sec}^{-1}$ and C is a constant.

In terms of weight gain,

$$\left(\frac{\Delta W}{A}\right)^2 = k_p t + C, \quad (8)$$

where $\left(\frac{\Delta W}{A}\right)^2$ is weight gain per unit area. Equation shows that the rate controlling step

for the corrosion is diffusion controlled and thus the scale is protective in nature. For pure

Fe, oxidation rate at 1000°C is $4.8 \times 10^{-7} \text{ g}^2 \text{ cm}^{-4} \text{ sec}^{-1}$ [7].

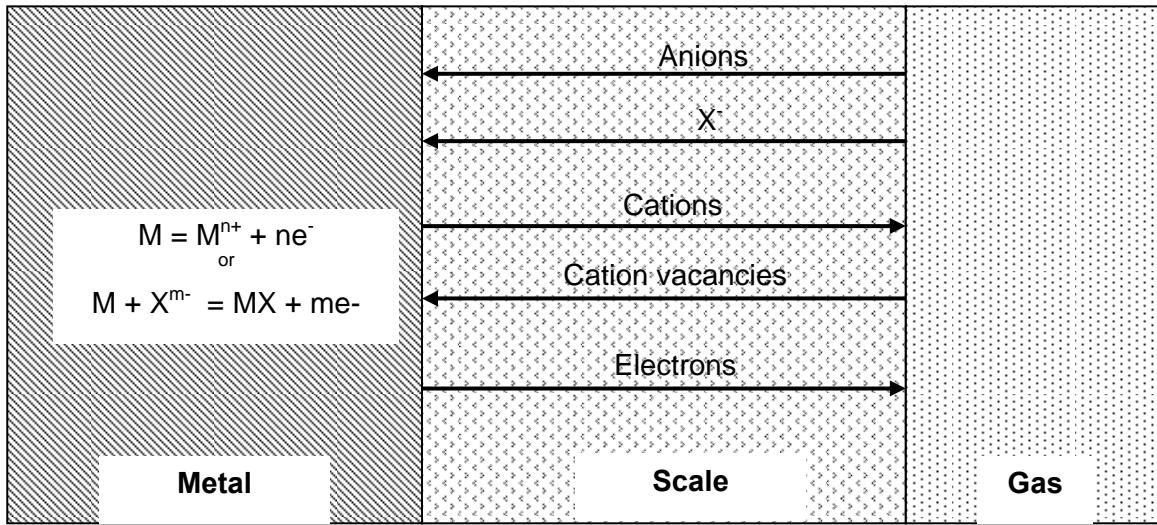


Figure 1.5: Diffusion controlled high temperature gaseous corrosion.

1.2.2 Linear rate law

When a phase boundary process is the rate-determining step for the reaction, metal oxidation obeys the linear rate law.

$$X = k_1 t \quad \text{or} \quad \left(\frac{\Delta W}{A}\right) = k_1 t \quad (9)$$

where k_1 is the linear rate constant with units $\text{cm}\cdot\text{sec}^{-1}$ or $\text{mg}\cdot\text{cm}^{-2}\cdot\text{sec}^{-1}$. The linear rate law is commonly observed when the oxidation is carried out in an atmosphere, which is diluted by inactive or inert gas or if the oxide formed is not protective. In the former case, the process of oxygen delivery to or adsorption onto the scale is so slow that it becomes the rate-controlling step rather than diffusion through the scale. In the latter case, a boundary reaction is the rate-controlling step rather than any mass transport process.

1.3 FLUCTUATING TEMPERATURES AND GASEOUS ENVIRONMENTS

Environments are frequently classified in terms of oxygen activity, as either “oxidizing or reducing”. An oxidizing atmosphere is an environment that contains molecular oxygen (O_2), such as air or a combustion atmosphere with excess “free” oxygen. Oxygen activity in this case is very high and is controlled by the concentration of molecular oxygen. A reducing atmosphere is generally produced in combustion systems under stoichiometric or substoichiometric conditions (combustion products are generally comprised of CO_2 , CO , H_2O , H_2 , and products of impurities coming from fuel and/or feedstock, such as H_2S) with no excess oxygen. The oxygen activity is very low in this case and is controlled by the ratio of gas constituents in the environment, like CO/CO_2 , H_2/H_2O or H_2/H_2S . The reducing environment is generally more corrosive for many corrosion scenarios, such as sulfidation, carburization, nitridation, and ash/salt deposit corrosion. Clearly, the protective oxide scale formation is more limited under such reducing conditions. It is for this reason that the reducing industrial environments are generally considered to be more corrosive than the oxidizing variety. The corrosion forms, that can be considered as high temperature corrosion are: oxidation, sulfidation, halogen corrosion, carburization, metal dusting, etc. Industries like chemical processing, refining and petrochemical industries, automotive, ceramic, pulp and paper, fossil fuel power generation, coal gasification, etc are faced with high temperature corrosion. Some of industrial fuels or coal grades used in these boilers also contain high concentration of sulfur. Kraft recovery boiler and black liquor gasifiers in the pulp and paper industry is one such example^[1-3] which uses black liquor as fuel to generate energy. Figure 1.6 shows a schematic of a typical Kraft recovery boiler.

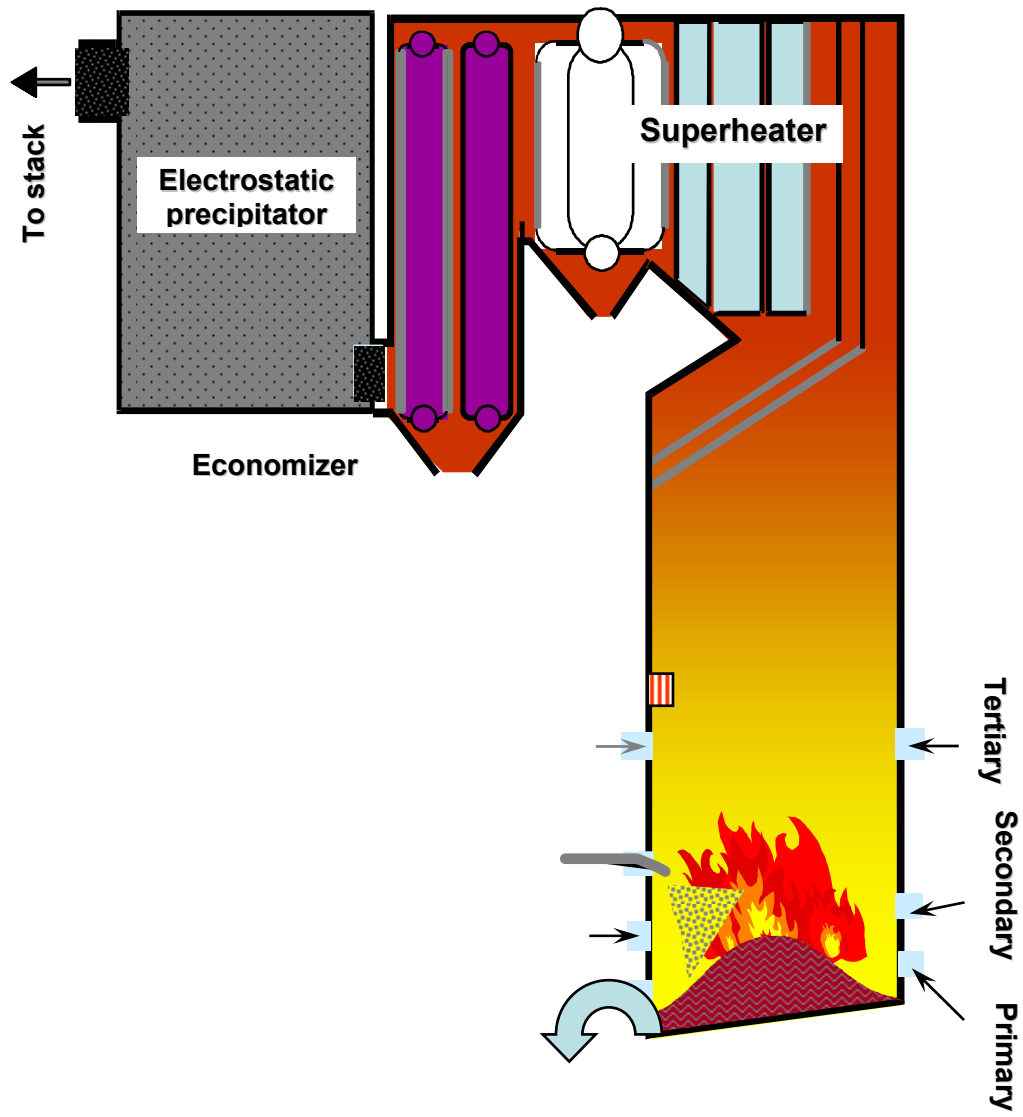


Figure 1.6: Schematic of typical Kraft Recovery Boiler used in pulp and paper industry for power generation

Typical composition of black liquor is shown in Table 1.1 ^[8] and gaseous environment generated due to combustion of black liquor in different power generation equipments used in pulp and paper industry is shown in Table 1.2 For kraft recovery boilers, the

Table 1.1: Black liquor chemical analysis and calculated solid content. Also shown is the gaseous environment generated during combustion of black liquor^[8].

Solid	%	66-69	CO	Dry %	30.23
C	Dry %	36.5	CH ₄	Dry %	11.33
H	Dry %	3.6	H ₂	Dry %	0.54
O	Dry %	32.41	H ₂ S	Dry %	1.24
S	Dry %	6.71	CH ₃ SH	Dry %	1.76
Na	Dry %	18.7	NH ₃	Dry %	0.44
K	Dry %	1.56	Fixed C	Dry %	11.14
Cl	Dry %	0.15	Na ₂ SO ₄	Dry %	2.9
N	Dry %	0.37	Na ₂ CO ₃	Dry %	28.41
Total	Dry %	100	K ₂ CO ₃	Dry %	2.75
HHV	MJ/kgDS	13.7	NaCl	Dry %	0.23
			Na ₂ S	Dry %	9.03
			Total	Dry %	100

environment in the lower parts of furnace is reducing due to availability of sub-stoichiometric amount of oxygen and constant consumption of oxygen and release of reducing gases during pyrolysis reactions like hydrogen sulfide and methyl mercaptans along with other reducing gases like hydrogen and carbon monoxide. In sulfur containing environments with low pO₂, rapid formation of metal sulfides is a major mode of degradation causing a premature failure of alloy components. It has been demonstrated by Strafford and Datta^[4] that the rates of sulfidation of these alloys are often several

magnitudes higher than respective rates of their oxidation under otherwise similar conditions.

Table 1.2: Gaseous environments generated due to combustion of black liquor in power generation equipments in pulp and paper industry

	Pulse Heater Combustor (vol%)	Reformer/ Gasifier Semi-Chem (vol%)	Reformer/ Gasifier Kraft (vol%)	Reformer/ Gasifier Sulfite (vol%)
H₂S		0.03	1.5	2.7
H₂		39	44.8	27.8
H₂O	10-25	40	27.4	49.8
CO	0-0.5	5.6	9.9	3.2
CO₂	5-15	14.2	15.1	14.4
Organics		1.4	1.3	1.8
O₂	2-10			
N₂	63-67			

Temperature has a significant effect on the kinetics of oxidation or sulfidation of steels. Thermal excursions experienced by the alloy surfaces can potentially damage the scale and may cause higher rates of corrosion by introducing micro-cracks in the scale ^[5,9]. Schulte et al. ^[10] reported the damage of sulfide scales by temperature fluctuations due to the differences in the coefficient of thermal expansion between the sulfide scale and the

steel. Osgerby et al.^[11] have reported significant cracking of the surface scale due to a thermal expansion mismatch between an oxide scale (haematite–magnetite-spinel) and the substrate due to a temperature excursion of the order of 300-400°C for 9-Cr martensitic steels. In boilers, tubes are known to experience thermal excursions of the order <500°C ^[12,13,14,15], depending on the location in the furnace and boiler operations. A previous study^[12] has shown that the rapid thermal cycling (~5cycles/day) over a small temperature range (300-400°C) can significantly increase the corrosion rate of carbon steels. Al-Hassan et al. ^[12] have shown that the temperature spikes did not change the scale composition for the carbon steel exposed to a sulfidizing environment for up to 15 days. This suggests that primary reason of increased corrosion rates is scale cracking/spallation leading to easy access of reactants to the exposed metal surface.

Previously researchers considered the environment at the surface of tubes to be similar to the bulk gas environments in boilers ^[13]. Environment characterization studies have shown that the bulk environment may be very different from the waterwall environment, especially in the lower furnace of boilers. However, for corrosion reactions, local environment at the tube surface are more important than the bulk environment. Thermodynamics calculations indicate that at pyrolysis temperature of 700°C (>waterwall surface temperature) or lower, CH₃SH and H₂S are more stable and are likely to be higher in concentration in the vicinity of waterwall tubes than in the bulk of the flue gas, particularly away from the airports^[13]. Recent studies ^[10] have shown that the thermal and the chemical environments at the surface of tubes may vary with the local environmental conditions like combustion of partially burnt black liquor at the surface. In

case where the black liquor or other sulfur containing fuel is sprayed on the boiler tube surface and undergoes a direct pyrolysis, the reduced sulfur gases may be available at the waterwall surface because of the low temperature and the low oxygen partial pressure. This can lead to a change in the ratio of methyl mercaptans and dimethyl sulfides to hydrogen sulfide ^[15]. This may also change the local oxygen to sulfur ratio and favor a sulfide corrosion product rather than an oxide. These variations in the oxygen to sulfur partial pressure can result into catastrophic corrosion conditions ^[16]. Corrosion behavior of metals and alloys in oxidizing-sulfidizing environments has been studied by a number of researchers ^[17,18,19,20,21] to simulate the industrial conditions. Yuan et al^[8] has recently studied, using computational fluid dynamics simulations (CFD), the changes in concentration of corrosive environments in kraft recovery boilers with changes in operating conditions such as air flow, droplet size, and temperature of black liquor feed. Figure 1.7 and 1.8 shows the changes in H₂S concentration with decrease in droplet size and increase in air flow respectively. It has been shown that reduced droplet size increases the fuel deposition on walls, thus increasing the sulfidizing environment at the surface of tubes. No apparent change in bulk environment is reported from these CFD models. Depending upon the boiler design, changes in the air flow may also increase the H₂S concentration in certain parts of boiler furnace. Figure1. 9 shows the changes in temperature due to increase in air flow by 10 volume %. A slight variation in tube temperature in the mid furnace area has been shown due to changes in operating conditions. It has been suggested that flow instabilities in the mid-furnace areas could make major contributions to the cyclic nature of oxidizing and reducing atmosphere.

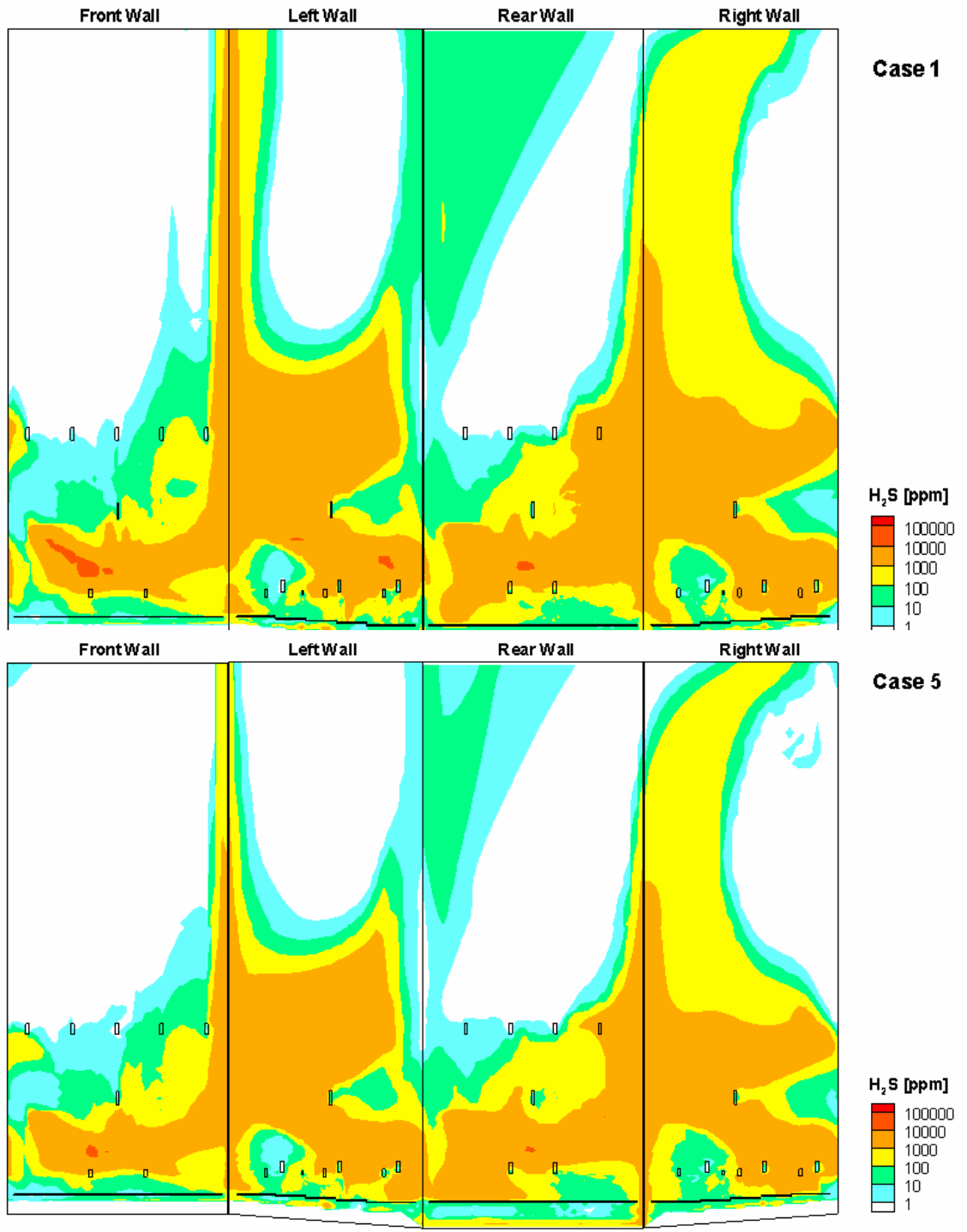


Figure 1.7: Changes in H₂S concentration by decreasing the droplet size of black liquor feed in Kraft recovery boiler.

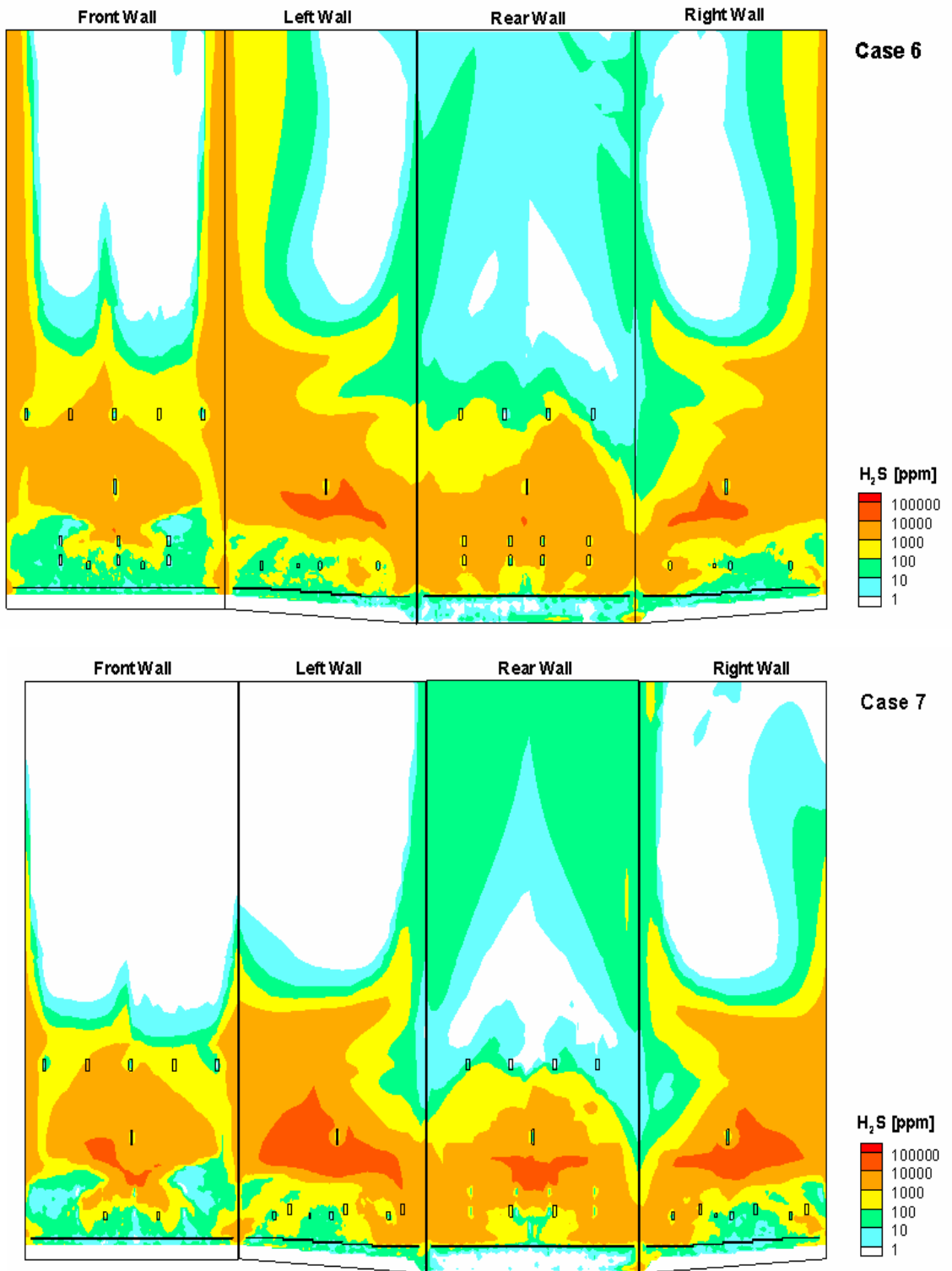


Figure 1.8: Changes in H₂S concentration by increasing the tertiary air flow by 10 volume % in Kraft recovery boiler.

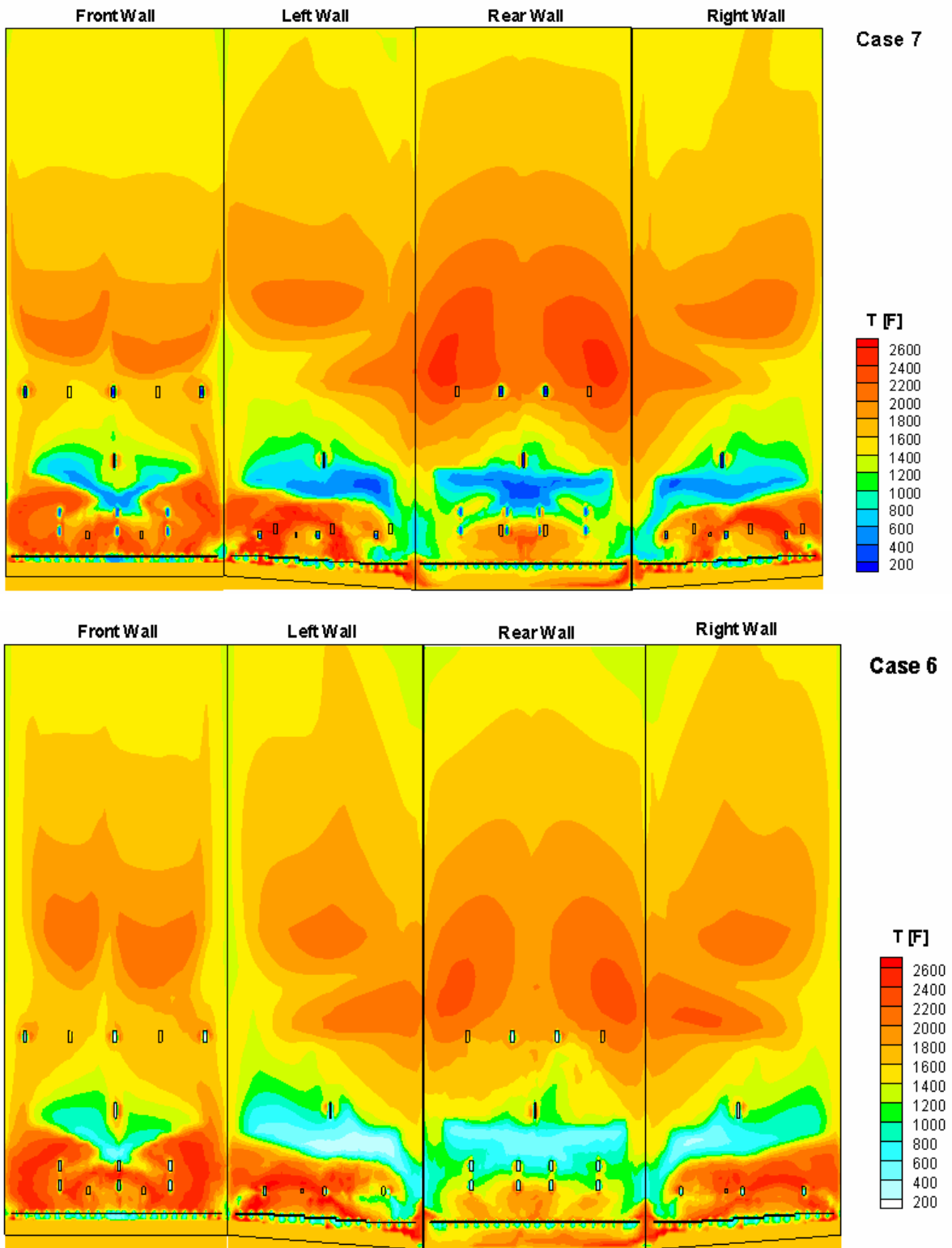


Figure 1.9: Changes in temperature in Kraft recovery boiler by increasing the tertiary air flow by 10 volume % .

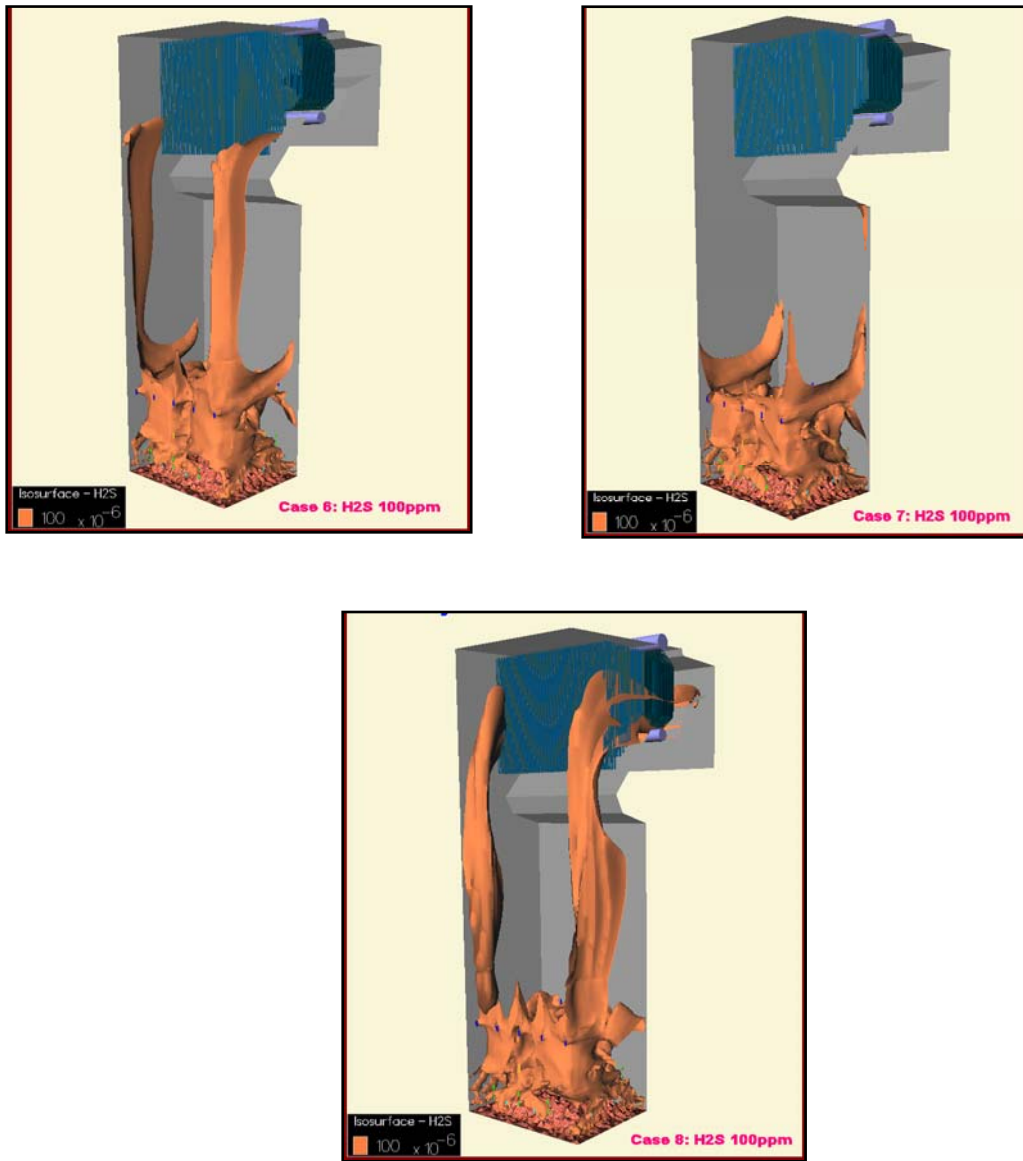


Figure 1.10: H₂S iso-surface with different tertiary air ratios and openings.

It is known that the oxide scale on the iron surface, in the boiler tube temperature range, is much more protective than the sulfide scale^[2]. If the gas environment cycles between the sulfidizing to the oxidizing compositions, the resulting scale formed on the metal tube surface may not be very protective and can result into a accelerated corrosion. Previous work has shown that the higher corrosion rate of carbon steel may result from:

- the presence of organo-sulfur compounds in gases;
- alternating oxidizing/reducing conditions;
- cyclic temperatures; and
- higher temperatures^[21].

The differences in corrosion rates in the high and the low corrosion areas will largely depend upon the stability of the scale. Conditions favoring the sulfide scale or an unstable scale will lead to accelerated corrosion. Instability in the local gas composition can lead to changes in the local environment, which may frequently change between the oxidizing and sulfidizing gases^[Error! Bookmark not defined.]. A number of other high-temperature commercial processes, such as oil refining, coal gasification, and fossil-fuel conversion, produce complex gaseous environments in certain areas that can vary between oxidizing and sulfidizing. The resulting multi-oxidant environments often are not at equilibrium and can vary in the degree of aggressiveness with changes in operating conditions. Fluctuating gas atmospheres (oxidizing-sulfidizing) and temperatures can change the scale composition and stability appreciably from a protective to non-protective scale. Generally, the activities of the principal reactants (p_{S_2} , p_{O_2}) have been modeled to cover the diverse range of commercial processes, assuming chemical equilibrium in the gas

phase. In power generation plants, however, the passage of the hot combustion gases over the much cooler metallic surfaces of the tubes is too rapid for chemical equilibration to take place. Thus, in reality, although the bulk of gases will be in equilibrium, but a situation exists in which the quenched or partially pyrolyzed process gas on the surface of tubes, still in a state of pseudo-equilibrium, reacts with the alloy under non-equilibrium conditions. [22] Gesmundo et al. [17] studied the corrosion behavior of steels at 600°C in gas mixtures where the gas composition changed cyclically with time from sulfidizing to oxidizing conditions and vice versa. Oxidation after the first sulfidizing cycle produced a layer of iron oxides over the initial sulfide layer at rates much higher than for the pure oxidation. The second sulfidizing stage produced a thin sulfide scale over the oxide layer, growing at a much slower rate than during the initial sulfidation. Finally, the second oxidizing stage produced a porous external oxide layer growing mainly directly in contact with the oxide layer formed during the first oxidizing stage, while the second sulfide layer tended to disappear with time. The corrosion behavior of the steels and in particular the growth of the complex, multilayered scales observed were a direct consequence of the change in the gas composition at the end of each cycle.

1.4 PROTECTIVE COATINGS

When carbon steels are exposed to sulfur containing gases at temperature below Fe-S eutectic, a compact and adherent scale is formed in initial stages. If the partial pressure of sulfur (p_{S_2}) is sufficiently high, the scale consists of a thin layer of FeS_2 over a thick layer of $Fe_{1-x}S$ and if p_{S_2} is low, a monosulfide layer is formed. Corrosion prevention can be achieved if the alloy forms a continuous, thermodynamically stable and self-healing

protective oxide scale on its surface. The protective action of such scales depends on their property of reducing the rate of the corrosion reaction by acting as a diffusion barrier between the metallic material and the corrosive environment. Alumina (Al_2O_3) and chromia (Cr_2O_3) are important protective oxides in this respect. Bulk addition of the relevant alloying elements (aluminum, chromium) is employed in some alloys for high temperature application to promote the formation of such protective oxide scales on the surface of metallic materials. Often, however, it is not possible to achieve optimum protection by this alloying route since the mechanical properties and the cost may be compromised due to addition of these alloying elements. For this reason, many high temperature alloys are optimized for their mechanical properties and then aluminide or chromized diffusion coatings are formed on the finished components, enriching their surface with the desired protective oxide scale-forming element(s) such as aluminum and chromium^[23,24]. Aluminides are well-known to have excellent oxidation and sulfidation resistance due to the formation of an external, protective alumina scale^[25,26,27,28,29].

A large number of coating techniques are available such as physical vapor deposition (PVD), chemical vapor deposition (CVD), pack cementation, thermal spray coating, vacuum plasma coating, laser surface alloying, etc. Although, many of these methods are used in practice, they are not perfect and have several limitations. Coating by PVD methods usually have poor mechanical bond and only a limited thickness is achievable, and coating of large intricate parts is difficult. CVD method is used only for a limited number of coatings and the method becomes complicated in case of alloy and ceramic coatings. To overcome some of the limitations of a CVD process, plasma-assisted

chemical vapor deposition (PACVD) technique was developed, but the low deposition rate limits the use of PACVD to films of less than micrometer thickness, such as those used in microelectronic integrated circuits. Thermal spray coatings are extensively being used because they are easy and inexpensive to apply, but high porosity, non-uniform surface and poor mechanical bond with the substrate, often limits their use in aggressive environments. Halide activated pack cementation technique (HAPC) is the most widely used process for applying protective coatings on materials, such as superalloys, which are used for high temperature applications^[30,31,32]. Because HAPC is a diffusion-controlled process, a metallurgical bond forms between the substrate and the coating. The process is easy to operate, inexpensive, can accommodate substrates of varying size and shape and can produce uniform and smooth coating of desired thickness.

1.5 PACK CEMENTATION

The first “cementation process” was described by *Allison and Hawkins* in 1914^[33], who deposited Al on iron and on steel. But it is only since the 1960's that this process stimulated broader interest because of the development of coatings for the protection of gas turbine blades especially those made of Ni-based superalloys. Co-deposition of two or three elements became possible with the theoretical understanding of the process. The extensive work on Cr-Al co-deposition published by *Rapp et al.* on steels^[34,35] and by *Young et al.* on nickel-based alloys^[36,39] are the major examples. Eventually, more recent investigations seem to focus on the addition of reactive elements like Y, Ce or Hf by co-diffusion^[30,37].

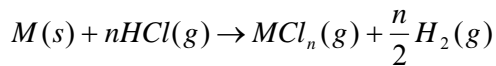
1.5.1 Pack

Typically the powder pack mixture consists of 3 components:

- a metallic source M: a fine powder of the element(s) to be deposited on the surface of the substrate (Al, Cr, Si, Ti or combinations of these elements) ~1-10 wt%
- a halide salt activator as for example: NaCl, NH₄Cl, AlCl₃, NaF, NH₄F ~1-5 wt%
- an inert filler powder (e.g. Al₂O₃) preventing the powder mixture from sintering at high temperature, >85 wt%.

1.5.2 Pack Reactions

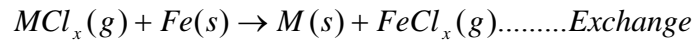
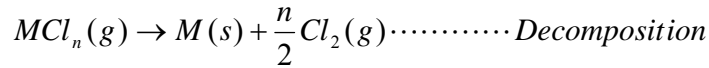
The whole process relies on the formation of gaseous halides of the coating metal/metals according to the general reaction:



AlCl₃(g), AlCl₂(g), AlCl(g), Al₂Cl₆(g) or Al₂Cl₄(g) are the gaseous chloride species involved in a chloride activated aluminizing process. The partial pressures of each of the gaseous metal-halides formed are established by their thermodynamic stability, which varies with the process conditions: composition of the pack, type of activator, temperature, pressure, and type of inert or reducing environment.

In the case of aluminum deposition, AlCl₃(g) is the major halide formed at low temperature, whereas at higher temperature the activity of AlCl(g) becomes higher.

Once formed the metal-halide molecules diffuse through the gas phase to the substrate (e.g. iron) surface, where they adsorb and decompose owing to the general reactions:



The aluminium formed at the surface of the substrate can then diffuse into the solid substrate, forming the desired coating. The predominance of the reactions depends on the stability of the gaseous halides involved. The deposition particularly occurs by disproportionation reaction when, first, the vapor pressure of the substrate halide (iron halide in steel) is low and secondly, when the coating element (M) also has higher and lower halides of comparable vapor pressures to set the atomic aluminium free at the substrate surface. When the vapor pressure of the substrate halide becomes comparable to the metal-halide, the contribution of the exchange reaction becomes important. The latter reaction is particularly undesirable if the vapor pressure of the substrate halide becomes higher than the coating element's metal-halide, as it would lead to a significant metal loss and formation of porous coatings.

Furthermore, it is a prerequisite for the pack cementation to work that the thermodynamic activity of the incorporated element (M) is always lower at the surface than in the pack. This activity gradient drives the gas phase diffusion of the metal-halide molecules from the pack to the substrate surface. As a consequence, a desired coating composition cannot be obtained by simply using a master-alloy of the same composition ^[38]. Moreover, the concept of "major depositing species" has been defined. This corresponds to the gaseous species that is responsible for the major part of the deposition. In the case of a Cr-Al co-deposition process by a chloride activated pack, Rapp et al. ^[38] and Da Costa et al ^[39]

showed that although the vapor pressure of $\text{AlCl}_3(\text{g})$ is several orders of magnitude higher than that of Cr halides and other Al halides, the co-deposition is possible by optimizing the process conditions so as to get comparable vapor pressures of $\text{AlCl}(\text{g})$ and $\text{CrCl}_2(\text{g})$. Indeed, $\text{AlCl}_3(\text{g})$ is significantly stable and does not decompose enough at the substrate surface. The Al transport occurs via $\text{AlCl}(\text{g})$. This is thus considered as the major transporting species for Al, whereas $\text{CrCl}_2(\text{g})$ is the major transporting species for the deposition of Cr^[37,38].

The HAPC technique is a form of *in-situ* CVD process because the halide activator decomposes at high temperatures to produce volatile halide vapors of the elements to be coated. The chemical potential gradient between the elements to be coated (M) and the substrate drives the gas phase diffusion of the metallic-halides and their decomposition at the substrate surface and result in a surface deposition of metallic element (M). Growth of the coating removes the arriving elements fast enough to maintain this chemical potential gradient. The activity of the metal determines which types of phases are stable at coating/pack interface^[40]. By controlling the activity of Al, Fe-Al based coatings, as required from Fe-Al phase diagram^[41] can be produced Figure 1.11. Datta et al.^[32] have shown that with a carefully chosen halide salt as an activator, the pack process could indeed be applied to aluminize alloy steels at temperatures below 700°C. In Datta's work^[42], the effect of different activators (AlCl_3 , NaCl , NH_4Cl , AlF_3 and NaF) on the aluminization potential of the pack was investigated. The largest weight gains were found with AlCl_3 as activator at 650°C and coating consisted of outer $\text{Fe}_{14}\text{Al}_{86}$ layer and an inner FeAl_3 layer. Coating thicknesses were found to be <40µm after aluminizing at

650°C for 8 hours. The coating morphology and composition depends on thermodynamics and kinetic factors such as the activity of coating element in gaseous phase, stability of formed phases and diffusivity of elements in these phases.

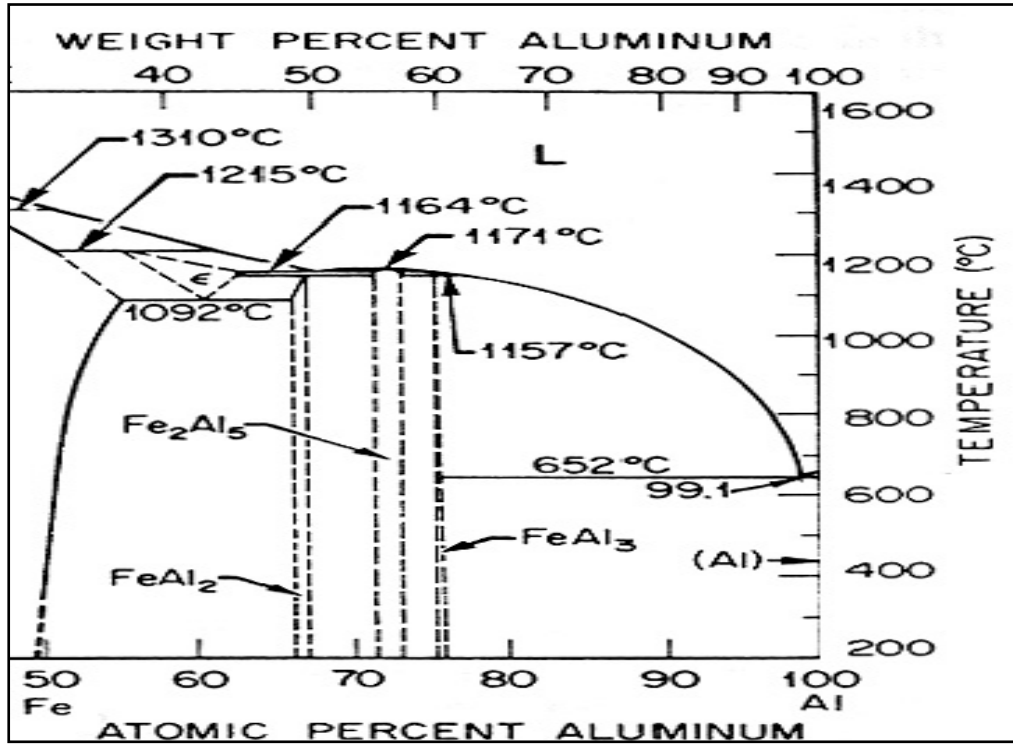


Figure 1.11: Fe-Al Binary Phase Diagram Showing Ordered Intermetallic Phases in the Area of Interest (>50% Al)^[41]

1.5.3 Kinetics of Pack Cementation

Like all vapor deposition processes, pack cementation involves gas-solid reactions. Figure 1.12 illustrates various steps involved in the formation of a single layered aluminide coating in case of outward growth, when thermodynamic equilibrium is achieved in the pack. The coating process can then be considered as six steps in series [43].

1. Gas phase diffusion of aluminum halide molecules from the pack to the coating surface across the Al depleted zone of the pack.
2. Deposition of the master-alloy element from the halide gas at the gas/coating interface.
3. Solid state diffusion of the iron through the coating towards the coating/gas interface.
4. Growth of the coating phase at the coating/gas interface.
5. Desorption of the halogen species from the gas/coating interface.
6. Gas phase diffusion of the halogen back into the pack.

Several authors showed the evidence for the formation of an Al depleted zone by measuring the remaining Al content in the pack near the coating surface ^[44,45]. Gupta and Seigle even showed that the Al loss of the depleted zone corresponds exactly to the Al uptake of the substrate ^[46]. This means that the Al consumed by the coating growth almost exclusively emanates from this depleted zone, which is growing as the deposition is going on. In a process in-series, the rate-limiting step determines the total rate of the process. The interfacial reactions, steps 2, 4 and 5 are not expected to be rate limiting steps for the growth of most coatings ^[47,48,49,50]. At the temperatures investigated, above 800 °C, gas phase diffusion, step 1 and 6, are rate limiting steps only in limited cases involving especially high stability activators ^[44]. However, it usually appears that the equilibrium in the pack is achieved after a certain transition time. Thus at the beginning of the coating process, the flux of master-alloy element delivered by the halide molecules on the surface (step 1) is slower than the limiting flux of this element dictated by the solid state diffusion (step 3). Consequently, the beginning of the process follows the gas

diffusion kinetics and the growth of the depleted zone is rate limiting. At the end of the transition regime, the aluminum flux delivered by the gas phase equals the maximum uptake into the solid phase. At that moment, the kinetics limitation of the process changes from gas diffusion to solid state diffusion^[43,44].

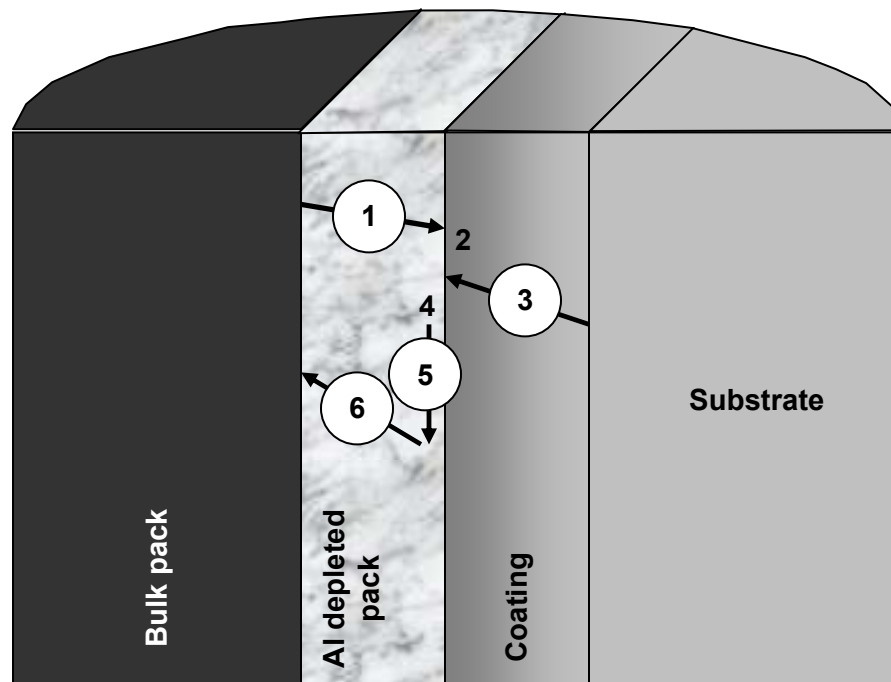


Figure 1.12: Kinetics of pack cementation coating process. (1) Gas phase diffusion of aluminum halide molecules from the pack to the coating surface across the Al depleted zone of the pack. (2) Deposition of the masteralloy element from the halide gas at the gas/coating interface. (3) Solid state diffusion of the iron through the coating towards the coating/gas interface. (4) Growth of the coating phase at the coating/gas interface. (5) Desorption of the halogen species from the gas/coating interface. (6) Gas phase diffusion of the halogen back into the pack

1.6 MODIFICATION OF COATINGS

Aluminized and chromized coatings have adequate resistance against high temperature corrosion in the environments with relatively high oxygen and sulfur activity due to formation of protective scales. During the steady-state stage, most of the new scale growth is composed of the most stable phase. The coating failure can occur by:

- a) the scale de-bonding from the substrate,
- b) the alloy becoming depleted of the steady-state scale forming element, or
- c) the chemical attack from atmospheric or metallurgical impurities (e.g. S, Na).

The failure mode pertinent to this work is spallation of protective oxide scale and the coating becoming depleted in aluminum concentration due to its diffusion into the substrate during high temperature application. Spallation occurs when a scale cracks and debonds from the substrate. Spallation is often accompanied by visibly observable flakes of oxide that have physically separated from the scale, sometimes exposing the alloy. When an alloy loses its scale, the associated loss of protection can cause very rapid corrosion. The principal cause of spallation is believed to be scale stress. Spallation is often observed when an alloy is cooled from the high temperature at which corrosion took place. The explanation proposed for this behavior is that the thermal expansion difference between the oxide scale and the metallic alloy generates stresses at the interface as well as in the scale. There are a large number of other possible contributions to residual-stress accumulation and relaxation, such as growth stresses, creep, scale phase composition, scale and alloy phase transformations, debonding, cracking, etc. A full treatment of this phenomenon is therefore extremely complex, especially when it is

difficult to make initial assumptions regarding which effects are likely to contribute most strongly in a given instance. But the residual stresses due to thermal expansion mismatch between metal, oxide and sulfide can play an important role in degrading the adherence of protective oxide scales and can cause spallation^[51,52,53,54]. Significant levels of compressive stresses are induced into the surface scale during thermal cycling, since the thermal expansion of oxides is less than that of the metallic substrate. Growth stresses in the oxide, as well as plastic deformation of the alloy at high temperature, can also contribute to the overall residual stress state of the protective scale^[54]. Also, the scale stability and spallation in the fluctuating gaseous environments have not been reported for aluminized or chromized coatings. Currently, there are three well-established methods of improving oxide scale adherence:

1. alloying with precious metals (Pt, Pd, or Ir)^[55],
2. addition of a reactive element (RE), such as Y, Hf, or Zr^[56,57,58,59,60], and
3. reduction of S impurities^[61,62].

Reduction of S impurities is not a cost effective solution as it will require significant changes in industrial processes and the materials used, which is not always possible. Beneficial effects of RE and Pt addition on the high temperature oxidation rate, particularly on the protective scale adherence on steel, are well established. This is achieved by the introduction of minor elements^[63,64,65,66,67] by implantation^[68] or by chemical processes^[69,70,71,72,73,74]. It has been shown that addition of a sufficient quantity of RE in the coatings/alloys can substantially reduce their rates of sulfidation, particularly under conditions of low pO_2 .^[30] Present work focuses on the RE (Hf and Y) modified Fe-Al coatings by co-depositing RE and Al by the pack cementation process, and

investigating the RE effect on overall corrosion behavior of the resulting coatings in fluctuating gaseous and thermal environments.

1.6.1 Hf and Y Modified Coatings

The beneficial effects of Hf, Y and Zr in Ni based alloys and coatings in oxidative environments have been extensively studied and discussed thoroughly.^[47,57,75,76] The role of reactive element (RE) dopants has been explained on the basis of their ionic segregation at interfaces in the external oxide scale^[56]. In attempting to optimize the RE benefits in alumina-forming alloys, it has been shown that the amount of interstitials relative to the RE concentration affects their performance^[77,78,79,80,81,82]. Reactive elements have been reported to affect the growth of alumina and chromia scales in the following ways:

- (i) In alloys without reactive element additions, oxidation occurs through outward cation diffusion from the substrate to the metal/scale interface, although there is also some inward oxygen diffusion. In alloys with reactive element additions the primary transport mechanism is reversed with outward cation diffusion being slowed while inward oxygen diffusion is enhanced. Oxygen tracer and platinum marker studies support these statements^[83,84,85,86,87]. The mechanism is shown schematically in Figure 1.13.
- (ii) In alloys with reactive element additions, the grain growth of the alumina and chromia scales is reduced via pinning of grain boundary and dislocations in the oxide scale^[84,85] resulting in an oxide scale with a small mean grain size^[84,88]. Alloys

without reactive element additions have oxide scales with larger mean grain sizes as growth is not impeded during high temperature exposures.

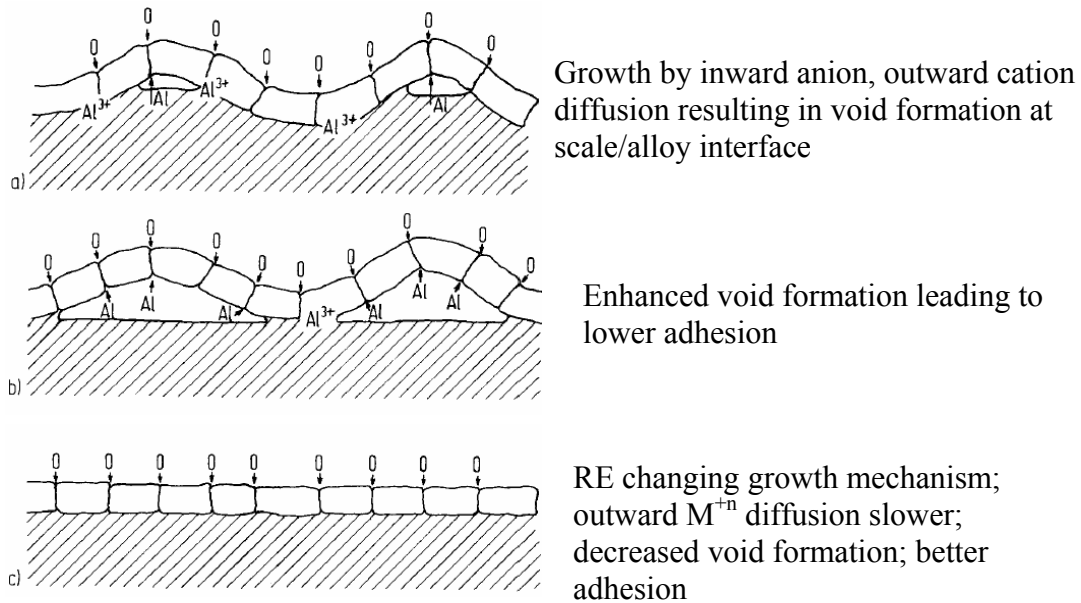


Figure 1.13 Reactive element effect: change in scale growth mechanism

Presently there is no consensus on the role of reactive elements on the mechanisms responsible for the improvement in scale adhesion. There have been a number of proposed mechanisms to explain the reactive element effects that include:

1. RE form oxide pegs at the metal-oxide interface to mechanically fix the scale^[89];
2. RE can act as a vacancy sink to eliminate the void precipitation at the metal-oxide interface^[90];

3. RE have also been shown to alter the growth mechanism of the oxide scale ^[91]. Schumann et al.^[92] showed that doping the FeCrAl alloy with Y changes the oxide grain structure from equiaxed to columnar and that the formation of microvoids at the metal/oxide interface is suppressed leading to better adhesion.
4. REs increase the scale plasticity for stress relaxation^[93],
5. REs segregate to the metal oxide interface to form a graded seal and strengthen the metal-oxide bond^[94], and
6. REs act as a sulfur getter to prevent segregation at the interface.^[61] The role of the RE-interstitial ratio may be related to a “gettering” mechanism ^[77-78,95] or interstitials may affect the RE activity, such that the flux of outward RE diffusion needed to continuously dope the metal-scale interface and alumina grain boundaries is reduced^[95].

There are a number of ways to incorporate the RE in coatings such as CVD using RE halides as a source material ^[96], DC magnetron sputtering of RE on surface ^[97] and adding Y, Zr and/or Hf in pack during pack cementation ^[98] It has been reported that Hf can be codeposited with Cr and Al on low-alloy steels by the pack cementation process ^[96].

1.7 STRESSES IN PROTECTIVE SCALES

For a truly protective corrosion scale, failure only occurs when the alloy is depleted of the scale-forming element. Accelerated chemical attack can, of course, greatly reduce the lifetime, but very often, the scales fail prematurely by cracking or spalling, particularly under thermal cyclic conditions. The driving force for these failures is the stress that

develops within the scale in response to the oxide growth process, the thermal expansion mismatch between the oxide and the substrate, and any phase transformation that may occur in the scale or in the alloy. The existence of oxide growth stresses has been known for decades ^[99]. At high temperatures, the oxidizing components often respond to the stress by plastic deformation of the substrate, especially if it is thin and weak ^[100], and/or by deformation of the fine grained oxide ^[101]. Unrelieved growth stresses can combine with thermal stresses that develop during cooling to initiate and cause scale failure. Although the level of residual growth stress may be just a fraction of the cooling stress, knowing its magnitude is still important for an accurate mechanistic modeling of scale or coating failure, which is critical to many industrial applications. To develop an understanding of the scale failure processes, and in order to develop ways of preventing them, it is important to obtain reliable methods for measuring stresses in the scales and for detecting the onset of scale failure. Although the ruby fluorescence has been used for decades as a stress indicator in diamond anvil cell, only recently has it been used to measure the stress levels in thermally grown oxide scales. This work has utilized piezospectroscopy (laser fluorescence) for investigating the effect of Hf and Y addition on the stresses in the corrosion scale under thermal cyclic conditions.

1.8 PIEZOSPECTROSCOPY (LASER FLUORESCENCE)

1.8.1 Theoretical background

When a semiconductor is illuminated with photon energy, $\hbar\omega$, electrons in the valence band can move into the conduction band, thus leaving a hole in the valence band (provided $\hbar\omega > E_g$). After relaxing to the bottom of the conduction band, the excited

electron can radiatively recombine with a hole to produce a photon with energy E_g i.e. fluorescence. In the case of insulators (e.g. $\alpha\text{-Al}_2\text{O}_3$) when the incident photon energy (1.7 to 3eV visible light) is less than the band gap energy (~ 9 eV), band gap fluorescence does not occur. Impurities in an insulator, however, can have electronic energy states that fall in the band gap. These states contribute to both absorption and emission of photons. The ruby fluorescence results from the excitation of Cr 3d electrons ^[102,103] when the Cr atoms are substituted for the Al atoms in $\alpha\text{-Al}_2\text{O}_3$ lattice. During high temperature exposure of alumina forming coatings and alloys, alumina first forms in the Θ -phase before transforming to the stable α -phase, which is the hexagonal (HCP) structure. The Cr^{+3} ion is completely soluble in the alumina and substitutes directly for the Al^{+3} ion in a site of trigonally distorted octahedral symmetry ^[104,105] (Figure 1.14). When the ions are viewed along the trigonal axis there are three oxygen ions in a triangle located above and below the chromium ion. The two triangles are of slightly different size and are rotated out of symmetry by approximately 4.3° , Figure 1.14. In addition, the chromium ion does not take up the exact same site as the Al^{+3} ion. The Cr^{+3} ion is displaced 0.06\AA from the usual Al site along the c-axis away from the nearest plane of oxygen atoms and toward the nearest occupied cation site ^[106]. When the Cr ions are substituted for the octahedrally coordinated Al^{+3} ions in $\alpha\text{-Al}_2\text{O}_3$ the electric field of the six nearest neighbor oxygen ions (i.e. crystal field) deform the 3d orbitals. The effect of the crystal field is to split the orbital degeneracies. Additional splitting occurs due to spin-orbit interactions. It has been shown that the 28-fold degenerate ground state of Cr^{+3} ion is split by the crystal field into three levels (two 12- fold and one 4-fold). These levels are in turn further split by the spin

orbit coupling yielding a total of 9 levels ^[102,103]. A few of these states are shown in Figure 1.15.

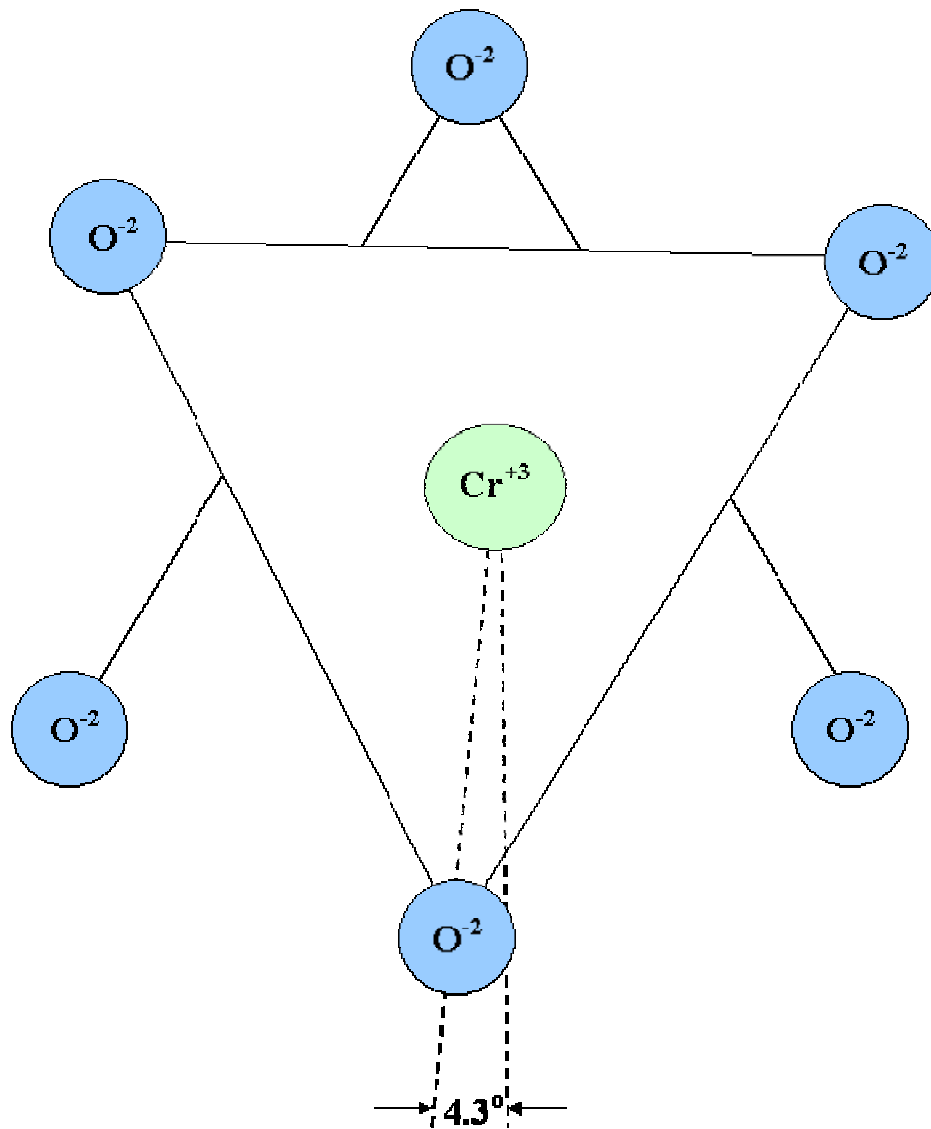


Figure 1.14: Cr³⁺ substitution for Al³⁺ in Al₂O₃ crystal structure.

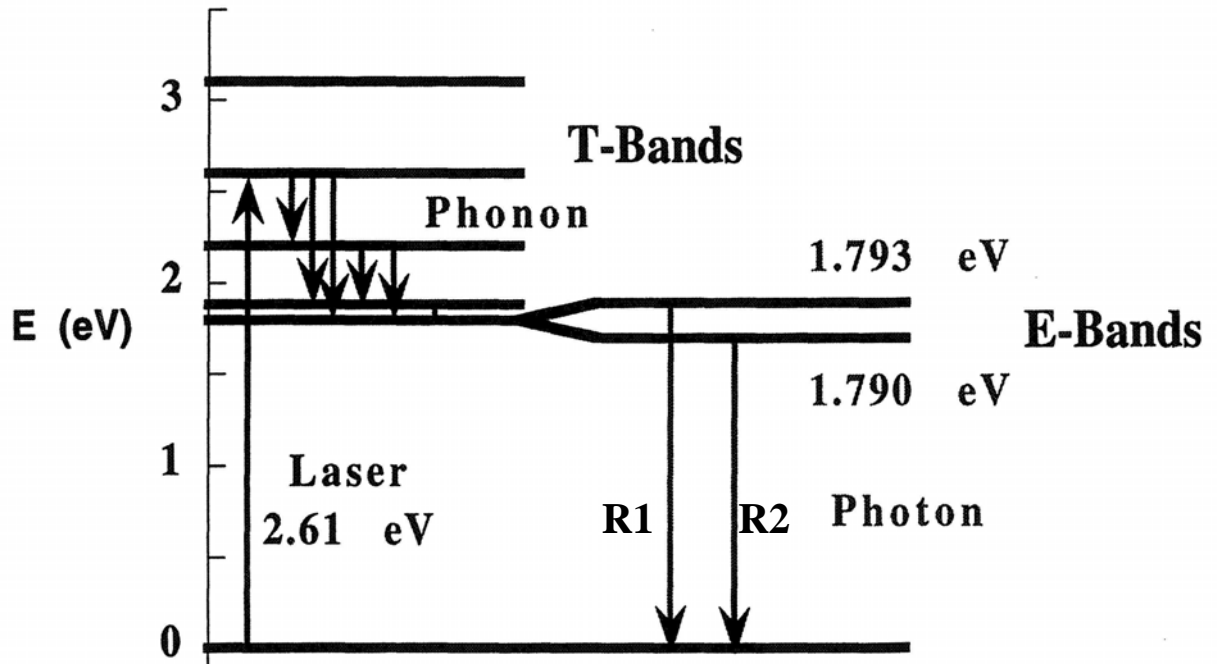


Figure 1.15: Electronic levels of Cr³⁺ in Al₂O₃. Transitions resulting in characteristic R1 and R2 lines are labeled.

Most of the Cr³⁺ ions energy states give rise to absorption bands, however few of these decay radiatively. When monochromatic blue light ($E_L = 2.6$ eV) illuminates the crystal, the 3d electrons are transferred into the higher energy T-bands of the electronic energy spectrum (Figure 1.15). Most of the excited atoms can decay to lower energy states by nonradiative processes. The nonradiative energy transitions occur by means of phonons-effectively due to the strong coupling between the electronic states and the vibrational lattice. Nonradiative decay is very probable between the closely spaced T-bands and between the T-bands and E-bands. However, the energy gap between E-bands and the

ground state is too large for nonradiative transitions. That is to say, there are no phonons of energy 1.79 eV available for nonradiative decay. Consequently the E-states to the ground state energy transitions occur by means of photons which produce the characteristic ruby fluorescence shown in Figure 1.16 with wavelengths of 692 and 695 nm . These lines are known as the R1 (14402 cm^{-1}) and R2 (14432 cm^{-1}) lines and are separated by approximately 30 cm^{-1} wavenumbers.

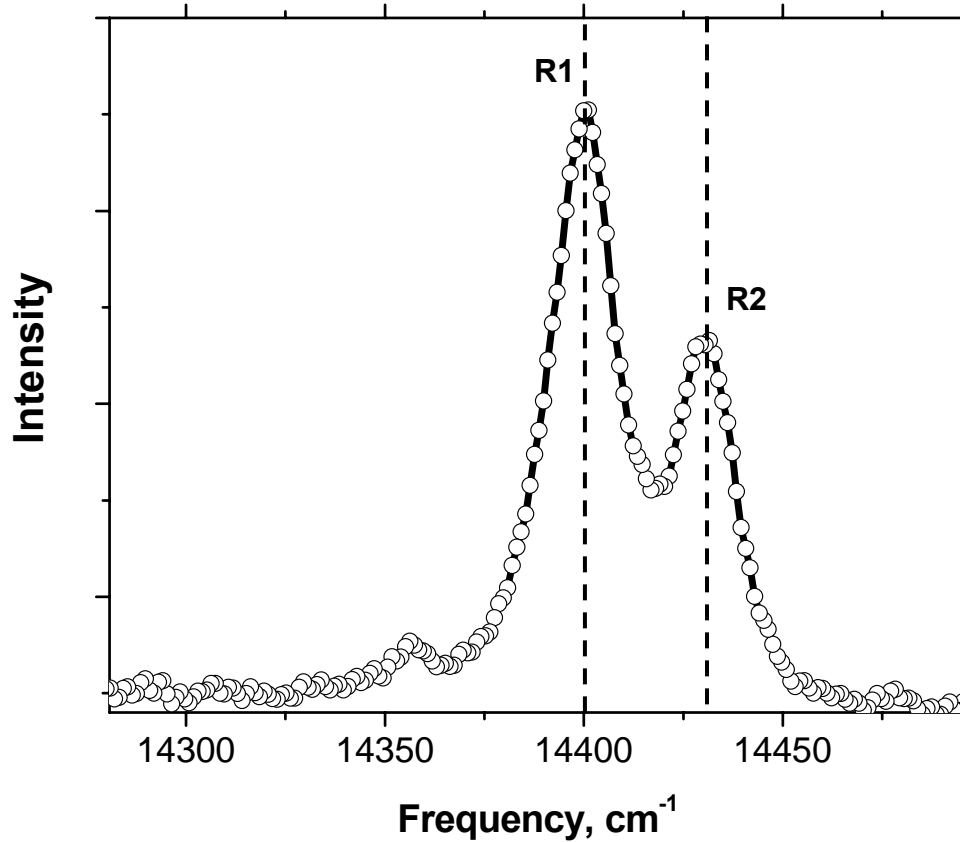


Figure 1.16: Cr^{+3} luminescence spectrum showing characteristic doublet of R1 and R2

The lifetime of the R1/R2 decay is approximately 3.79 ms at room temperature and pressure ^[107]. Because the excited electron undergoes several nonradiative energy transitions before it arrives at the radiative E-states to ground state transition, the frequency of the ruby fluorescence is unaffected by the frequency of the excitation light. Because the 3d electrons are on the outside of the Cr⁺³ ions, they are particularly sensitive to the changes in the crystal field produced by the neighboring atoms. As pressure is applied to the crystal, the energy gap between the conduction and the valance bands is reduced. The result is a shift in the R1 and R2 lines toward lower wavenumbers as compressive stress increases (Figure 1.17).

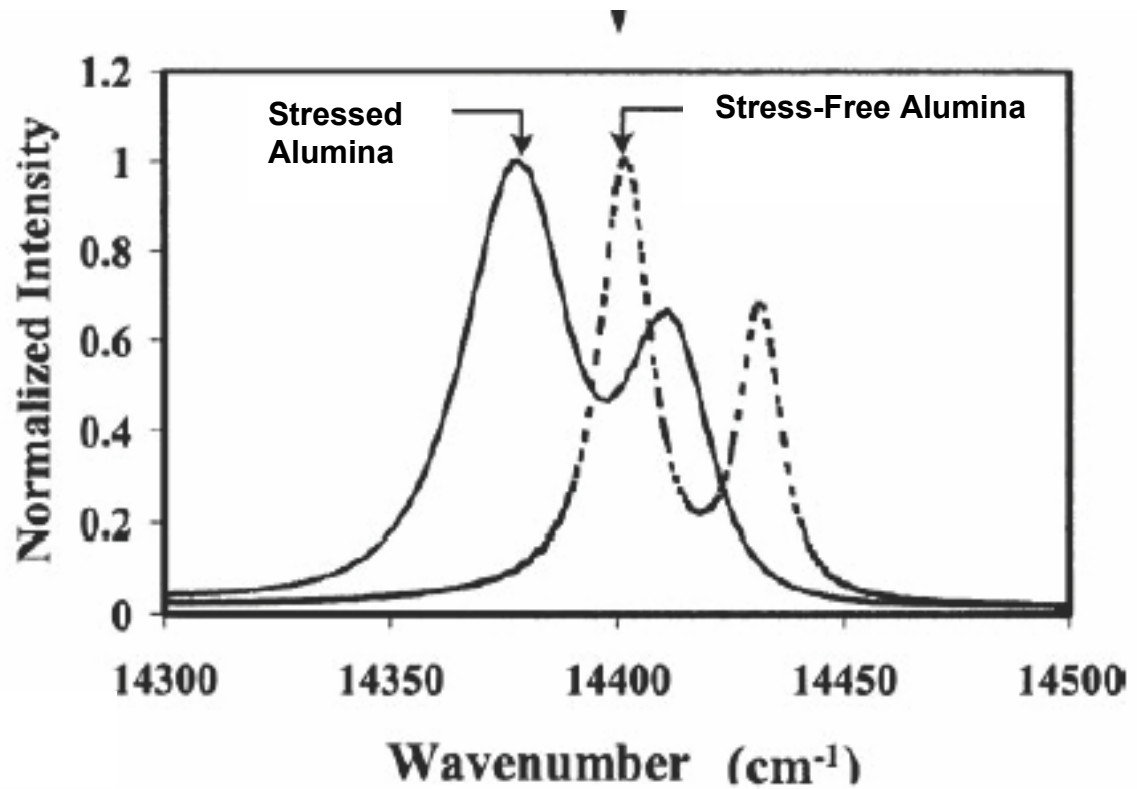


Figure 1.17: Effect of stress on R1 and R2 lines of Cr⁺³ spectrum. Shift towards left signifies compressive stresses in Al₂O₃ crystal.

This shift can be described by:

$$\Delta\nu = \Pi_{ij}\sigma_{kl} \quad (10)$$

Where, Π_{ij} are piezospectroscopic coefficients and σ_{kl} is stress in the crystal. In order to apply the technique, an assumption is made that for fully coherent films the stress is biaxial. Therefore

$$\begin{aligned} \sigma_{xx} &= \sigma_{yy} = \sigma_{avg} ; \\ \sigma_{zz} &= 0 \end{aligned} \quad (11)$$

An additional assumption is also made that the area sampled consists of many randomly orientated grains. This removes the effect of stress due to crystallographic orientation. Using these assumptions Clarke et al. ^[104,105,108] has defined the relation between stress and wavenumber shift to be:

$$\Delta\nu = \frac{2}{3}\Pi_{ii}\sigma_{avg} \quad (12)$$

where Π_{ii} is the piezospectroscopic coefficient, $\Delta\nu$ is the wavenumber shift, and σ_{avg} the average stress in the probed volume of the scale. In order to determine the piezospectroscopic coefficients, He and Clarke^[104] conducted experiments with single crystal ruby at different crystallographic orientations. Ruby specimens (5 mm X 1 mm X 1 mm) with their long axis along one of the three principle crystallographic axes were tested in uniaxial compression and in shear. The piezospectroscopic coefficients have been measured under uniaxial compression are listed in Table.1.3. The

piezospectroscopic coefficients for ruby under hydrostatic loading were determined to be 7.59 for R1 and 7.61 for R2^[104].

Table 1.3: Experimentally determined piezpspectroscopic coefficients for R1 and R2 lines in Cr⁺³ spectrum^[104]

	Π_{11}	Π_{22}	Π_{33}	$\Pi_{11}+\Pi_{22}+ \Pi_{33}$
	(cm ⁻¹ /GPa)	(cm ⁻¹ /GPa)	(cm ⁻¹ /GPa)	(cm ⁻¹ /GPa)
R1	2.56	3.5	1.53	7.59
R2	2.77	3.41	1.17	7.35
R1	2.65	2.8	2.16	7.61
R2	2.18	2.87	2.09	7.14
R1				7.53

1.8.2 Effects of chromium concentration on R1 and R2

Concentration of chromium in the Al_2O_3 will affect the frequency shift of the R1 and R2 lines. Tolpygo and Clarke^[109] have measured the shift and found the relation to be

$$\Delta\nu^* = 0.99 \times C_{cr} \quad (13)$$

where C_{Cr} is the chromium concentration expressed in weight %. Therefore as the chromium concentration increases, it reduces the frequency shift of the R1/R2 lines making the measurement less compressive, i.e. $\Delta\nu - \Delta\nu^*$.

1.8.3 Effects of Temperature on R1 and R2

Specimen heating will also cause a shift in R1 and R2 lines. As specimen temperature increases the width of the peaks also increases^[104]. He and Clarke have found the change in peak width to be linear. The position of the R1 and R2 peaks also changes with temperature. Molis and Clarke^[110] have found the shift to be $0.14 \text{ cm}^{-1}/^\circ\text{C}$ to lower wavenumbers with increasing temperature, i.e. stresses becoming more compressive.

CHAPTER II

EXPERIMENTAL PROCEDURES

2.1 BOILER ENVIRONMENT CHARACTERIZATION

The environment, that the carbon steel tubes in a boiler are exposed to, varies among industrial boilers depending upon the composition of fuel and boiler operation conditions. Local environment at the waterwall surface also varies from one part of boiler to other. Most of previous corrosion work was based on the bulk boiler environment assuming that the waterwall is exposed to similar environment. However it was found not to be true in a study related to the corrosion in lower furnace of kraft recovery boilers^[5]. Present study was aimed at the boiler and gasifier parts where gaseous environments vary from oxidizing to sulfidizing. Mid furnace of boilers typically experience environmental cycling. Extent of cycling depends upon the sulfur content of fuel along with other boiler design and operating conditions. To characterize waterwall gaseous environments in a boiler, mid-furnace areas with high and low corrosion rates of carbon steel tubes were selected, based on the waterwall thickness data from their annual inspection. Identified areas for the environment characterization in the selected boilers were above their last level of air supply ports (airports) and cutline, as is shown schematically in Figures 2.1 and 2.2. Air-tight, stainless steel gas-sampling ports were welded through the web membrane to support the ceramic tubes that were used to take samples of boiler gases (Figure 2.3). Gas sampling ports were designed to eliminate any air leaks into the sample and were accessible from the cold side of the boiler. Gas samples were collected in specially designed glass sampling containers with a composite septum seal. Samples were

taken from the waterwall tube surface by keeping the sampling tube flush with the waterwall surface. Multiple samples were collected from each port to get the information on variation in the gas composition over time.

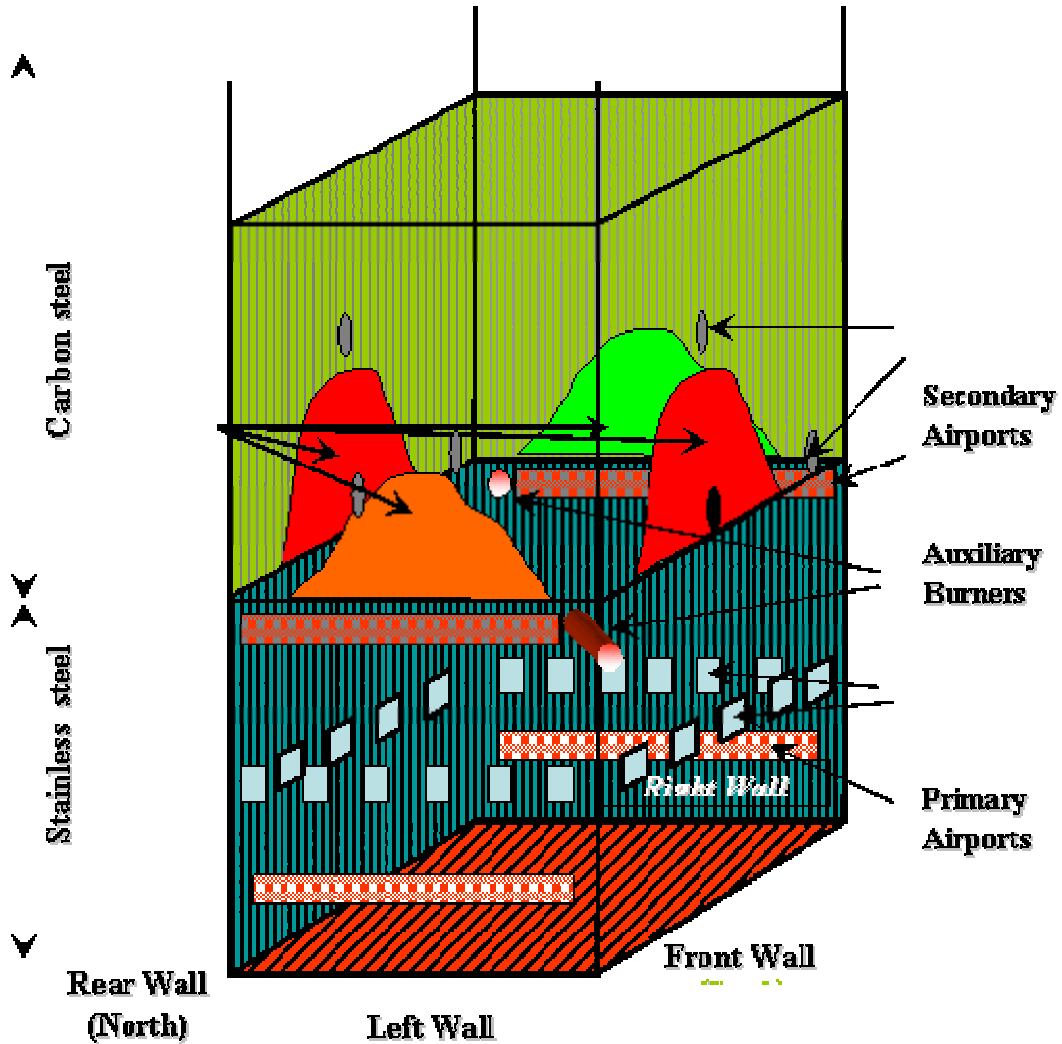


Figure 2.1: Schematic of Boiler showing corrosion patterns and port locations on the waterwall surface in mid-furnace area (above the cut-line). Notice that the boiler had two air levels and higher corrosion rates were experienced till higher elevations in middle of side walls compared to the corners.

Location of installed ports is shown in Figure 2.2. Figure 2.4 shows an installed port for gas sampling with a thermocouple to measure temperature online. Samples were analyzed

in the laboratory using a Perkin-Elmer Gas Chromatograph (Perkin Elmer, Inc., Wellesley, MA 02481-4078, USA). Two thermal conductivity detectors (TCD), for the light gases and a flame photometric detector (FPD) for the sulfur-bearing gases were used to analyze the collected recovery boiler gases. The chromatographic equipment was calibrated using standard gases. The gas composition was converted to partial pressures of sulfur and oxygen using thermodynamic calculation software (HSC Chemistry, Outokumpu Research Oy, Finland, 28101) so that the boiler conditions could be simulated in laboratory using mixtures of H_2S , N_2 and O_2 . Selected boiler for this study had experienced mid-furnace corrosion. Boiler was a retrofitted B&W boiler with three air levels. Boiler pressure was 10.3 MPa (1500 psig) with the steam temperature around 320°C. Composite tubes were used till the tertiary airport elevation. This boiler experienced a significant corrosion of the carbon steel in three corners of the boiler. The front-wall and the rear-wall had accelerated corrosion on the carbon steel tubes extending almost 12 feet above the cutline, as is shown in Figure 2.1. Data collection and gas characterization for each boiler port was similar. Glass gas storage bottles with composite septum were used to store these gas samples till they were tested. Gas samples from one storage bottle were analyzed over a week time period to see any changes in the gas composition over time. Data indicated that over tested time period there was no significant difference in the composition of sulfur bearing gases or other light gases like hydrogen, oxygen etc. Multiple gas samples were taken from each sampling port. Gas sampling data was used to choose corrosion test conditions in the present study.

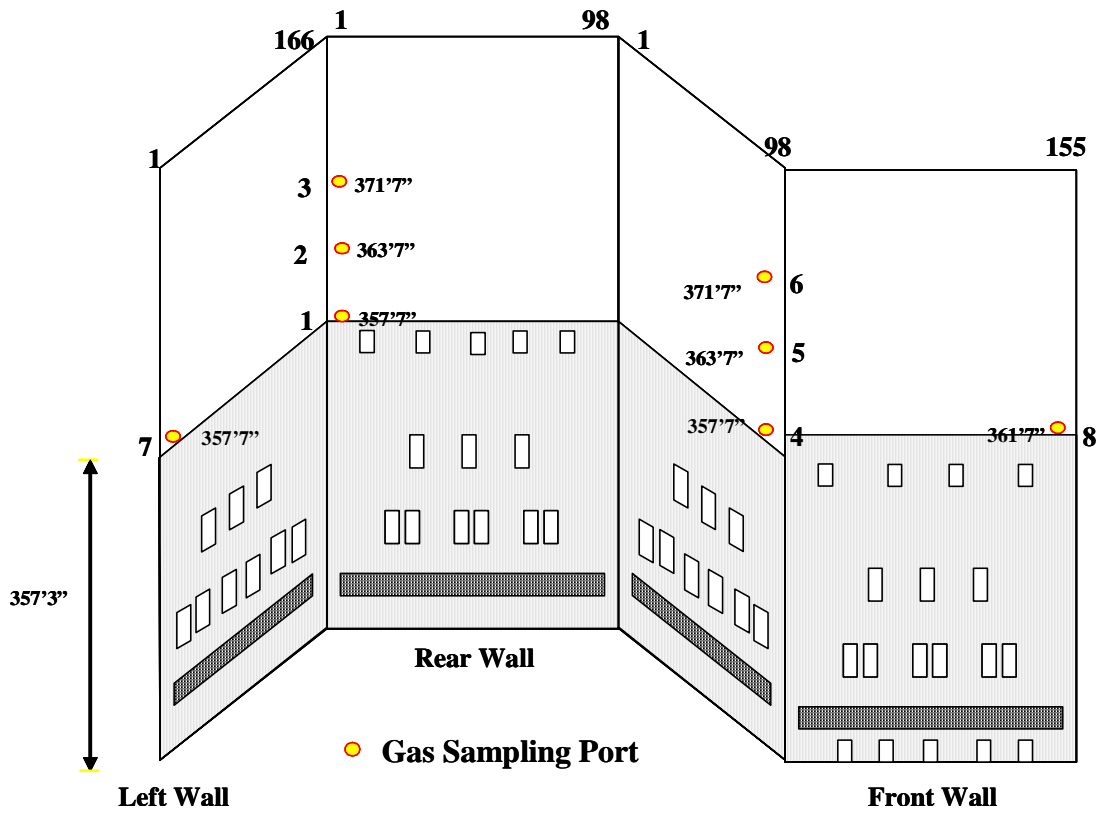


Figure 2.2: Schematic of Boiler showing corrosion patterns and port location on the waterwall surface in mid-furnace area (above the cut-line).

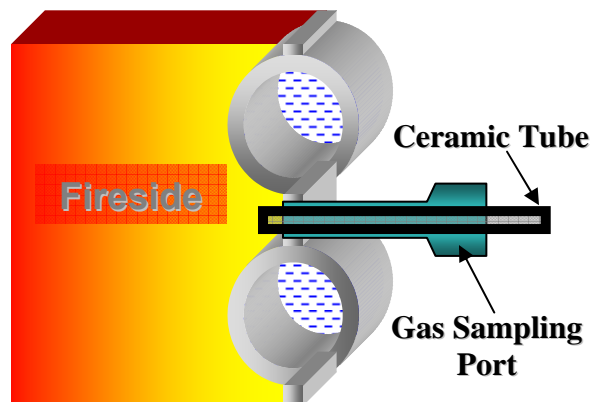


Figure 2.3: Gas-sampling port installed in recovery boiler to collect samples from the tube surface.



Figure 2.4: picture of a port installed in recovery boiler waterwalls to collect samples from the tube surface.

2.2 PACK CEMENTATION

Coupons (30mm X 20mm X 5mm) of commercial SA210 carbon steel were cut from unused boiler tubes and used as a substrate for diffusion coatings. The composition of the base alloys are listed in Table 2.1. These coupons were ground to 600 grit finish, ultrasonically degreased in acetone and ethanol, dried and weighed. Coupons were placed in alumina crucible (2.5cm X 5cm, Vesuvius McDanel, Beaver Falls, PA) with pack of Al_2O_3 (99.5%, Alfa Aesar, Ward Hill, MA)-Al/Cr (99.5%, -325 mesh, Alfa Aesar, Ward Hill, MA)- NH_4Cl (granular, Alfa Aesar, Ward Hill, MA) for chromizing/aluminizing. All pack composition are given in weight percent (wt%). For reactive element modified aluminide coatings, powder mixture of the pure reactive element, its oxide, and its chloride were used along with the aluminium pack to co-deposit RE with Al. Powders used were Hafnium (Hf, -325 mesh, 99.6%, Alfa Aesar, Ward Hill, MA) Hafnium oxide

(HfO₂, 99%, Alfa Aesar, Ward Hill, MA) and Hafnium chloride (HfCl₃, Sterm Chemicals, Newburyport, MA) for Hf; Zirconium (Zr, 99.5%, Sterm Chemicals, Newburyport, MA), Zirconium chloride (ZrCl₄, 99.5% ,Sterm Chemicals, Newburyport, MA), and Zirconium oxide (ZrO₂, 99.7%, Alfa Aesar) for Zr and, Yttrium (Y, -40mesh, 99.9%, Alfa Aesar, Ward Hill, MA), Yttrium oxide (Y₂O₃, Alfa Aesar, Ward Hill, MA) and Yttrium chloride (YCl₃, Alfa Aesar, Ward Hill, MA) for Y.

Table 2.1. Chemical composition (in weight %) of carbon steel tube (SA210) used in this study.

C	Mn	Si	S	P	Fe
0.27	0.93	0.1	0.058	0.048	Balance

A hole (~1mm diameter) was drilled in the carbon steel coupon before cementation process to get an even coating on every surface exposed to test environments.. The crucible was sealed with alumina cap using high temperature alumina cement (ZIRCAR Ceramics, Inc., Florida, NY). Cement was allowed to cure overnight before placing the crucible in a horizontal tube furnace (Figure 2.5). Furnace was purged with argon for 2 hours to remove any residual oxygen present in the tube. Sealed crucible was further held at 150°C for 2 hours in argon atmosphere to further cure the cement. The furnace temperature was then raised to the coating temperature and held for the required duration of the process. Argon was used throughout the coating process to prevent any oxidation. After cooling in the furnace under argon, coated surface of the test sample were cleaned

ultrasonically and reweighed. Coating times reported here were the times at the coating temperature. Weight gain of the sample was normalized by its surface area. Surface and cross-section of the coated samples were characterized with Scanning Electron Microscopy (SEM-LEO GEMINI 1530 Thermally-Assisted Field Emission (TFE) SEM, Zeiss, Oberkochen) with Energy Dispersive Spectrometer (EDS- Oxford Instruments, Witney, Oxon, OX29 4TL, UK) and Electron Back Scattered Diffraction (EBSD-HKLTechnology/Oxford Instruments, Concord, MA) to examine the concentration profile and growth kinetics of the coated surface. Thickness of coating reported were estimated from the elemental concentration profiles measured using EDS. Phases were identified using X-Ray Diffraction (PW 1800 X-ray diffractometer, Philips, USA) with Cu-K α radiation.

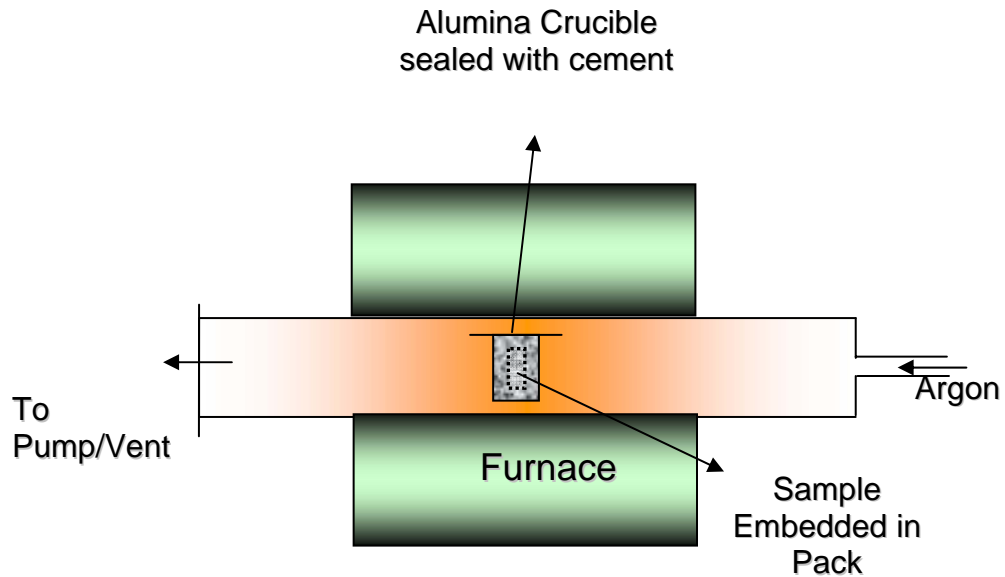


Figure 2.5: Experimental setup for pack cementation coatings.

2.3 HIGH TEMPERATURE CORROSION KINETICS

Coupons of SA210 carbon steel (30mmX20mmX5mm) were cut from unused boiler tubes and used for high temperature corrosion kinetics study in thermogravimetric analysis (TGA) experiments. All surfaces of test coupons were ground through 1000 grit SiC paper, polished to 5nm Al₂O₃, ultrasonically degreased in acetone, dried and weighed. TGA with Cahn D101 microbalance, (Thermo Fisher Scientific, Inc., Waltham, MA 02454) with an accuracy of 10⁻⁶ g, was used to study kinetics of corrosion as shown in Figure 2.6.

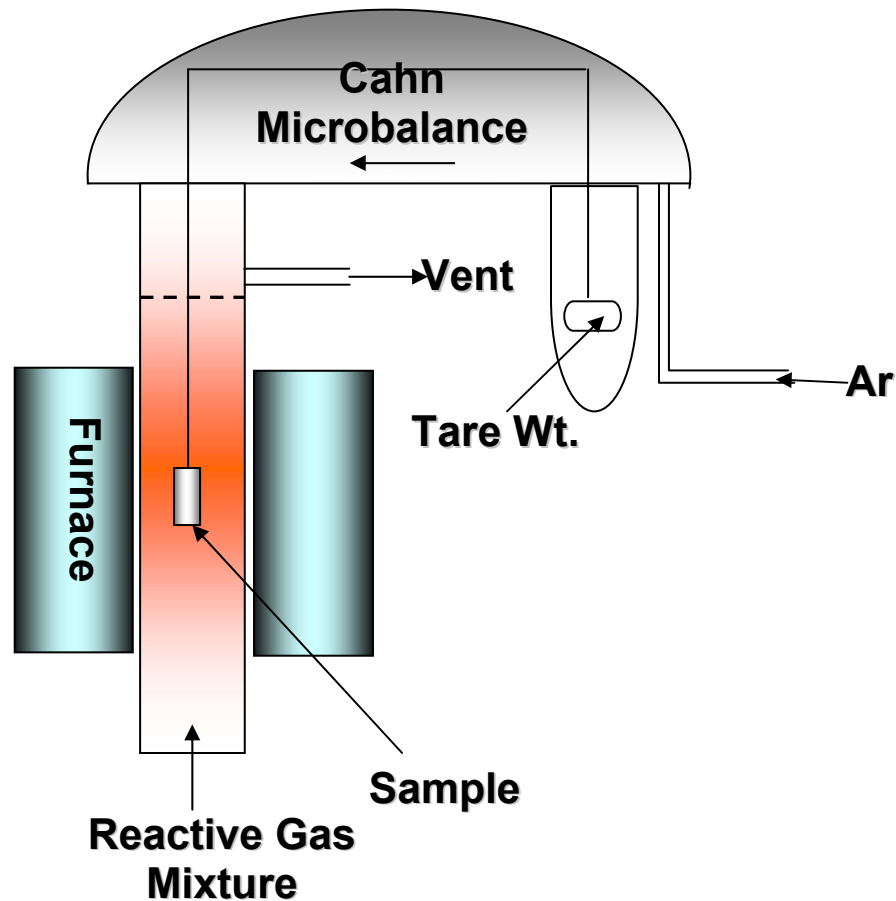


Figure 2.6: TGA setup for corrosion kinetics studies in sulfidizing-oxidizing environments

In first series of tests, SA210 samples were exposed to 1% H₂S in N₂ (pS₂ ≈ 10⁻¹⁴atm at 300°C) at 300°C. Weight change was normalized to the exposed surface area to compare different samples. Multiple samples were tested to confirm reproducibility of the test procedures. In another series of tests, the carbon steel samples were exposed to cyclic environments at a given temperature. Two different types of cyclic environments were simulated in this study. In first type of cyclic tests gaseous environments were cycled between the extreme, sulfidizing (pS₂ =10⁻¹⁴atm) and oxidizing (pO₂=10⁻²atm) environments, identified from our boiler-furnace environment characterization study. In the second type of cyclic tests the environment was cycled between the gas composition, where the gas mixture was oxidizing with sulfur-bearing gases (pSO₂ = 10⁻¹atm), and the other extreme gas composition was sulfidizing without any presence of oxygen bearing gases (pS₂=10⁻¹⁴). Figure 2.7 shows the measured and simulated environments at 320°C superimposed on a (Fe-Al-Cr)-O-S phase stability diagram. Corrosion kinetics tests were also performed for aluminized carbon steel samples in cyclic environments where the gas composition was cycled between an oxidizing environment (air, pO₂=0.21 atm) and a sulfidizing environment (pS₂ = 10⁻¹⁴atm). Data from the weight change was used to determine the possible reaction mechanisms and corrosion kinetics for tested carbon steel or coated samples. Calculated rate constants from the plot of (Δm/A)² vs time gives parabolic rate constant K_p , as shown in equation (1) whereas linear rate constant K_l was calculated from plot of (Δm/A) vs time as shown in equation (2), where Δm is change in weight and A is area of the sample.

$$\left(\frac{\Delta m}{A}\right)^2 = K_p t + C \quad (1)$$

$$\frac{\Delta m}{A} = K_l t + C \quad (2)$$

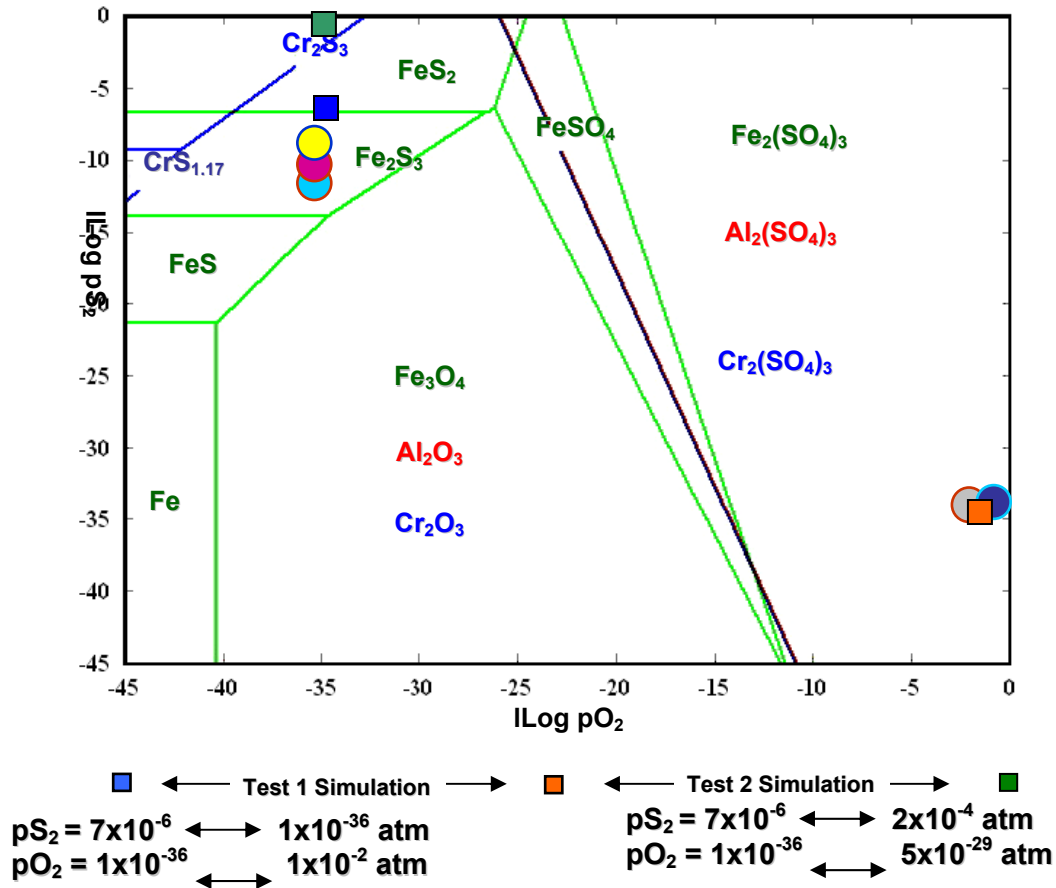


Figure 2.7: Stability diagram for (Fe,Al,Cr)-O-S system with superimposed measured boiler conditions (circular dots) and simulated conditions in laboratory (square dots) using mixture of N₂, O₂ and H₂S

These results were used to understand the effect of cyclic gas composition on the overall corrosion kinetics of carbon steel tubes in local areas of mid furnace of kraft recovery boilers. Composition and morphology of the scale formed under each tested condition was characterized by mounting and sectioning the scale and examining it using SEM (LEO GEMINI 1530 Thermally-Assisted Field Emission (TFE) SEM, Zeiss, Oberkochen), with EDS (Oxford Instruments, Witney, Oxon, OX29 4TL, UK). Care was taken to make sure that the corrosion scale is not damaged during the sectioning and polishing.

2.4 MECHANICAL PROPERTIES

Performance of coatings depend upon their chemical as well as mechanical properties. Mechanical behavior of coatings, interdiffusion zone and the base metal was characterized by using Nanoindenter. Nanoindentation experiments were used to quantify the mechanical properties such as nano-hardness (H) and elastic modulus (E) in the local areas. MTS Nanoindenter XP (MTS Nano Instruments, Oak Ridge, TN) equipped with a Berkovich shaped diamond tip was used to get the load-displacement curves from which the mechanical properties could be extracted. The tests were conducted on metallographically mounted and polished cross-sections of the coating systems at a constant load of 100 and 200 mN. Coating, interdiffusion zone and substrate areas were indented to compare the properties as a function of aluminum content. Aluminum content at the nano-indentation location was measured by EDS after the indentation experiments. The hardness and modulus over a defined range is based on continuous stiffness and hardness readings. Continuous stiffness measurements are accomplished by applying a small oscillation to the force signal at a relatively high frequency. The amplitude of the force oscillation is small enough that it does not affect the deformation process. The hardness and modulus from unload is based on the unloading stiffness. The theory behind hardness and modulus calculation is presented in Appendix B . Load-displacement curves are evaluated by Oliver and Pharr ^[111] method to get modulus of elasticity and hardness. This work reports both the average and calculated on unloading values of E and H.

2.5 LUMINESCENCE PIEZOSPECTROSCOPY FOR STRESS MEASUREMENTS

Stresses in the oxide scale after high temperature corrosion test were measured using luminescence piezospectroscopic technique. Figure 2.8 shows a schematic of the experimental setup used to acquire luminescence spectra from exposed aluminide coating samples. The samples, typically an oxidized aluminide coated SA210 carbon steel, are illuminated with a focused laser beam. The area of illumination is a circular spot with diameters in the range of 30-120 μm . The laser used for this study was argon gas laser (Omnichrome Corporation/Melles Griot, Carlsbad, California) with laser line of 488nm. The laser power was <500mW. A bifurcated optical fiber ($\phi=600\mu\text{m}$, Ocean optics, Dunedin, FL) was used to transmit laser to the microscope and collect the emission spectra from the sample. The spectra were transmitted to a high resolution spectrometer (HR4000 high resolution spectrometer, Oceanoptics, Dunedin, FL) which was calibrated to measure the spectra in the range of 650-750nm with 0.5cm^{-1} spectral resolution. The spectrometer analyzes the scattered light by using diffraction gratings to spatially separate the various frequencies. The resulting spectrum is imaged onto a CCD detector (Toshiba TCD1304AP linear CCD array) with 3648 pixels elements with sensitivity of 100 photons/count. The detector sends an electronic signal to the computer where the data acquisition software (Spectrsuite[®], Ocean Optics, Dunedin, FL) displays the spectrum in digital format. Microscope used in this study was Nikon LSM (Nikon, Inc.,USA) with 5X, 10X, and 20X objective lenses illuminating surface with laser spots of 120 μm , 60 μm and 30 μm respectively.

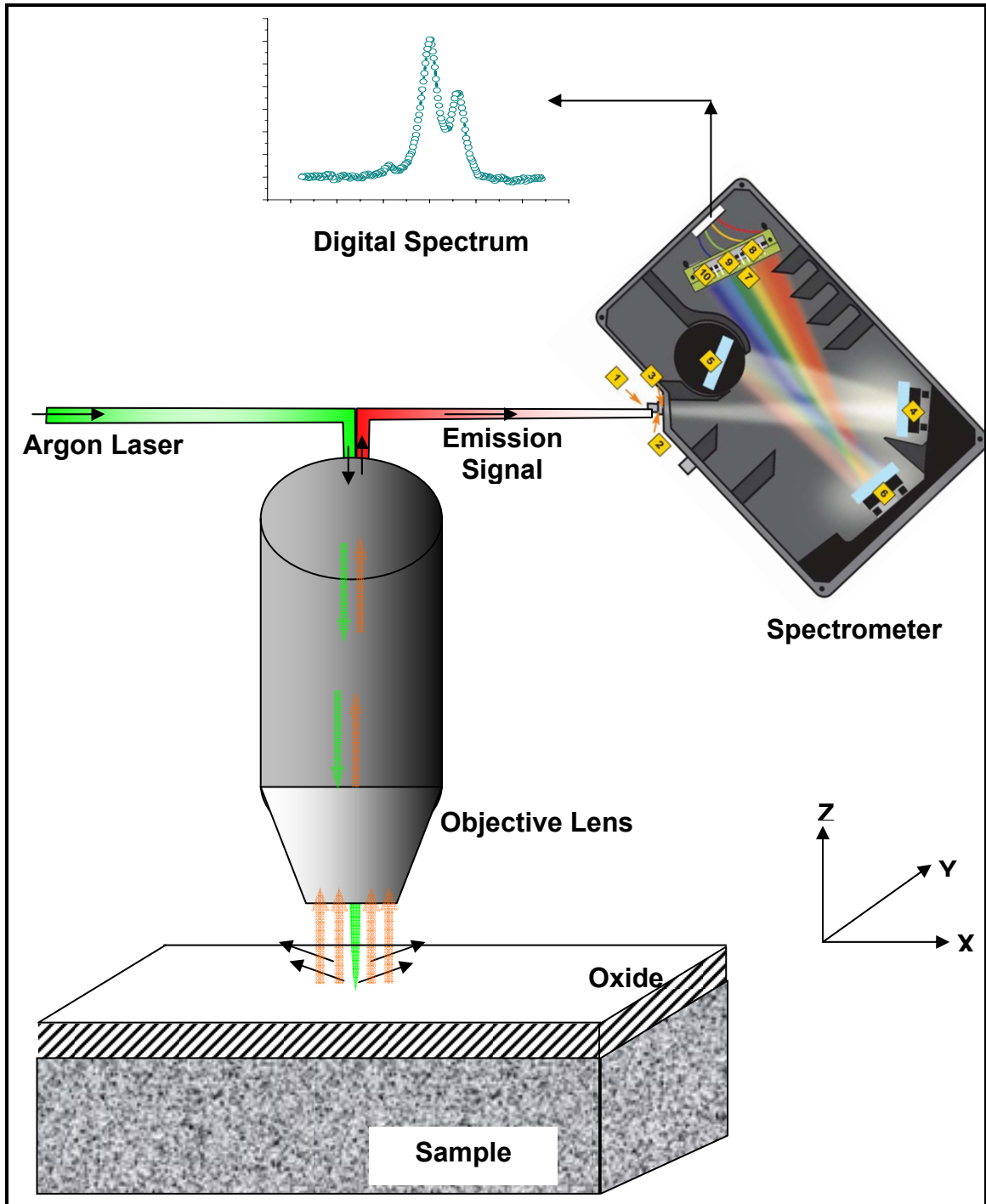


Figure 2.8: Experimental setup for acquiring luminescence spectra from oxidized aluminized SA210 samples

2.5.1 Spectrometer

Emission signal from the oxide layer enters the optical fiber in reflection geometry and is efficiently transmitted to the spectrometer (Figure 2.8). Once in the spectrometer, the divergent light emerging from the optical fiber is collimated by a spherical mirror. The collimated light is diffracted by a plane grating, and the resulting diffracted light is focused by a second spherical mirror. An image of the spectrum is projected onto a linear CCD array, and the data is transferred to a computer through an onboard A/D converter. Light impinges on photodiodes with the CCD pixels. These reverse-biased photodiodes discharge a capacitor at a rate proportional to the photon flux. When the integration period of the detector is complete, a series of switches close and transfer the charge to a shift register. After the transfer to the shift register is complete, the switches open and the capacitors attached to the photodiodes are recharged and a new integration period begins. Integration time used for this study was 1000 msec. At the same time that the light energy is being integrated, the data is read out of the shift register by an A/D converter. The digitized data is then displayed on the computer.

2.5.2 Stress mapping

Stress in the oxide scale was mapped by luminescence piezospectroscopy using a Nikon LSM (Nikon, Inc., USA) microscope, equipped with a motorized stage (Prior Scientific, USA) which can move in x and y direction with accuracy of $1\mu\text{m}$. Stage was controlled and programmed for acquiring data at regular distance in a selected area using a software (Advanced serial port monitor, AGG Software, USA) and synchronized with the spectra analysis software (Spectrasuite[®], Oceanoptics, USA) to create a desired spectral mapping

grid. A fine grid with step size of 50 μm was employed to map the stress distribution in the oxide layer. Total of 2500 spectra were recorded from the oxide scale in the selected area between the edge and at the center of sample. All spectra were fitted using Origin 7.0 (Originlabs, USA) to deconvolute the peak positions (Figure 2.9) which were then used to calculate stresses in the scale by the method discussed in chapter 1 (section 1.8). Detailed peak fitting procedure will be discussed in chapter 6.

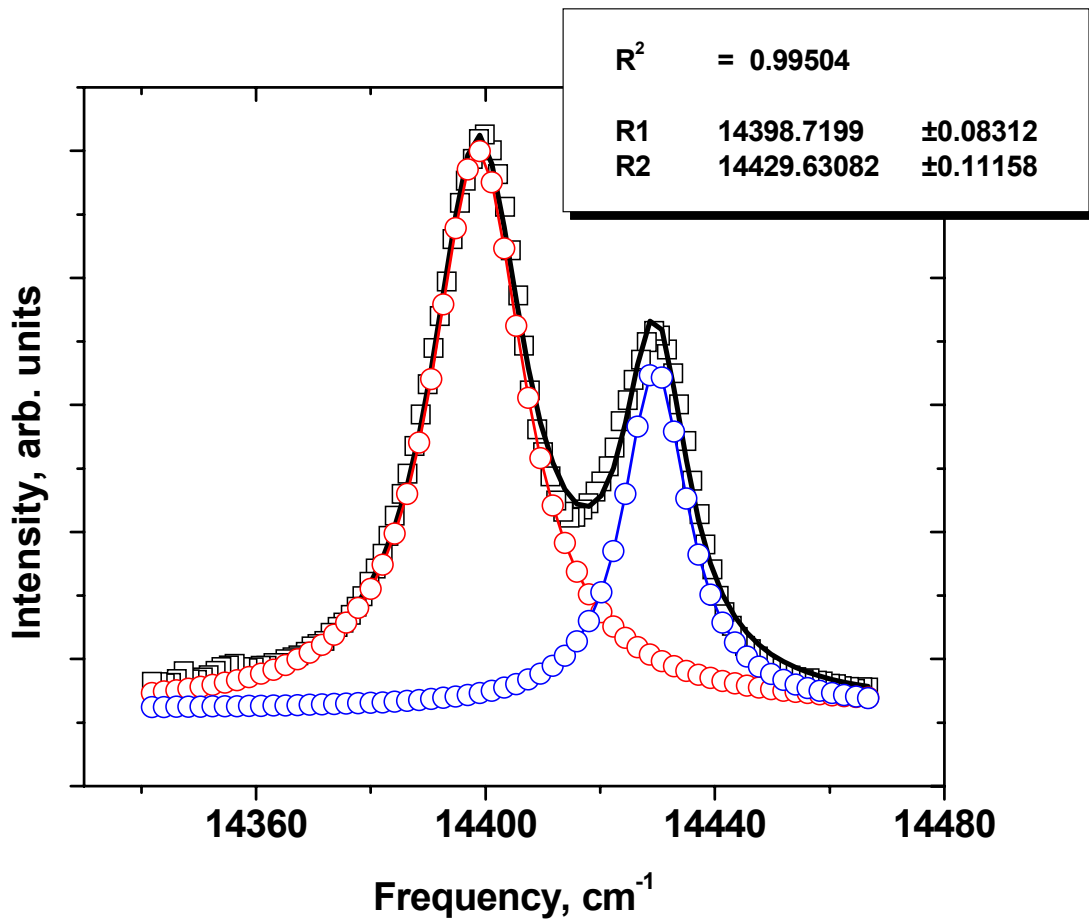


Figure 2.9: Spectrum collected for oxidized aluminide coating at 1000 $^{\circ}\text{C}$ and corresponding deconvolution of R1 and R2 peaks

CHAPTER III
FLUCTUATING SULFIDIZING-OXIDIZING ENVIRONMENTS AND ITS
EFFECT ON PHASE STABILITY OF PROTECTIVE SCALE ON SA210
CARBON STEEL

INTRODUCTION

Corrosion by hot gases is possible in processes such as: petroleum refining, gas processing, fired equipment, process heaters, burners, flares, furnaces, boilers, hydrocracking, coking, oil refining, hydrotreating, coal/coke/oil gasifying, petrochemical production, waste incineration, hydrogen plants, heat treatment, and electric heaters^[112]. Examples of the types of process equipment where sulfidation is a concern are kraft recovery boilers, black liquor gasifiers, coal gasifiers, hydrotreater charge furnaces, crude distilling columns, vacuum flashers, petroleum coking units, and sulfur removal plants (gas sweetening plants). Although environments frequently fluctuate between sulfidizing and oxidizing at the equipment surfaces due to sulfur content of fuel and combustion aid (i.e. air) flow variations, researchers generally consider the bulk environment as a baseline to test the alloys. Kraft recovery boilers in pulp and paper industry is such an example and was chosen as a representative of power generation processes for this study. Gaseous environment in the mid-furnace of kraft recovery boilers was generally considered to be oxidizing and not very corrosive to carbon steel waterwall tubes. Mid-furnace corrosion is prominent above the cut-line where composite tubes, with a stainless steel outer layer, are welded to the carbon steel waterwall section. However, an accelerated corrosion can extend tens of feet above the cut-line in certain areas of boilers.

Certain areas in the lower and mid-furnace of kraft recovery boilers have shown higher corrosion rates than others in the nearby areas at the similar elevations at similar tube temperatures as show in Figure 3.1. This suggests that there is instability in the local gas flow in the mid furnace leading to changes in the local environment which may frequently change between the oxidizing and sulfidizing gases. Composition of local gaseous environments, responsible for waterwall corrosion, in the mid furnace areas was not known. Differences in the gaseous environment in the low corrosion and high corrosion areas were not clear. To understand the corrosion mechanisms behind accelerated corrosion in the mid-furnace operating, local environments were characterized. Results from the boiler environment characterization and its effects on stability of protective oxide scale on SA210 carbon steel are discussed in this chapter.

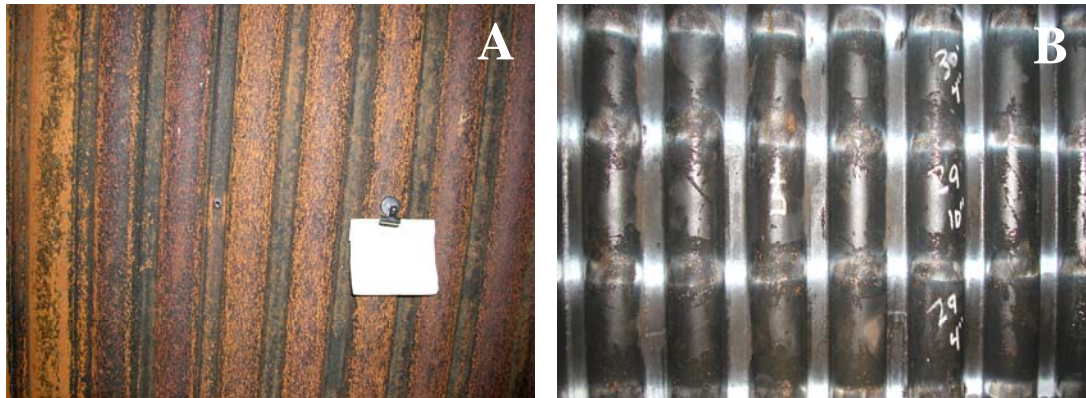


Figure 3.1: (A) areas of high corrosion in kraft recovery boiler 6 feet above cut line, (B) areas of low corrosion at the same elevation as (A).

3.1 BOILER ENVIRONMENT CHARACTERIZATION AT TUBE SURFACE

Mid furnace of a boiler is an area which separates the reducing and sulfidizing lower furnace from the oxidizing upper furnace. Corrosion rates of carbon steel tubes in some of this region of boiler were even higher than for the lower furnace. It is known that the gaseous environment in these areas is instable as discussed in chapter 1; however, the extent of environment fluctuations and frequency of fluctuation was not known. To characterize these parameters, multiple gas samples were collected over a year from the sampling ports installed in the mid furnace area of a kraft recovery boiler. A kraft recovery boiler was chosen as a representative example of power generation processes for this study and boiler specifications are discussed in chapter 2. Figure 3.2 shows the schematic of the boiler, observed corrosion patterns and installed ports to collect the gas samples from tube surface. Shaded regions shows the areas of high corrosion as measured from the ultrasonic wall thickness data during annual inspection reports of two previous years, shown in Figure 3.1. During the time period of gas sampling, roughly a year, the boiler operation parameters were not changed in this mill, so the results in this chapter were taken under the same normal boiler operation conditions. Gas samples in the boiler were collected and analyzed using an identical procedure discussed in chapter 2. Although a large number of samples were collected from the boiler, only a limited representative data is presented in this chapter to illustrate the variation in gaseous environments in the mid-furnace of the kraft recovery boilers. Detailed concentrations of all the sulfur and oxygen containing gases are presented in Appendix A.

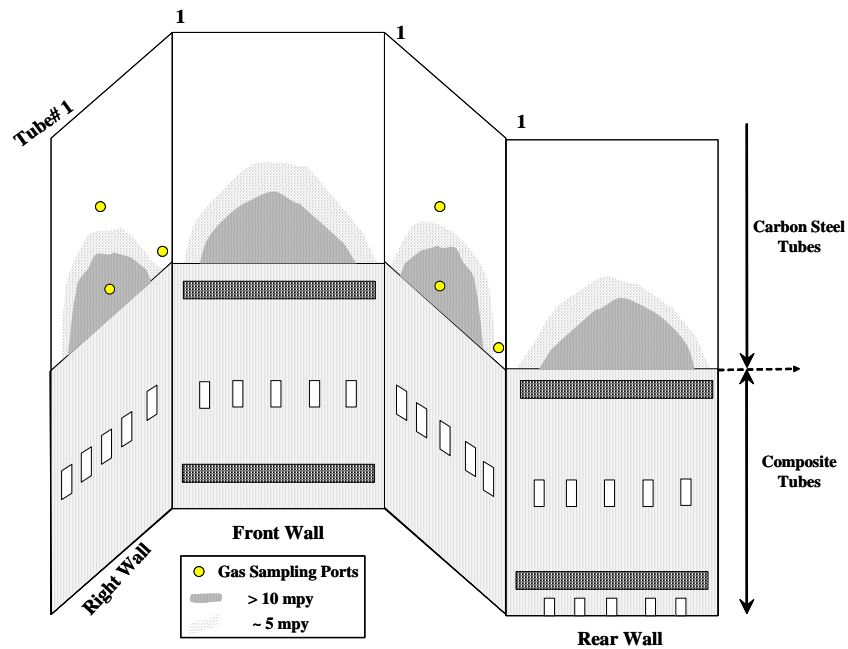


Figure 3.2: Schematic of kraft recover boiler showing corrosion patterns and port locations on the tube surface in mid-furnace area. Notice that the boiler had two air levels and higher corrosion rates were experienced till higher elevations in middle of side walls compared to the corners as shown in Figure 3.1.

Average gas composition at the waterwall surface in the area of each sampling port on different days was calculated from the multiple gas samples taken from each port. Average gas composition data from each port was used to calculate the partial pressure of oxygen and sulfur in boiler gases at the waterwall surface, assuming that the gases were at equilibrium. Typical gas samples taken from the waterwall surface in the mid furnace area contained light gases like oxygen (O_2), nitrogen (N_2), hydrogen (H_2), carbon dioxide (CO_2), methane (CH_4), carbon monoxide (CO), and sulfur-bearing gases like hydrogen sulfide (H_2S), carbonyl sulfide (COS), methyl mercaptan (CH_3SH), di-methyl sulfide ($(CH_3)_2S$), sulfur dioxide (SO_2). H_2S and other sulfur bearing gases were detected in almost all selected areas of the lower mid-furnace near cut-line (Appendix A). Figure 3.3 shows the concentration of H_2S in the total gas composition at different port locations in

the mid-furnace of the boiler on eight different days and Figure 3.4 shows the calculated partial pressure of sulfur from gas samples collected.

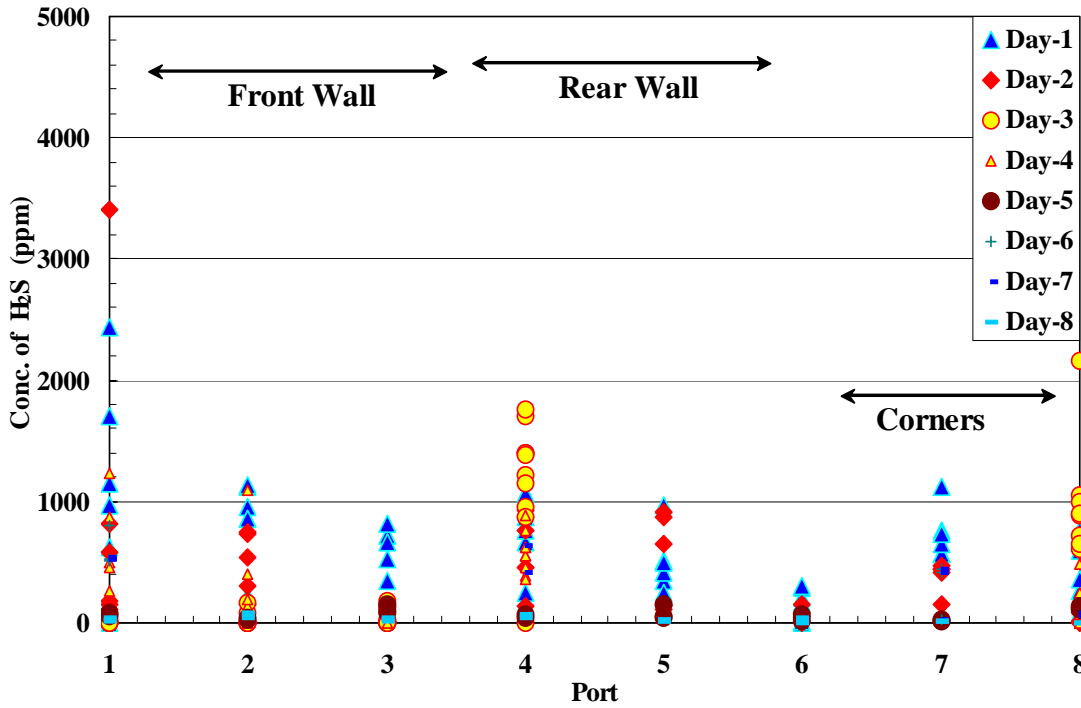


Figure 3.3: Concentration of H₂S in gas samples collected at the waterwall surface of Kraft Recovery Boiler on 8 different days under normal operating conditions. Gas-sampling port positions are shown in Figure 3.2.

Similarly, Figures 3.5 and 3.6 show the concentration and the calculated partial pressure of oxygen respectively from the same gas samples. It is clear from this data that the hydrogen sulfide in the port #1 area varied from ~3500 ppm to 0 ppm, whereas at higher elevations in the same corner of the rear wall of this boiler, at port# 2 and #3, the

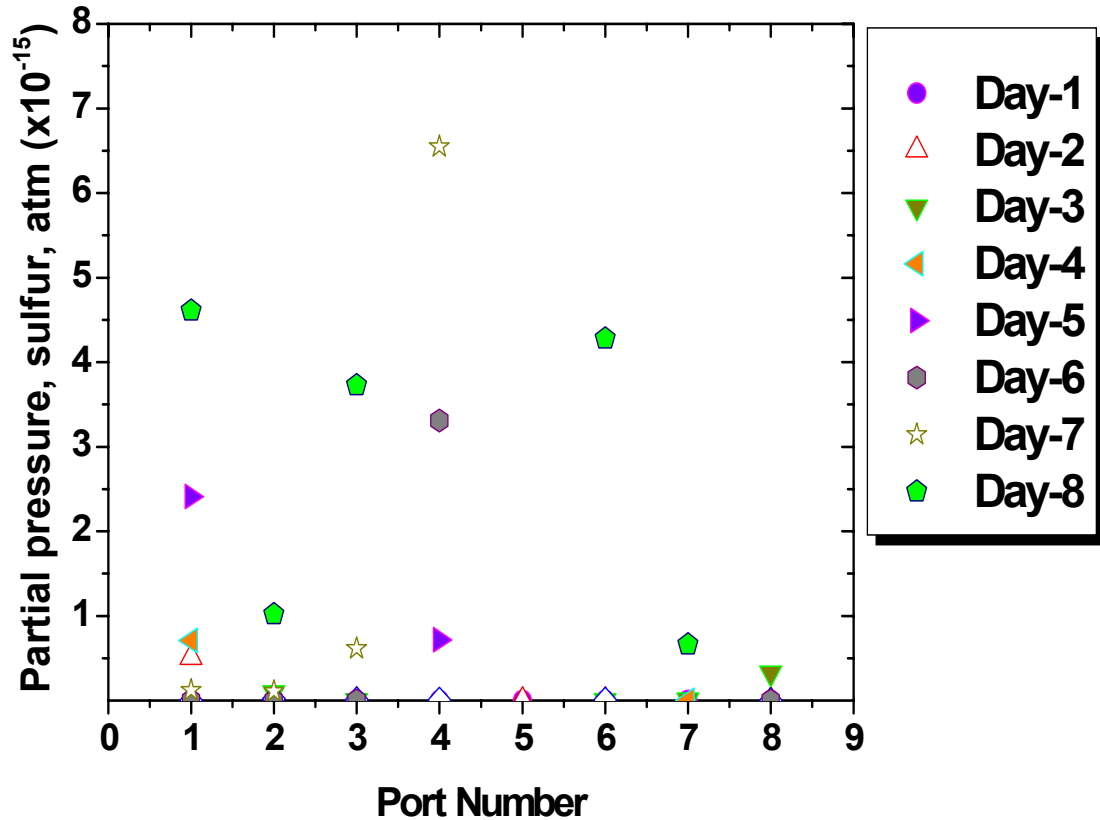


Figure 3.4: Variation in the partial pressure of sulfur in gas samples taken from different ports in the mid-furnace, shown in Figure 3.1 calculated from assuming equilibrium in all sulfur bearing species.

variation was smaller and the maximum concentration of H_2S were significantly lower than port #1. Similarly on the right wall, port #4 had more variation and higher concentration of H_2S compared to locations at the higher elevation. This data shows that the lower elevations in mid-furnace, near tertiary airport, have more instability in the gas composition. Fluctuations on the order of 0 to 10^{-2} atm were measured for sulfur and 10^{-2} to 10^{-4} atm for oxygen.

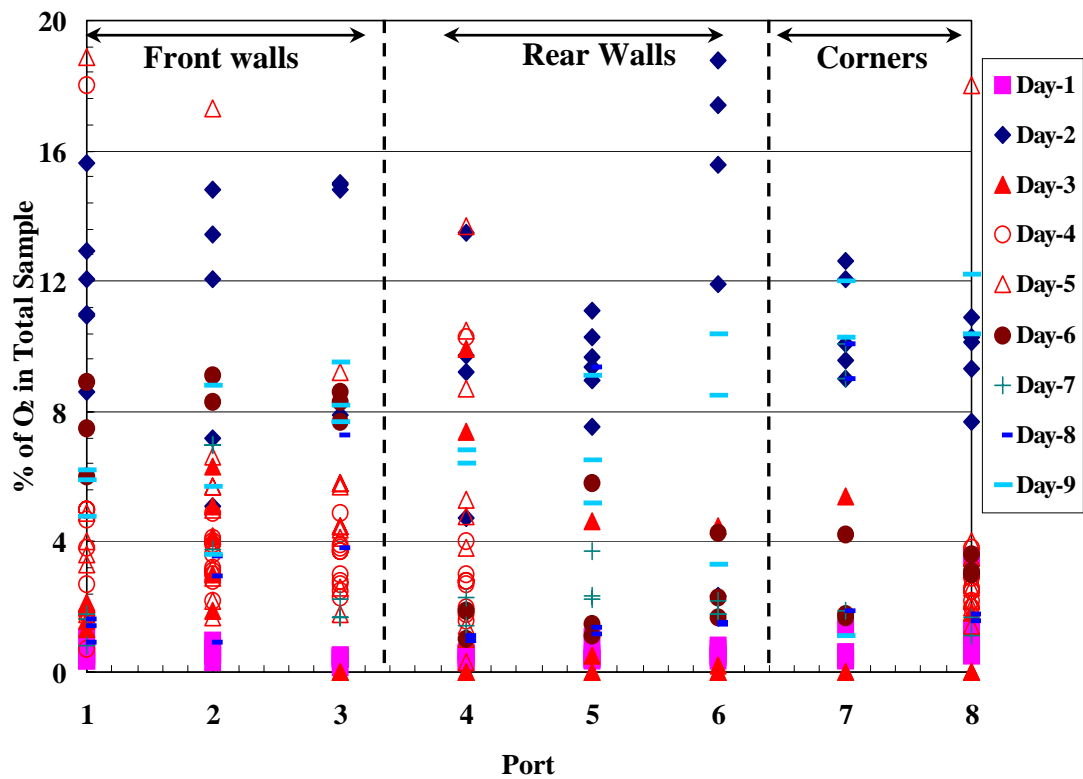


Figure 3.5: Concentration of O₂ in gas samples collected at the waterwall surface of Kraft Recovery Boiler on 8 different days over a-year period under normal operating conditions. Port positions are shown in Figure 3.1.

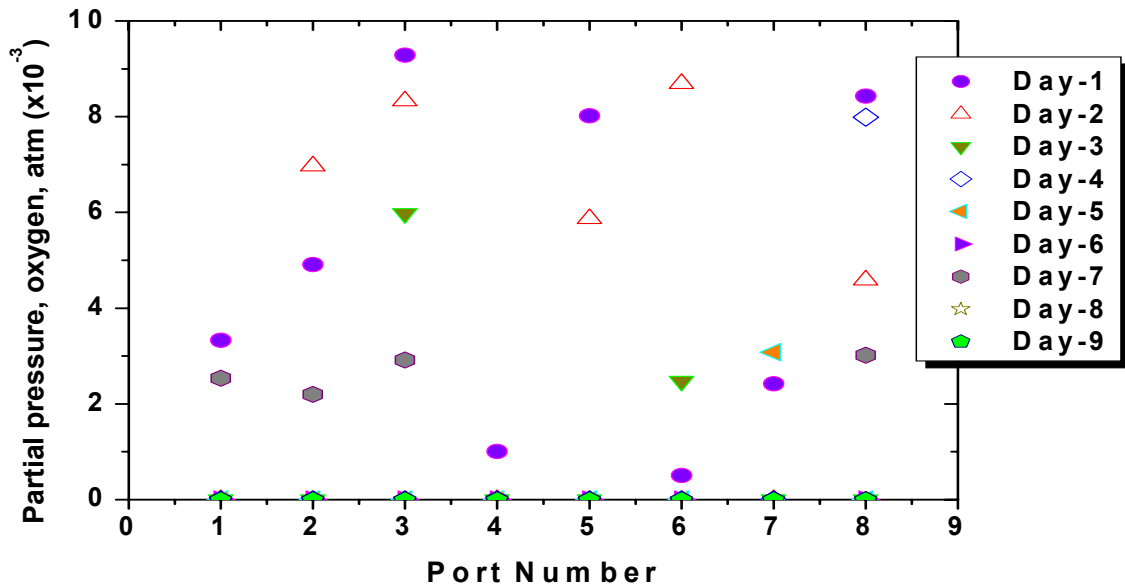


Figure 3.6. Variation in the partial pressure of oxygen in samples taken from different ports in the mid-furnace, shown in Figure 3.1. Partial pressures were calculated from oxidizing species.

Figure 3.7 shows the ratio of partial pressures of oxygen to sulfur at the mid-furnace waterwall of selected boiler. Analysis of boiler gases indicated that the gas compositions fluctuated significantly in the mid furnace area from one sample to other and from one day to other. Overall gas composition fluctuates between the oxidizing to reducing and sulfidizing. However, at higher elevations, near upper furnace area, the gas composition does not fluctuate to the same extent. The mill-operation records were checked to verify if any changes were made in boiler operations during gas sampling in terms of liquor temperature, liquor pressure, air temperature, or air distribution etc. However, no correlation could be found between the changes in the local gaseous environment in the mid-furnace and the boiler operating parameters. This clearly indicates that the gas compositions vary significantly in the mid-furnace of this boiler due to the instability in t

he gas flow patterns near waterwall surface. Highest concentration of H_2S in the mid-furnace area was found to be $\sim 1\%$ in areas with high corrosion rates of carbon steel waterwall tubes. This observation was in disagreement to the notion that mid-furnace environments are oxidizing as $\sim 1\%$ H_2S was typically associated with the bulk gas composition in the lower furnace of kraft recovery boilers. Data from this study suggests that the black liquor reaches the mid-furnace areas and the liquor pyrolysis on the waterwall surface in these areas may be the main reason for the higher concentrations of reducing and reduced sulfur-bearing gases in the mid-furnace which cause accelerated corrosion of carbon steel in these local areas. Figure 3.8 shows the extrapolated values of gas composition fluctuations in the temperature range pertinent to this study (boilers and gasifiers). These partial pressure fluctuations were used in the present study to establish a baseline for the effect of gas fluctuations on the corrosion kinetics of carbon steel samples. These environments were also used for subsequent tests on diffusion coatings developed in this study.

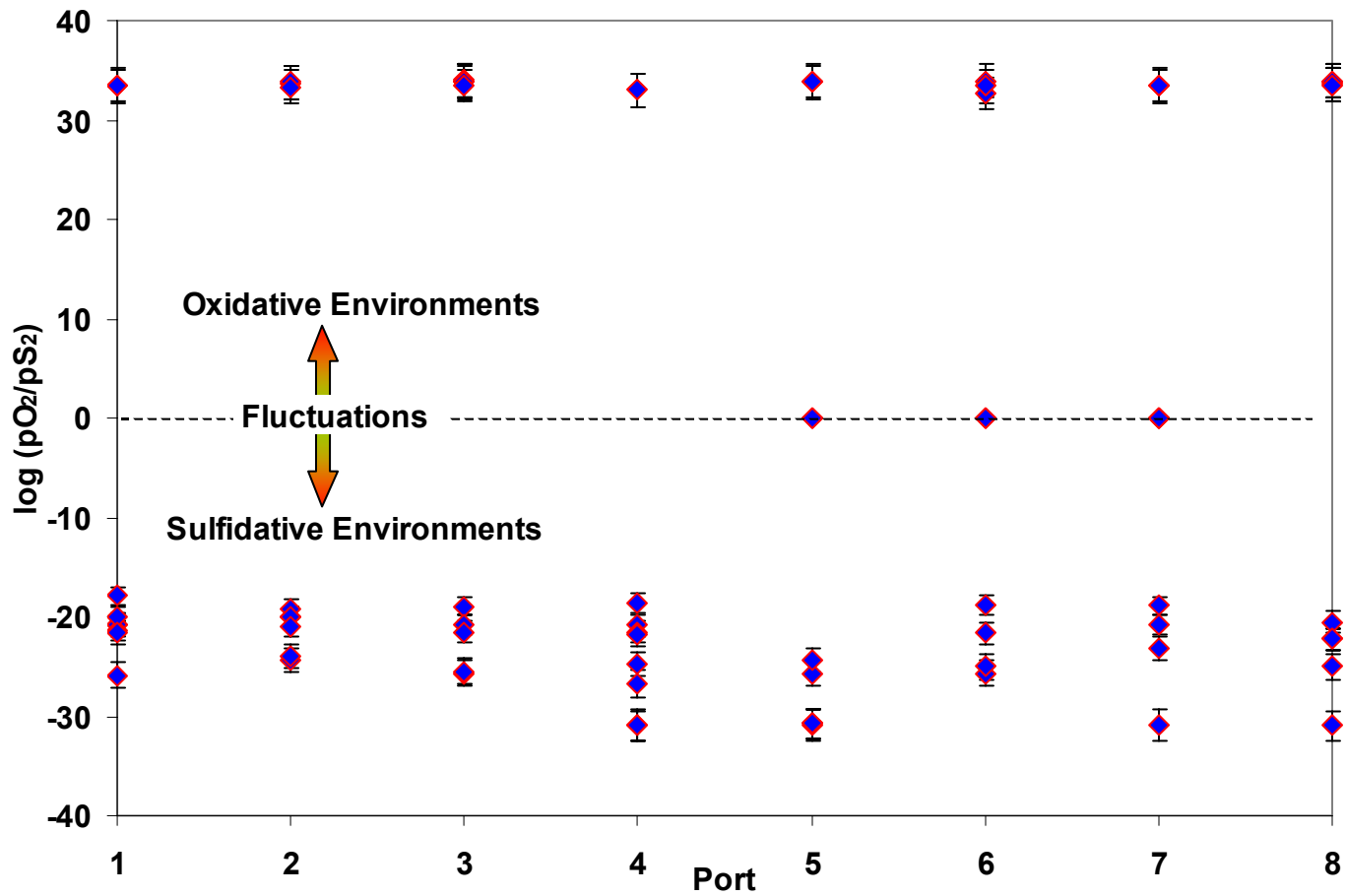


Figure 3.7: Fluctuations in gas composition measured in Kraft Recovery Boiler. Significant cycling between oxidizing and sulfidizing environments was observed. Partial pressures of oxygen and sulfur were calculated from measured gas composition.

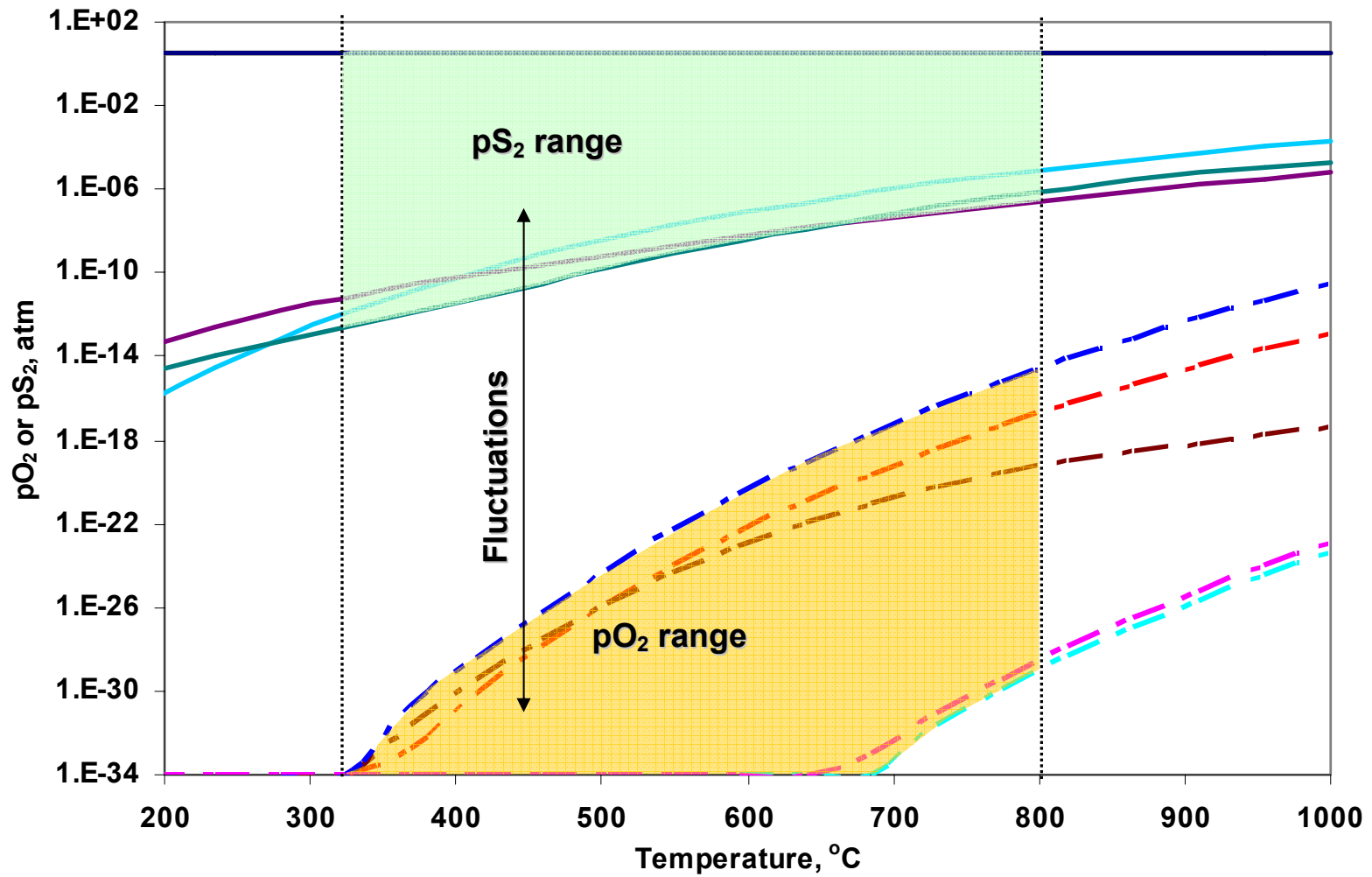


Figure 3.8: Ranges of gas fluctuations measured in boiler extrapolated to the gasification temperatures. Solid line represents pS₂ and dashed line represents pO₂.

3.2 EFFECT OF GAS COMPOSITION ON CORROSION PRODUCT

Composition of corrosion scale developed on the metal surface at high temperature strongly depends upon the gas composition. Sulfide scales develop when the gases are reducing and sulfidizing, whereas an oxide scale develops when the gases contain higher concentrations of oxidizing gases. Figure 3.9 shows the regions of thermodynamically stable phases as a function of oxygen and sulfur partial pressures in a Fe-O-S system at 320°C. Gas samples for Figure 3.9 were taken from the same port location (i.e. port#1) in the selected boiler, but on seven different days. Average gas composition of samples taken from each port on each day were used to calculate the partial pressure of oxygen and sulfur in each area. It can be seen that the subtle changes in the gas composition may favor one scale composition over the other and under certain conditions Fe_3O_4 , FeS_x and FeSO_4 can be simultaneously thermodynamically stable at 320°C for the measured environments. However, the overall scale composition will not only depend on the thermodynamic stability but also on the kinetics of formation and rate of conversion reactions from one corrosion product to other in the case of fluctuating gas compositions. Environmental cycling between the sulfidizing and the oxidizing gases may lead to the formation of an unstable and non protective mixed oxide/sulfide/sulfate scale on the waterwall surface and can result into an accelerated corrosion of the carbon steel.

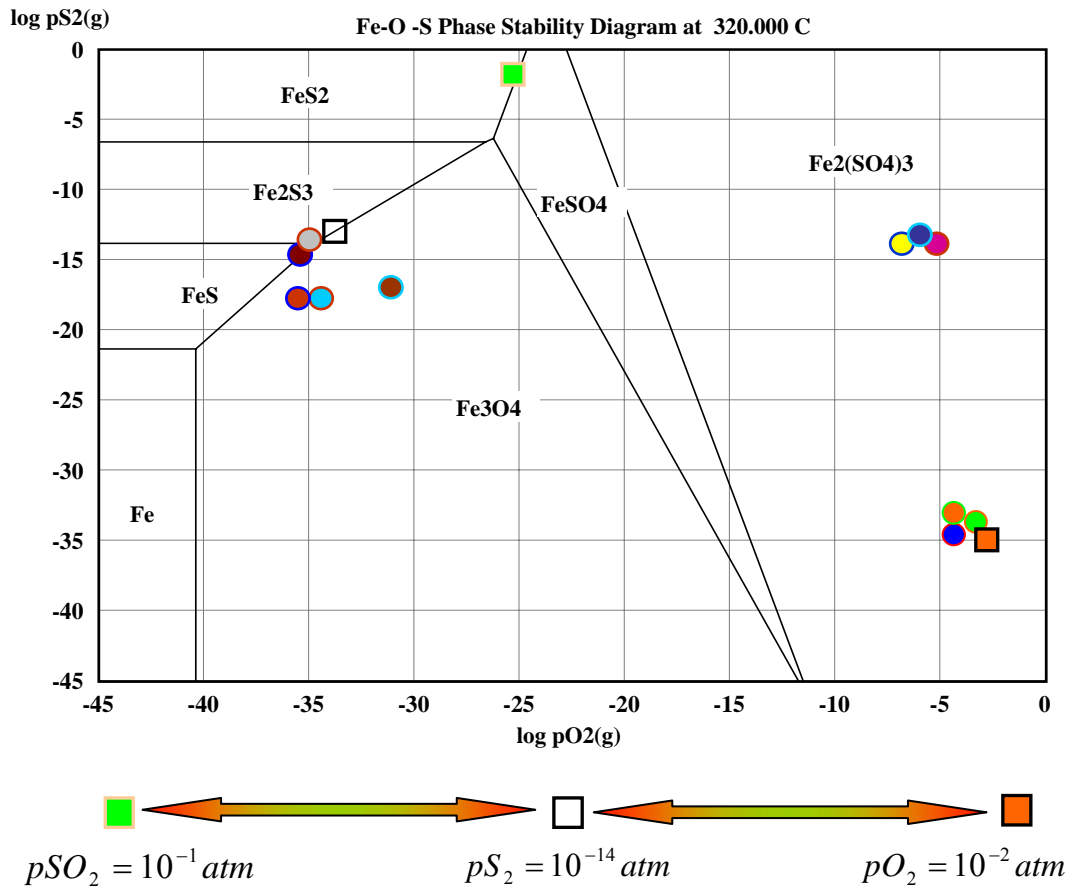


Figure 3.9: Phase Stability diagram for Fe-O-S system at 320°C. Diagram shows partial stability regions for different possible scale compositions as a function of oxygen and sulfur partial pressure in contact with iron. Round symbols show measured partial pressures in gases sampled from the port #1 on different days and the square symbols show simulated cyclic environments used in laboratory tests.

3.3 EFFECT OF CYCLIC SULFIDIZING-OXIDIZING ENVIRONMENTS

To understand the effect of gas composition fluctuation on scale stability for the carbon steel, laboratory tests were designed where the test environment was cycled every 12 hours between different gas compositions. Two types of cyclic environments were chosen for this study. In the first case, extreme gas compositions from the gas characterization study results were used where the composition cycles between an oxidizing mixture to a reducing and sulfidizing mixture. To simulate that, in the Test-1 the gas composition was cycled between 1% H₂S + N₂ (pS₂ = 10⁻¹⁴atm) and 1% O₂ + N₂ (pO₂ =10⁻²atm) every 12 hours. In other two cases, the composition of test gas mixture was changed between 1% H₂S + N₂ (pS₂ = 10⁻¹⁴atm) and [(1%H₂S + 1%O₂) + N₂] (pSO₂ =10⁻¹atm) every 12 hours. Difference between the last two tests was that the Test-2 started with an oxidizing environment whereas the Test-3 was started with a sulfidizing environment. Tested environments represented various scenarios that may be experienced in the mid-furnace of kraft recovery boilers where the gases were generally sulfidizing due to black liquor pyrolysis locally at the waterwall surface, but the area may also be exposed to the oxidizing gases frequently due to the instability in the gas flow. Partial pressure of sulfur and oxygen for the environments used in these tests were also superimposed on the phase stability diagram in Figure 3.9 to compare the laboratory conditions with the boiler conditions measured in our characterization study. SA-210 carbon steel samples were exposed in the cyclic environments and the weight change was recorded continuously every 1 second isothermally at 300°C. Results from these tests are shown in Figure 3.10. Figure 3.10 has alternating 12-hours zones marked as A and B, which represent the different gas compositions during that time, as indicated in the figure caption.

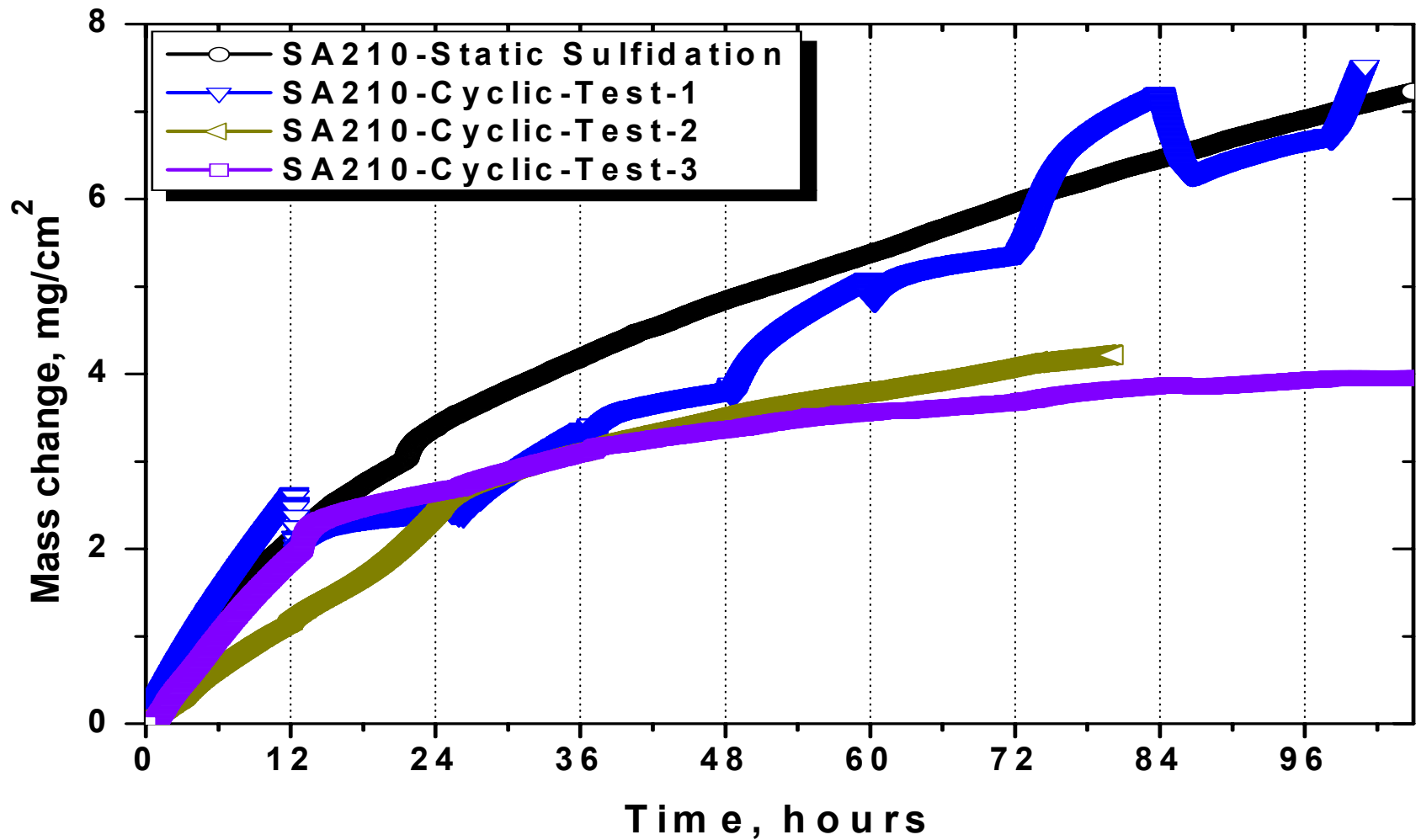


Figure 3.10: Effect of fluctuating sulfidizing/oxidizing atmosphere on corrosion behavior of SA210 at 300°C. A and B denotes gas atmosphere as: Test-1: (A) $p_{S_2} = 10^{-14}$ atm, (B) $p_{O_2} = 10^{-2}$ atm; Test-2: (A) $p_{SO_2} = 10^{-1}$ atm, (B) $p_{S_2} = 10^{-14}$ atm; Test-3: (A) $p_{S_2} = 10^{-14}$ atm, (B) $p_{SO_2} = 10^{-1}$ atm

3.3.1 *Cycling between sulfidizing $pS_2=10^{-14}$ atm and oxidizing $pO_2=10^{-2}$ atm.*

Figure 3.11 shows the mass change per unit area for a SA210 carbon steel sample with time at 300°C for the environments fluctuating between $pS_2=10^{-14}$ atm and $pO_2=10^{-2}$ atm every 12 hours. Sharp mass loss was observed after each environmental cycle, which indicates spallation of scale, as shown by the magnified view of the curve after first gas cycling event in Figure 3.11(b). Weight loss due to scale spallation of the order of $1\text{mg}/\text{cm}^2$ was observed at the beginning of every gas cycle. Scanning electron micrograph in Figures 3.12 (a) and (b) shows a cross-section of the surface scale formed after 100 hours of exposure at 300°C. Scale shows a layered structure due to the formation of alternating oxides/sulfides during each environmental cycle. Sulfide layers were $\sim 20\mu\text{m}$ thick whereas the oxide layers were $\sim 50\mu\text{m}$ thick with the total scale thickness of $\sim 200\mu\text{m}$. The qualitative composition of scale was determined by energy dispersive X-ray spectroscopy (EDS) maps over the scale cross-sections, as shown in Figure 3.13. During first sulfidizing period, the sulfide scale forms as the most stable corrosion product. As the test atmosphere changes to oxidizing, the oxide scale forms above the preformed sulfide scale resulting in a layered structure. Large mismatch between the oxide and the sulfide layers can cause the scale to crack and spall, increasing the corrosion rate of the carbon steel. Table 3.1 shows the comparison of thermal expansion coefficients of substrate with sulfides and oxides of iron.

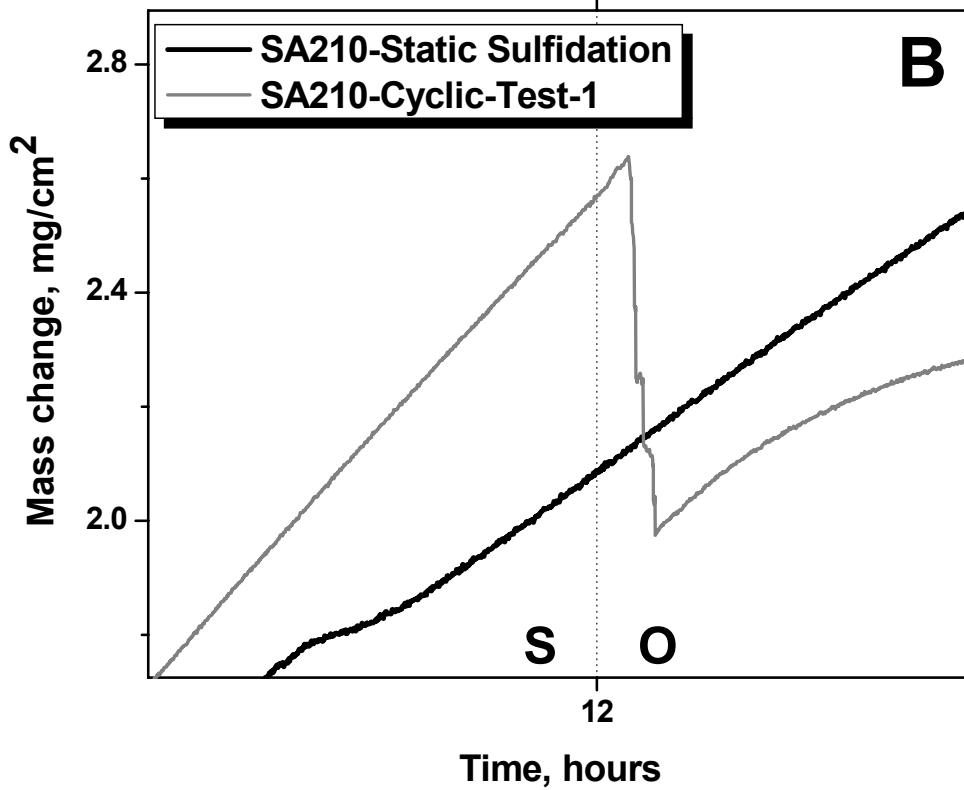
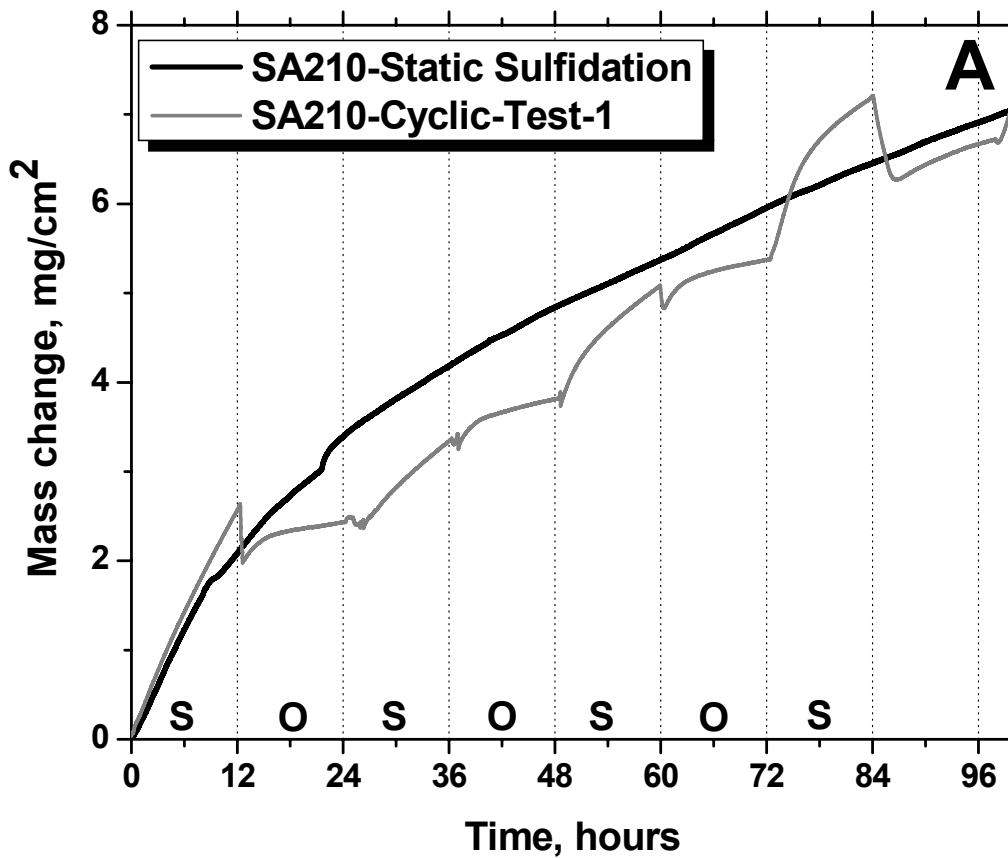


Figure 3.11: (a) Corrosion kinetics of SA210 in test-1 conditions as compared to static sulfidation, (b) Kinetic changes on environmental cycling shows extensive spallation

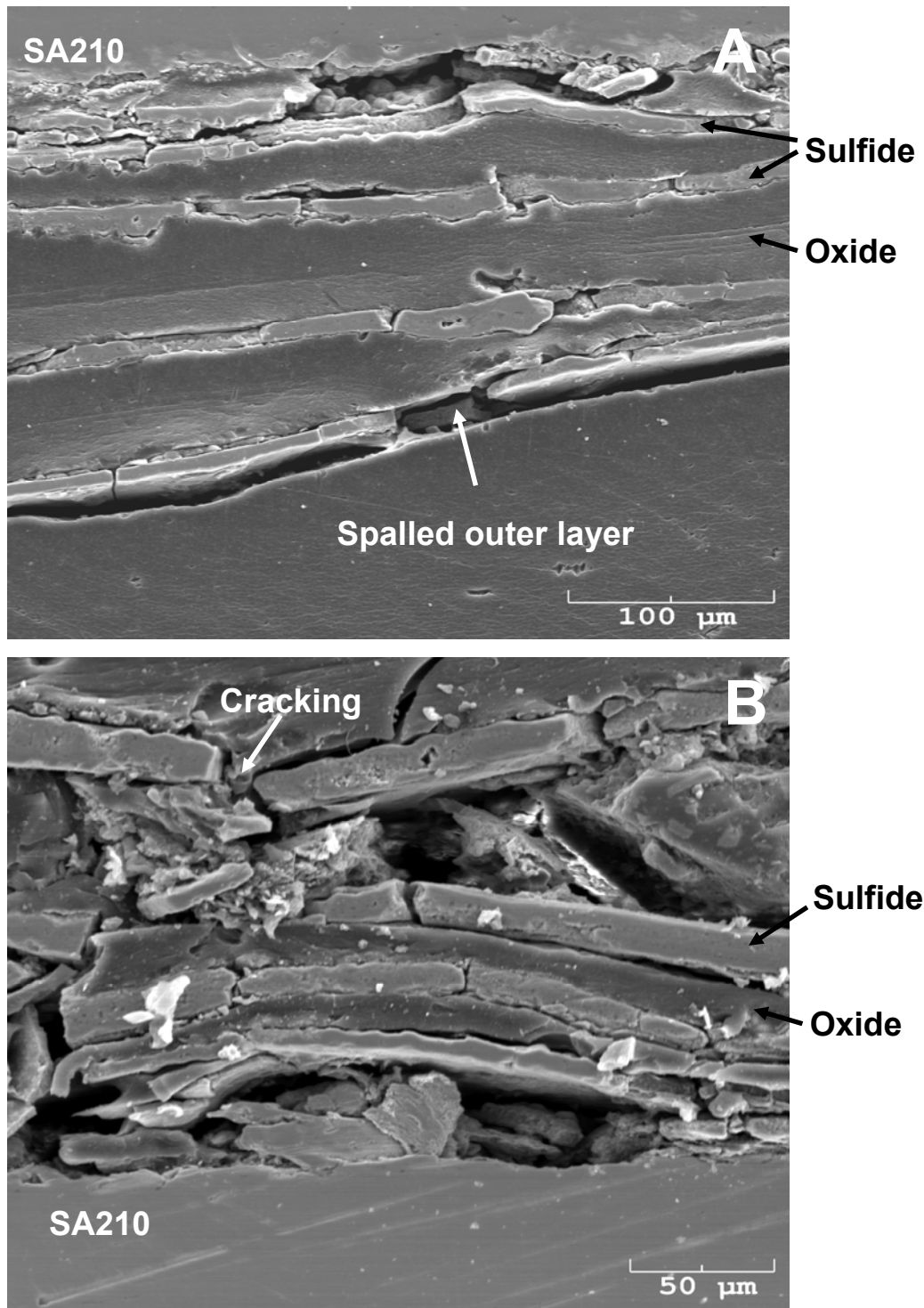


Figure 3.12: SE micrographs of laminated scale after test # 1.

(A) Alternative oxide/sulfide scale corresponding to each cycle, (B) Extensive cracking in scale. Oxide scale is relatively continuous and free from cracking.

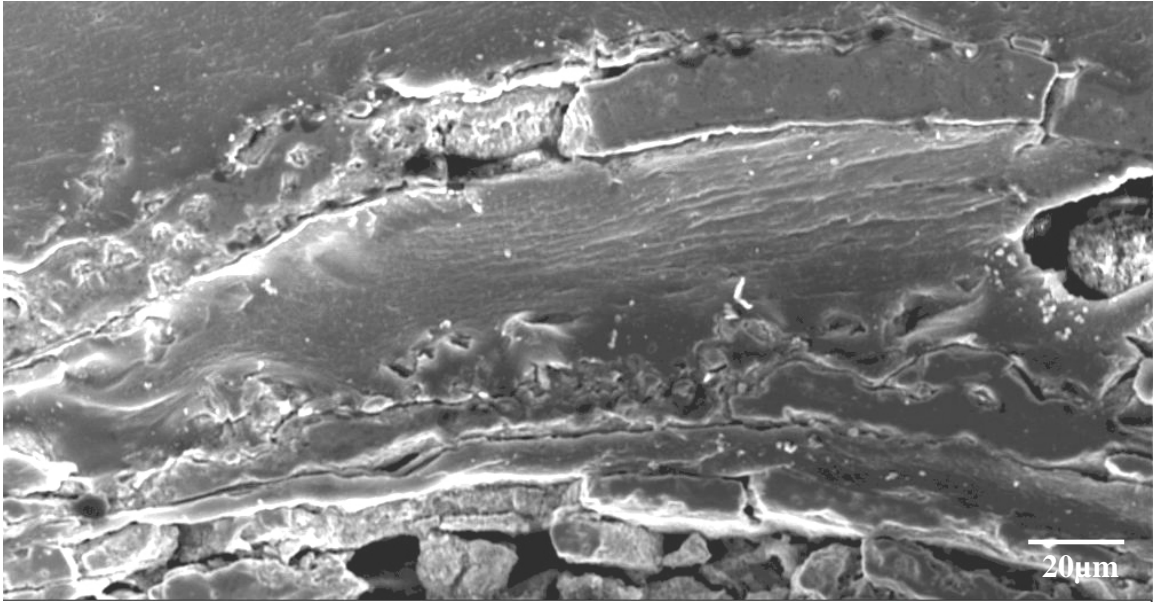


Figure 3.13: Layered microstructure of scale on carbon steel sample after Test-1 with Sulfur-X-Ray maps showing presence of alternate oxide/sulfide layers of the scale. A layer with absence of sulfur in EDS maps was assumed to be an oxide.

Extensive rumpling of scale was observed at alloy/scale interface as shown in Figure 3.13(a) due to large CTE mismatch between sulfide/oxide and metal and resulting stress generation. Oxide scale was found to be relatively more dense and free from big cracks compared to the sulfide scale, as shown in Figures 3.13(b). Figure 3.14 shows the spalled oxide region sandwiched between two sulfide layers as evident from the EDS sulfur map. The Test-1 was started with a sulfidizing environment and last cycle for this test was oxidizing. Number of layers on this sample and number of gas cycles correlated for this test. Layers on the scale were also in the same order as the gas composition. Weight change during each environmental cycle was used to determine the corrosion kinetics during that time period and determine if the reaction rate was linear or parabolic. Resulting values of parabolic and linear rate constants for different parts of Test-1 are listed in Table 3.2. During first two sulfidizing cycles, corrosion reaction in sulfidizing environment showed a linear behavior whereas parabolic behavior was seen during the oxidation period. As the scale grows, the sulfidation behavior showed a dependence on diffusion through unspalled/adherent scale indicating a transition to parabolic corrosion rate. Weight of the spalled scale was accounted-for from the thermobalance data. Total mass gain for the SA-210 carbon steel sample in Test-1, with fluctuating gas environment was $\sim 8.1 \text{ mg/cm}^2$ (after accounting for the weight of spalled scale). This was more than for the SA-210 sample exposed to a static 1% $\text{H}_2\text{S} + \text{N}_2$ environment ($\sim 6.1 \text{ mg/cm}^2$) as shown in Figure 3.11. Data after about 96 hours indicate a clear accelerated corrosion for carbon steel under extreme cycling environments at 300°C . However, this effect is expected to be more significant for longer exposure times, of relevance to industrial equipment.

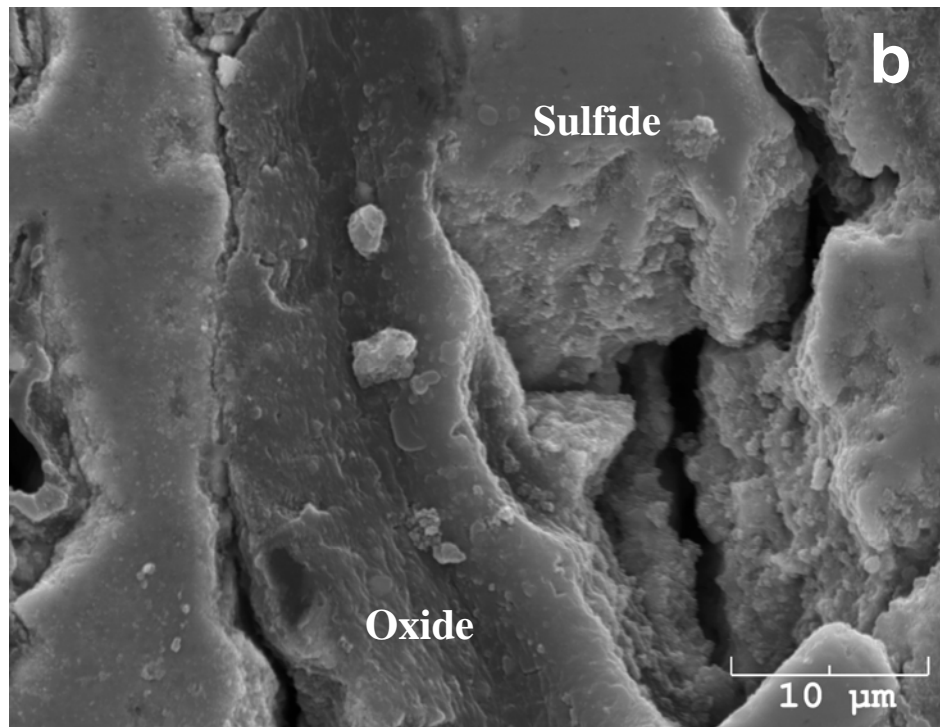
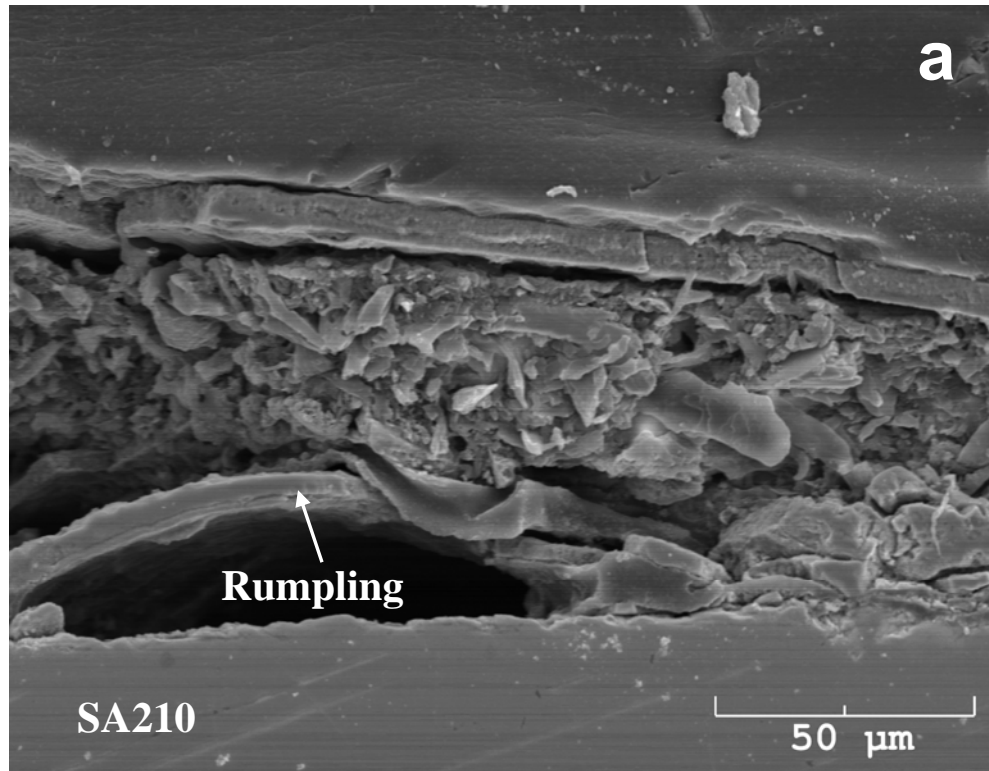


Figure 3.14: (a) rumpling in scale at scale scale/alloy interface due to CTE mismatch of scale and alloy, (b) highly porous sulfide scale and dense oxide microstructure

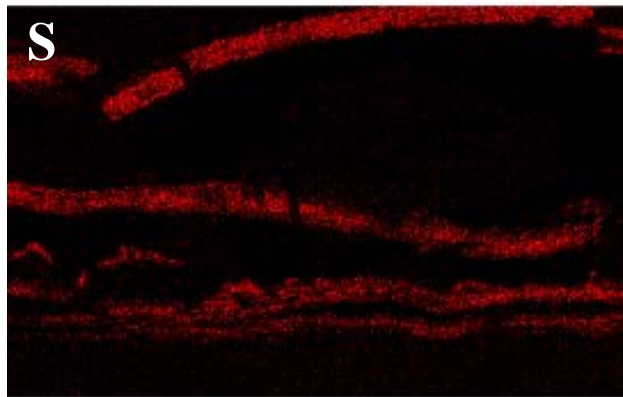
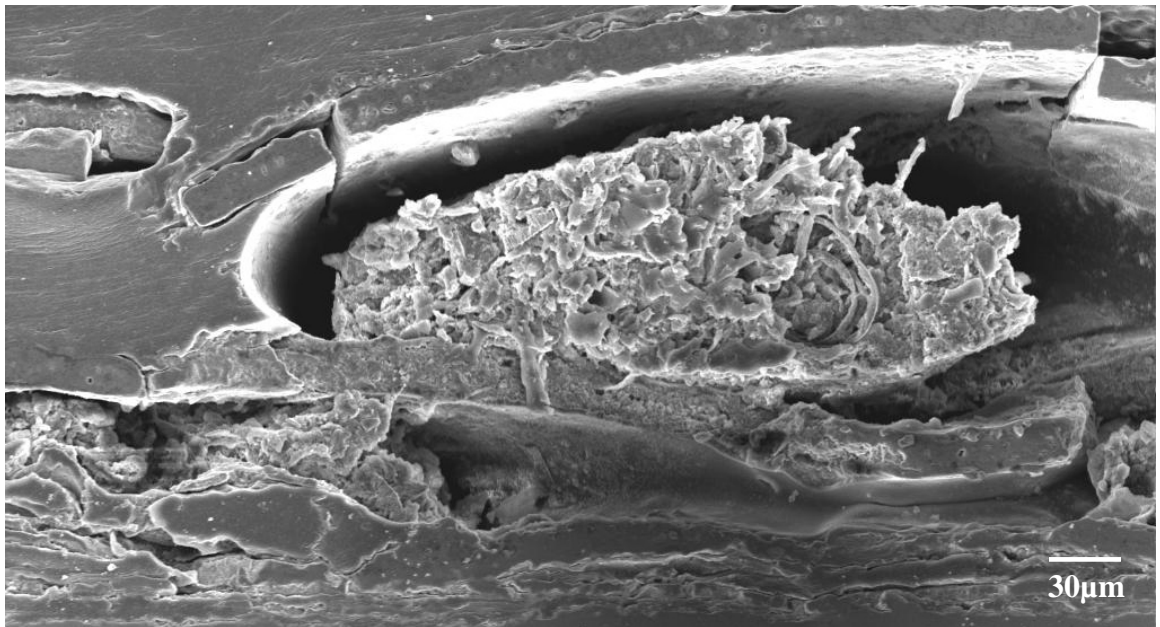


Figure 3.14: (c) Cracking between oxide-sulfide layered scales. EDS maps shows that some cracking was observed in oxide too.

Table 3.1: Corrosion kinetics parameters for different stages in Test-1, where S indicates $pS_2 = 10^{-14}$ atm and O indicates $pO_2 = 10^{-2}$ atm.

Stage	Environment	Rate law to describe the kinetics during this stage	K_p ($mg^2/cm^4.hr$)	K_i ($mg/cm^2.hr$)
1	S	Linear	-	0.21
2	O	Parabolic	0.10	-
3	S	Linear	-	0.09
4	O	Parabolic	0.23	-
5	S	Parabolic	0.94	-
6	O	Parabolic	0.38	-
7	S	Parabolic	1.86	-

3.3.2 Cycling between $pS_2=10^{-14}$ atm and ($pSO_2=10^{-1}$ atm) at 300 °C

As discussed in chapter 1, situations between extreme sulfidizing-oxidizing cycling, can exist when environment is sulfidizing and changes in air feed intermittently introduces oxygen in the vicinity of waterwall tubes causing formation of mixed sulfidizing/oxidizing environment. Further tests were carried out in different cyclic environments representing the situation where sulfur-bearing gases are always present but the conditions vary from reducing to oxidizing. Figure 3.15 shows the mass change of SA210 carbon steel sample under gas cycling between sulfidizing ($pS_2=10^{-14}$ atm) and mixed sulfidizing-oxidizing ($pSO_2=10^{-1}$ atm) environments at 300°C.

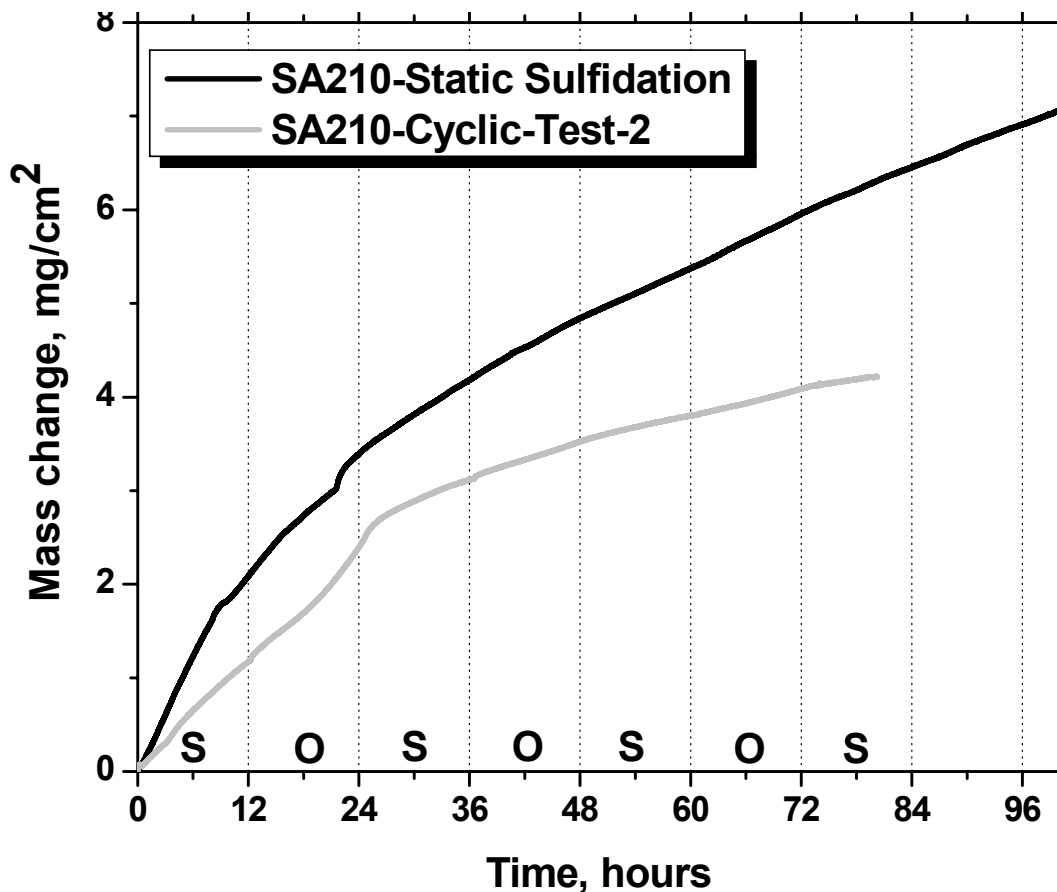


Figure 3.15: Corrosion kinetics of SA210 in test-2 conditions as compared to exposure to static sulfidizing environment

Unlike Test-1, in Test-2 the sulfide scales on the carbon steel, SA210, did not show any significant spallation (i.e. absence of any sharp mass loss), as is evident from the data shown in Figure 3.16. There were no signs of scale spalling or cracking after the sample was removed from the TGA apparatus.

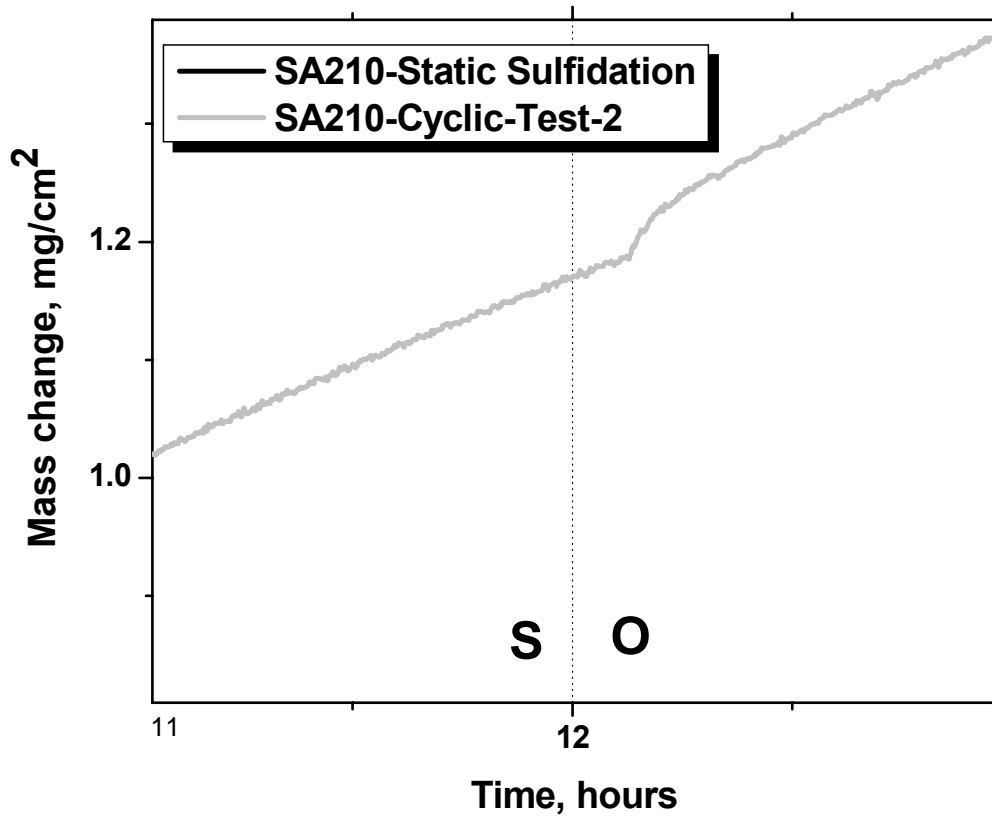


Figure 3.16: Change in corrosion kinetics of SA210 on environmental cycling in test-2 conditions.

Scanning electron micrograph in Figures 3.17-3.19 shows the cross-section of scale after 100 hours of exposure at 300°C in Test-2 at three different locations. Morphology of this scale suggests the formation of layered structure with oxide-sulfide layers. Although the scale looks continuous through thickness, but some cracking was observed at the scale/alloy interface at some spots due to a large CTE mismatch between the scale and the steel as shown in Figure 3.17. Scale thickness was roughly 60-80µm with an outer dense layer-1 of ~50-60µm thick, which consists primarily of sulfides/sulfates as evident from EDS maps in Figure 3.18, and a porous layer-2, ~10-20µm thick, which consists primarily of oxide at the scale/alloy interface. Table 3.3 shows the parabolic rate constant calculated from Figure 3.15 for each environmental cycle. Measured rates in Table 3.3 suggest that after first cycle, there was no significant change in kinetics of corrosion irrespective of environment and the process was primarily governed by diffusion. Perhaps the presence of thin oxide layer and its interdiffusion in the sulfide layer provides good adherence to the scale in Test-2 conditions as shown in Figure 3.19. Figure 3.20 shows the physical appearances of sample after Test-1 and 2 respectively. Significant delamination of outside layer is evident for Test-1 conditions and negligible spallation was observed after exposure to Test-2 conditions.

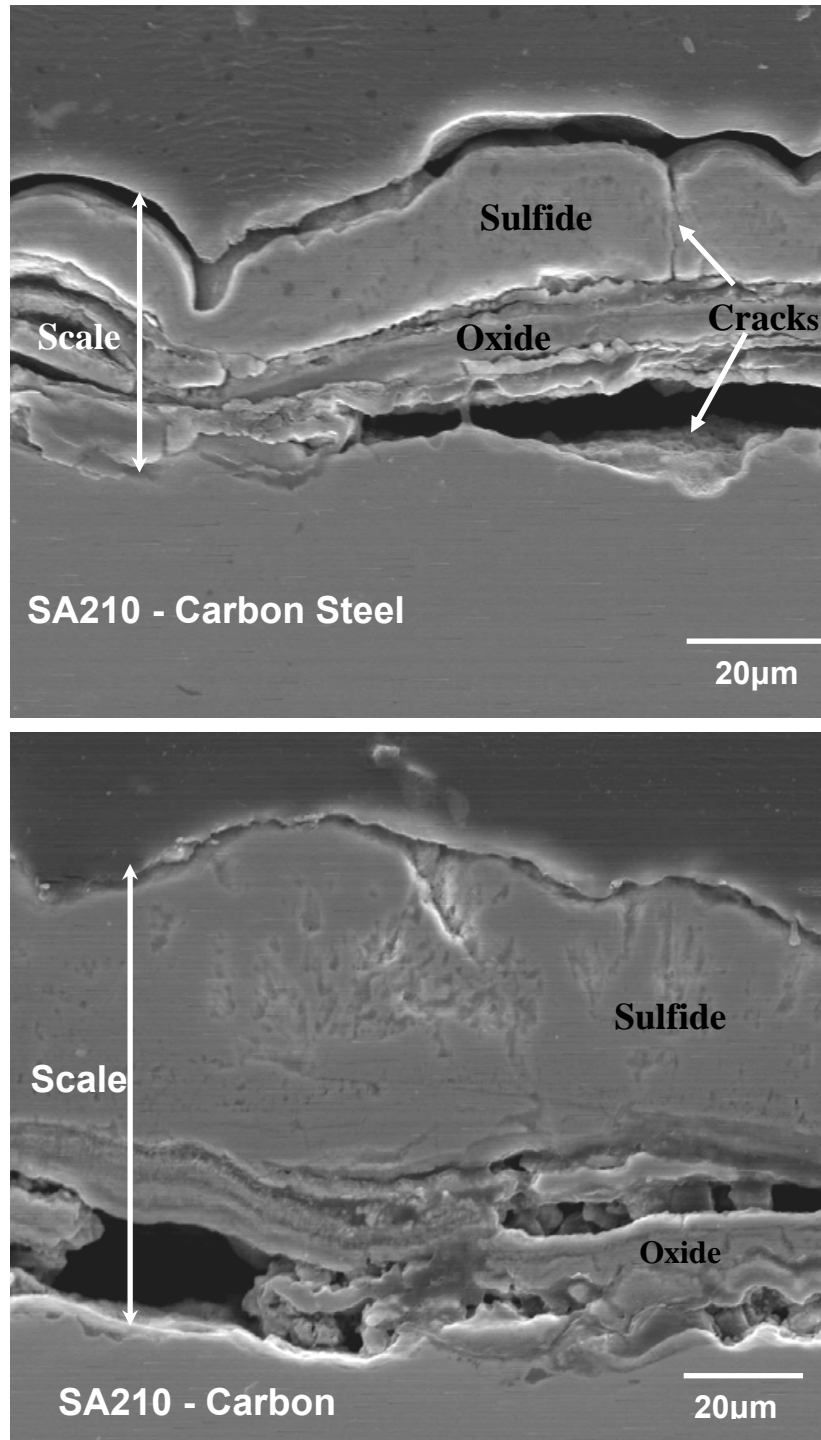


Figure 3.17: Cross-sectional SE micrographs of scale after Test # 2 (cycling between $p\text{SO}_2 = 10^{-1}$ atm and $p\text{S}_2 = 10^{-14}$ atm starting with oxidizing). Laminated structure is evident due to cycling of gaseous atmosphere between oxidizing and sulfidizing

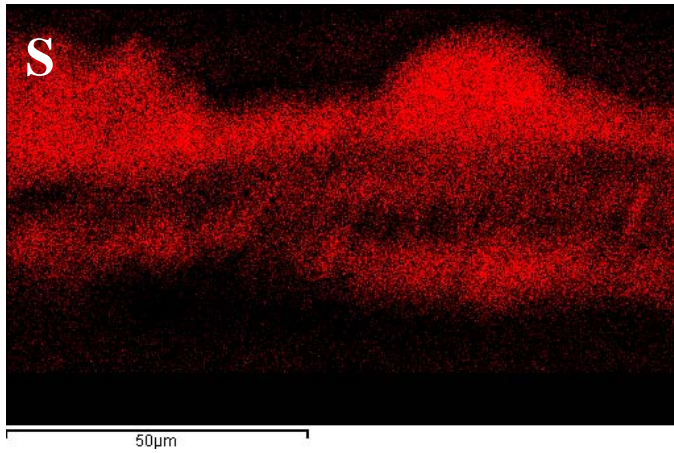
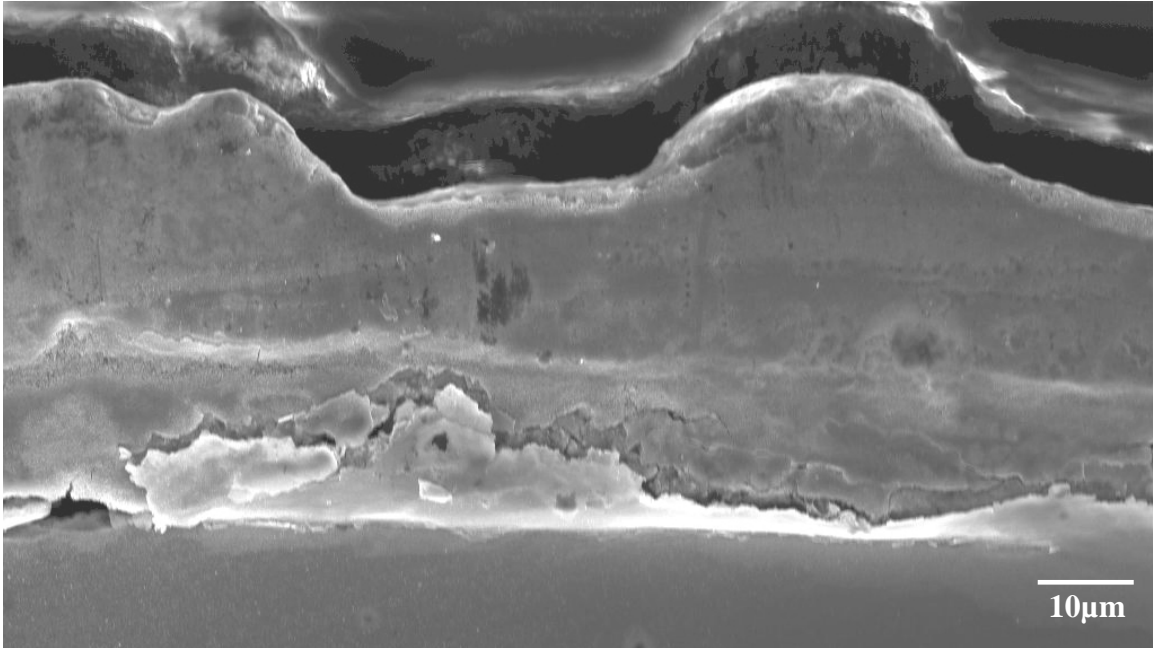


Figure 3.18: Sulfur-X-Ray map of scale after Test-2. Unlike Test-1, oxide was observed at the scale-alloy interface.

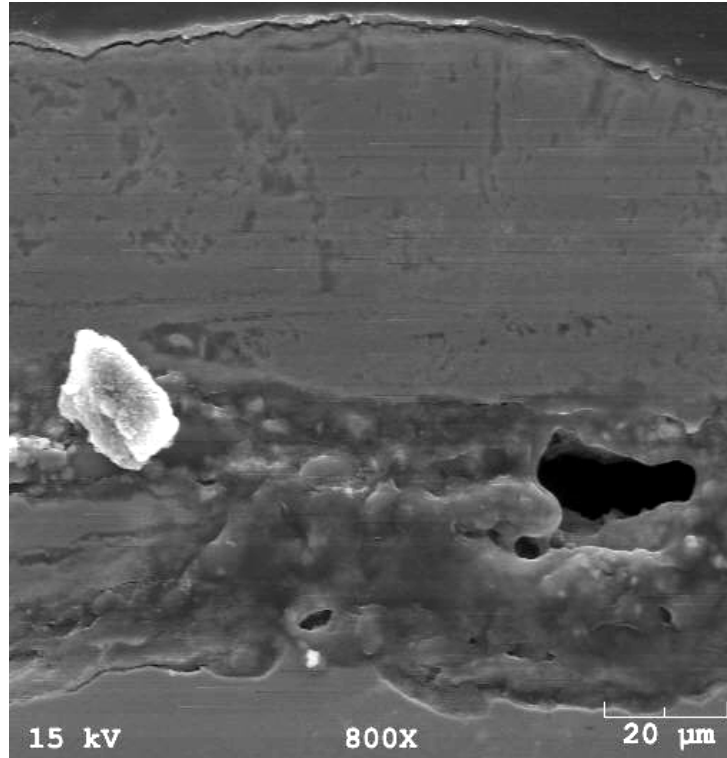


Figure 3.19: Scale/alloy interface showing good adherence of oxide for test-2

Table 3.2: Corrosion kinetics parameters for different stages in Test-2, where S indicates $pS_2 = 10^{-14}$ atm and O indicates $pSO_2 = 10^{-1}$ atm. Note that test started under oxidizing environment.

Stage	Environment	Rate law to describe the kinetics during this stage	K_p ($mg^2/cm^4.hr$)	K_I ($mg/cm^2.hr$)
1	O	Parabolic	-	0.12
2	S	Linear	0.36	-
3	O	Parabolic	0.27	-
4	S	Parabolic	0.21	-
5	O	Parabolic	0.16	-
6	S	Parabolic	0.20	-

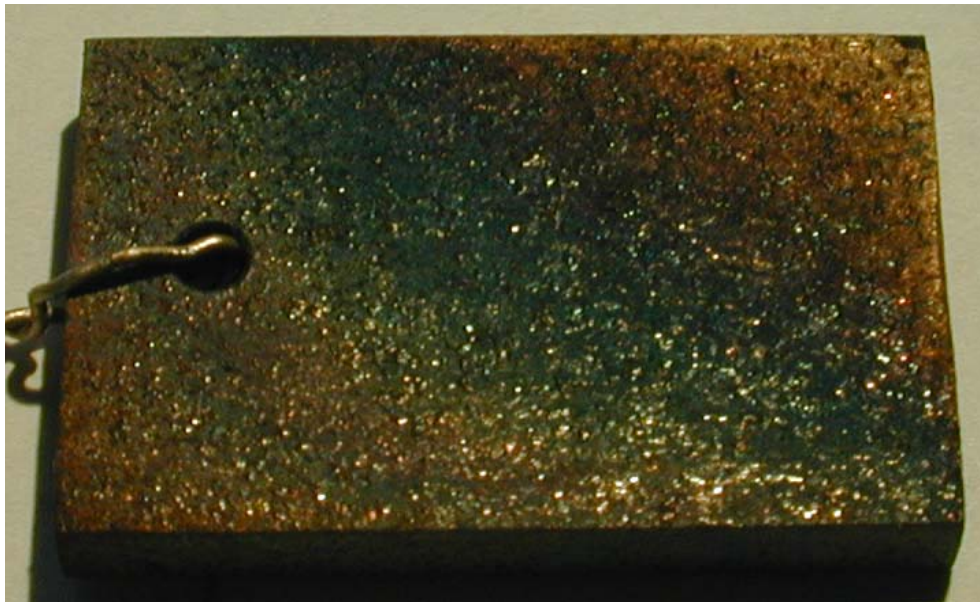


Figure 3.20: Physical appearance of samples after 100 hour exposure at 300°C
(A) Test-1: cycling between $p_{S_2} = 10^{-14}$ atm and $p_{O_2} = 10^{-2}$ atm
(B) Test-2: cycling between $p_{SO_2} = 10^{-1}$ atm and $p_{S_2} = 10^{-14}$ atm

Tests-1 and Test-2 were started in sulfidizing environments. This raised a concern that the onset of corrosion with the formation of sulfide scale on the surface can affect the subsequent corrosion kinetics under cyclic conditions. Test was designed where the carbon steel sample was first exposed to a oxygen containing environment to develop an oxide scale on the surface. Test-3 was started in an oxidizing environment with similar cycling as Test-2. Results for this test are shown in Figure 3.21. The Test-2 was started under a mixed gas, oxidizing environment, whereas Test-3 was started under sulfidizing environment.

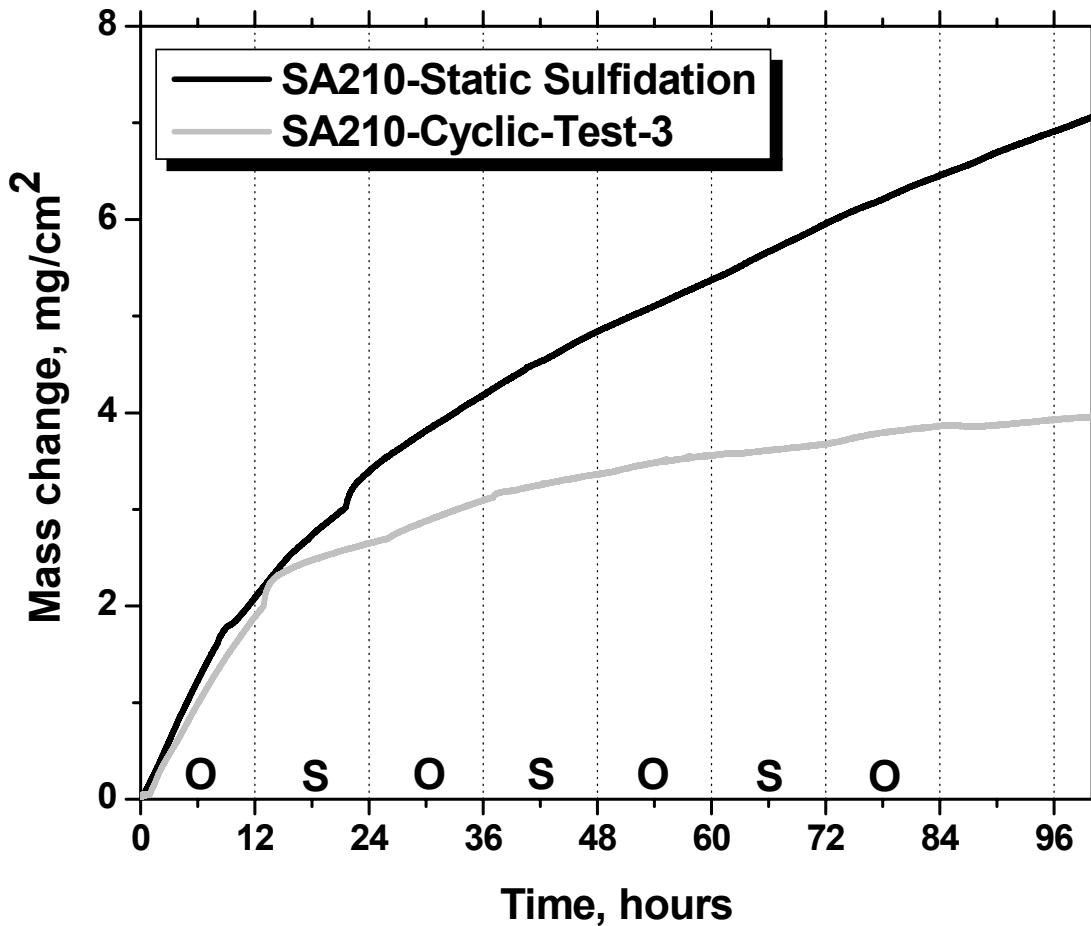


Figure 3.21: Corrosion kinetics of SA210 in Test-3 conditions. Note that the conditions are similar to Test-2 with the first environment being oxidizing

No spallation was observed on environmental cycling as shown in Figure 3.22. Results show that the sample tested in Test-2 and 3 showed lower mass gain than Test-1 as the scale was adherent and the reaction kinetics was primarily governed by the diffusion through the scale with overall parabolic rate constant of $0.25\text{mg}^2/\text{cm}^4\cdot\text{hr}$. Resulting values of parabolic rate constants for different stages of 3 are listed in Tables 3.4. The results from Test-2 and 3 indicate that even small amount of oxygen introduced during atmosphere cycling forms a stable oxide layer on the carbon steel sample to provide protection against further corrosion reaction. No apparent advantage of pre-oxidation was observed in Test-3 as the kinetics observed in every cycle, except for the first cycle, was similar to the one for Test-2. Samples tested in both tests had similar corrosion rates (Table 3.3 and 3.4).



Figure 3.22: Kinetic change of environmental cycling in Test-3 conditions.

Table 3.3: Corrosion kinetics parameters for different stages in Test-3, where S indicate $pS_2 = 10^{-14}$ atm and O indicates $pSO_2 = 10^{-1}$ atm. Note that test started under sulfidizing environment.

Stage	Environment	Rate law to describe the kinetics during this stage	K_p ($mg^2/cm^4.hr$)	K_i ($mg/cm^2.hr$)
1	S	Linear	-	0.16
2	O	Parabolic	0.18	-
3	S	Parabolic	0.22	-
4	O	Parabolic	0.12	-
5	S	Parabolic	0.11	-
6	O	Parabolic	0.08	-
7	S	Parabolic	0.11	-

Scale microstructure for the carbon steel sample from Test-3 is shown in Figure 3.23. Scale morphology suggests that the first exposure to an oxidizing environment had no apparent effect on the subsequent corrosion kinetics or mechanism. Presence of an oxide layer at the alloy/scale interface and the sulfide layer at the oxide/gas interface also suggests that the kinetics of sulfidation is primarily governed by an outward diffusion of metal ions and the oxidation-sulfidation is governed by the inward gaseous diffusion unlike Test-1. Results from Tests-1, 2 and 3 shows that the local corrosion behavior in the mid-furnace areas of recovery boilers depends on the stability of scale formation on carbon steel tubes. Extreme changes in the local environment can lead to a non-protective scale on the tube surface, like in Test-1, whereas in case where the oxygen is available intermittently in sulfidizing areas, the scale may be more protective compared to the static sulfidizing environment alone as in test-2 and 3.

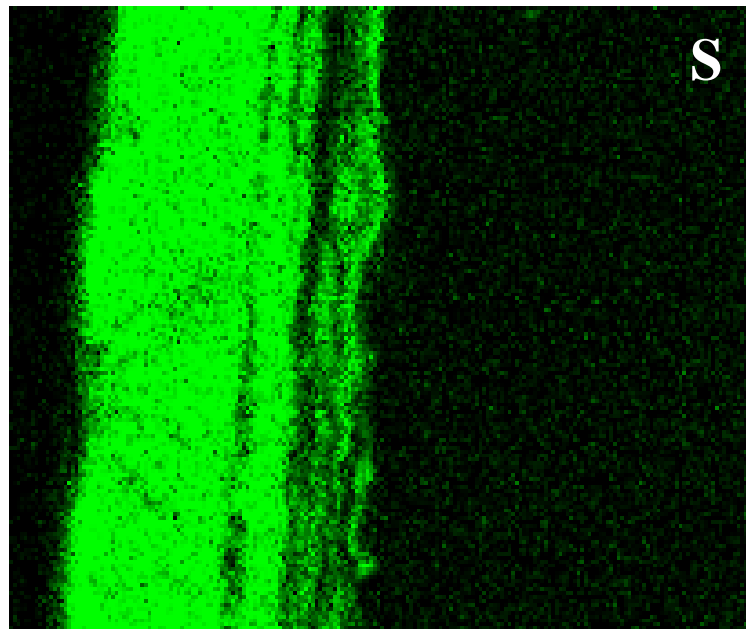
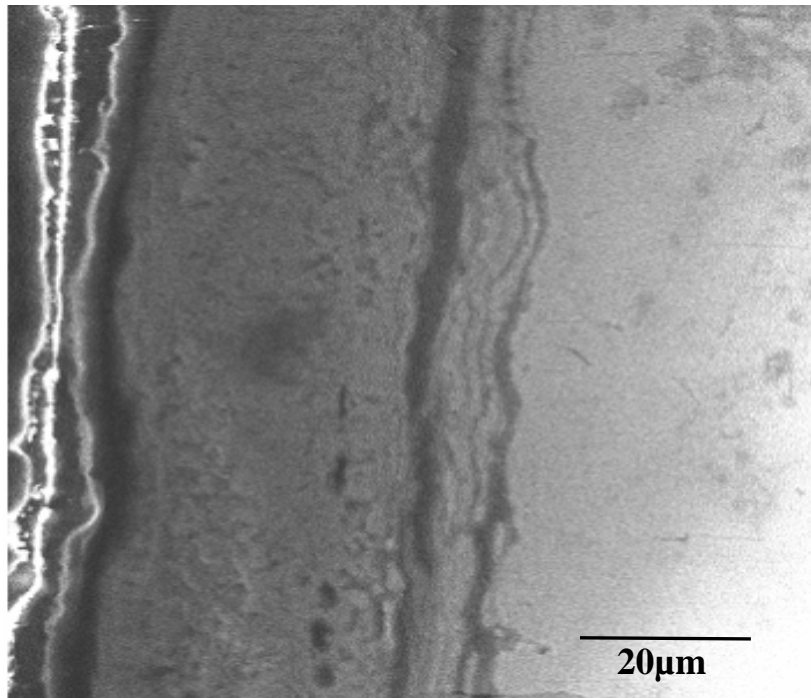


Figure 3.23: Cross-sectional SE micrographs of scale after Test – 3 with sulfur x-ray map. (cycling between $p\text{SO}_2 = 10^{-1}$ atm and $p\text{S}_2 = 10^{-14}$ atm starting with mixed sulfidizing-oxidizing environments).

SUMMARY

Characterization of gaseous environments in the mid-furnace areas of a boiler have shown that gas compositions are not stable and may fluctuate frequently between oxidizing to reducing and sulfidizing, especially in areas with high corrosion rates of carbon steel tubes. Local instability of gas-flow and presence of reducing and sulfidizing gases may cause an accelerated corrosion of carbon steel tubes in these environments.

Results from laboratory simulation tests have shown that the fluctuating sulfidizing/oxidizing atmosphere in the mid furnace leads to an unstable layered sulfide/oxide scale formation at the surface. This may result into scale cracking and spallation, and accelerated corrosion rate for carbon steel tubes at 300°C. However, Intermittent introduction of oxygen in sulfidizing environments resulted in adherent and protective scale with significant improvement in corrosion behavior.

CHAPTER IV

CHROMIZED AND ALUMINIDE DIFFUSION COATINGS

INTRODUCTION

Diffusion coatings are gaining revived interest due to a need for high temperature resistant materials and coatings for the new and existing power generation technologies based on high sulfur containing fuels. Pyrolysis of high sulfur fuels may create a reducing environment containing H_2S , which may accelerate the degradation and failure of commonly used carbon steels and other alloys^[113]. This necessitates the development of high temperature sulfidation/oxidation resistant alloys and coatings. Diffusion coatings can provide substantial high temperature oxidation-sulfidation resistance, without compromising the mechanical properties of the base iron based alloys, through formation of a continuous and stable Cr_2O_3/Al_2O_3 scale that can act as a protective barrier between the corrosive environment and the base material. Coating composition and thickness from pack cementation varies depending on substrate microstructure, deposition temperature, time and pack composition. The work presented in this chapter investigates the synthesis of chromized and aluminized coatings on carbon steel and kinetics of iron aluminide coating growth on SA-210 A1 carbon steel which is a commonly used as the tube material in utility and industrial boilers. Pack process parameters were optimized to get high aluminium activity coating. However, materials were also evaluated for the new gasification technologies for sulfur containing fuels like black liquor gasifiers. Therefore, sulfidation-oxidation behavior of Fe-Al coatings was also studied at gasification temperatures and in high sulfur containing environments under static and cyclic gaseous

environments. Mechanical properties of the coating, interface and the base material were characterized. Main goal of the present work is to evaluate the performance of chromized and aluminized SA210 as candidate materials for the high sulfur containing fuel based power generation equipment.

4.1 CHROMIZED SA210

4.1.1 Microstructure

Chromizing process by pack cementation generally leads to different microstructures depending on the carbon content of steel. Pack cementation was carried out at 800°C to make the carbon steel sample surface rich with Cr. Samples were cleaned and characterized for their microstructure and composition Figure 4.1 shows the XRD pattern for the surface of a chromized SA210 carbon steel sample. Analysis of diffraction peaks indicated that the carbides and nitrides of iron and chromium were formed on the surface during chromizing of SA210. The primary phases in the coatings were identified as $(Cr,Fe)_7C_3$, $(Cr,Fe)_{23}C_6$ and $(Cr,Fe)_2N_{1-x}$. Chromium carbide was formed due to an outward diffusion of carbon and the strong affinity of Cr towards carbon. Whereas, nitrides of chromium form due to the reaction of chromium with N_2 and H_2 which are byproducts of pack activator NH_4Cl decomposition.

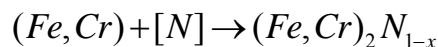
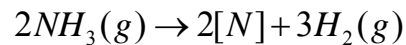


Figure 4.2 shows the surface morphology of Chromized SA210. Granular microstructure is evident from the surface micrograph. Chromized carbon steel samples were sectioned to characterize its thickness and composition through thickness. Samples were examined

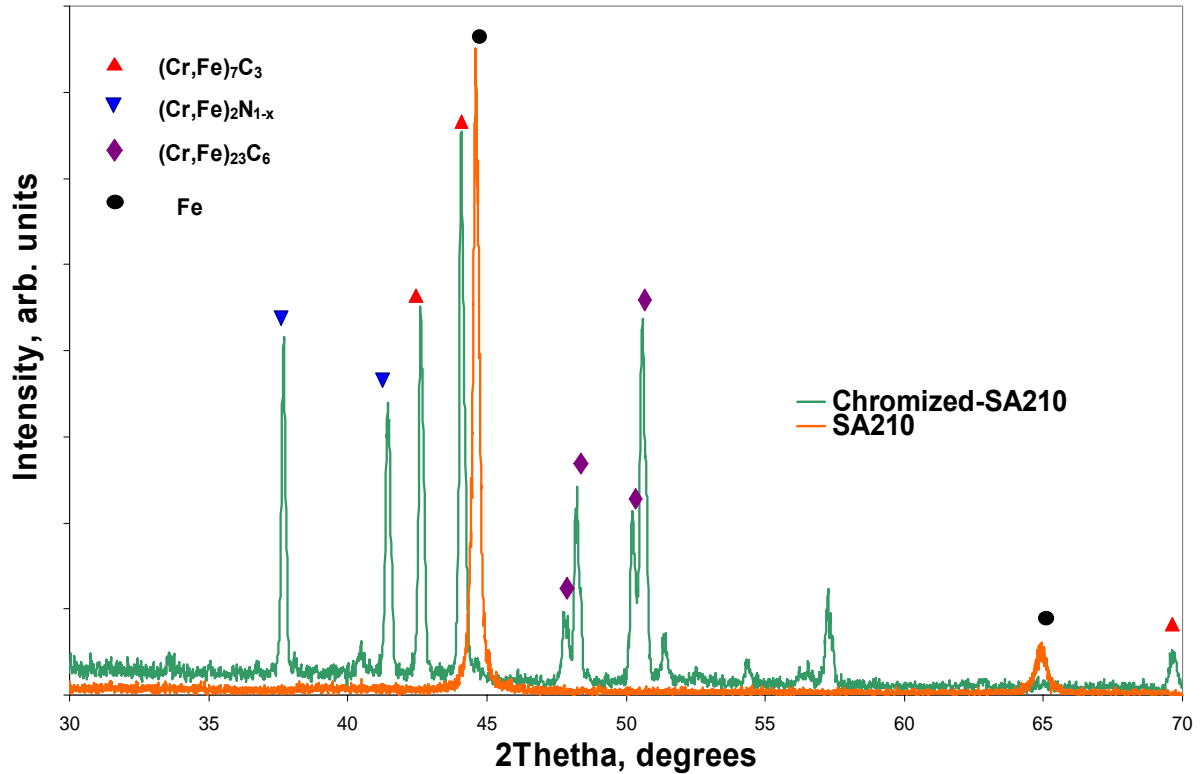


Figure 4.1: XRD pattern of SA210 chromized at 800°C for 6 hrs showing formation of carbides and nitrides

under SEM and the coating composition was determined by EDS. Just below the coating/carbon steel interface, a carbon deficient zone was observed, as is evident from results in Figure 4.3(a). Presence of this layer suggests that the carbon from this region was consumed by carbide reaction with chromium and a chromization induced ferrite layer was formed between the coating and normal substrate. A similar phenomenon of formation of chromized induced ferrite has been reported by Tsai et al [14] in chromizing dual phase Fe-Mn-Al alloy. Figure 4.3(b) shows typical chromium concentration profile for pack chromized SA210 at 800°C for 6 hours which shows 20µm thick chromized layer.

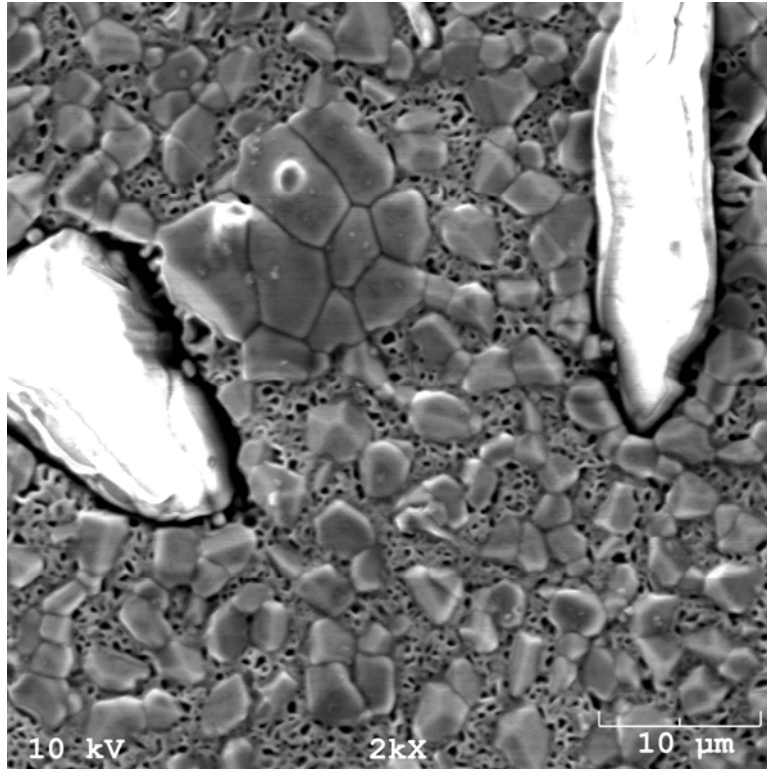


Figure 4.2: Surface microstructure of chromized SA210 at 800°C for 6 hours. Network like granular structure is evident with trapped inert filler particles.

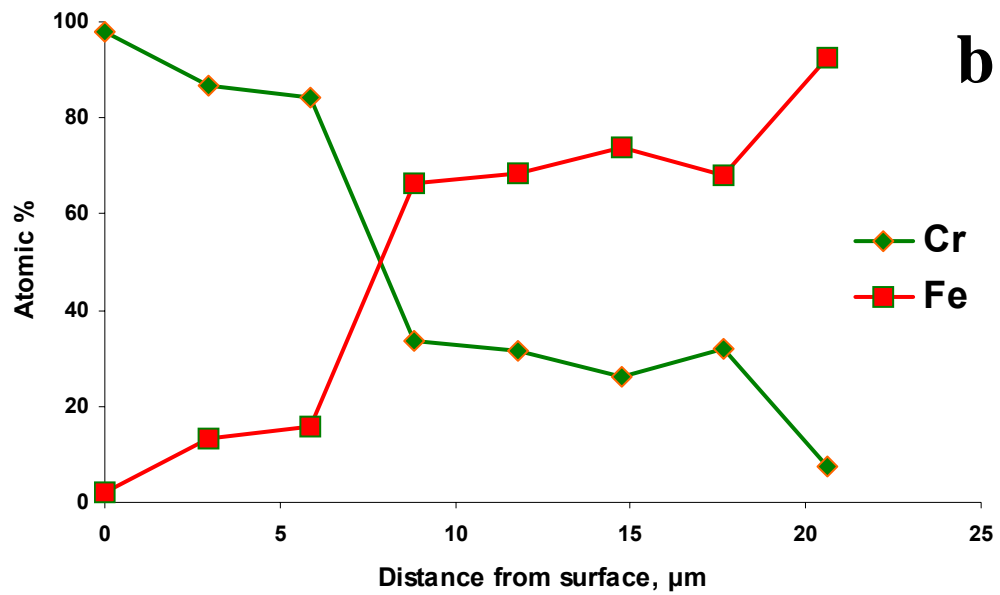
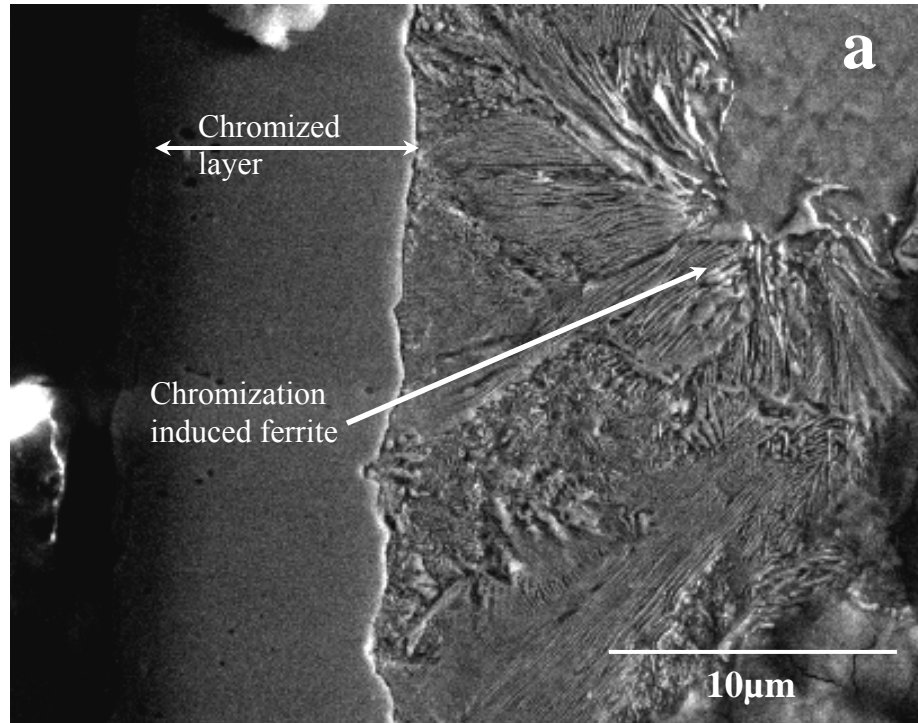


Figure 4.3: (a) Cross-section micrograph of chromized SA210 at 800°C for 6 hours. Chromized induced ferrite is evident in carbon-deficient regions, (b) EDS concentration profile of Cr and Fe

4.1.2 Corrosion behavior

Corrosion behavior of chromized SA210 was studied in simulated environments as discussed in chapter 3. Samples were exposed to the test environment in TGA. Coating performance was tested in static sulfidizing as well as cyclic sulfidizing/oxidizing environments and the results were compared with the equivalent results from the uncoated carbon steel data from chapter 3. Figure 4.4 shows the stability diagram of (Cr,Fe)-O-S system at 300°C with measured and simulated environments. It is clear from these calculated results that the Cr_2O_3 is stable under higher partial pressures of sulfur compared to the iron system. Partial pressures of sulfur and oxygen from the test environments are superposed on the phase stability diagram. Results indicate that chromium oxide was stable even under the sulfidizing gases environments 300°C used in this study. Figure 4.5 shows the similar diagrams at 600 and 800°C.

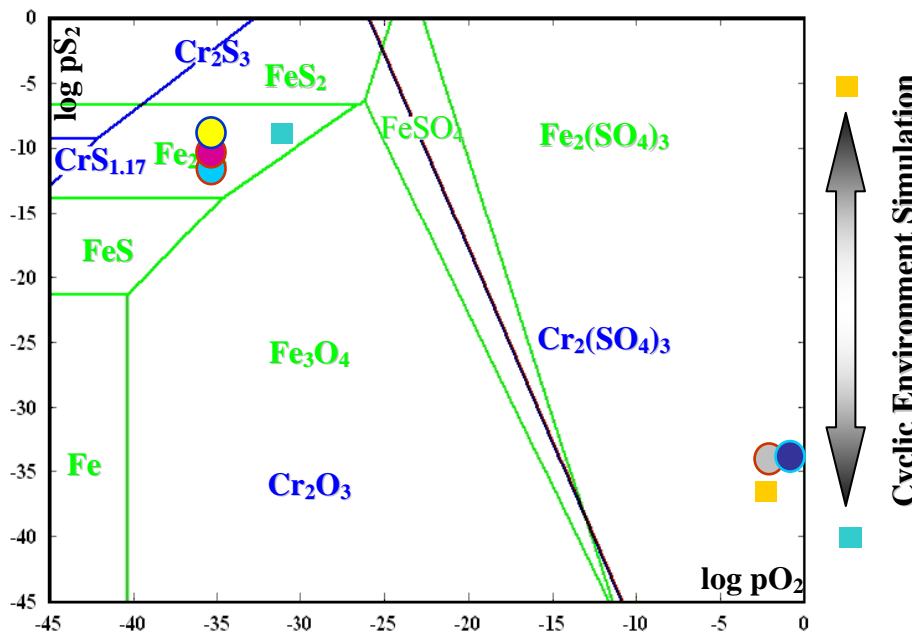


Figure 4.4: (Fe,Cr)-O-S stability diagram at 300°C with points showing measured partial pressures of oxygen and sulphur. Circular dots show measured values and square dots show simulated values

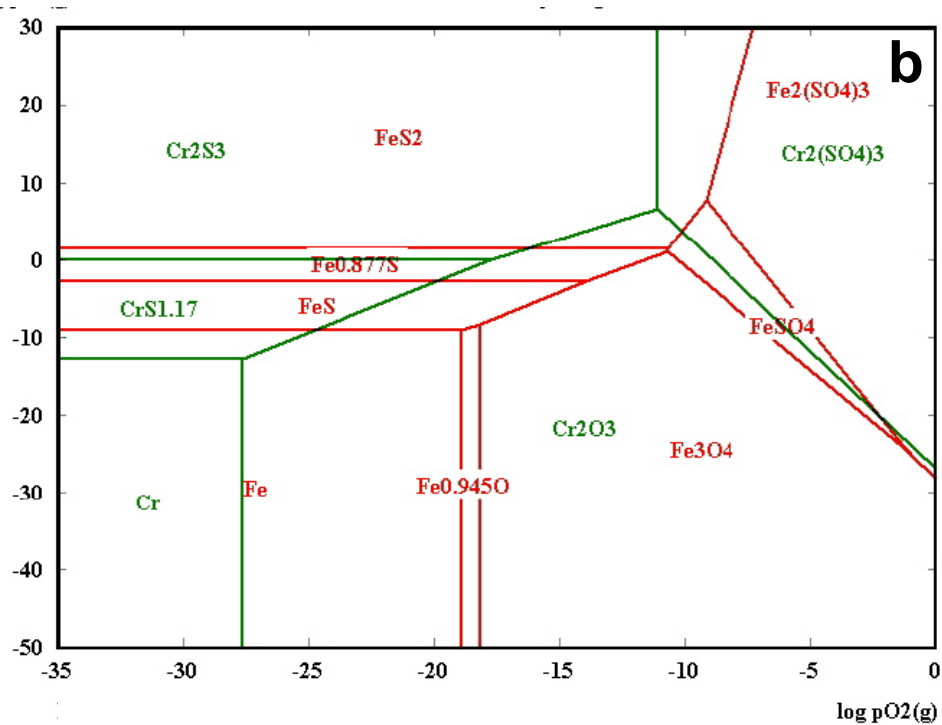
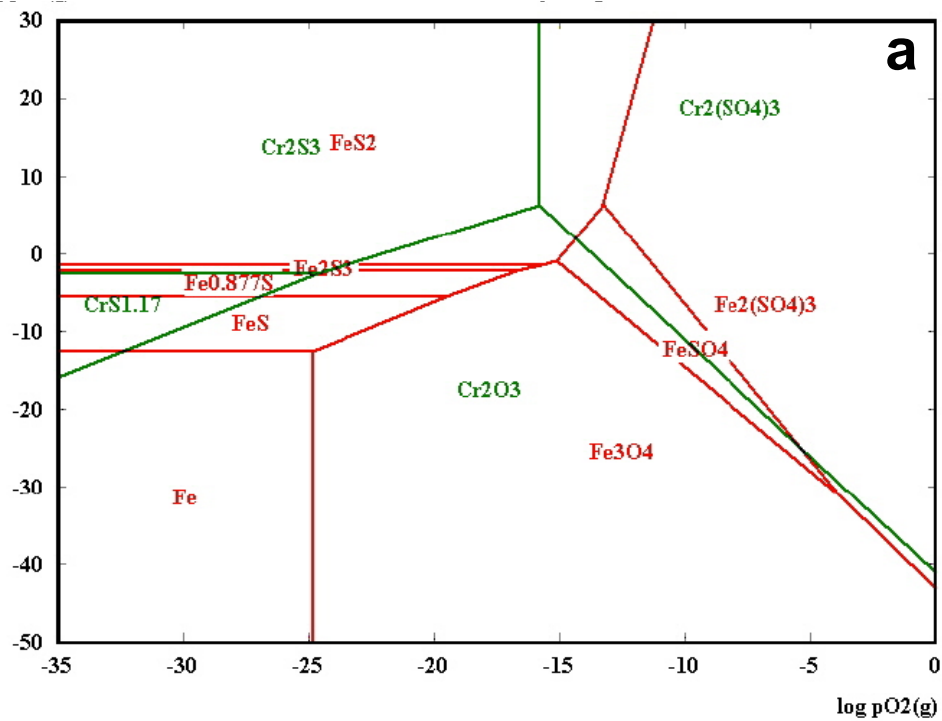


Figure 4.5: (Fe,Cr)-O-S stability diagram at (a) 600°C, (b) 800°C

4.1.2.1 Tests in static sulfidizing environments

Chromized carbon steel samples were evaluated for their corrosion behavior in sulfidizing environments of in boiler and gasifiers using high sulfur fuel. Results were compared with the un-coated carbon steel samples. Figure 4.6 shows the corrosion kinetics of chromized carbon steel as compared to uncoated SA210 in static sulfidizing environment with pS_2 of 10^{-15} atm.

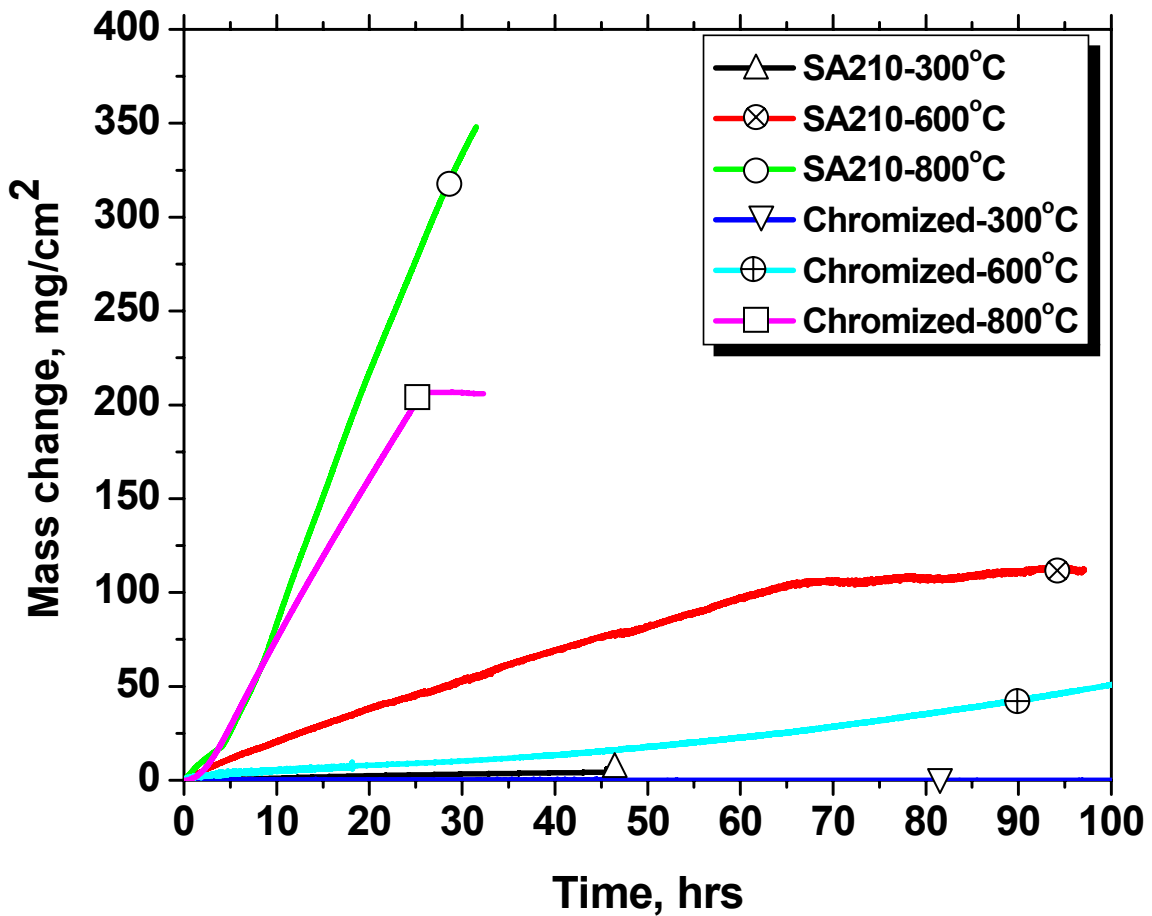


Figure 4.6: Corrosion behavior of chromized SA210 as compared to uncoated SA210 in static sulfidizing environments with $pS_2 = 10^{-15}$ atm .

Results show that under static sulfidizing environment, chromizing can increase sulfidizing resistance of SA210 up to 300°C. At 600°C and 800°C, chromized samples showed no resistance to sulfidation and failed within first 2 hours of test. Chromized steel

showed total mass gain of $\sim 0.5 \text{ mg/cm}^2$ at 300°C with a spallation event on the order of 0.3 mg/cm^2 . Much higher mass gain were observed at 600°C (50 mg/cm^2) and 800°C (200 mg/cm^2). Figure 4.7 shows the magnified view of the first 48 hours of exposure for the chromized and uncoated SA210 carbon steel at different temperatures. Corresponding corrosion rates are listed in Table 1.1.

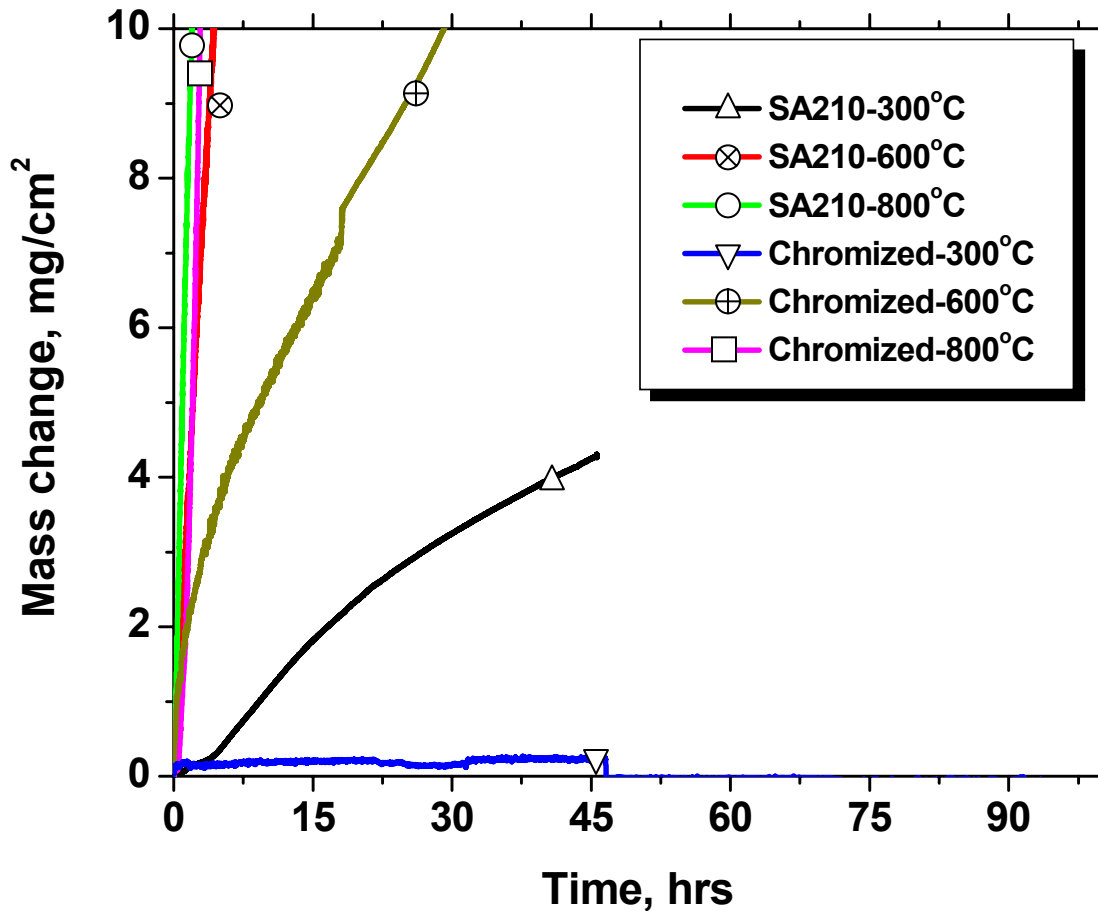


Figure 4.7: Magnified view of sulfidation behavior of chromized SA210 showing excellent behavior at 300°C and catastrophic failure at 600°C and 800°C . Corrosion rates are listed in Table 1.

Table 4.1: Corrosion rates of uncoated as compared to chromized SA210 in the temperature range of 300-800°C

Coating	Temperature (°C)	Rate law to describe kinetics	K _i (mg/cm ² .hr)
Uncoated	300	Linear	0.12
Uncoated	600	Linear	1.12
Uncoated	800	Linear	12.07
Chromized	300	Linear	0.002
Chromized	600	Linear	0.8
Chromized	800	Linear	7.58

At 300°C, SEM/EDS showed formation of a mixed Cr₂O₃/Cr₂S₃ scale with protective nature on chromized sample. However at 600°C, a porous and thick (~60µm) Cr₂S₃ scale was formed on the surface. XRD of the surface scale confirmed the Cr₂S₃ scale formed on the surface as shown in Figure 4.8. SEM micrograph in Figure 4.9 shows porous nature of this sulfide scale at 600°C. Table 1.1 shows that the corrosion rates increase from 0.02 mg/cm².hr to 7.6 mg/cm².hr as the temperature was increased from 300 to 800°C. Nishidat et al^[115] studied the sulfidation of Cr₂₃C₆ in a broad range of pS₂ and reported that at high pS₂, overall sulfidation rate is determined by the cation diffusion in the sulfide scale. This has been confirmed by the marker experiment, where an inert marker dots were deposited at the surface prior to the sulfidation tests, that the scale growth was solely due to outward metal ion diffusion. Chromium sulfides possess a considerable range of non-stoichiometry^[116,117], from CrS_{1.30} to CrS_{1.54}, and the predominant defects are reported to be chromium interstitials. At T>300°C, chromium

sulfides can form kinetically faster than oxides, thus the high diffusion rate of metal ions and high growth rate of sulfide scale was observed along with its non-protective nature. With regard to the use of Cr, although it is able to promote the formation of a stable Cr_2O_3 layer at these temperatures, several sulfides of chromium are also thermodynamically stable and these have significantly higher growth kinetics compared with that of the oxide^[118]. Thus, sulfidation attack is often initiated before a stable oxide can grow and completely cover the surface of the alloy in mixed gas environments.

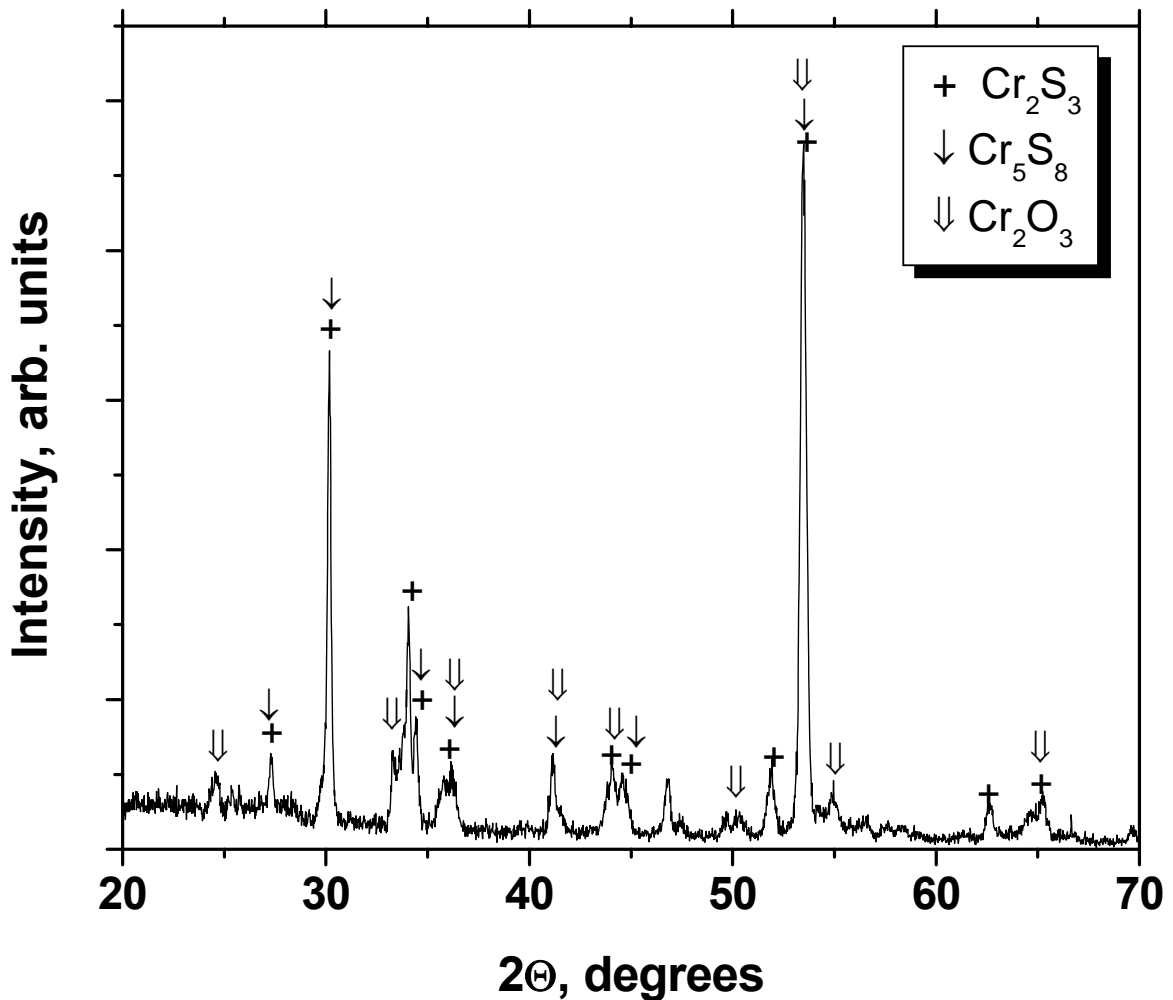


Figure 4.8: XRD pattern of scale on chromized SA210 after exposure to $p\text{S}_2=10^{-15}$ atm for 100 hrs at 600°C showing formation of chromium sulfides.

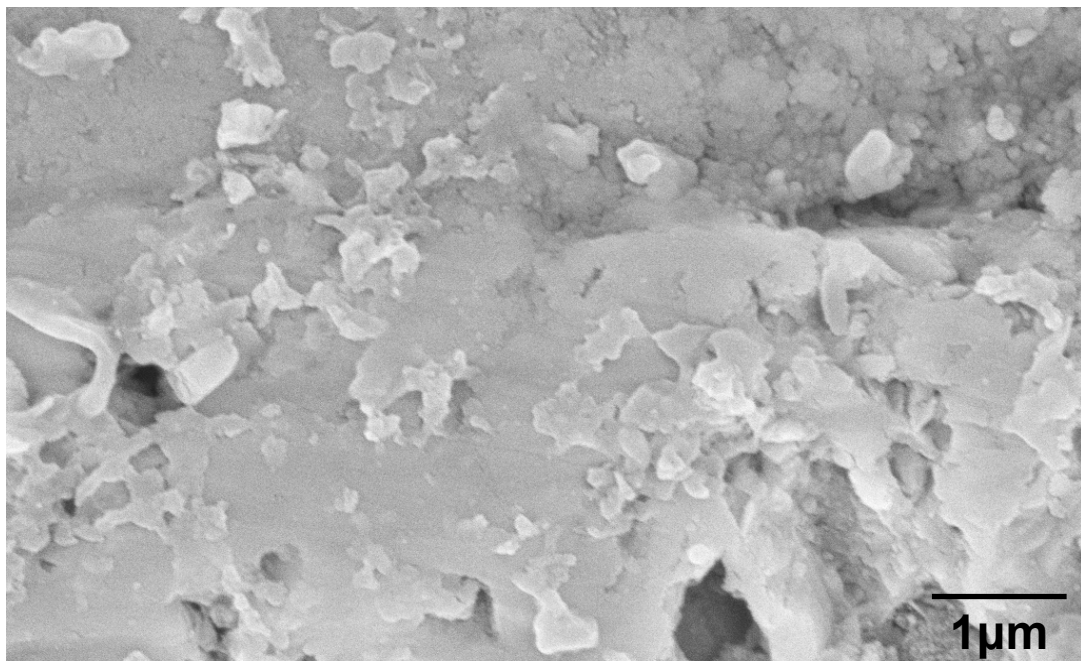
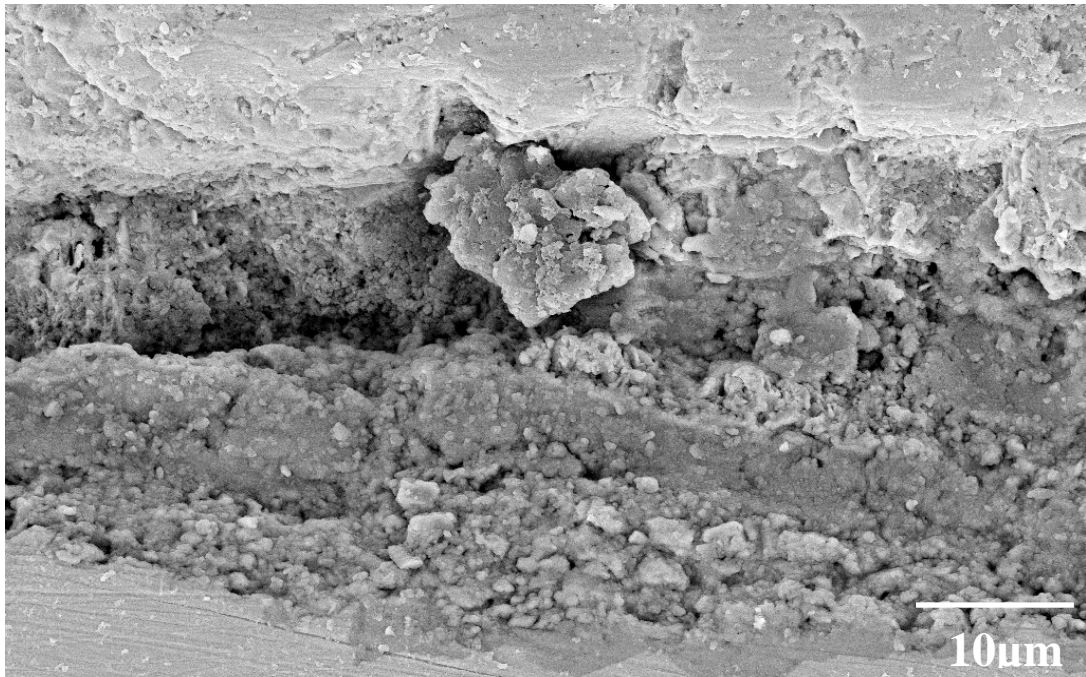


Figure 4.9: (A) Cross-section of chromized SA210 after exposure to sulfidizing environment ($p_{S_2} = 10^{-15}$ atm) at 600°C. Thick and porous chromium sulfide scale was observed with significant spallation on removal from the TGA, (B) porous microstructure of Cr-sulfide scale

Results for this study indicate that the carbon steel could be protected in sulfidizing environments at boiler temperatures, $\sim 300^{\circ}\text{C}$, but for high sulfur fuel gasifiers operating above 600°C , alloys relying or coating on Cr_2O_3 formation will not be suitable.

4.1.2.2 Tests in cyclic Sulfidizing-oxidizing environments

Results from mid-furnace environment characterization (in chapter 2) and laboratory tests (in chapter 3) have indicated that the environment cycling between oxidizing and sulfidizing gases can cause accelerated corrosion rates for carbon steel. Chromized coatings were also tested in cyclic environments at typical boiler temperatures, at 300°C . Results in Figure 4.10(a) show the corrosion behavior of chromized SA210 under cyclic gaseous environments at 300°C , with alternate 12 hr oxidizing and sulfidizing cycles marked as O and S respectively for the cyclic test marked on the figure. It is evident that during every sulfidation cycle, the chromized sample linearly gained weight. As gas composition was changed to an oxidizing mixture, an intermittent mass loss was observed during first part of this cycle followed by mass gain in the later stage as shown in Figure 4.10(b). Unlike sulfidation in the static sulfidizing environment, no apparent spallation was observed in the cyclic tests on chromized samples at 300°C . Scale was also intact after removing the sample from the TGA rig with a total mass gain of $0.3\text{mg}/\text{cm}^2$ after 100 hours of exposure. Data and observations show formation of adherent scale at 300°C .

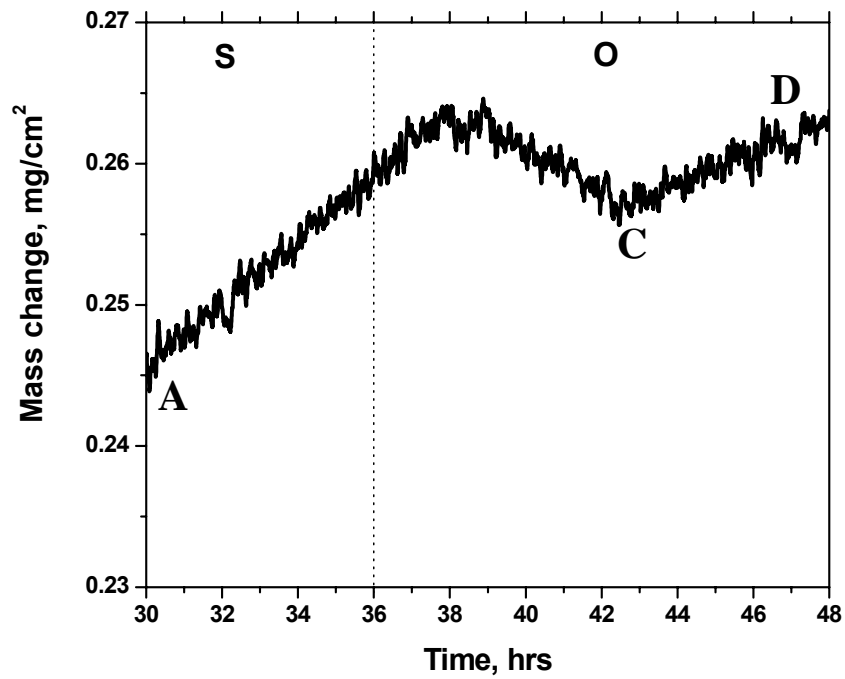
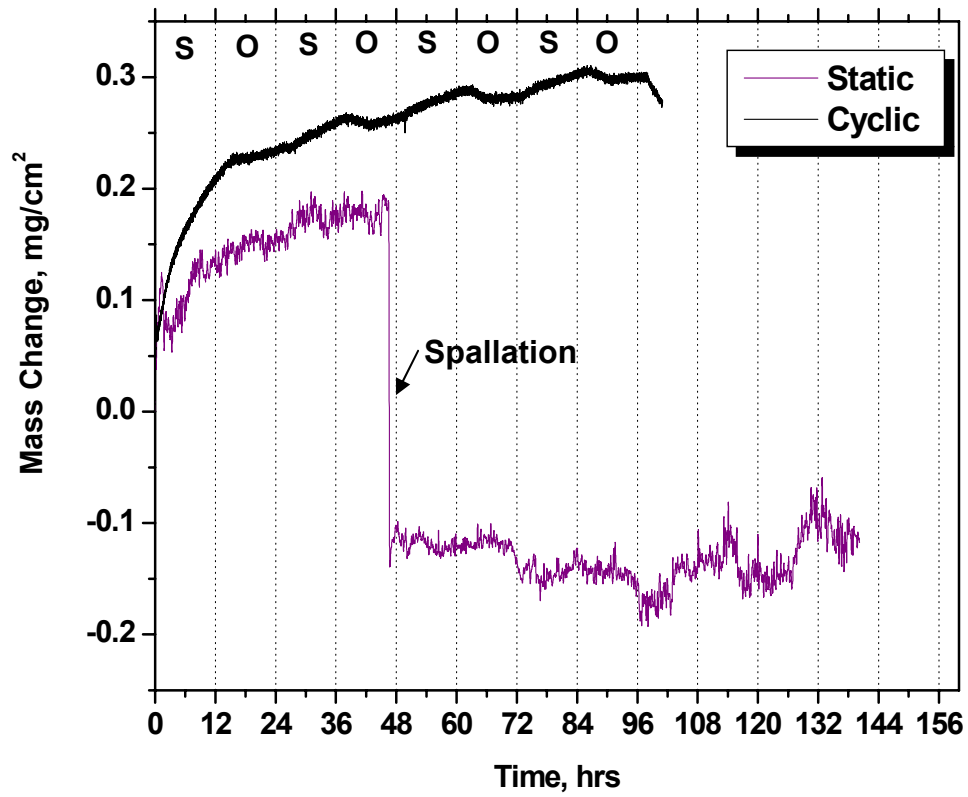
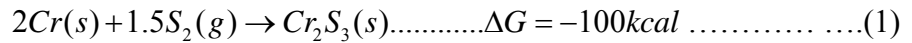


Figure 4.10: (a) Comparison of mass change behavior of chromized SA210 in cyclic and non cyclic environments at 300°C, (b) kinetics at environment change from sulfidizing to oxidizing

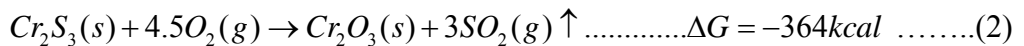
Under cyclic environments at 300°C, the corrosion kinetics can be characterized by two different mechanisms operating, depending upon the reacting gas species as shown in Figure 4.10(b):

1. At high pS₂, sulfidation with formation of Cr₂S₃.



2. As environment changes to higher pO₂,

- Conversion of non-protective Cr₂S₃ to protective- Cr₂O₃



- Formation of Cr₂O₃ as a result of oxygen reaction to Cr from coating



Data in Figure 4.10(b) shows that the reaction kinetics changes after each cycle. From the stage A-B, reaction (1) governs the rate whereas during stage B-C, reaction (2) is the rate determining step with loss of SO₂ causing the loss in mass during initial stages of oxidizing cycle while during stage C-D, mass increases due to oxidation of Cr on the surface to form Cr₂O₃. The step A-C promotes formation of thermodynamically more stable Cr₂O₃ and thus shows excellent resistance to the sulfidation in during subsequent

high pS_2 exposures unlike in the static exposure tests, Figure 9a, which shows spallation in ~ 42 hours. XRD of scale showed a formation of Cr_2O_3 with minor amounts of CrS_x ($x = 1-1.5$) as shown in Figure 4.11. Figure 4.12 shows the surface micrographs of chromized SA210 after exposure to the cyclic test environments for 100 hours. X-ray maps shows the presence of more oxygen (~ 23 wt%) than sulfur (~ 6 wt%) and the cross-sectional micrograph in Figure 4.13 shows the scale thickness to be $\sim 3-4$ μm .

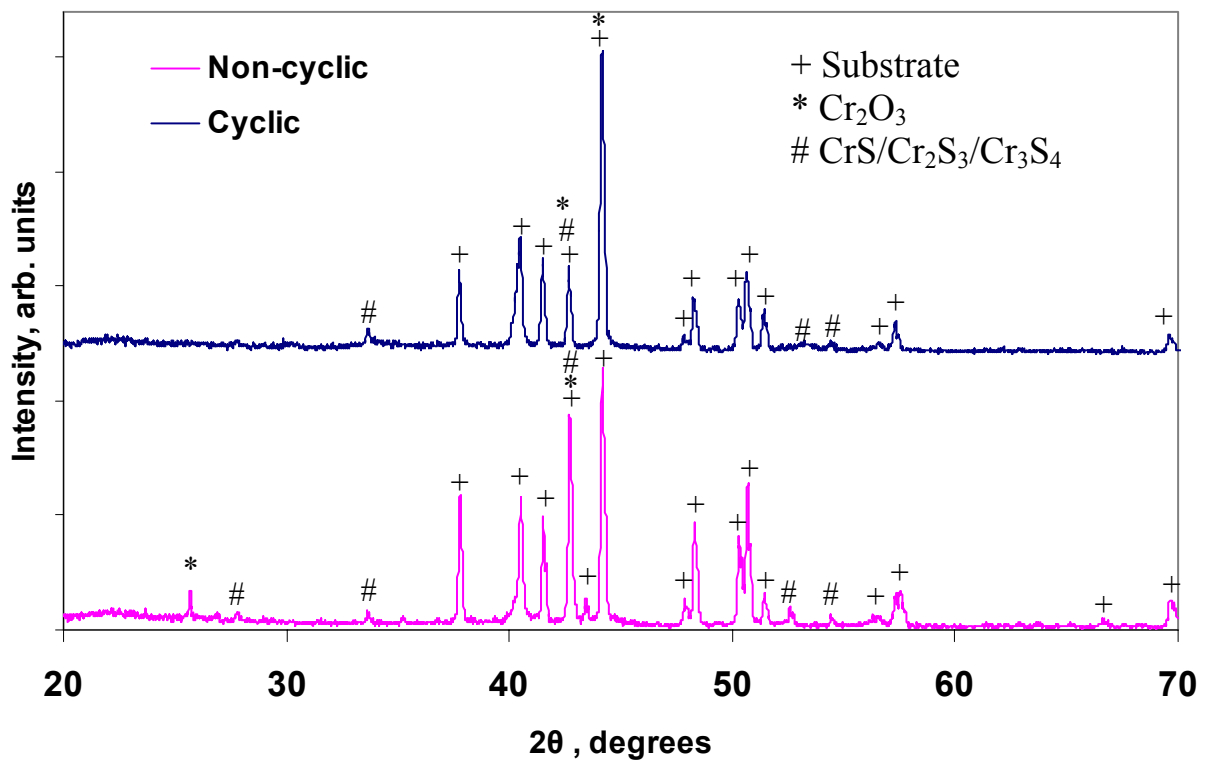


Figure 4.11: XRD patterns of chromized SA210 after 100 hours exposure to cyclic and noncyclic environments at $300^\circ C$

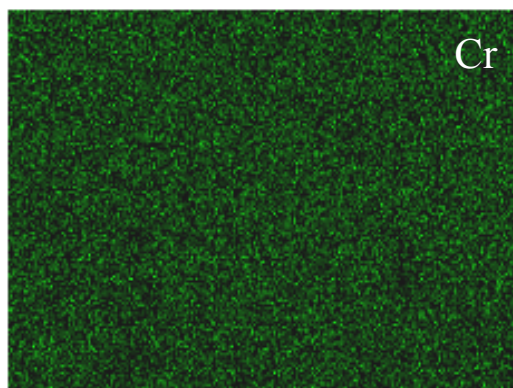
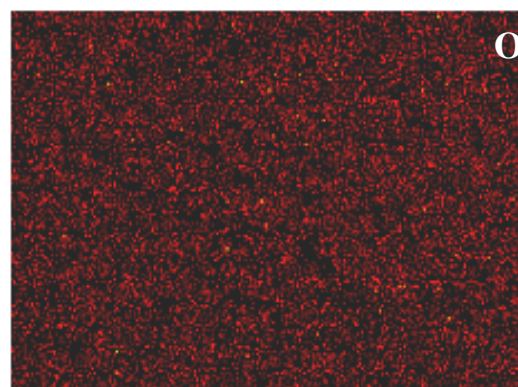
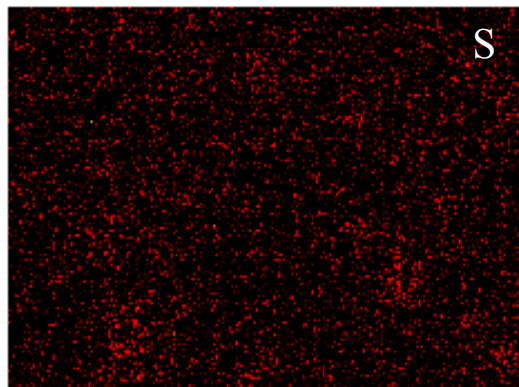
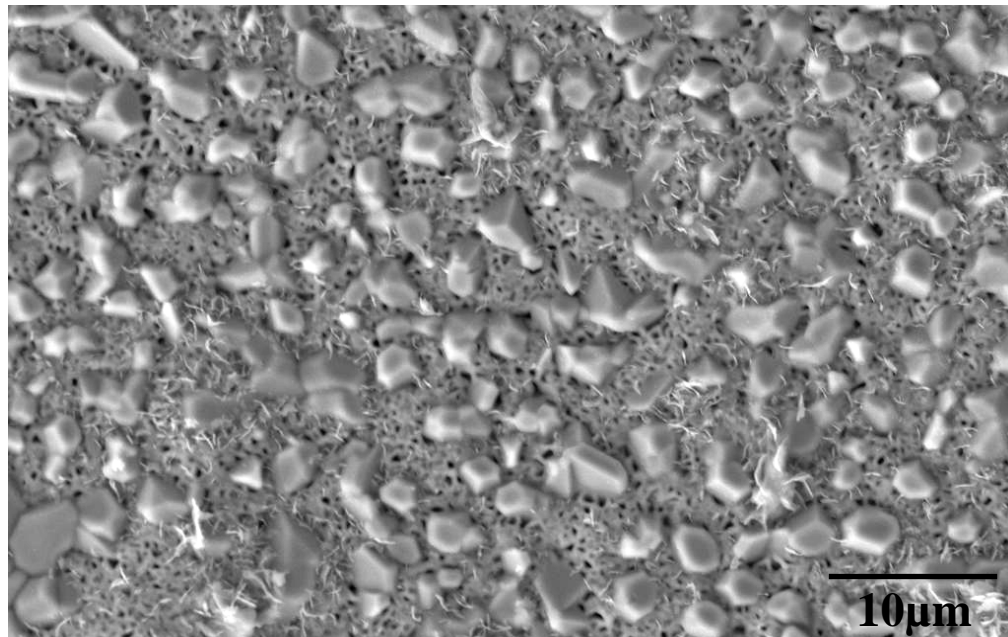


Figure 4.12: Surface microstructure of Cr-diffusion coated SA210 after 100 hours exposure to cyclic sulfidizing-oxidizing environments at 300°C with X-Ray maps of Sulfur, Oxygen and, Chromium. Mass change with time is shown in Figure 4.10.

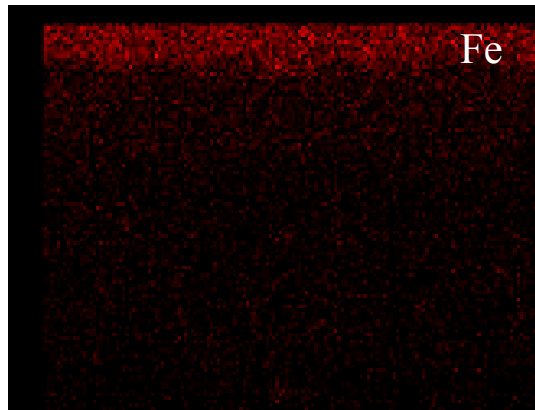
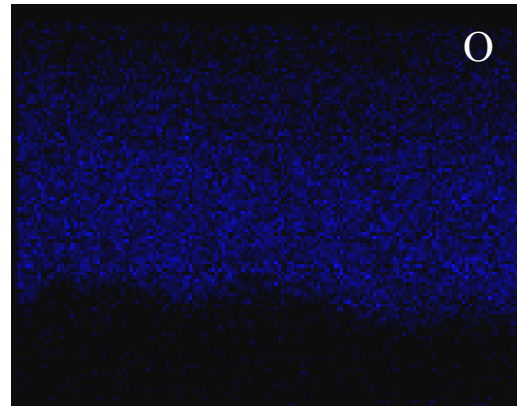
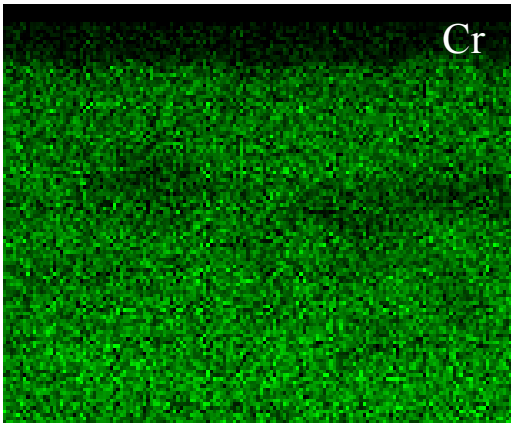
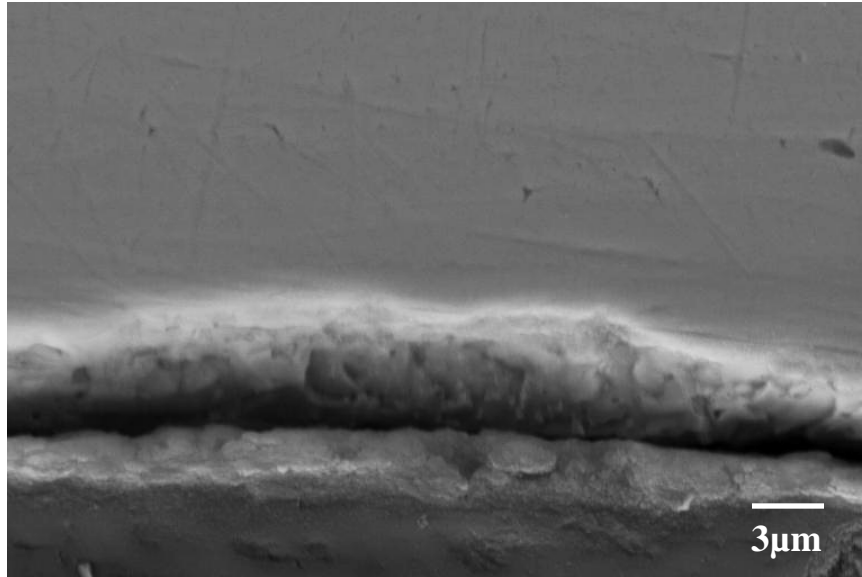


Figure 4.13: Cross-section micrograph of chromized SA210 after 100 hours exposure to cyclic sulfidizing-oxidizing atmosphere at 300°C with X-Ray maps of oxygen, chromium and iron.

Results show that for current boiler operations, chromized carbon steel can serve as a cost effective solution to mitigate corrosion irrespective of cyclic or noncyclic environments, as cyclic environments can be beneficial to form intermediated protective and stable Cr_2O_3 scale unlike uncoated SA210. However, at higher temperatures, chromized coatings may not provide adequate protection to the base metal.

4.2 ALUMINIDE COATINGS ON CARBON STEELS

Results from the previous section shows that an application of chromized coatings is limited to lower temperatures in sulfidizing gaseous environments. Future technologies such as gasification generally operate at much higher temperatures (from 600°C up to 1000°C). This necessitates the coatings to sustain higher temperatures. Aluminum oxide and sulfides are thermodynamically more stable than chromium and iron oxides-sulfides. Thus, this section will discuss the development on aluminide coatings for carbon steel substrate and their corrosion behavior in different gaseous environments at temperatures ranging from 300°C (current boiler operating temperature) to 800°C (black liquor gasification temperature).

4.2.1 Aluminide coating growth kinetics

Pack cementation method, as described in chapter 2, was selected to aluminize surface of carbon steel to make surface rich with aluminium to form Al_2O_3 protective layer. To investigate the diffusion kinetics of coating process, several pack cementation process parameters such as pack composition, deposition time and temperature were used as

listed in Table 4.2. Parameters were selected in order to study the effect of time, temperature and pack composition on coating growth process.

Table 4.2: Pack composition, process parameters and results for pack-aluminizing of SA-210 low carbon steel investigated in this study

Sample	Pack Composition (Wt%)	Temperature (°C)	Time (hrs)	Mass Gain (mg/cm ²)	Thickness (µm)
1	10Al-3NH ₄ Cl-87Al ₂ O ₃	625	8	6.31	41.2
2	10Al-3NH ₄ Cl-87Al ₂ O ₃	750	8	19.58	108
3	10Al-3NH ₄ Cl-87Al ₂ O ₃	800	8	35.00	156.39
4	10Al-3NH ₄ Cl-87Al ₂ O ₃	850	8	48.00	211
5	10Al-3NH ₄ Cl-87Al ₂ O ₃	900	8	71.00	307
6	5Al-3NH ₄ Cl-92Al ₂ O ₃	625	8	2.26	20.36
7	5Al-3NH ₄ Cl-92Al ₂ O ₃	750	8	9.55	60.9
8	5Al-3NH ₄ Cl-92Al ₂ O ₃	800	8	29.45	133.29
9	5Al-3NH ₄ Cl-92Al ₂ O ₃	850	8	45.00	170.27
10	5Al-3NH ₄ Cl-92Al ₂ O ₃	900	8	65.00	300.45
11	10Al-3NH ₄ Cl-87Al ₂ O ₃	800	2	9.50	67.19
12	10Al-3NH ₄ Cl-87Al ₂ O ₃	800	4	14.96	102.56
13	10Al-3NH ₄ Cl-87Al ₂ O ₃	800	6	30.60	131
14	10Al-3NH ₄ Cl-87Al ₂ O ₃	800	8	35.00	156.39
15	10Al-3NH ₄ Cl-87Al ₂ O ₃	800	10	45.00	195.76

Figure 4.14(a) shows a representative micrograph of a coated sample with corresponding x-ray elemental map (Figure 4.14(b)), which indicates that surface was rich in

aluminium. X-ray diffraction of surface of aluminized sample showed the presence of Fe_2Al_5 at the surface. Samples coated above 800°C , showed some entrapped pack particles in the coating, as shown in Figure 4.14(c), which indicates that the coating was formed through outward diffusion of Fe.

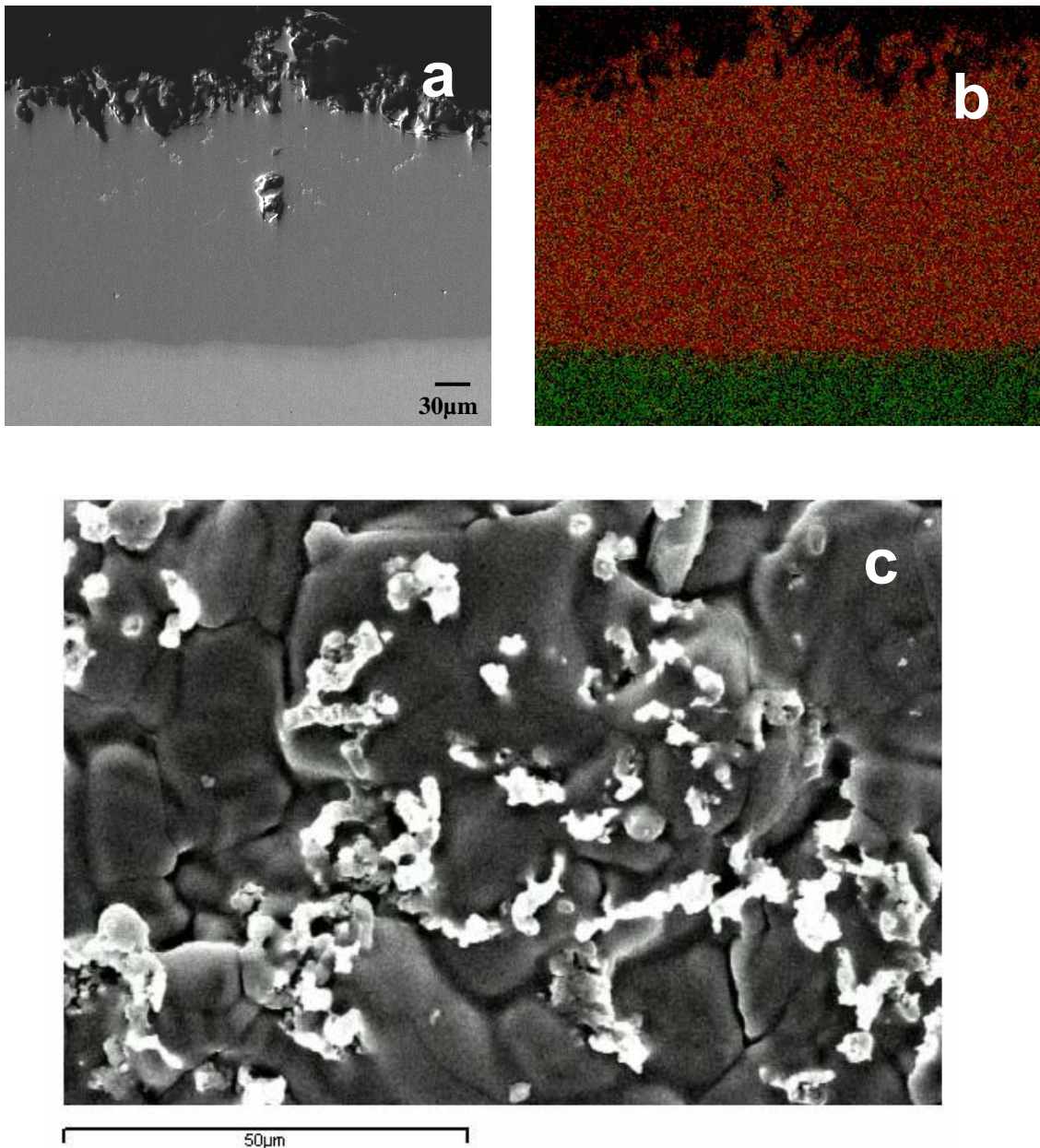


Figure 4.14: (a) Fe_2Al_5 pack cementation coating formed by high activity pack. (b) EDS map shows the Al (red) and Fe (green) elemental profiles, (c) surface microstructure of coating showing entrapped pack particles.

Coated samples were sectioned and polished and observed in SEM to quantify the coating thickness and composition. Coating thickness and the weight gain of carbon steel specimens under different processing conditions are listed in Table 4.2. Composition of sectioned coated samples were characterized by EDS and the line scan results for these samples, coated under different process conditions, are shown in Figures 4.15(a) and (b). EDS line scan results were also used to determine the coating thickness. Coatings under these conditions were found to be a single phased Fe_2Al_5 , where the coating thickness showed a linear relationship with the specimen weight gain regardless of the pack composition, time and temperature of deposition (Figure 4.16). The linear regression gives:

$$x = 4.396m + 11.18 \quad (4)$$

Where the x is the thickness of Fe_2Al_5 coating in microns and m is the mass gain of steel coupons in mg/cm^2 . Slope of the equation (4) can be used to calculate the density of Fe_2Al_5 using equation (5):

$$\rho_{Fe_2Al_5} = \frac{2M_{Fe_2Al_5} m}{M_{Al} x} \quad (5)$$

Despite some scatter, density $\rho_{Fe_2Al_5}$ calculated from the equation 5 was 4.36 gm/cm^3 , which is very close to the theoretical density of Fe_2Al_5 , 4.2 gm/cm^3 [119]. The higher experimental value of density observed in this study can be attributed to the boundary effects. Experimental coupons with edges provide the higher surface area for deposition where the Al intake per unit area at edges can be more than the faces of the sample. The high offset value of 11.18 may also be due to heating/cooling time of coating process, which was not accounted in the deposition times for the data shown in Figure 4.16.

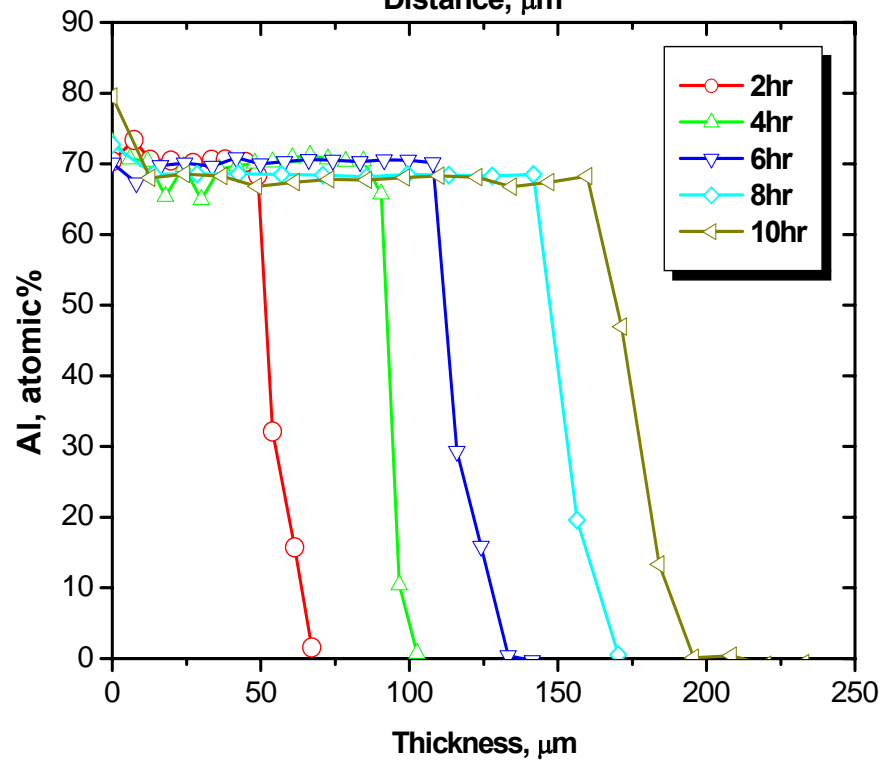
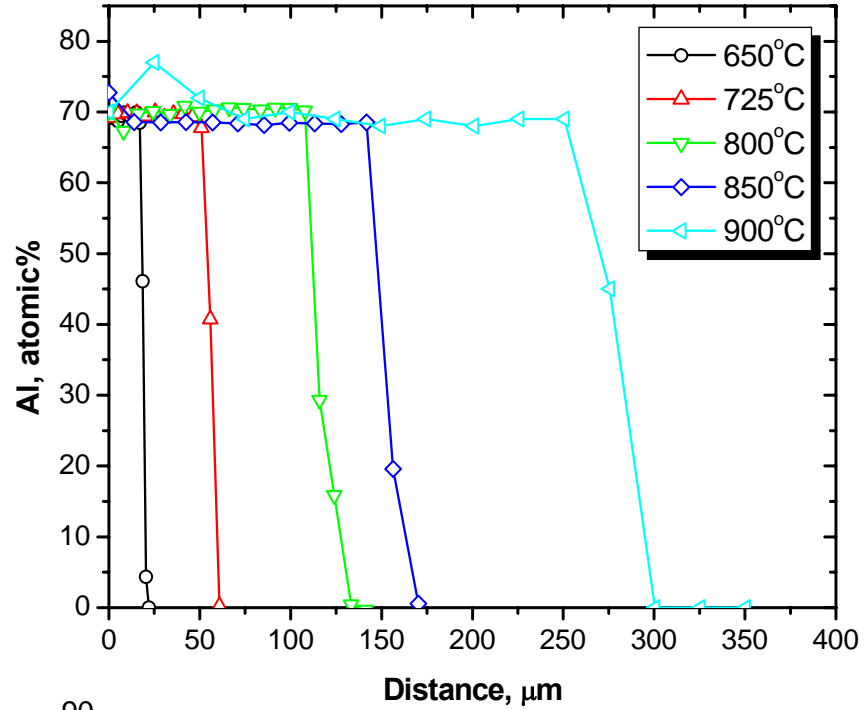


Figure 4.15: EDS line profile for samples coated at
 (a) varying temperatures
 (b) varying deposition time

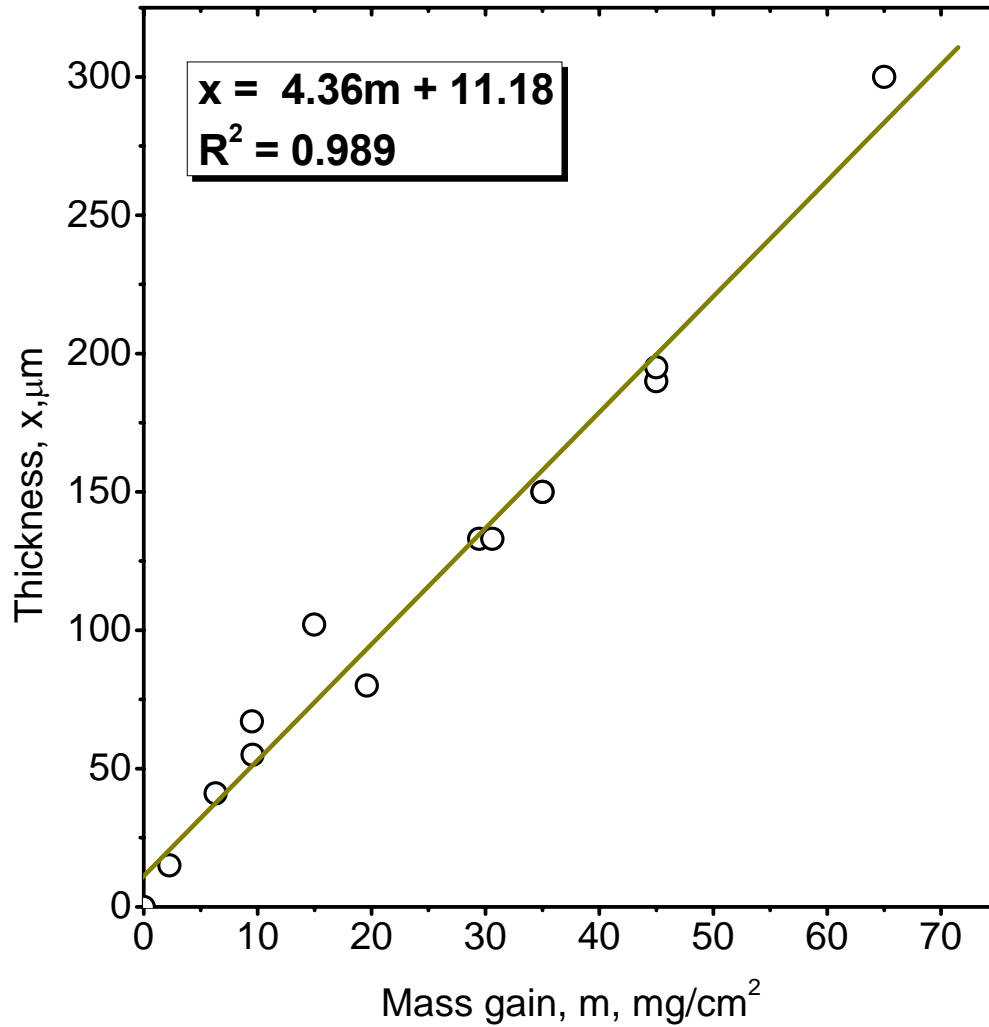


Figure 4.16: Mass gain of coated sample as a function of thickness. Calculated density of Fe_2Al_5 was 4.36 gm/cm^3

4.2.1.1 Effect of Temperature on Aluminizing of Carbon Steel

Pack compositions with $10\text{Al}-3\text{NH}_4\text{Cl}$ and $5\text{Al}-3\text{NH}_4\text{Cl}$ were used to determine the effect of temperature and Al-content in the pack on coating kinetics at temperatures between $650-900^\circ\text{C}$. Figure 14(a) shows the Al concentration profile for samples coated in $10\text{Al}-3\text{NH}_4\text{Cl}$ pack at different temperatures. Aluminizing time was kept constant at 8 hours for these samples. EDS results show that the surface Al concentration was about 71

atomic % regardless of deposition temperature up to 900°C. The coating thickness increased with an increase in temperature. It was confirmed from the XRD results that all coatings were single-phase Fe₂Al₅. Figure 4.17 shows the thickness of coatings obtained for 10Al pack as a function of 1000/T. The linear regression gives:

$$\ln(x) = \frac{-11280.05}{T} + 15.31 \quad (6)$$

The activation energy of aluminizing calculated from the data for 10Al pack was 93.78 kJ mol⁻¹. The results show that the temperature affected the coating growth while the phase composition was unaltered.

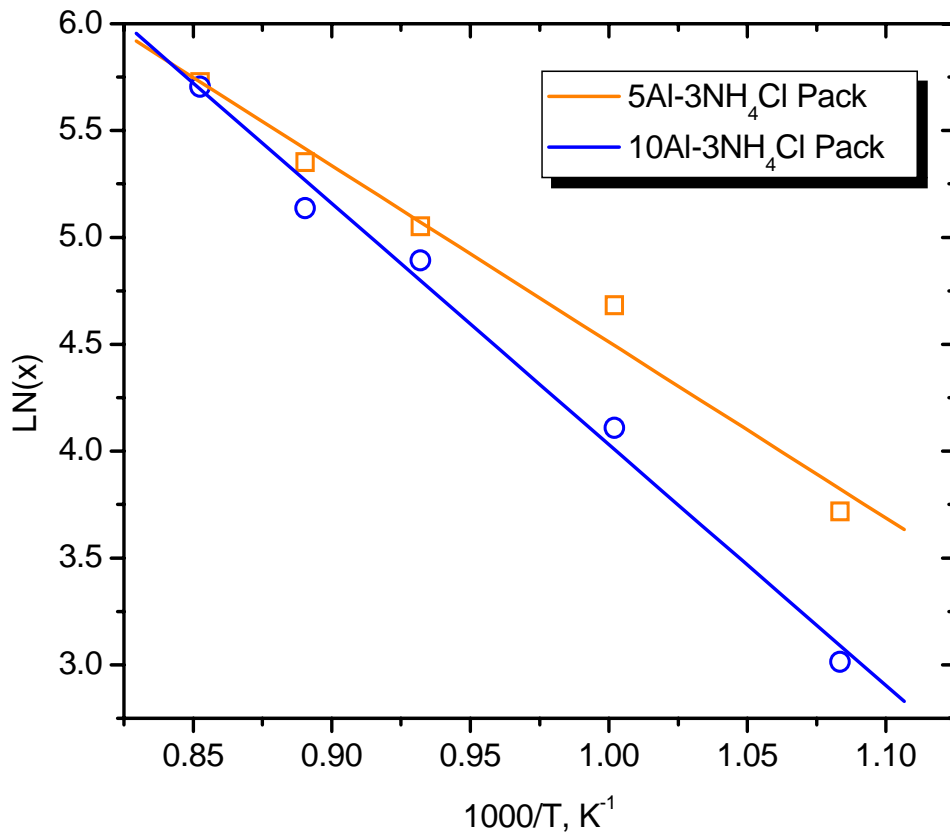


Figure 4.17: Activation energies of coating formation for 5 and 10 wt% Al packs

Similar results were also obtained for 5Al pack as shown in Figure 4.17. The linear regression of data gives:

$$\ln(x) = \frac{-8249.29}{T} + 12.76 \quad (7)$$

Activation energy for 5Al pack was found to be 68.58 kJ mol⁻¹. This shows that value of activation energy (E_a) strongly depends on the Al content of the pack. Caves et al [120] suggested that as the aluminum content of the pack increases, the rate determining step for coating growth shifts from the gas phase diffusion in the pack to a solid state diffusion of aluminum in the coating/substrate. It is evident from this study that as aluminum content of pack increases from 5 wt% to 10 wt%, activation energy of coating growth changes from 68.58 kJ mol⁻¹ to 93.78 kJ mol⁻¹. Vandenbulcke et al [121] studied relative effects of gaseous diffusion and solid state diffusion in formation of aluminide coatings by theoretical models and experimental observations. The reported for packs with varying Al activities, the mechanism of coating growth changes depending on the activity of aluminium in pack. This suggests that the controlling step for the coating growth for 5 wt% Al pack is gas phase diffusion of Al-chloride species to substrate surface, whereas that for 10 wt% Al pack is solid state diffusion of aluminium in steel to form coating phases. This can be due to an increase in the vapor pressure of AlCl(g) in the pack, which keeps activity of Al-chloride species on the surface high enough over the deposition time and thus making solid state diffusion to be the rate controlling factor. Whereas for 5 wt% Al pack, as Al-chloride depleted zone appears near substrate due to the diffusion of vapors from pack to substrate surface controls the process. Datta et al [122] reported the activation energy for packs with Al content of 1-6 wt% to be 73.3 kJ mol⁻¹ which is close to the value obtained in this study for 5 wt% pack, Denner and Jones [123] reported that the

activation energy to be 160–170 kJ mol⁻¹ for hot dip aluminizing of mild steel from molten aluminum bath. El Mahallaway et al ^[124] reported that the activation energy values for hot dip aluminizing of low carbon steel (0.19 wt.% C) in pure aluminum bath and silicon doped aluminum bath to be 138 and 108 kJ mol⁻¹, respectively.

4.2.1.2 Effect of Time on Aluminizing of Carbon Steel

Pack composition with 10Al–3NH₄Cl was chosen to determine the effect of time on coating growth. Pack composition with 10 wt% Al was chosen to ensure that the AlCl(g) vapor pressure on the substrate surface was high enough during coating duration and the rate controlling step for coating growth was solid state diffusion (see section 4.2.1.1). Deposition temperature was kept constant at 800°C whereas the coating time was varied from 2 to 10 hours. EDS results in Figure 4.15(b) shows the Al profiles in the coating after 2, 4, 6, 8 and 10 hours. The coating deposition time was the time at the deposition temperature and this time did not include the cooling and heating times. Figure 4.18 shows the coating thickness as a function of (time)^{1/2}. Least square fit for coating growth data gives:

$$x = 58.85t^{1/2} - 8.43 \quad (8)$$

Where x is coating thickness in microns and t is the coating time in hours. The coating growth kinetics follows the parabolic behavior with a parabolic rate constant of 58.85 μm sec^{-1/2}. The offset value of -8.43 can be due to loss of substrate to the pack due to a reaction of Fe with Al-chloride gaseous species. XRD showed no change in the phase

composition of coating with time at 800°C. Similar offset values were reported for Fe-(9-12)Cr-1Mo steels by Datta et al.^[122]

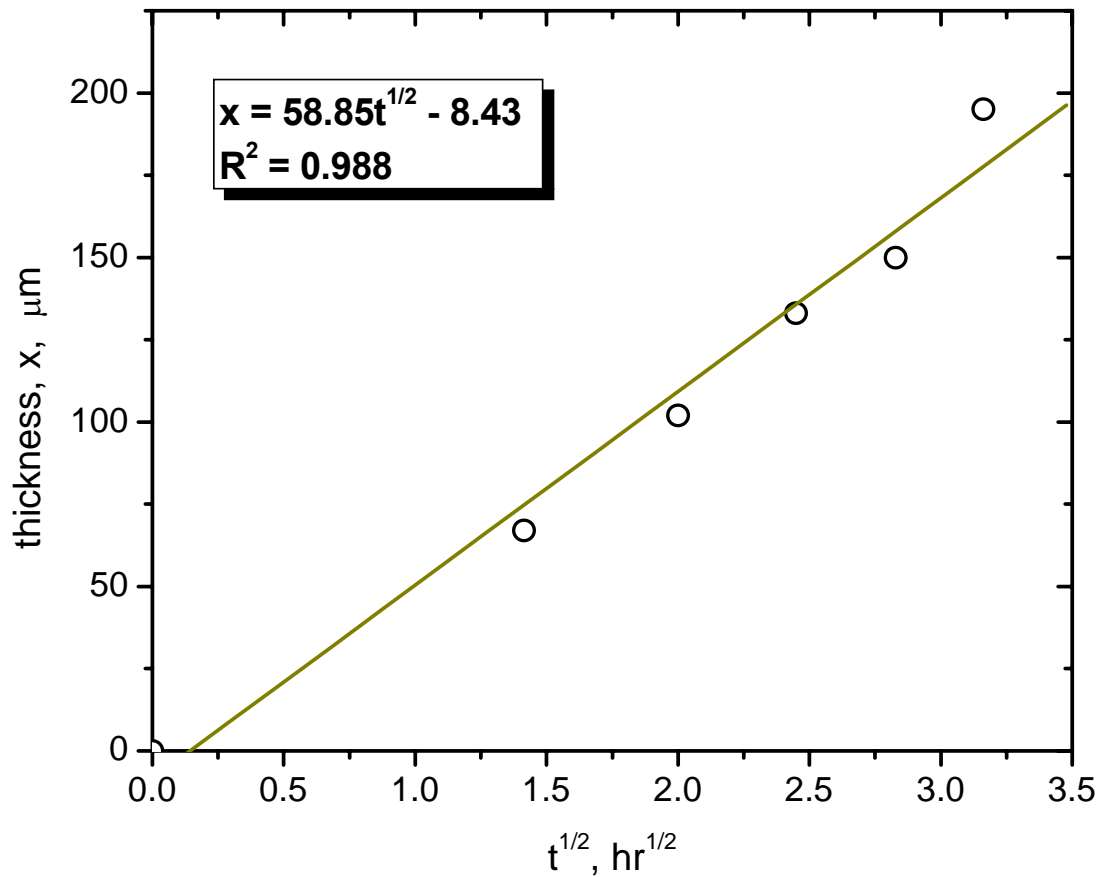


Figure 4.18: Effect of time on coating thickness. Parabolic fit suggests that coating growth follows diffusion kinetics.

4.2.2 Texture Analysis by EBSD

Coating composition on carbon steel surface for both 5% and 10% Al packs at 800°C was Fe_2Al_5 , as confirmed by the XRD and EDS analysis. Fe_2Al_5 is an intermetallic compound with an orthorhombic crystal structure ($Cmcm$, $a=7.6559$, $b=6.4154$, $c=4.2184$ Å). Figure 4.19 (a) and (b) shows the unit cell and the superlattice structure^[119] of Fe_2Al_5 respectively. Aluminum atoms are located at the partial node positions along the C axis in Fe_2Al_5 structure and there are about 30% vacancies in these positions^[125].

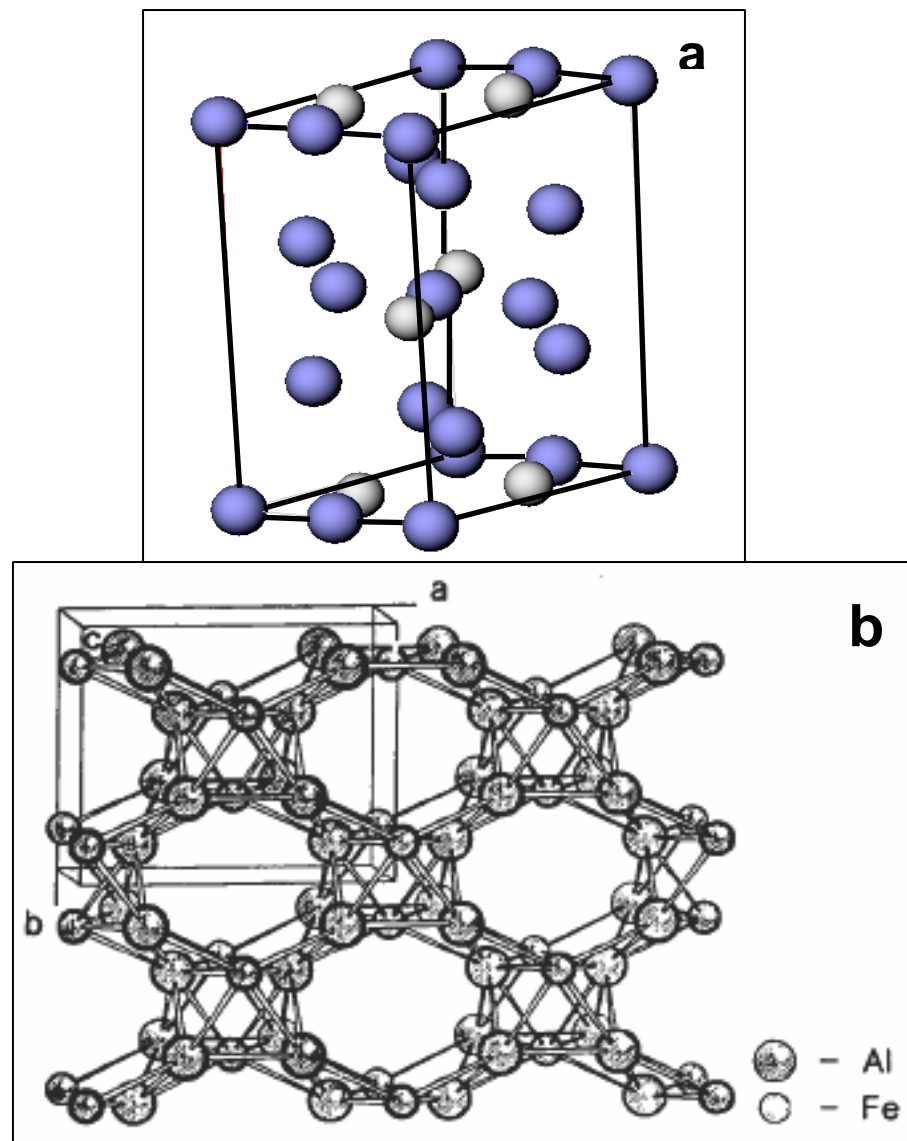


Figure 4.19: (a) Orthorhombic unit cell of Fe_2Al_5 , (b) superlattice structure

XRD pattern in Figure 4.20 shows the strong texture in the (002) direction as evident from a strong diffracted intensity for {002} planes. Texture of coatings was characterized by EBSD technique. Figure 4.21 shows a typical Kikuchi map obtained for the Fe_2Al_5 phase with calculated indexing.

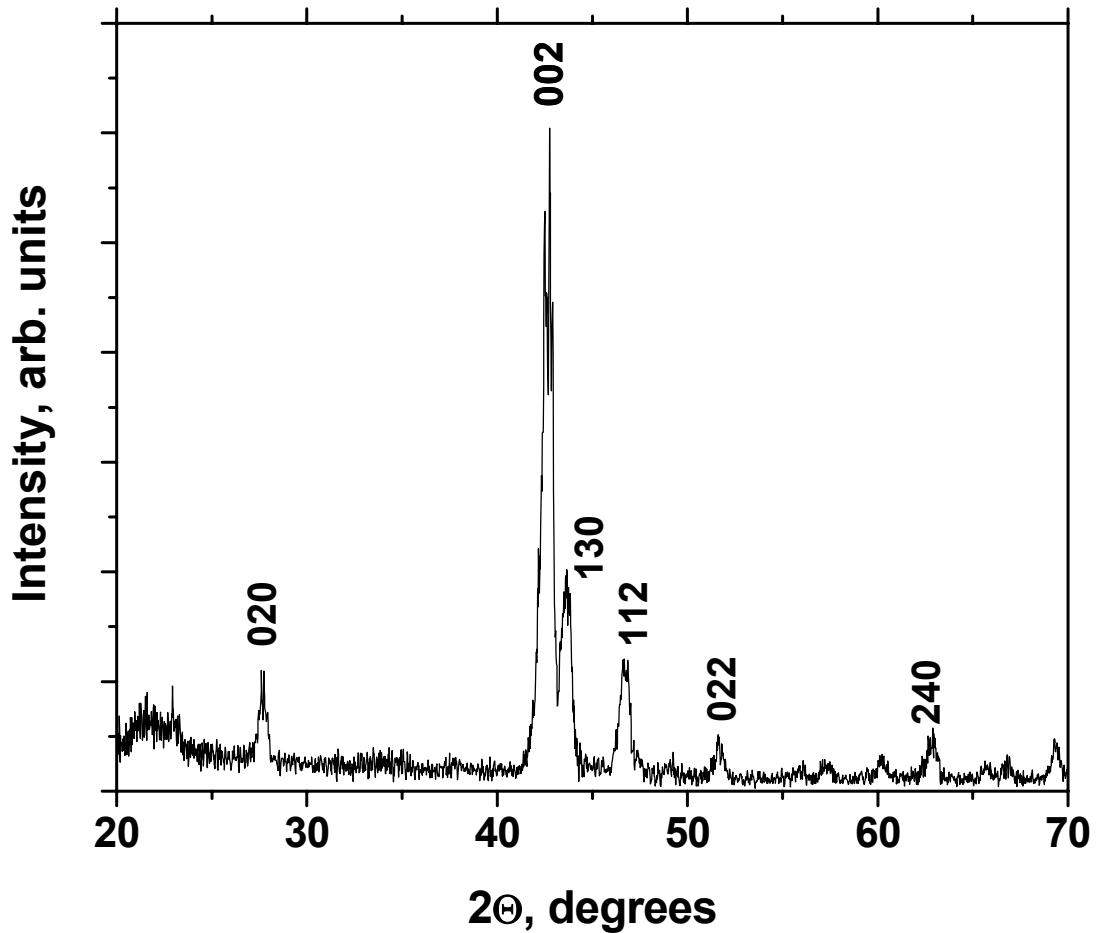


Figure 4.20: XRD pattern of Fe_2Al_5 coating showing {002} preferred orientation

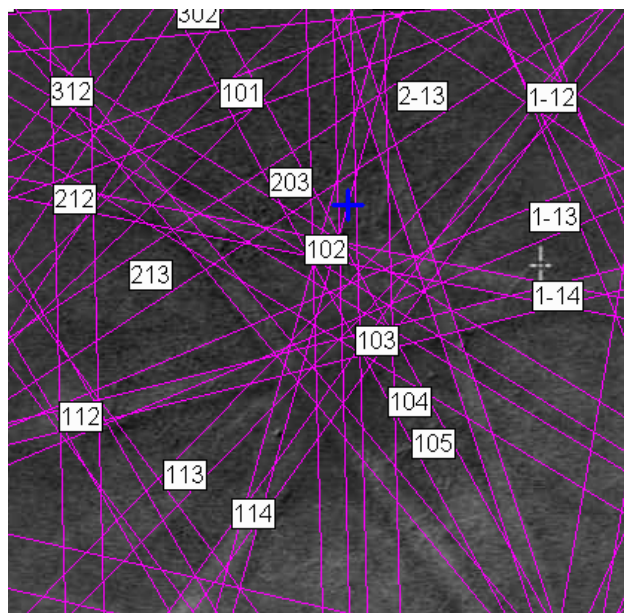
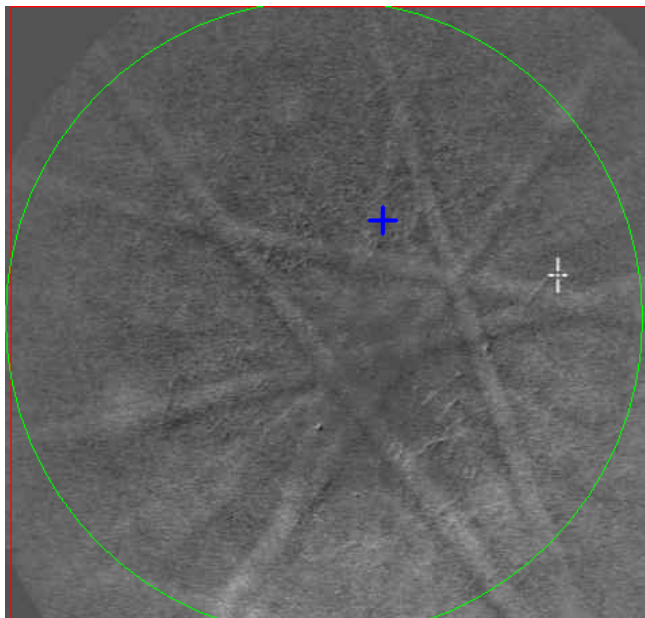


Figure 4.21: Typical kikuchi pattern obtained for Fe₂Al₅ phase and calculated indexing using lattice parameters from the literature.

Figure 4.22(a) and (b) shows the phase map and all Euler maps for the coating/substrate interface respectively. Phase map clearly distinguished Fe_2Al_5 phase from the interdiffusion zone after indexing Kikuchi maps as shown in Figure 4.21. Interdiffusion zone was not indexed properly (<60% successful indexing) due to sharp variations in Al activities, thus the region between successfully indexed Fe_2Al_5 and Fe (substrate) was assumed to be the interdiffusion zone.

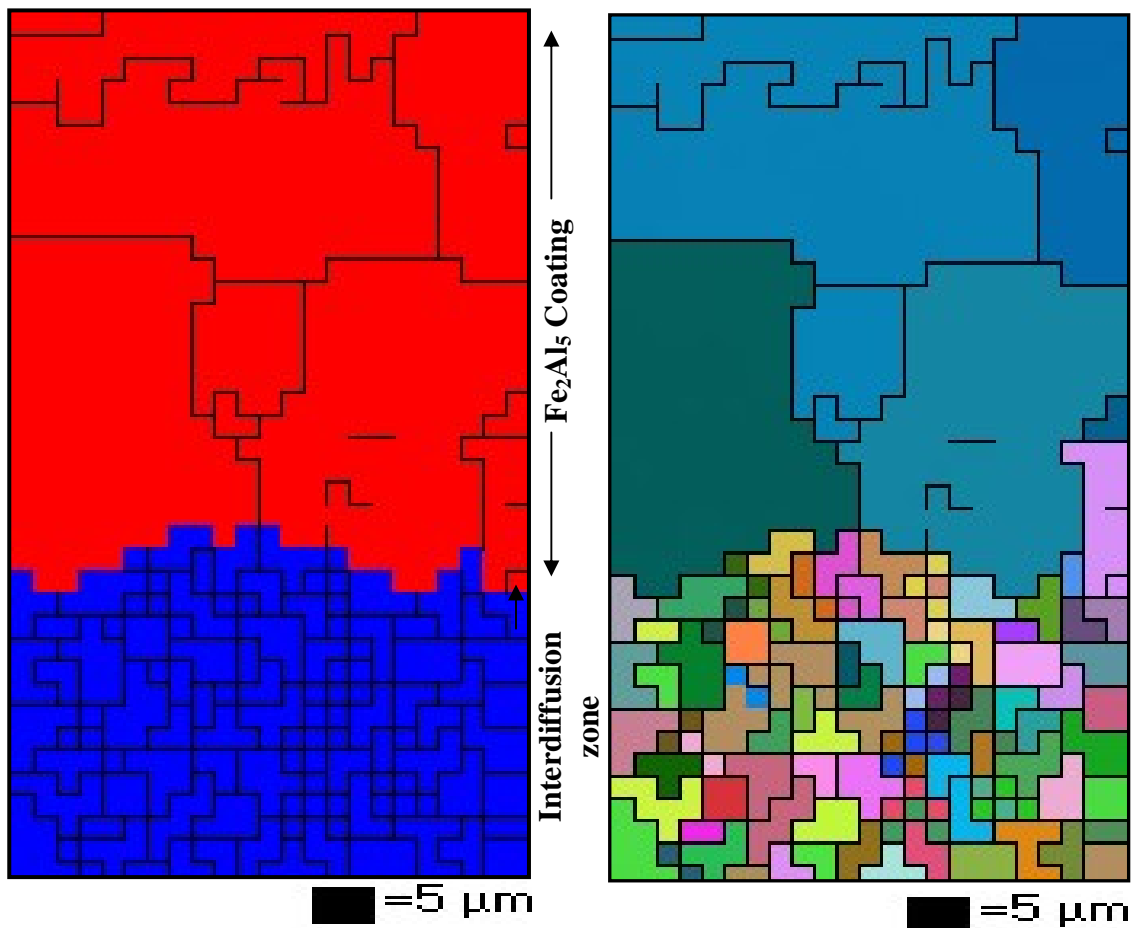


Figure 4.22: EBSD phase map and Euler map for coating and interdiffusion zone. Phase map clearly distinguishes Fe_2Al_5 .

Figure 4.23 shows the $\{002\}$, $\{200\}$, and $\{020\}$ pole figures of Fe_2Al_5 . All pole figures of intense diffraction line show that the coating is highly textured with the c-axis aligned parallel to transverse direction (perpendicular to the substrate) with texture component as $\langle 002 \rangle \parallel [010]$. Substrate SA210 had $\{110\}$ planes aligned at the surface and the preferred orientation of growth of Fe_2Al_5 in $\langle 002 \rangle$ direction shows that Al did not deposit epitaxially but nucleated and grew Fe_2Al_5 phase with c-direction of orthorhombic crystal perpendicular to the substrate surface. The coating grows primarily due to an outward diffusion of Fe^{+3} ions and the c-axis direction provides vacancies for Fe^{+3} ions to diffuse through coating Fe_2Al_5 layer by vacancy exchange and react with the depositing aluminium to form new coating at the surface. These vacancies coalesce at the coating/substrate interface to form Kirkendall voids as evident from Figure 4.24(a). The intergranular regions are clearly recognizable in the cross-section of a fractured coating in Figure 4.24(b) suggesting that the grains are actually columnar, which grew perpendicularly to the surface. Sequeira et al^[126] also reported the formation of columnar Fe_2Al_5 grains perpendicular to the substrate surface for the aluminized iron based alloys.

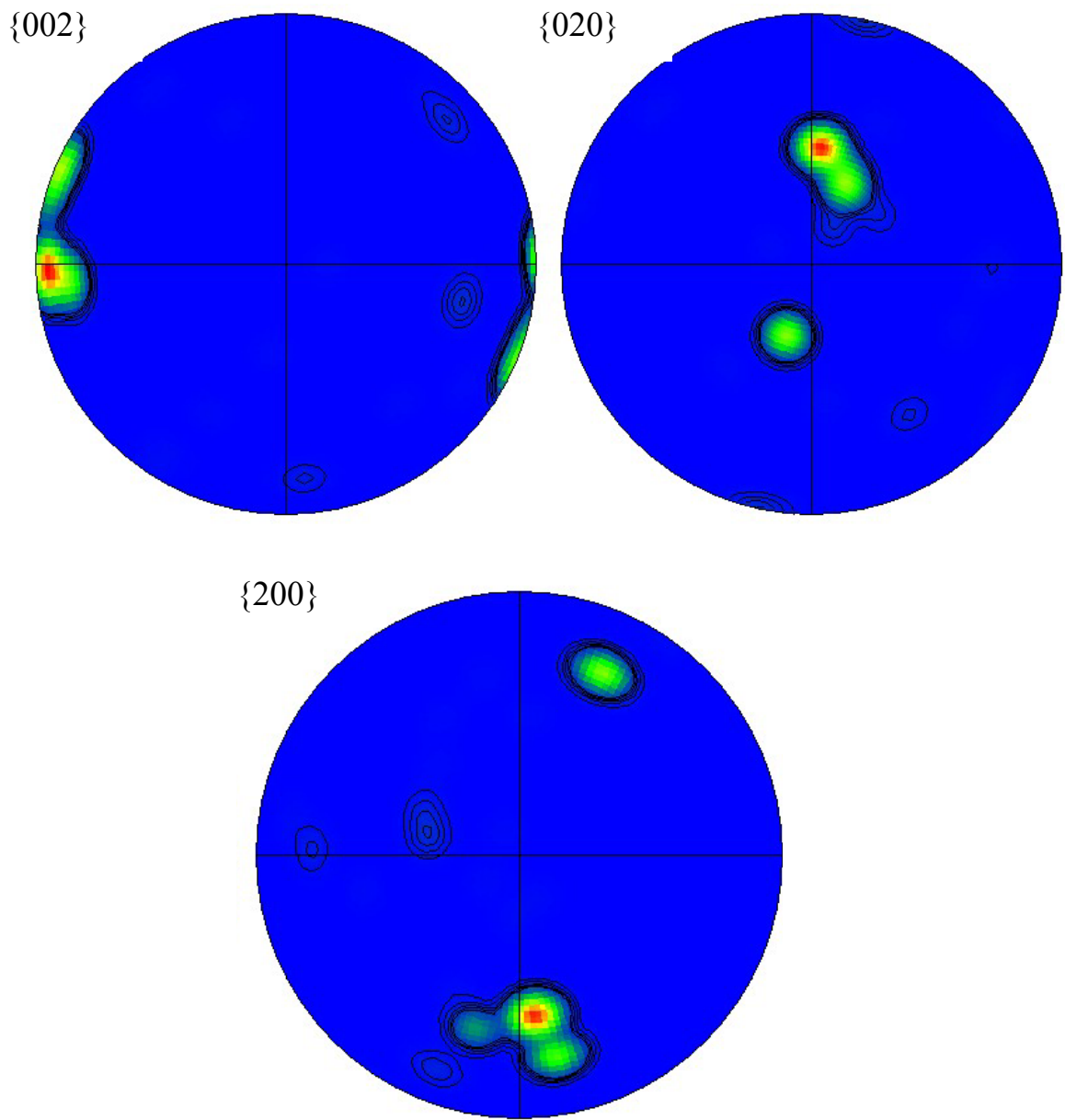


Figure 4.23: $\{002\}$, $\{020\}$, and $\{200\}$ pole figures for Fe_2Al_5 phase.

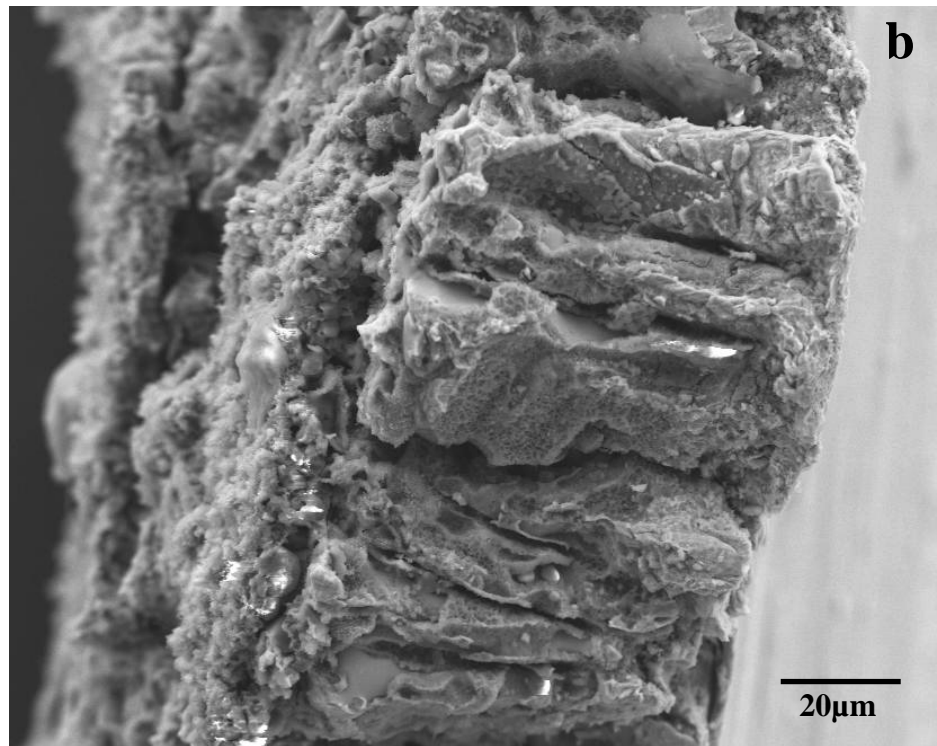
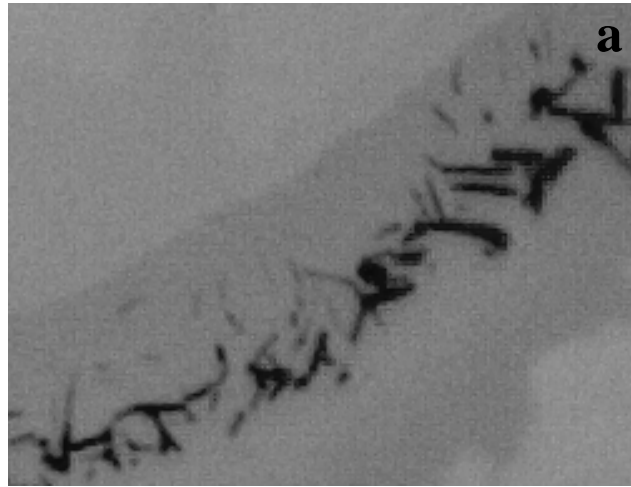


Figure 4.24: (a) Kirkendall voids formed due to outward diffusion of Fe^{+3} ions and coalescence of vacancies left behind, (b) Fracture cross-section of coating showing columnar grains growing perpendicular to the substrate surface.

4.2.3 Mechanical Properties of Aluminide Coatings and Interface

Mechanical properties of aluminide coating and interdiffusion zone was characterized by nanoindentation with Berkovich shaped indent. Figures 4.25(a) and (b) show the nanoindents on the coated specimen; in the aluminide coating, interdiffusion zone and the carbon steel substrate. Several points were chosen to get a comparison of mechanical properties such as hardness and elastic modulus. Indents were made at a constant load of 100mN and 200mN to study the effect of load. Corresponding load-displacement curves for the indentations are shown in Figure 4.26 and 4.27. All indents in Figure 4.25(a) were made at a constant maximum load of 100mN whereas those shown in Figure 4.25(b) were made at 200mN. Hardness and modulus was extracted from the average over the experiment and also during unloading as discussed in Appendix B. Indent size difference in the three areas of these samples clearly shows differences in their hardness. A correspondence between a step in the load-displacement curve and a cracking morphology provoked by a nanoindentation fracture has been frequently reported in depth-sensing indentation experiments in coating-substrate systems^[127,128]. However, the absence of any such steps in the load-displacement curves for the aluminide coating in Figure 4.26 and 4.27 indicates that cracks were not formed in the coating during nanoindentation at test loads.

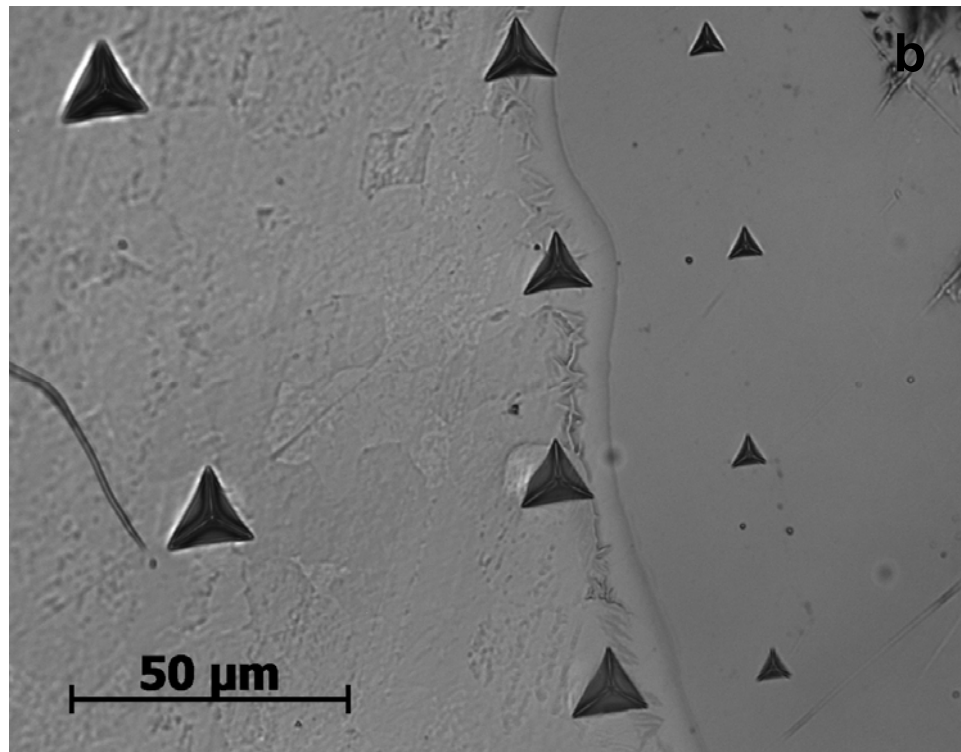
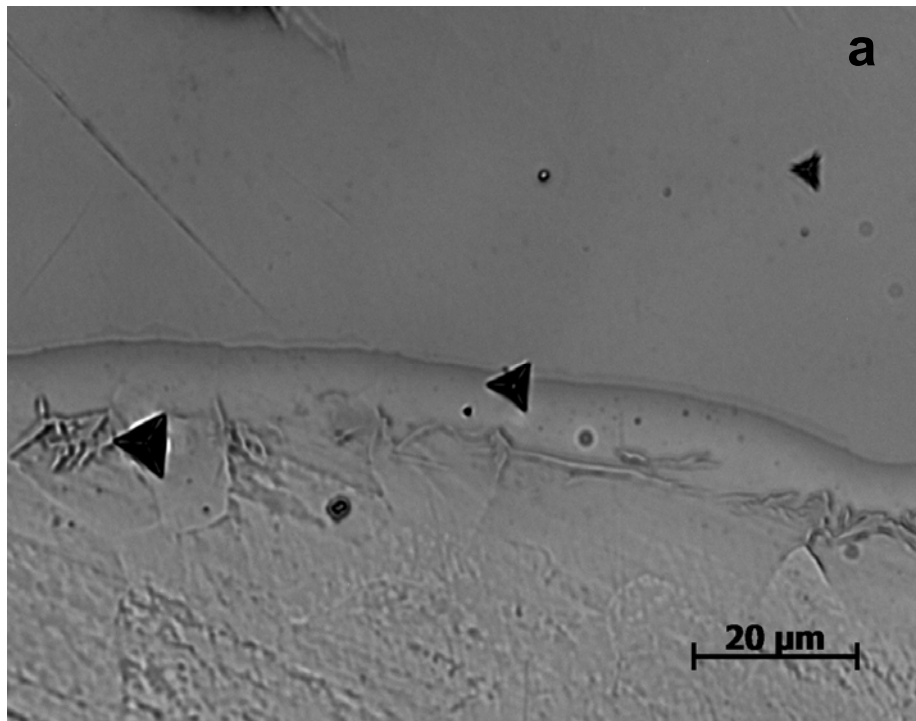


Figure 4.25: Nanoindentation matrix chosen to study the mechanical properties of coating, substrate and interdiffusion zone.
(a) 100mN load, (b) 200mN load

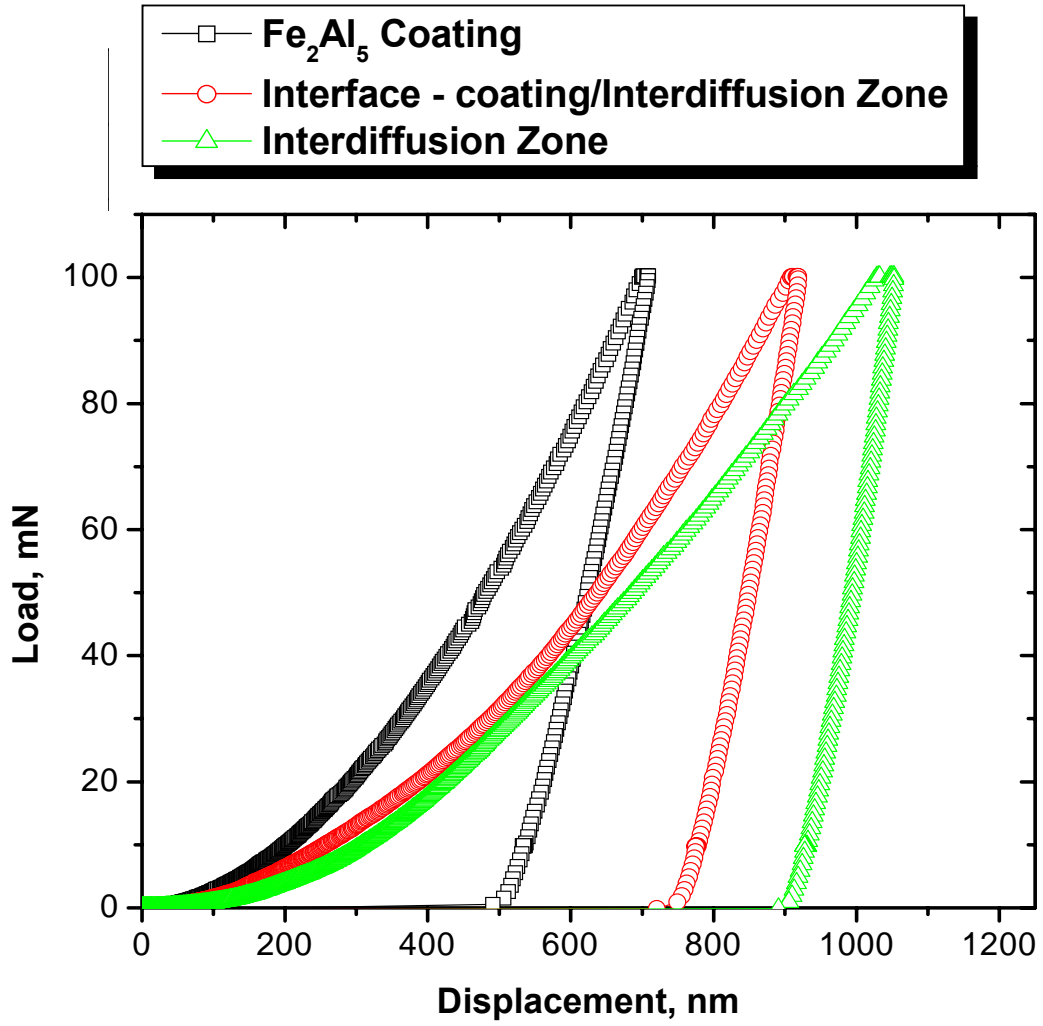


Figure 4.26: Load displacement curve for matrix chosen in figure 4.25(a) for 100mN maximum load.

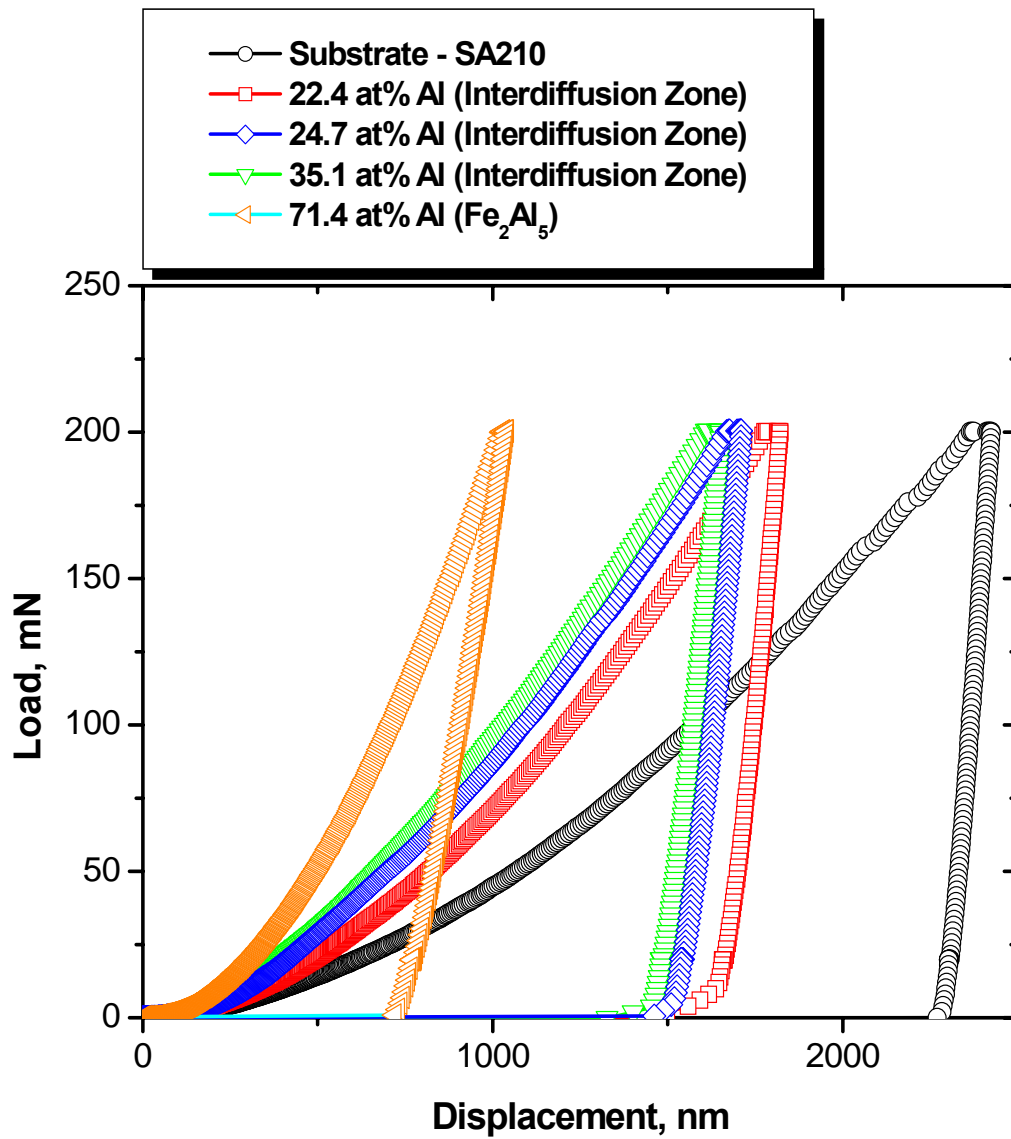


Figure 4.27: Load displacement curve for matrix chosen in figure 4.25(b) for 200mN maximum load.

EDS was used to get the Al content at the indent positions to evaluate the effect of Al on the local mechanical properties of the coating and interface. Average hardness (H) and the elastic modulus (E) values from nanoindentation experiments, as a function of Al content (in at%), are presented in Figure 4.28(a), and Figure 4.28(b). Hardness and the elastic modulus were calculated from the unloading curves. It is evident from this data that as the Al/Fe ratio in the coating increases, the H and E values also increase considerably. Substrate showed an average hardness of 2.5GPa and the elastic modulus of 132 GPa, whereas coating was much harder with the H in the range of 12.5 – 13.5 GPa and E in the range of 200 - 225 GPa. Test results are summarized in Table 4.3.

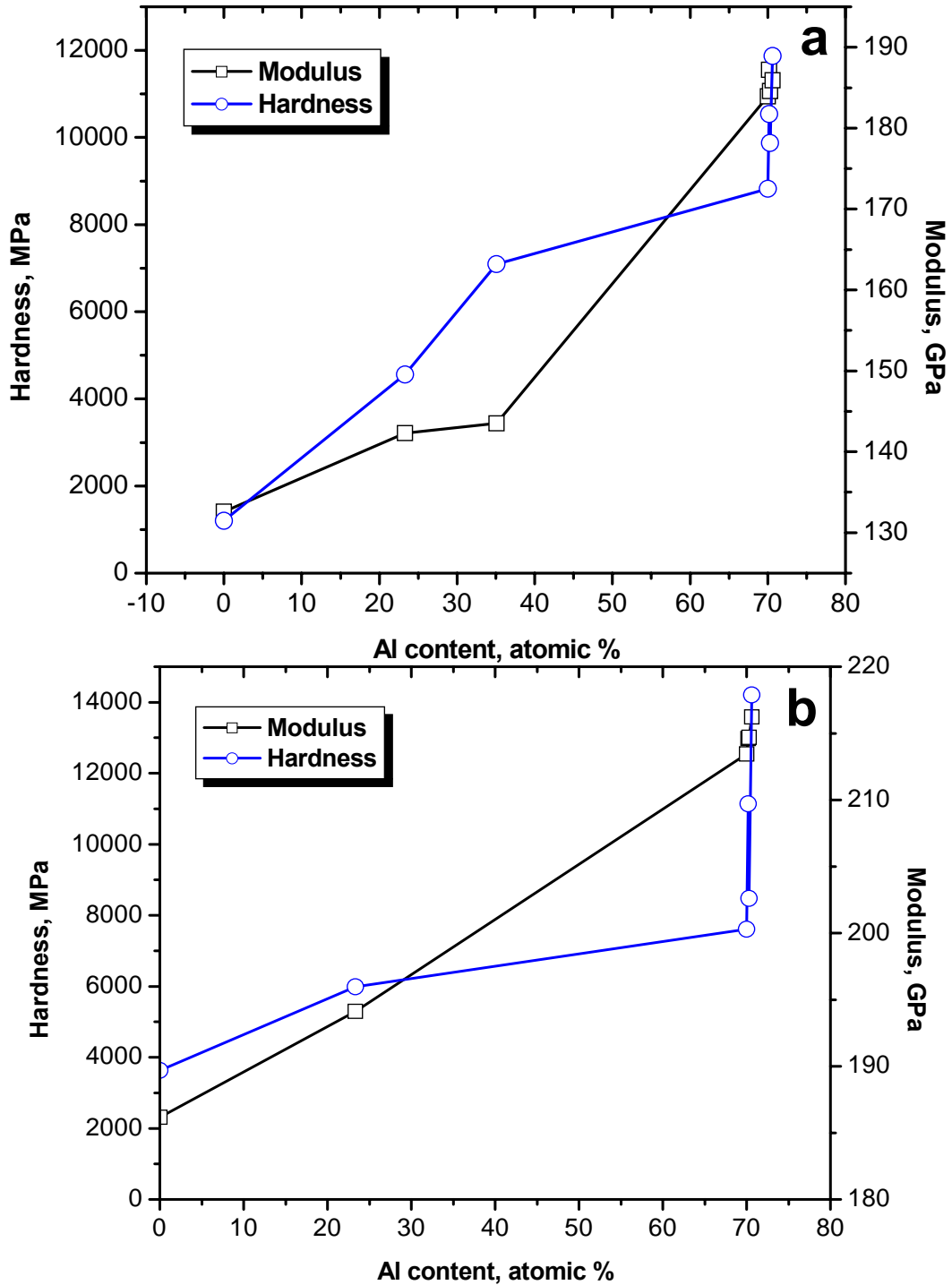


Figure 4.28: Effect of Al content on mechanical properties (hardness and elastic modulus). Al content was measured by EDS after indentation experiments. Results are listed in Table IV, (a) Average over the range from continuous stiffness measurements. (b) Calculated from method by Pharr method.

Table 4.3: Effect of aluminum concentration on coating average hardness and elastic modulus

Al Concentration, (atomic %)	Zone	Load (mN)	Elastic Modulus (Gpa)	Berkovich Hardness (Mpa)
0	Substrate	200	132.09	2502.74
22.33	Interdiffusion Zone	200	188.47	3401.33
24.7	Interdiffusion Zone	200	185.76	3913.97
67.74	Coating	200	217.89	13590.08
69.73	Coating	200	209.70	12976.99
70	Coating	200	200.28	12541.70
70.17	Coating	200	209.70	12976.99
70.29	Coating	200	202.60	13009.65
70.62	Coating	200	217.89	13590.08
70.88	Coating	200	200.28	12541.70
71	Coating	200	227.38	5987.36
71	Coating	100	222.51	14215.74
47.3	Interdiffusion Zone	100	187.62	7400.43

4.2.4 Corrosion Behavior

Main reason to develop surface metallic coatings is to provide corrosion protection to the substrate at high temperature in boiler or gasifier environments using high sulfur fuel. Tests were carried out to evaluate the corrosion behavior of aluminide coatings developed in this study. Two gaseous environments chosen for this study were based on the field characterization of gaseous environments in a recovery boiler as discussed in Chapter 3. Calculated partial pressures of sulfur for 1% H_2S in N_2 , using HSC chemistry, were 10^{-10} to 10^{-4} atm in the selected temperature range of 600-1000°C. The second environment used for aluminide testing was air ($p_{\text{O}_2} = 0.21$ atm). Samples coated in packs containing 5%Al at 800°C for 8hrs were used to compare the environmental effects under different gaseous environments and at different temperatures. Effect of environmental parameters on coating performance are discussed separately in following sections.

4.2.4.1 Performance of Aluminide Coatings in Sulfidizing Environment

Uncoated carbon steel and aluminized carbon steel samples were exposed to 1% H_2S environment at different temperatures to evaluate their relative susceptibility to high temperature sulfidation in simulated boiler and gasifier environments. As discussed previously, uncoated steel showed higher mass gain ($\sim 8\text{mg}/\text{cm}^2$) at 300°C after 100 hour exposure, with the formation of a porous, non adherent sulfide scale. Whereas at 600°C and 800°C, uncoated carbon steel samples failed within the first few hours of the test converting the coupon to powder sulfides. However, iron aluminide coated carbon steel samples showed an excellent corrosion resistance in the sulfidizing environments at temperatures up to 800°C, as shown by the results in Figure 4.29.

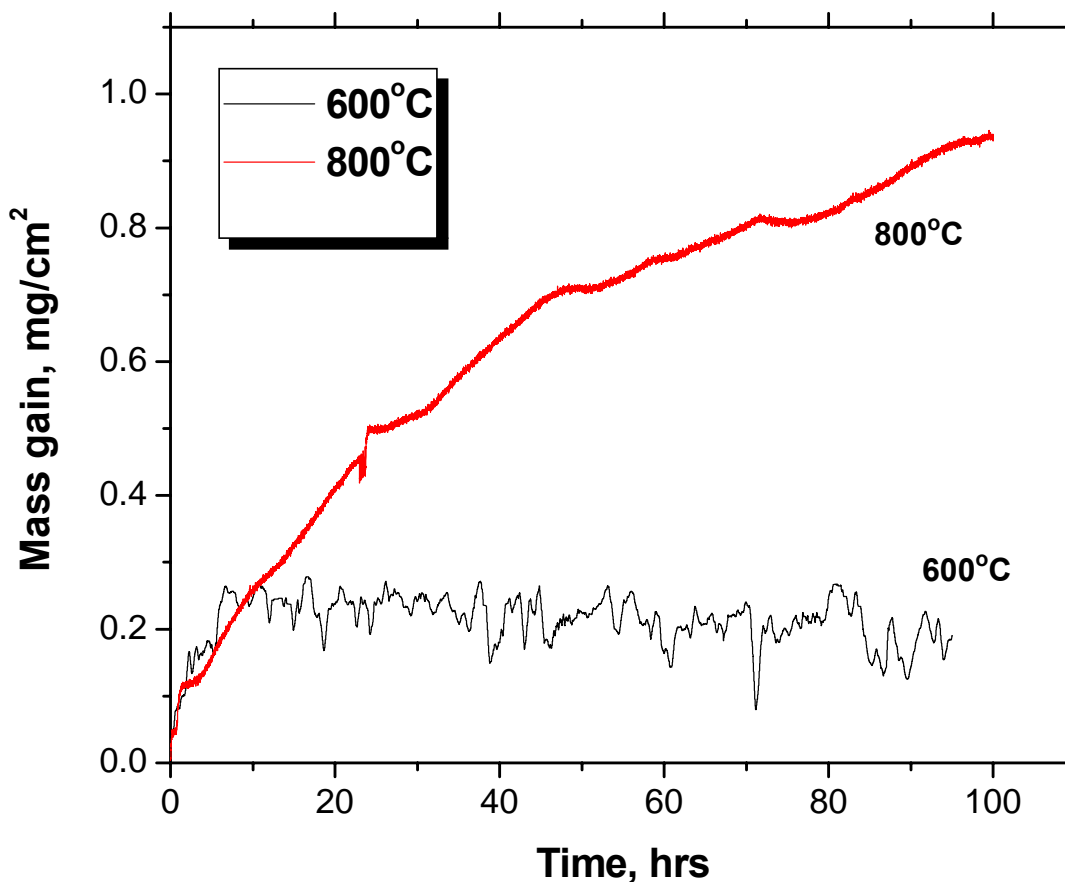


Figure 4.29: Sulfidation behavior of Fe-Al coating. Parabolic rate constants are listed in Table 4.4.

XRD analysis of the scale has shown that the scale was predominantly θ - Al_2O_3 on the surface with minor Al_2S_3 (Figure 4.30). Aluminized samples showed an overall mass gain of $<1 \text{ mg/cm}^2$ after 7 days at 600°C , and 1.5 mg/cm^2 in 100 hours at 800°C . Iron aluminide showed better resistance than uncoated carbon steel as θ - Al_2O_3 scale was present on the surface and also the Al_2S_3 is thermodynamically more stable than iron sulfides, and has relatively lower growth rate. Its large molecular volume results in a large Pilling-Bedworth ratio, so the scale can be more protective than the sulfides of iron. Corrosion rates under tested conditions, as listed in Table 4.4, show a parabolic reaction

kinetics with significantly lower rates suggesting that the scale growth process was diffusion controlled and that the θ - Al_2O_3 provided a good barrier to the gaseous diffusion.

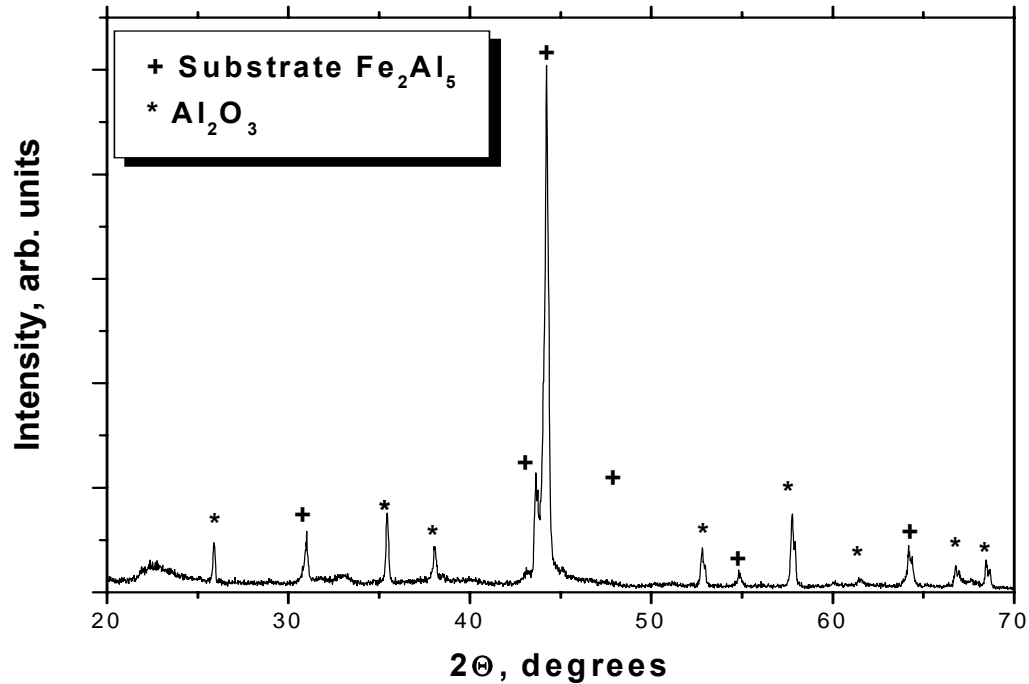


Figure 4.30 : XRD pattern of scale after sulfidation at 800°C

Micrograph in Figure 4.31 shows the surface of scale formed on the aluminized sample by exposure to sulfidizing environment at 800°C for 100hrs. Scale showed two different morphologies as shown in Figure 4.31(b) and (c). One with small loosely packed needle shaped whiskers (Figure 4.31b) and other with dense adherent product (Figure 4.31c). EDS maps confirmed that whiskers are high in sulfur and oxygen (Figure 4.32). Spot elemental analysis suggested that whiskers are Al_2S_3 , which is consistent with our XRD results and stability diagram of Al-O-S at 800°C. Adherent product was low in sulfur and high in oxygen suggests that it was primarily Al_2O_3 , as shown by EDS results in Figure 4.33.

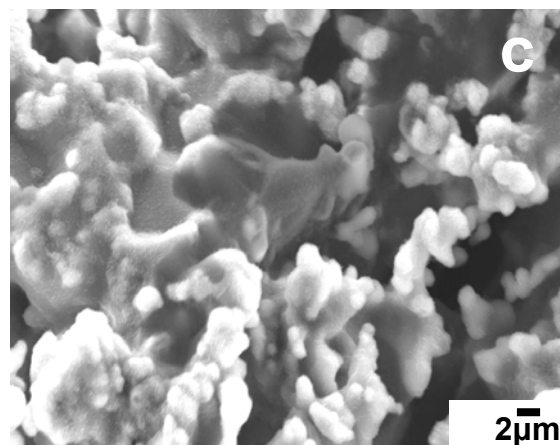
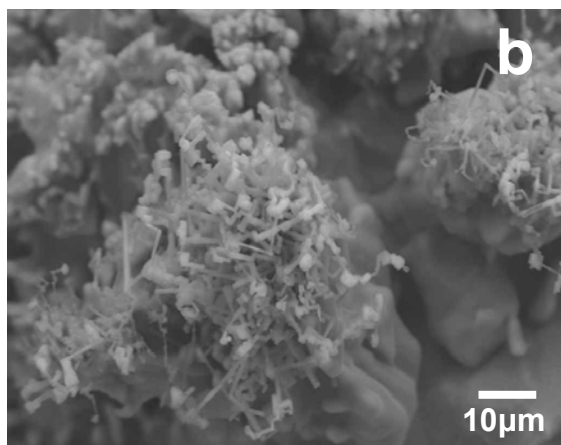
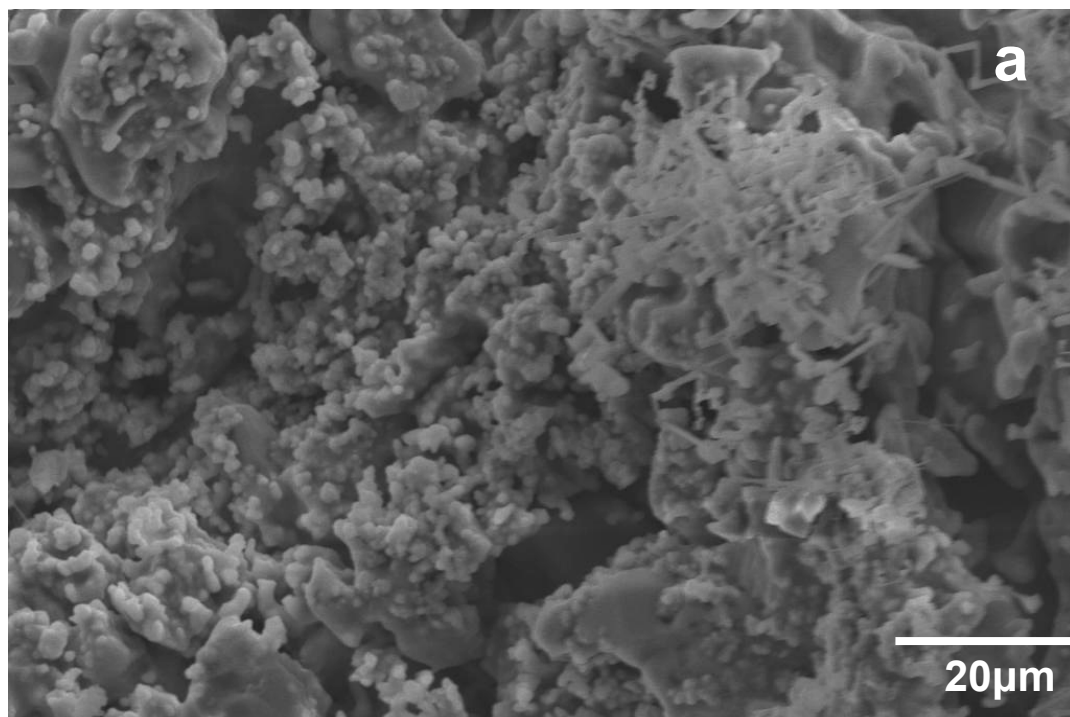


Figure 4.31: (a) Surface SE micrograph of sulfidized Fe-Al coating. Two different morphologies were observed. The compositions were characterized by EDS and XRD:
(b) whiskers of Al_2S_3
(c) adherent $\Theta\text{-Al}_2\text{O}_3$

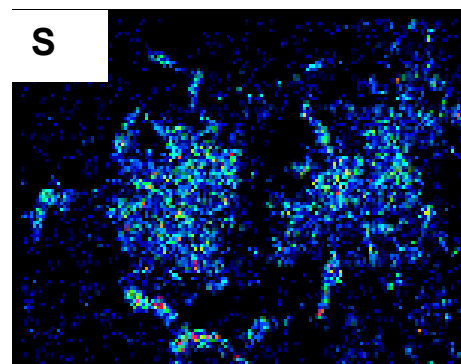
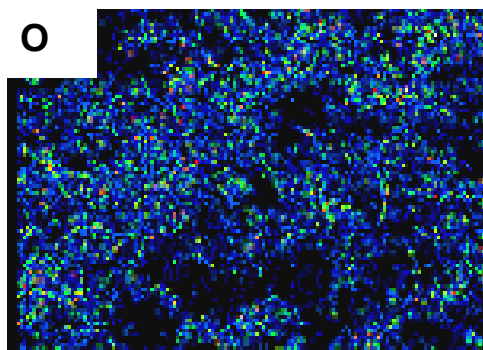
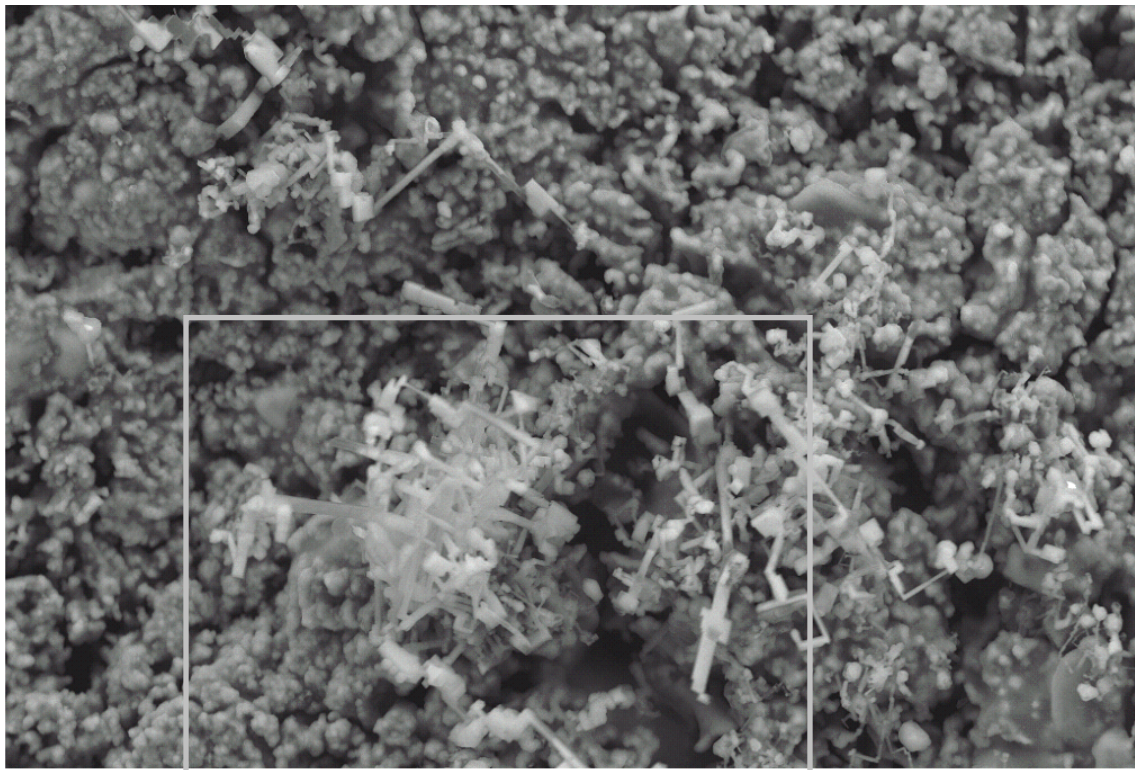


Figure 4.32: SE micrograph and EDS sulfur and oxygen maps of whiskers showing whiskers are rich and sulfur and oxygen

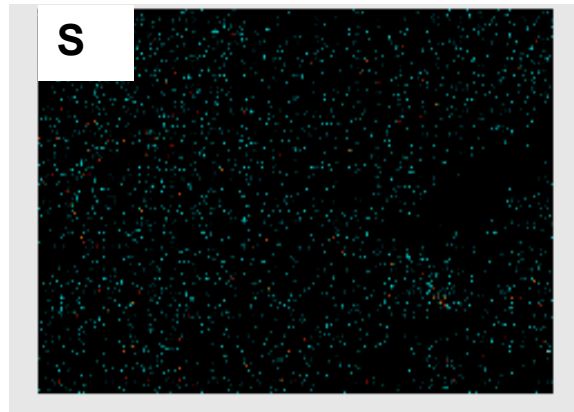
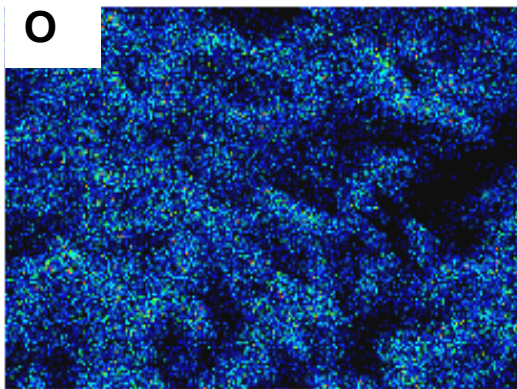
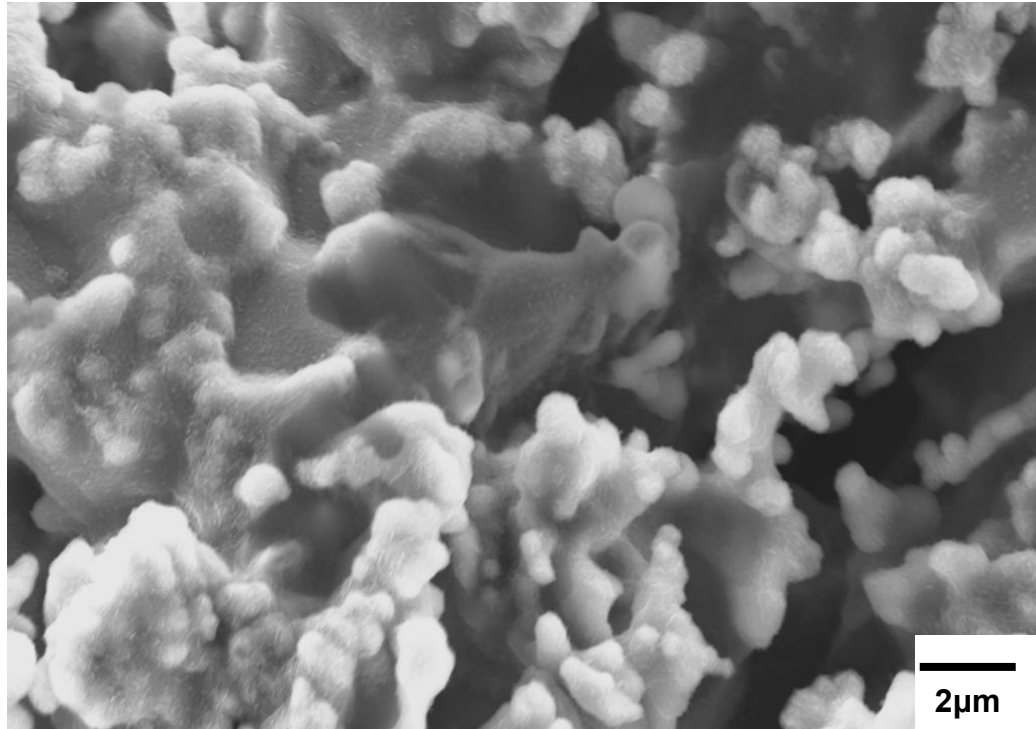


Figure 4.33: SE micrograph of adherent scale. EDS maps shows high oxygen content and negligible sulfur confirming Al_2O_3 phase.

4.2.4.2 Oxidation

Aluminide coated samples were also exposed to oxidizing environments to compare their relative corrosion resistance in these environments. Aluminized samples showed an excellent corrosion resistance behavior up to 1000°C in air with mass gains $\sim 1\text{mg}/\text{cm}^2$ in 100 hours tests. Figure 4.34 shows the kinetics of oxidation for aluminized SA210 carbon steel samples in dry air at 800 °C and 1000°C. Parabolic rate constants calculated from data in Figure 4.34 during the steady state oxidation are listed in Table 4.4. A slow growing Al_2O_3 was observed at all tested temperatures. Representative surface micrograph of oxidized coating at 1000°C is shown in Figure 4.35 which shows a formation of whiskers covering the surface of sample. XRD showed that the oxide is primarily $\Theta\text{-Al}_2\text{O}_3$ for samples exposed to air at higher temperatures up to 1000°C with $<10\mu\text{m}$ thick scale as shown in Figure 4.36.

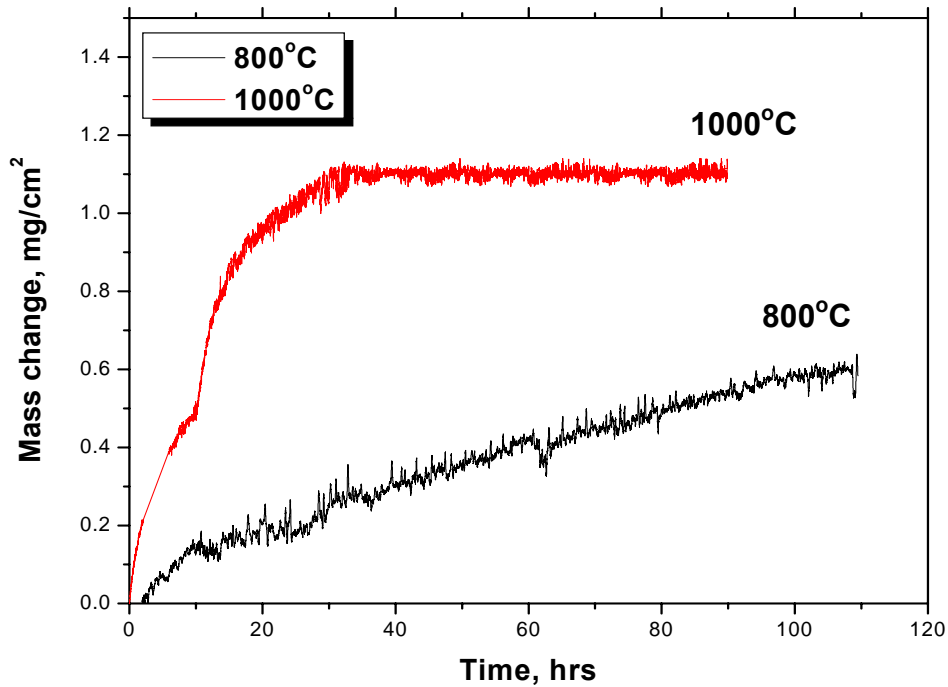


Figure 4.34: Mass change behavior of Fe-Al coating in air at 800 and 1000°C. Parabolic rate are listed in Table 4.4.



Figure 4.35: Surface morphology of oxidized coating in air at 1000°C shows formation of Θ - Al_2O_3 whiskers.

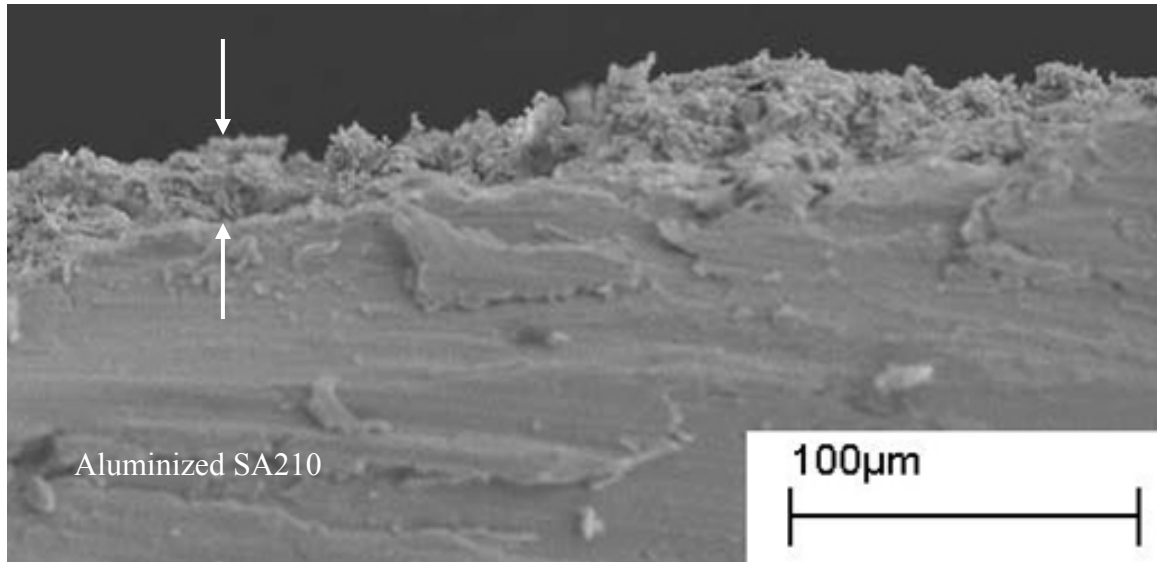


Figure 4.36 Alumina scale on aluminized SA210 after 100 hours of oxidation at 1000°C

Table 4.4: Corrosion rates of samples exposed to different environments. k_l denotes linear rate and k_p denotes parabolic rate. S shows sulfidizing environment and O shows oxidizing environment.

Sample	Temperature (°C)	Environment	K_l ($\text{mg.cm}^{-2}.\text{h}^{-1}$)	K_p ($\text{mg.cm}^{-2}.\text{h}^{-1/2}$)
SA210	300	S	0.12	-
SA210	600	S	1.12	-
SA210	800	S	12.07	-
Aluminized	800	O-Air	-	0.066
Aluminized	1000	O-Air	-	0.081
Aluminized	600	S	-	0.013
Aluminized	800	S	-	0.086

4.2.4.3 Cyclic sulfidation-oxidation

Aluminide coatings were also tested under cyclic environments. Test were done at 300°C and 600°C showed excellent stability with mass gain $<1 \text{ mg/cm}^2$, thus to elucidate the effects of cyclic environments, results from test at 800°C are presented in this section. Figure 4.37(a) shows the corrosion kinetics of aluminized SA210 at 800°C in environments cycling between $p_{\text{S}_2} = 10^{-9} \text{ atm}$ and $p_{\text{O}_2} = 0.21 \text{ atm}$ every 12 hours as compared to aluminized SA210 in static sulfidizing conditions. In cyclic environments, total mass gain $\sim 2 \text{ mg/cm}^2$ was observed in 100 hours and spallation on the order of 0.05 mg/cm^2 at the change of gas cycle from sulfidizing to oxidizing as shown in Figure 37(b). No spallation was observed when the environment was changed from oxidizing to sulfidizing. This suggests that sulfides/sulfate scales are more prone to spallation than oxide. Figure 38 shows the XRD patterns of scale formed after cyclic and static exposures, and Figure 39 shows the surface microstructure of scale after cyclic exposures. XRD primarily detected Al_2O_3 and $\text{Al}_2\text{S}_3/\text{Al}_2\text{SO}_4$ in the scale formed on aluminide coating tested under static sulfidizing environments whereas the scales were primarily Al_2O_3 on equivalent samples exposed to the cyclic environment. Needle shaped particles suggests that $\theta\text{-Al}_2\text{O}_3$ is formed during sulfidation-oxidation tests and covered the entire surface as confirmed by XRD measurements. High intensity substrate peaks show that the alumina layer is very thin. Results from this study show that Al containing coatings can be a suitable candidate for high temperature gasification applications because of the relatively slow growth kinetics of Al_2O_3 and better protection under cyclic and static sulfur containing environments.

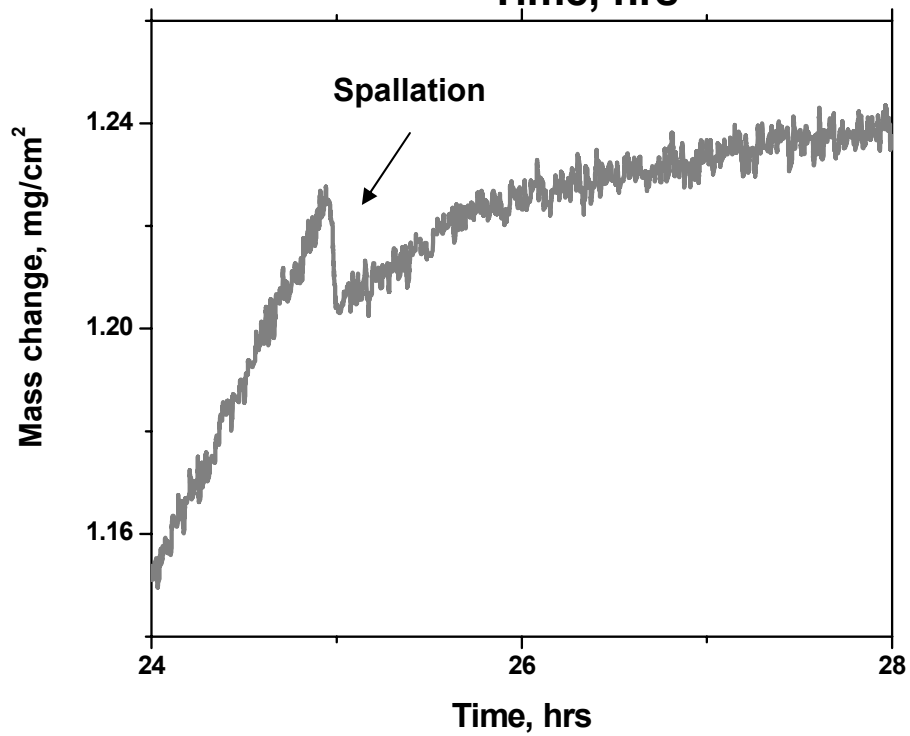
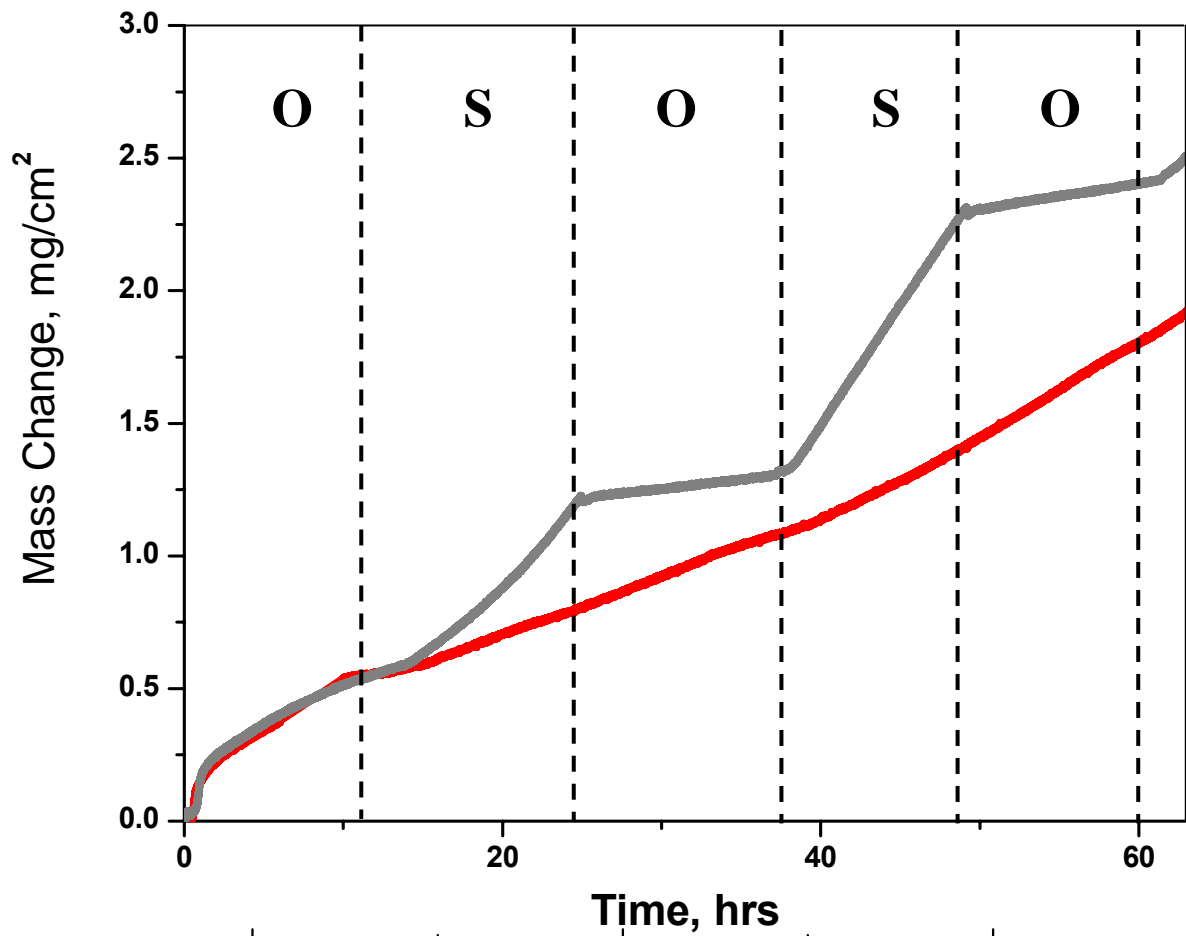


Figure 4.37 : (a) Behavior of aluminide coatings in cyclic and noncyclic environments at 800°C, (b) spallation as environment changes from sulfidizing to oxidizing.

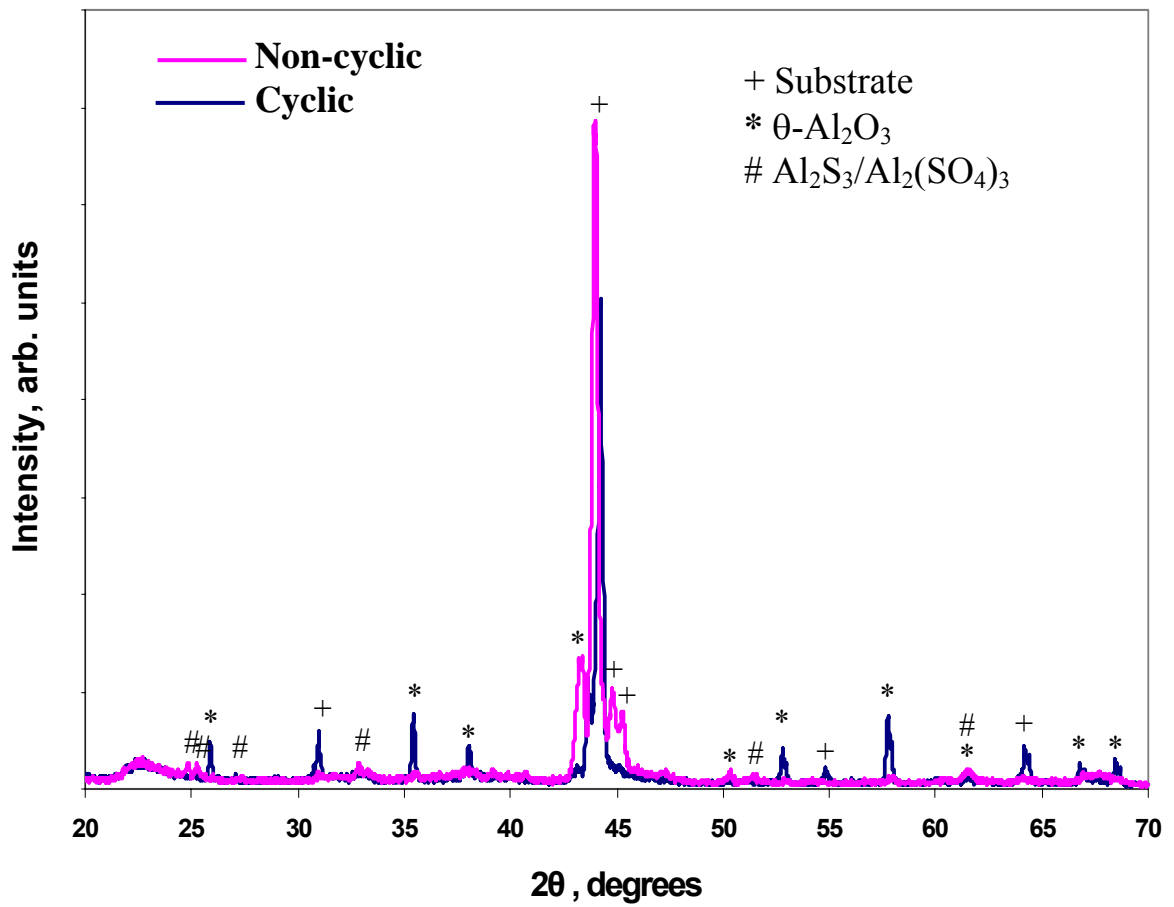


Figure 4.38 : XRD pattern of aluminized SA210 after 100 hour exposure to cyclic and noncyclic environments at 800°C

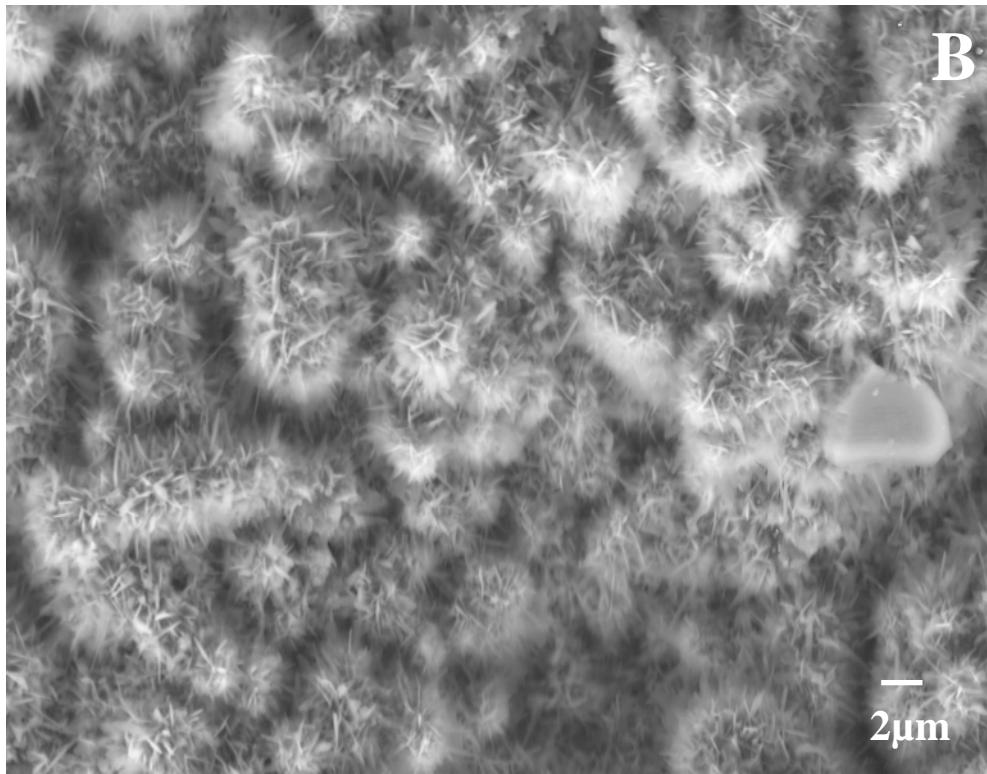
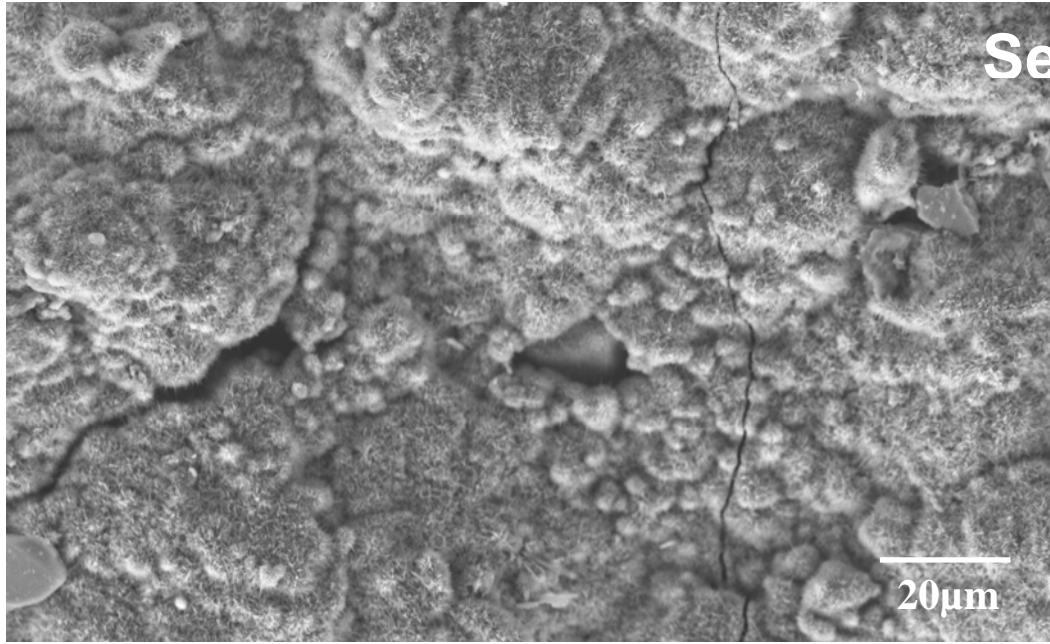


Figure 4.39: (A) Surface microstructure of scale formed on iron aluminide diffusion coating after 100 hours exposure to cyclic sulfidizing-oxidizing environments at 800°C. Alumina whisker network is covering the surface with minor amount of Al₂S₃. Significant cracking is evident, (B) alumina whisker network.

SUMMARY

1. Chromized and aluminized coatings were prepared by pack cementation process on SA210 carbon steel.
2. Chromizing of carbon steel showed formation of chromium carbides and nitrides with 10-50 μ m thick coatings at 800°C for 6 hours.
3. Chromized SA210 carbon steel showed improved corrosion behavior in static sulfidizing environments up to 300°C and, but failed at 600°C and 800°C with formation of porous chromium sulfide scale.
4. In cyclic environment exposure, chromized SA210 showed excellent behavior at 300°C as compared to uncoated steel with formation of adherent and protective scale.
5. Aluminizing of carbon steel was used to form iron aluminide coatings on surface which showed an improved corrosion resistance even at gasification temperatures.
6. Fe-Al pack cementation coating growth kinetics was investigated in temperature range of 650-900°C, and 2-10 hrs of deposition time. Pack cementation coating showed an activation energy dependence on Al content of the pack, where a pack with 5 wt% Al showed E_a of 68.58 kJmol⁻¹ and with 10 wt% Al showed 93.78 kJmol⁻¹.
7. Fe₂Al₅ coating phase showed strong {002} texture with outward growth of coating phase as columns perpendicular to the substrate surface.
8. Hardness and modulus showed strong dependence on Al content from coating to substrate. Interdiffusion zone showed intermediate values between substrate and coating.

9. Aluminide coating on carbon steel showed excellent oxidation and sulfidation resistance up to 800°C with formation of continuous protective Al₂O₃ scale in cyclic sulfidizing-oxidizing environment. In air, corrosion rates for aluminide coated sample were low even at 1000°C.

CHAPTER V
REACTIVE ELEMENT (Hf AND Y) MODIFIED Fe-Al INTERMETALLIC
COATINGS

INTRODUCTION

Addition of reactive elements (RE) in minor concentrations (<1 at %) to alumina forming alloys has shown considerable improvement in adherence of oxide scales in oxidizing environments under high temperature thermal cycling conditions. As discussed previously in chapter 3, cyclic gaseous environments can also cause significant spallation of protective scales and accelerate the corrosion of alloys. To improve the adhesion of scales, reactive elements (Hf and Y) were co-deposited with Al using pack cementation process to form modified coatings. Coatings were prepared by adding elemental RE, oxide of RE and halide of RE with elemental aluminum in pack consisting of 5wt% Al-3wt% NH₄Cl. Different pack compositions and temperatures used to optimize the coating parameters for co-deposition of Hf/Y with Al. Hf modified aluminide coating deposition was performed with different process parameters to optimize the coating process before preparing Y modified coatings. The plausible parameters from Fe-Al-Hf coating experiments were adopted for preparing Y modified coating. It is considered that in order for the intended co-deposition of reactive element and aluminum to take place in the pack, two necessary thermochemical assumptions are:

1. Sufficiently high vapor pressures of halide species of different depositing elements can be generated in the pack.

2. Vapor pressures can be brought into a comparable range by adjusting the composition of the pack powder mixture and/or by selecting a suitable halide salt as an activator.

The partial pressures of halide vapor species responsible for deposition were calculated using HSC Chemistry, thermochemical software, for pack compositions used for Hf and Y modified coatings. Calculations were based on the Gibb's energy minimization process and the mass conversion reactions. All the calculations in this study were carried out by assuming a constant total pressure of one atmosphere. Mixtures of pure Al and RE powders with respective RE-oxides were investigated as the depositing source with a mixture of NH_4Cl and RE-chloride as halide activators, and Al_2O_3 powders as the inert filler. Microstructural characterization of coatings and the effect of fluctuating oxidizing/sulfidizing gaseous environments on scale stability have been discussed in this chapter.

5.1 Hf -MODIFIED IRON ALUMINIDE COATINGS

5.1.1 Thermodynamic considerations

The pack powder for co-depositing Al and reactive elements consisted of a mixture of elemental aluminum as source for Al, NH_4Cl and chlorides of reactive elements (HfCl_4) as activators, elemental reactive element powders (Hf) and oxides (HfO_2) as source for RE, and Al_2O_3 as inert filler. Table 5.1 shows the pack cementation process parameters for co-deposition of Hf and Al on SA210 substrate. Different pack composition were chosen to optimize the RE concentration in the coating without compromising the aluminum activity (i.e. $\text{Al/Fe} = 2.5$). Of all the vapor species generated, those containing Al and RE include AlCl , AlCl_2 , AlCl_3 and, HfCl_4 , HfCl_3 and HfCl for Hf deposition. The AlCl species is predominantly responsible for both transporting and depositing Al within the pack, and HfCl_4 for depositing Hf^[31]. Thus, in order to assess whether co-deposition of Al and Hf is possible in these packs, it is only necessary to compare the partial pressure of AlCl with that of HfCl_4 . Figures 5.1 and 5.2 shows the calculated partial pressures of AlCl and HfCl_4 as a function of temperature for co-deposition of Hf and Al. Table 5.1 also shows the calculated activities of depositing species (AlCl and HfCl_4) at deposition temperatures. Pack-1 contains no Al and this condition was used to investigate the plausibility of Hf deposition with HfCl_4 and NH_4Cl as halide activators. High partial pressure of HfCl_4 was observed from calculation suggesting that Hf can be deposited by pack cementation process. After introduction of elemental aluminum in the pack (Pack-2), high AlCl partial pressure was expected and HfCl_4 partial pressures increased slightly from pack-1 condition. For Pack-2, it can be seen that the vapor pressure of AlCl is more than one order of magnitude higher than that of HfCl_4 at 1000°C , indicating that although

Table 5.1: Pack cementation process parameters used for synthesis of Hf-modified iron aluminide coatings

No.	T (°C)	Time (hrs)	Pack Composition						Partial pressures of depositing species		Wt gain (mg/cm ²)
			NH ₄ Cl (Wt%)	RE-Cl (Wt%)	RE (Wt%)	Al (Wt%)	Al ₂ O ₃ (Wt%)	RE-O (Wt%)	P _{AlCl} (atm)	P _{HfCl₄} (atm)	
Hf1	1000	10	1	2	3	0	94	0	-	4.35x10 ⁻²	4.9
Hf2	1000	8	2	1	0	5	92	0	3.26x10 ⁻²	4x10 ⁻³	70.6
Hf3	1000	8	2	0	0	5	92	1	6.7x10 ⁻¹¹	4.4x10 ⁻³³	68.8
Hf4	800	8	3	0	1	5	90	1	8.4x10 ⁻³	3.59x10 ⁻²	74.1
Hf5	800	8	2	0	0	5	92	1	1.6x10 ⁻¹⁰	1.67x10 ⁻³³	32.6

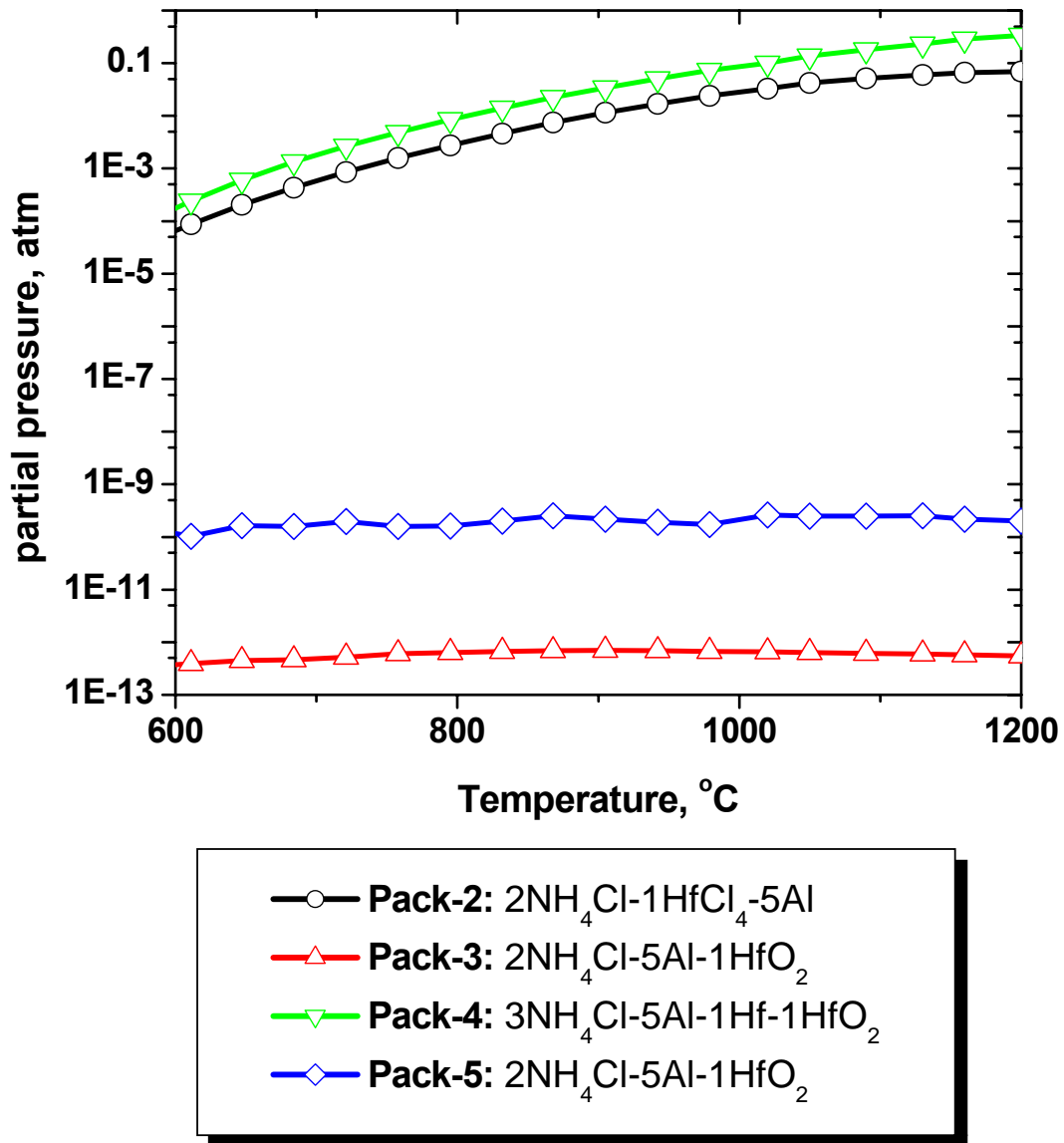


Figure 5.1: Calculated partial pressure of $\text{AlCl}(\text{g})$ for the pack compositions listed in Table 5.1. Note that pack-1 has no Al.

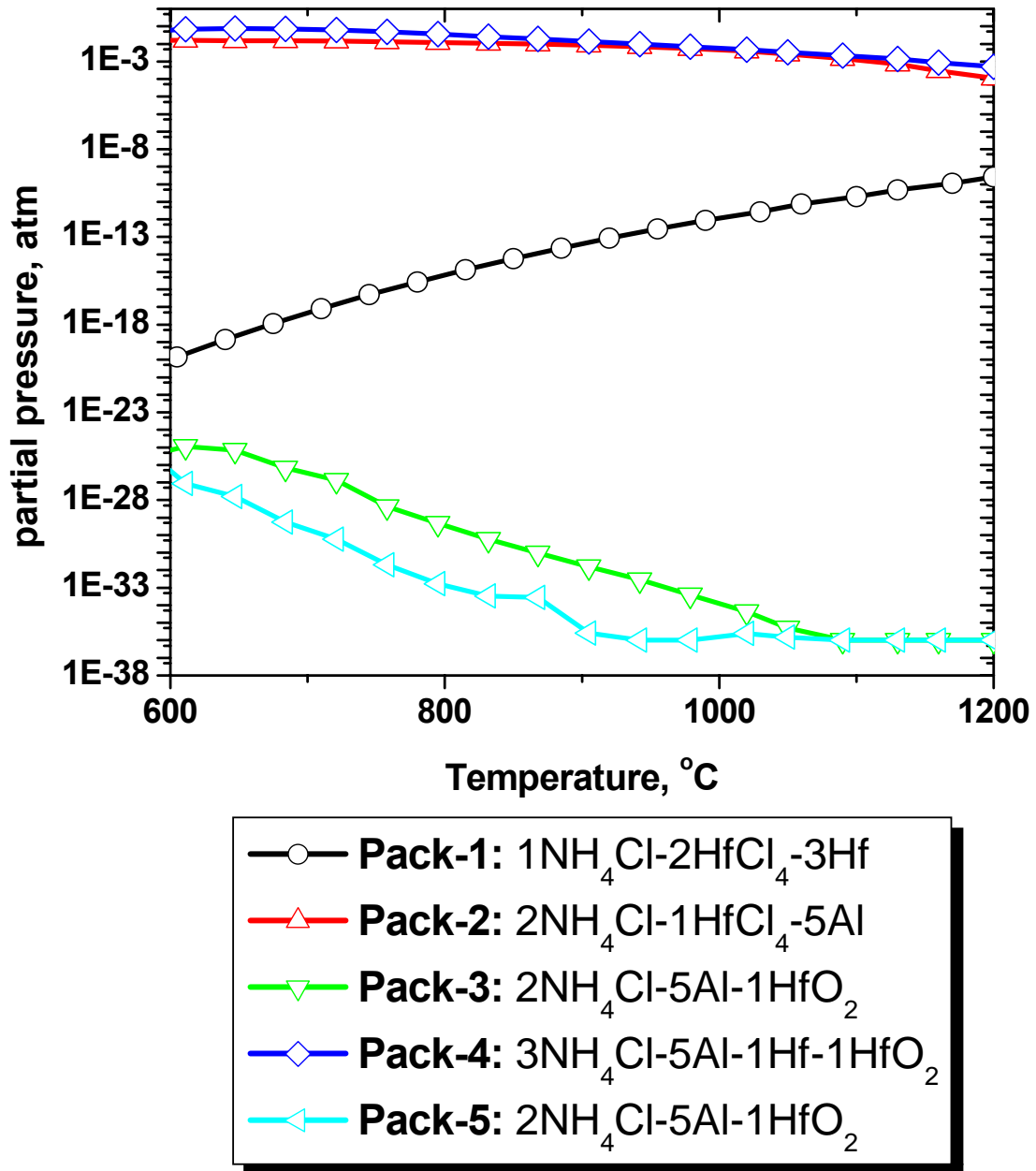


Figure 5.2: Calculated partial pressure of $\text{HfCl}_4(\text{g})$ for the pack compositions listed in Table 1.

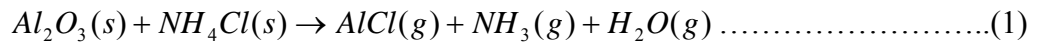
the pack has a stronger tendency of depositing Al than depositing Hf, but co-deposition may occur in these packs. For base alloy, this temperature may still cause grain growth compromising the mechanical properties of steel. Pack 3 and 5 both had only HfO₂ as a source for Hf at 1000°C and 800°C respectively. At 800°C, the partial pressure of AlCl in Pack-4 showed similar partial pressures of HfCl₄ as pack 1 and 2, but AlCl partial pressure decreased significantly. Pack 1 and 2 contained both NH₄Cl and HfCl₄ as activators, while pack 4 had only NH₄Cl as activator. This suggests that HfCl₄ does not have any effect on HfCl₄ partial pressure, but HfCl₄ acts as an additional activator for Al, thus increasing AlCl partial pressure in pack. Pack 4, which contained additional Hf showed increased partial pressure of HfCl₄. After coating deposition, pack-2 and 4 with high AlCl partial pressures showed similar mass gain primarily due to Al deposition and minor Hf deposition. Pack-1 showed lower mass gain due to absence of any elemental Al-source. Although, the reactive element concentration <0.5 at% in alloys have shown improvement in spallation resistance in oxidizing environment with thermal cycling, its behavior and optimum concentration in the sulfidizing or cyclic sulfidizing-oxidizing environments had not been investigated.

Calculations suggest that the higher partial pressure of HfCl₄ can be generated in the pack by varying the pack composition and deposit Hf at higher concentration than that required for the optimum protection. On the other hand, lower partial pressure can also be generated, which may not be sufficient to deposit any Hf. To optimize the reactive element deposition, five pack coating experiments as listed in Table 5.1 were performed and characterized using SEM/EDS and XRD. Several researchers have considered sulfur-impurities present in minor amount to be detrimental to the stability of protective scale

(see chapter-1) and have argued that reactive elements acts as “getter” for sulfur to increase the adhesion. Coating parameters depositing hafnium >1 at% and <0.5 at% were also chosen to form yttrium modified coatings and to further investigate the effect of reactive element concentration in coatings on their performance in corrosive environments. These experiments were also able to address the reactive element effects on the mechanism involving sulfur induced deterioration of protective scale adhesion.

5.1.2 Microstructure of RE modified iron aluminide coatings

Figure 5.3 shows the cross-section microstructure with respective hafnium, iron and aluminum x-ray maps for the pack-1 coating (T=1000°C, $P_{HfCl_4} = 4.35 \times 10^{-2}$ atm). It is evident that significant amount of Hf (~1.4 at%) was co-deposited with Al content of ~50 at% as shown by the x-ray line scan results in Figure 5.4. Al deposition occurs irrespective of the presence of any elemental Al in the pack, as the Al₂O₃, used as inert filler, can act as a source for Al deposition via reaction:



EDS maps in Figure 5.3 show the Hf segregation at the coating/substrate interface. This suggests that in the absence of any elemental Al, the system acted as a low Al-activity pack and the coating was formed by an inward diffusion of the depositing elements, causing the coating to grow at the coating/substrate interface. This is different from the high activity pack, which shows a coating growth by outward diffusion of substrate ions to form the coating at gas/coating interface (see Chapter 4).

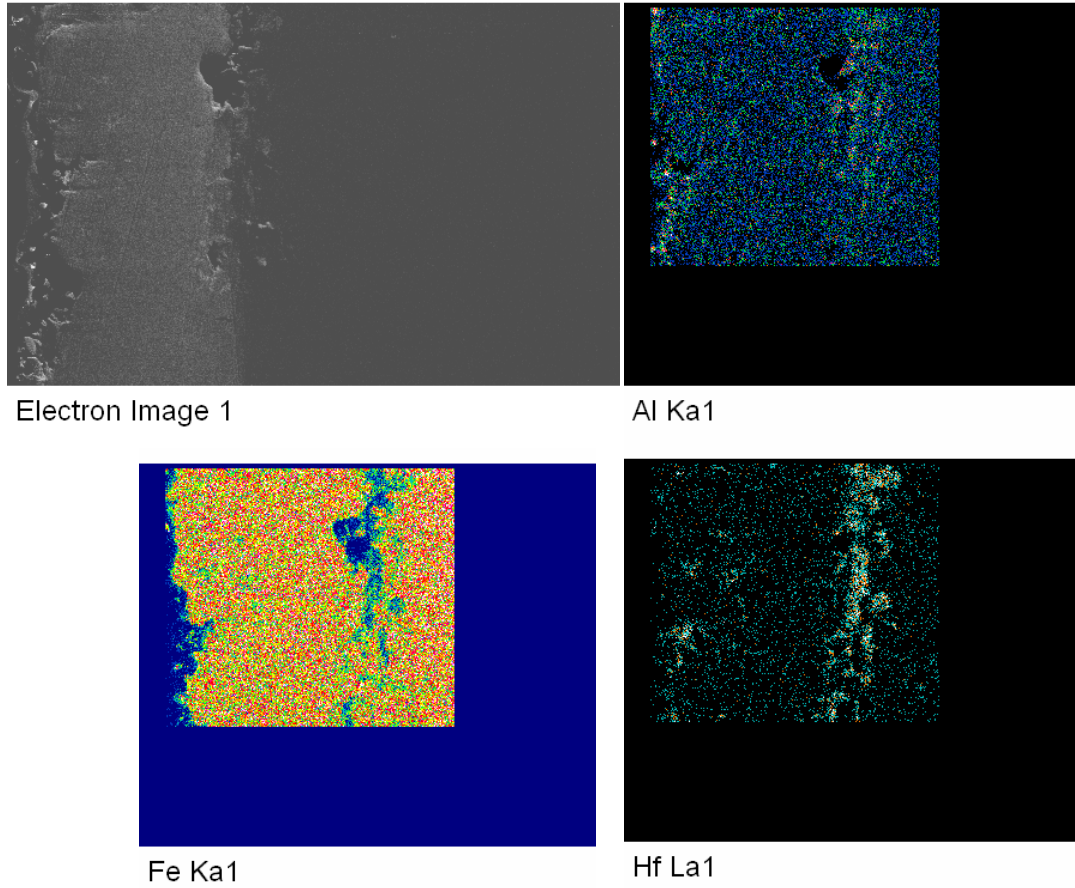


Figure 5.3: Cross-section of Hf-modified iron aluminide coating coated with pack-1 condition listed in Table 5.1 and corresponding EDS maps for aluminum, iron and hafnium

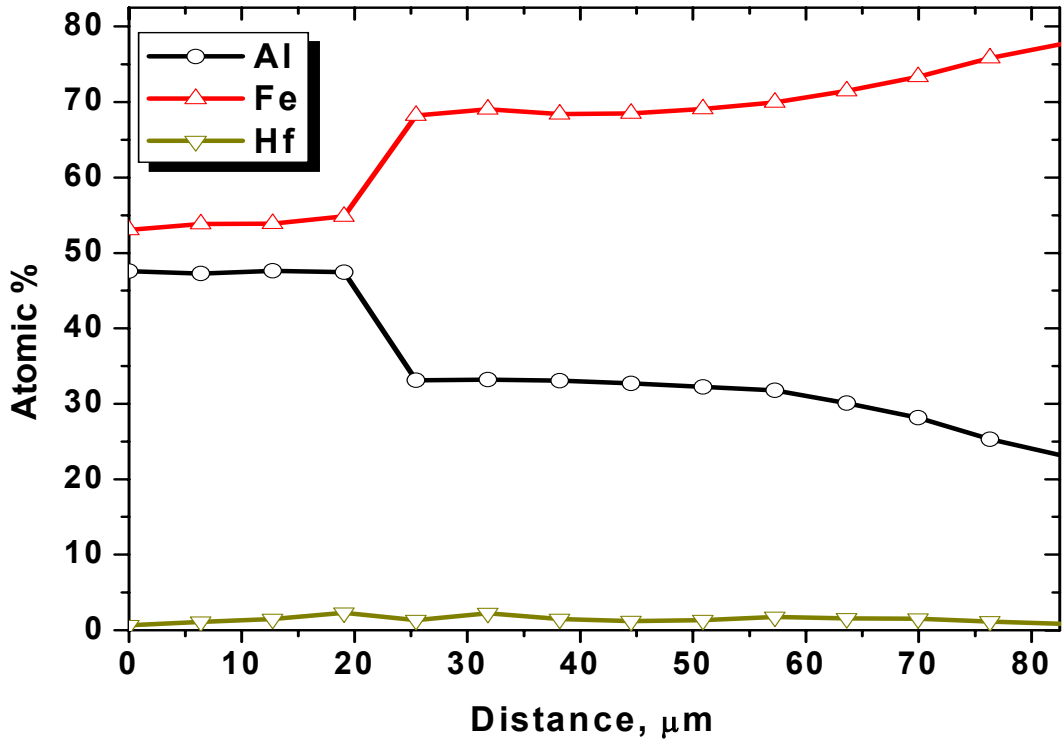
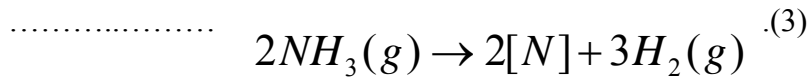
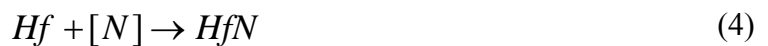


Figure 5.4: EDS line profile of Hf-modified aluminide coating for pack condition 1.

Figure 5.5 shows the XRD pattern of pack-1 coating showing formation of hafnium carbide and nitride along with the FeAl as a major aluminide phase. Carbides form due to a reaction of Hf with carbon in the substrate and also a reaction with NH_3 , which is byproduct of NH_4Cl , to form nitride as shown by the following reactions:



This provides conditions for nitridation as:



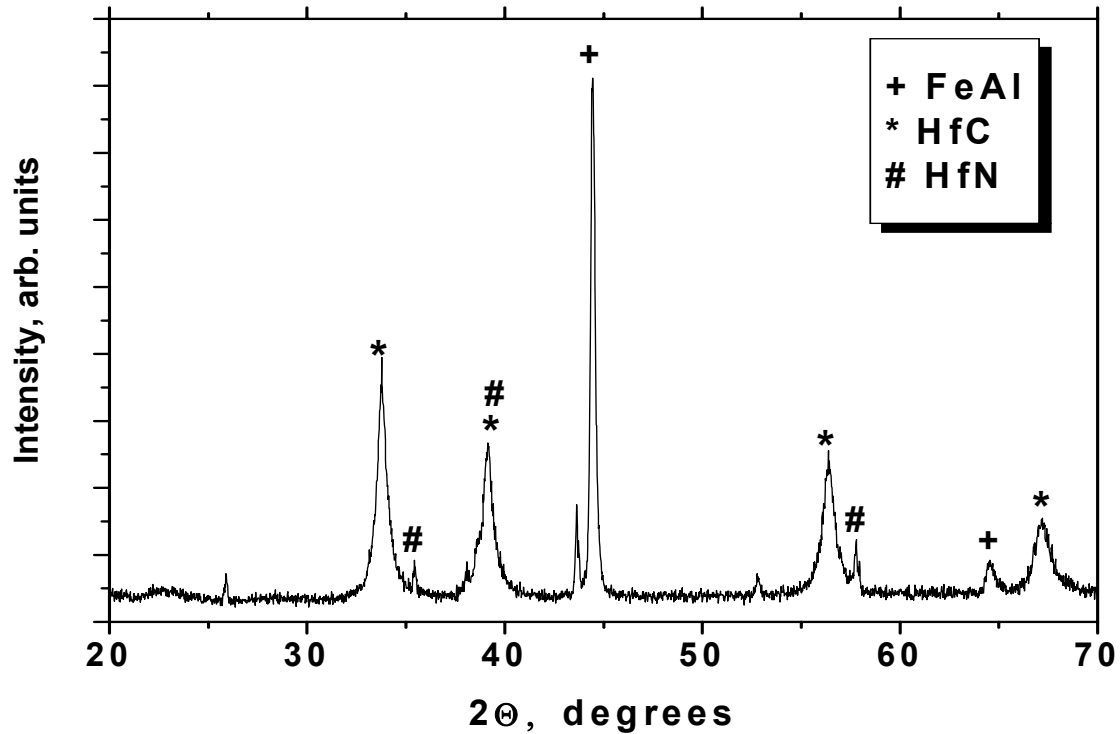


Figure 5.5: XRD pattern of Hf-modified aluminide coating for pack-1 condition

Figure 5.6 shows the cross-section of pack-2 coating ($T=1000^{\circ}\text{C}$, $P_{\text{AlCl}} = 3.26 \times 10^{-2}$ atm, $P_{\text{HfCl}_4} = 4.0 \times 10^{-3}$ atm) with X-ray maps of Hf, Fe and Al. XRD results for the sample surface are shown in Figure 5.7. These results indicate that a significant concentration of Hf was co-deposited, ~ 1.5 at% as Hf_3N_2 , HfN, along with the FeAl as a major phase in the coating. Higher nitrides of hafnium were formed due to an increase in the NH_4Cl content of pack as shown in Table 5.1. Figure 5.8 shows the surface micrograph of the pack-3 ($T=1000^{\circ}\text{C}$, $P_{\text{AlCl}} = 6.7 \times 10^{-11}$ atm, $P_{\text{HfCl}_4} = 4.4 \times 10^{-33}$ atm) coating. Composition of Pack-3 was similar to the pack-2 except for the substitution of Re-Cl (HfCl_3) with Re-O (HfO_2) XRD detected FeAl as the major phase as shown in Figure 5.9 and EDS results showed that ~ 0.4 at% Hf was incorporated in the coating. Trapped pack particles in coating surface suggests that the coating is formed by an outward diffusion of Fe ions.

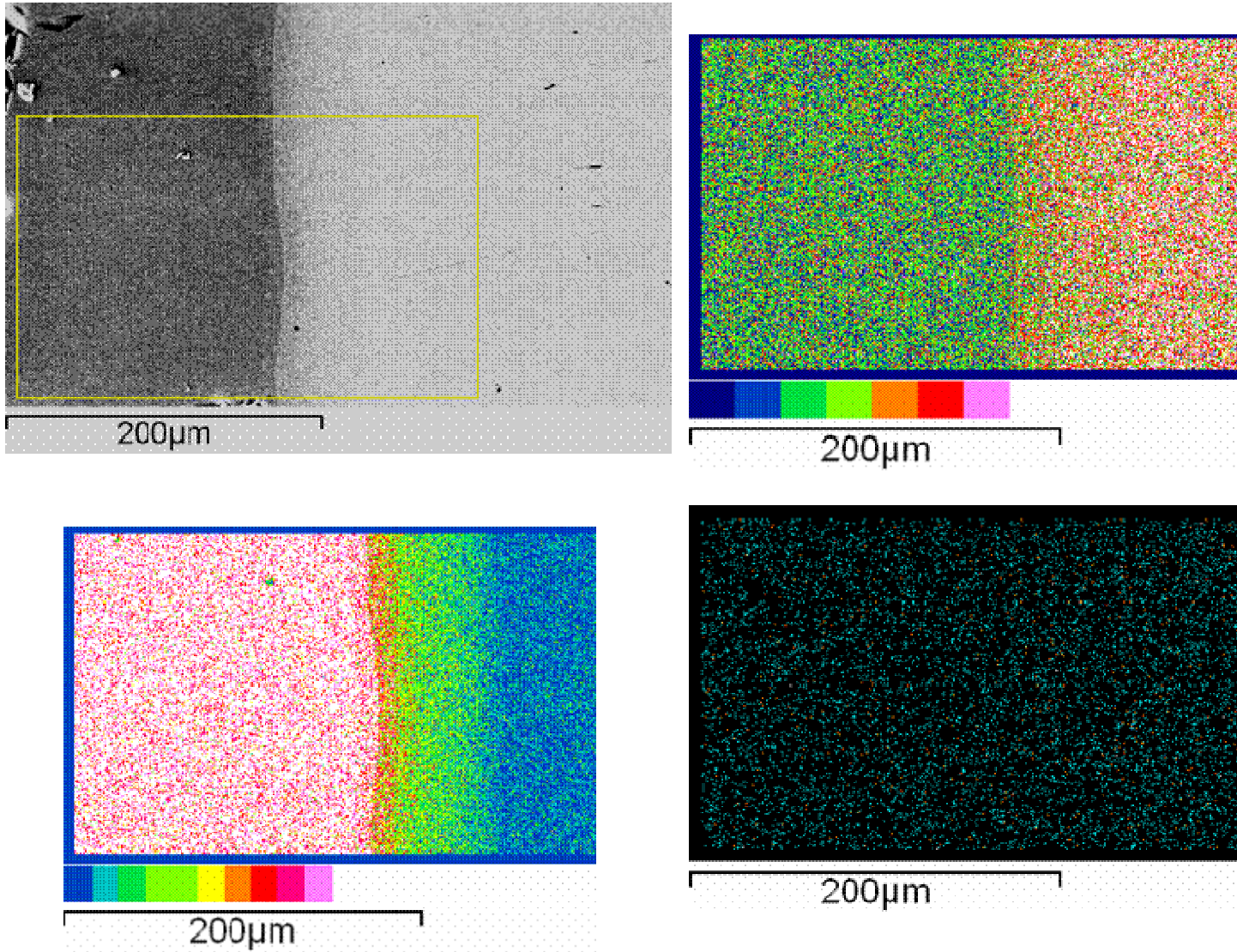


Figure 5.6: Cross-section of HfFeAl coating for pack-2 condition listed in Table 5.1.

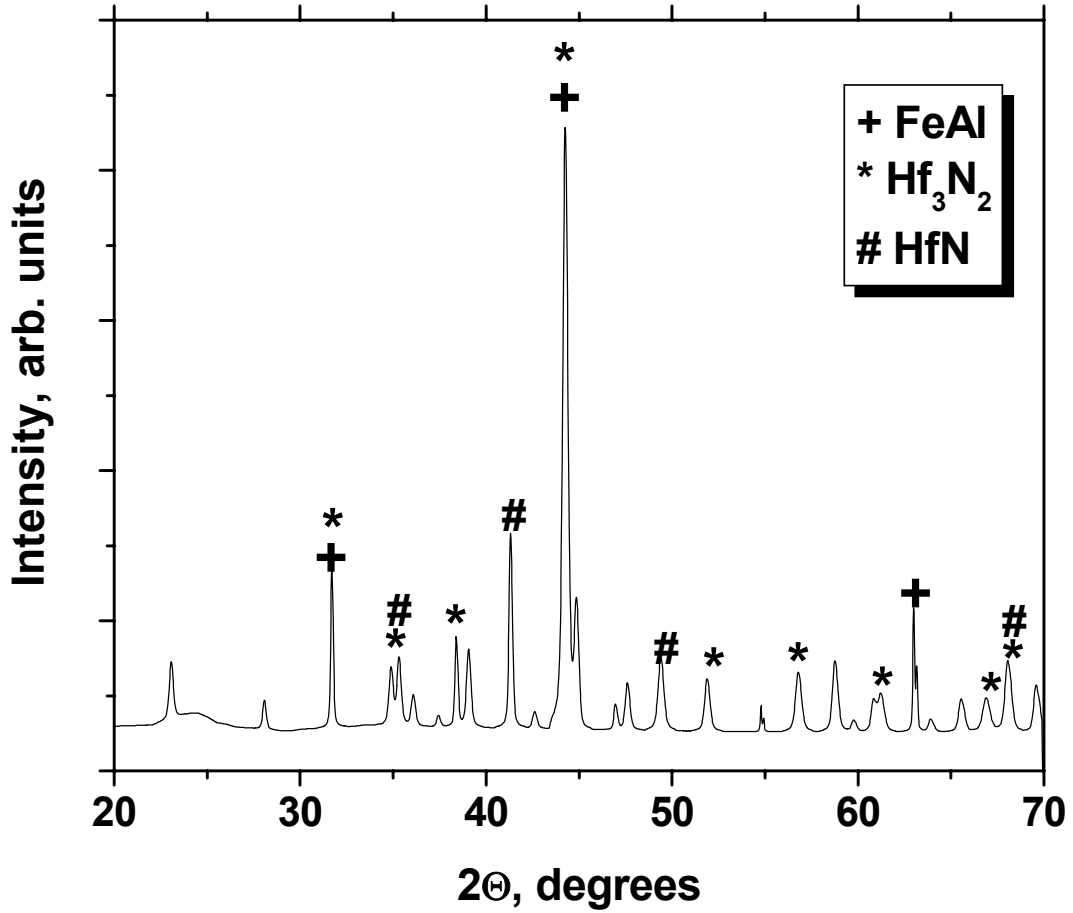


Figure 5.7: XRD pattern of HfFeAl coating prepared using pack-2 condition. FeAl, HfC and HfN peaks were observed as primary phases

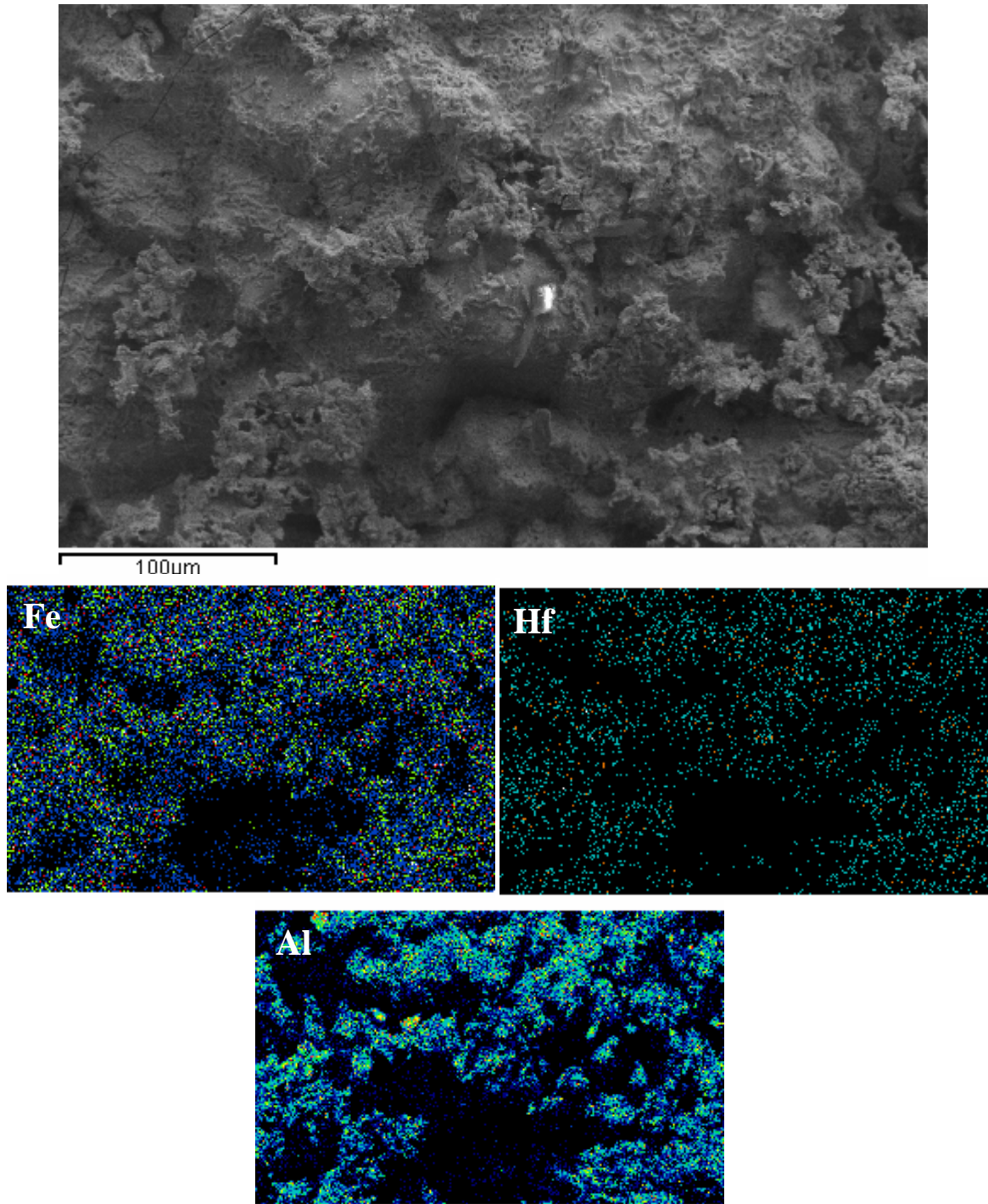


Figure 5.8: Surface micrograph of HfFeAl coating prepared using pack-3 condition listed in Table 1. Fe, Hf and Al EDS maps confirming co-deposition of Al and Hf

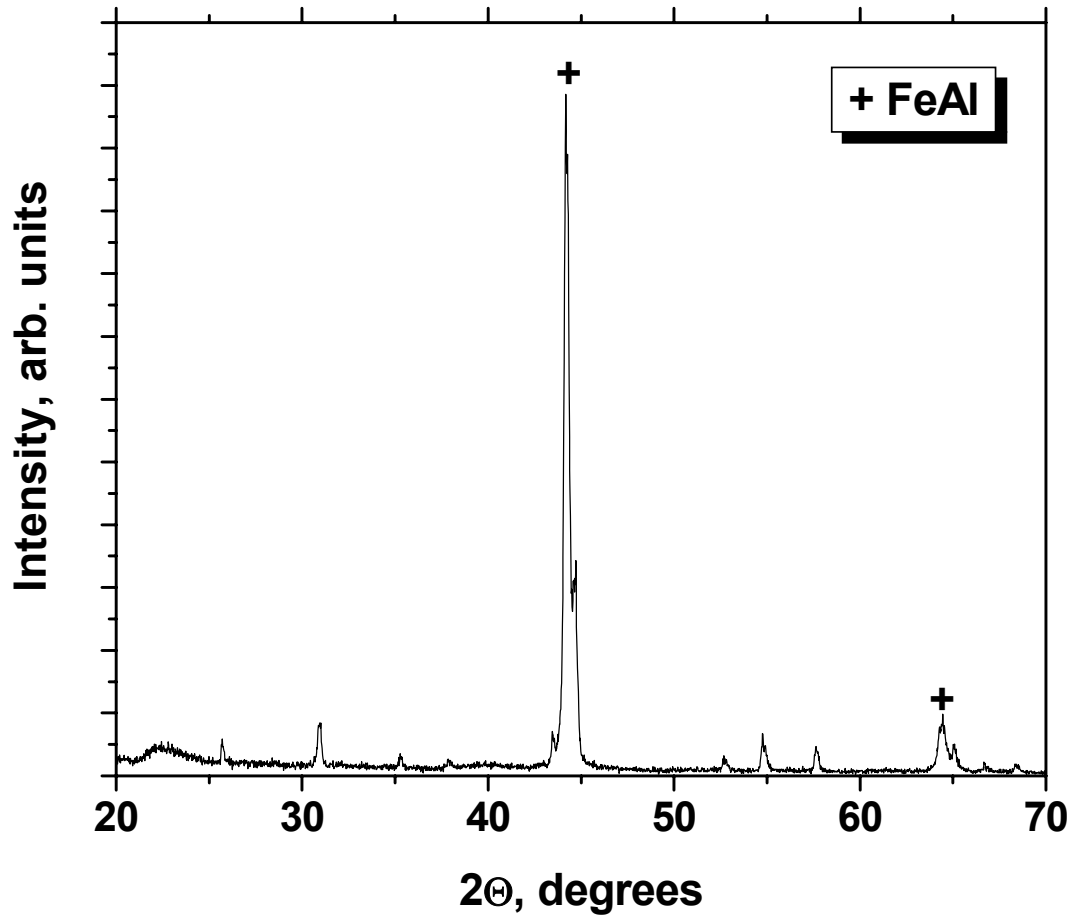


Figure 5.9: XRD pattern of HfFeAl coating prepared using pack-3 condition. Major phases detected were FeAl and HfN.

Pack-1, 2 and 3 were performed at 1000°C and all showed formation of FeAl as the major phase formed in the coating with different amounts of Hf co-deposition in the range of 0.4-1.5 at %. Although, these parameters co-deposited Hf and Al, it compromised the Al surface activity (Al/Fe=1 for FeAl) unlike coatings prepared at 800°C (Al/Fe=2.5 for Fe₂Al₅) as discussed in chapter 4. High aluminum activity at the surface is required to increase the equipment life by the aluminum in the coating serving as the reservoir for scale healing process in case of spallation. Lower Al activity at surface can reduce the equipment life significantly. To get higher surface activity of Al, further co-deposition experiments were done with pack-4 and 5 compositions at 800°C with different reactive elements sources as listed in Table 5.1.

Figure 5.10 show the surface micrograph of the coating developed in pack-4 (T=800°C, $P_{AlCl} = 8.4 \times 10^{-3}$ atm, $P_{HfCl_4} = 3.59 \times 10^{-2}$ atm). Micrograph in Figure 5.10 also indicates the areas where EDS analysis of coating and trapped pack particles was done. It is evident from Table 5.2 that the low Hf concentration in the range of 0.2-0.5 at% has been deposited along with the Fe₂Al₅ as a major phase, as shown in XRD pattern in Figure 5.11. Figure 5.12 shows the surface micrograph for the coated sample from pack-5 (T=800°C, $P_{AlCl} = 1.6 \times 10^{-10}$ atm, $P_{HfCl_4} = 1.67 \times 10^{-33}$ atm) with corresponding Fe, Al and Hf x-ray maps. Composition of pack-5 was same as that for the Pack-3 but the deposition temperature was 800°C for the Pack-5. Co-deposition of Hf was obtained but the concentration of hafnium was in the range of 0.1-0.2 at% as shown in Table 5.3 with Fe₂Al₅ as a major phase as shown in Figure 5.13.

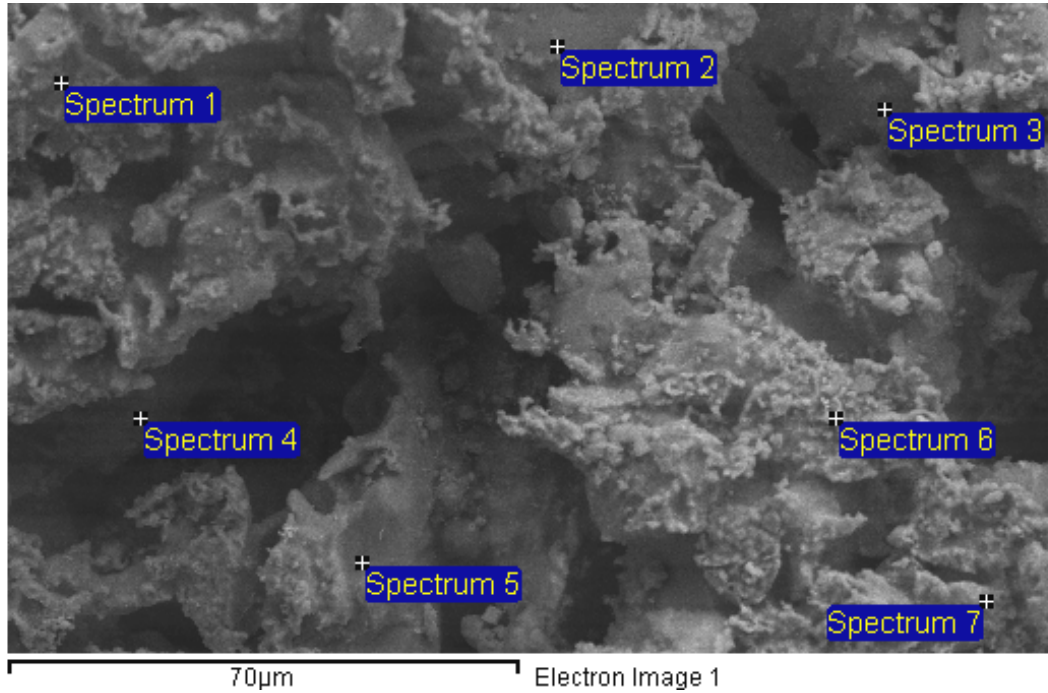


Figure 5.10: Surface micrograph of HfFeAl coating prepared using pack-4 condition listed in Table 1. Fe, Hf and Al EDS spot analysis confirming co-deposition of Al and Hf as shown in Table 2.

Table 5.2: Surface concentration of Al, Fe and Ff at spots shown in Figure 5.10.

Spectrum	Al (at%)	Fe (at%)	Hf (at%)
Spectrum 1	33.708	65.87	0.421
Spectrum 2	19.832	80.168	0.7
Spectrum 3	20.112	79.79	0.098
Spectrum 4	15.941	83.853	0.206
Spectrum 5	8.482	91.503	0.015
Spectrum 6	69.791	29.196	1.013
Spectrum 7	69.69	29.714	0.596

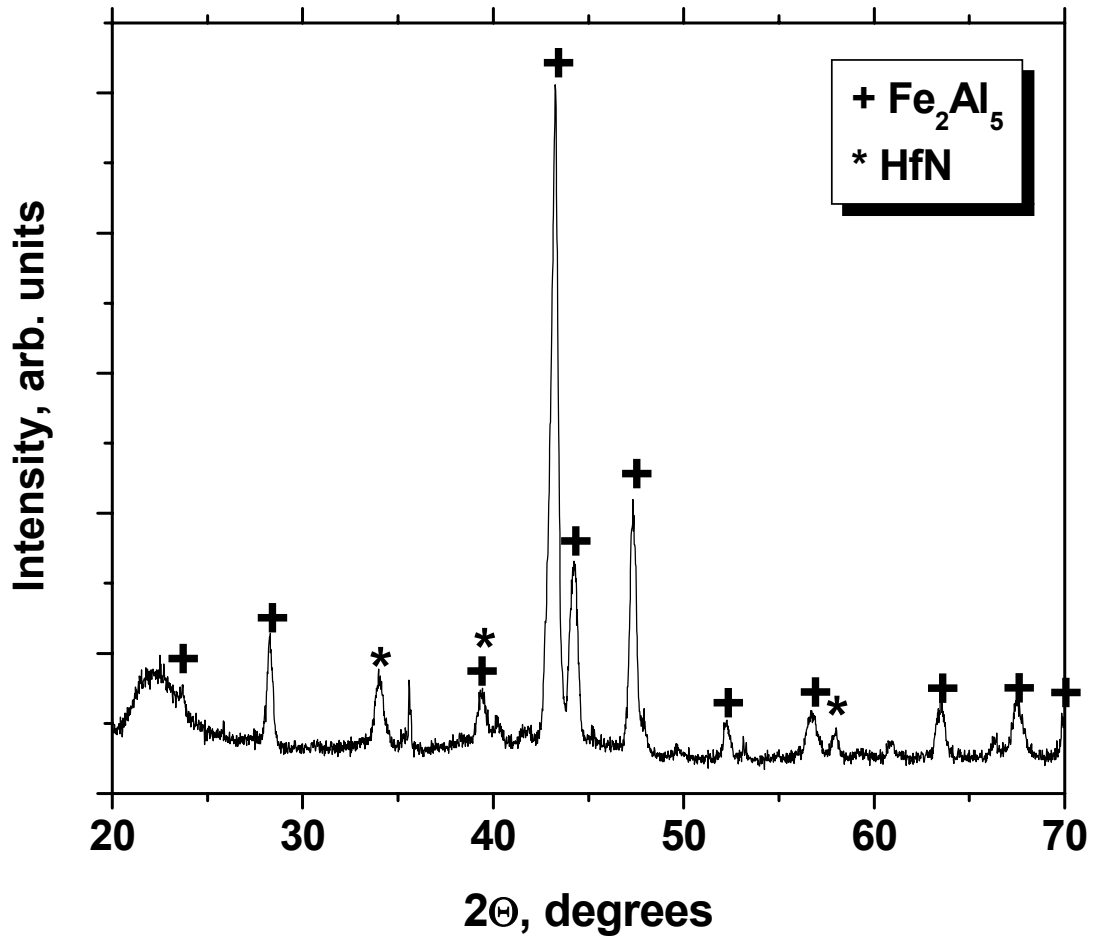


Figure 5.11: XRD pattern of HfFeAl coating prepared using pack-4 condition. Major phases detected were FeAl, and HfN.

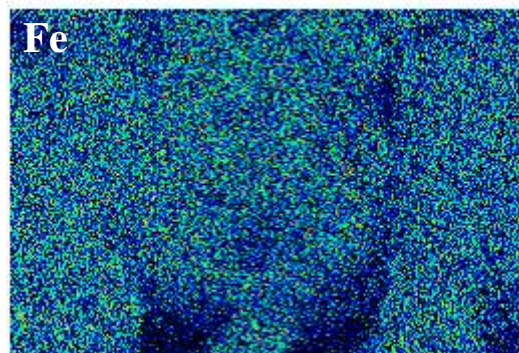
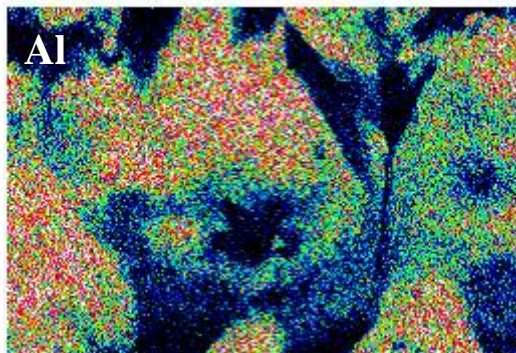
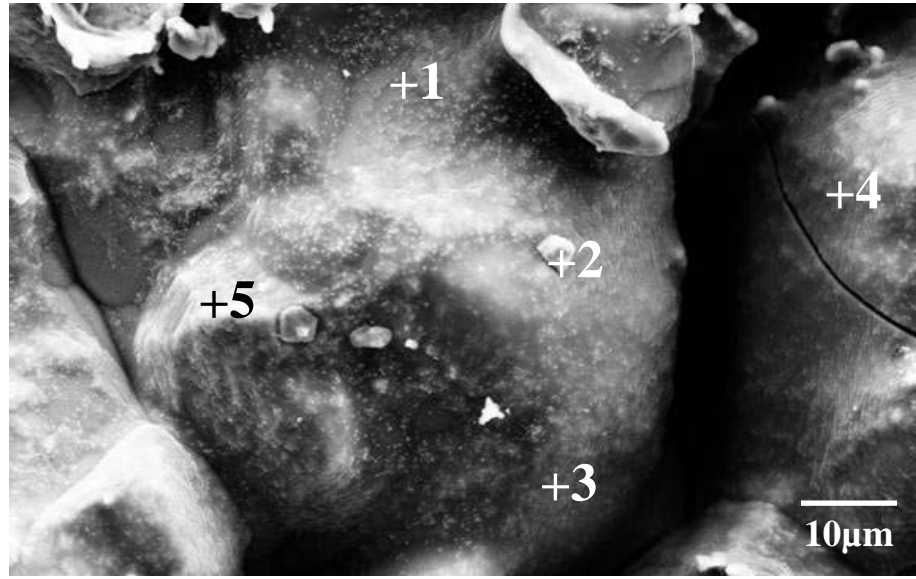


Figure 5.12: Surface micrograph of HfFeAl coating prepared using pack-5 condition listed in Table 1. Fe, Hf and Al EDS maps and spot analysis confirming co-deposition of Al and Hf as shown in Table 3.

Table 5.3: Spot EDS analysis of HfFeAl coating shown in Figure 5.12 .

Spectrum Label	Al (at%)	Fe (at%)	Hf (at%)
Spectrum 1	73.11	26.78	0.11
Spectrum 2	65.45	25.82	8.73
Spectrum 3	63.35	36.5	0.15
Spectrum 4	70.59	29.27	0.14
Spectrum 5	72.4	27.42	0.18

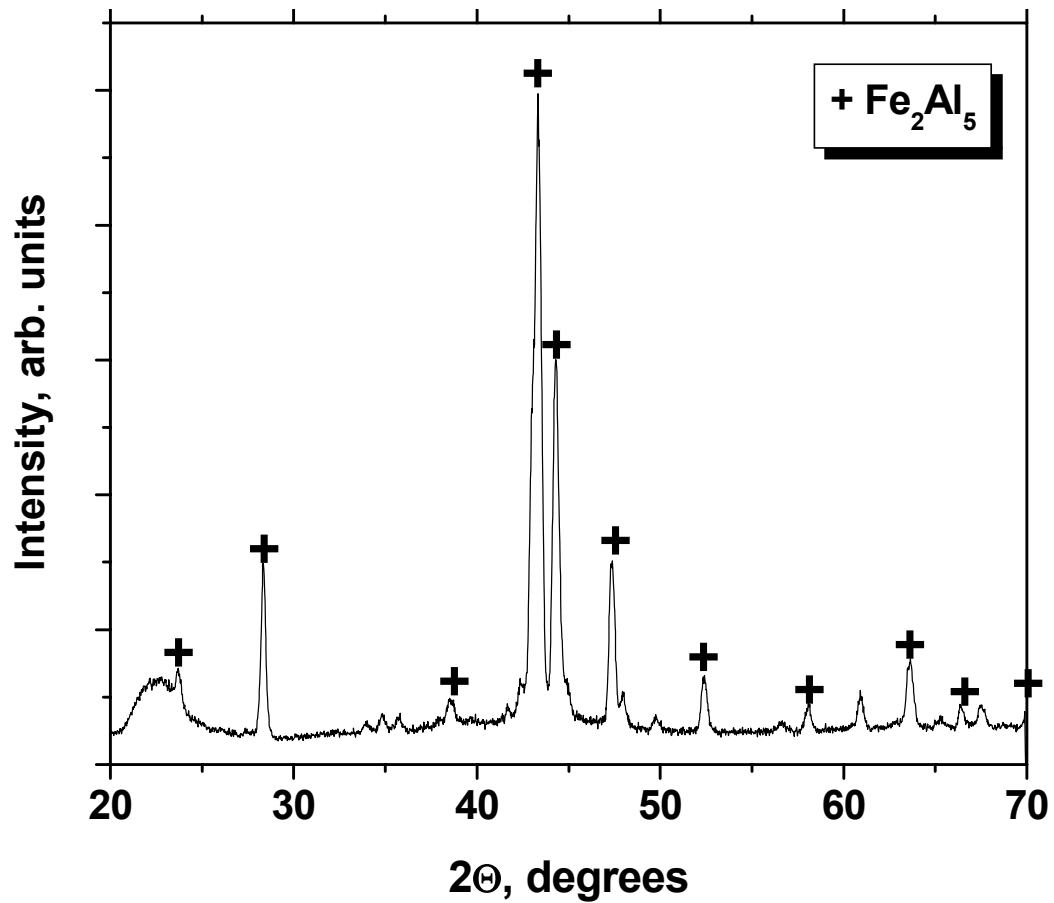


Figure 5.13: XRD pattern of HfFeAl coating prepared using pack-5 condition. Major phase detected was Fe_2Al_5 .

The results for the coating optimization experiments are summarized in Table 5.4. This suggests that:

1. At 1000°C, Hf and Al can be co-deposited with Hf in a wide range of 0.4-1.5 at% along with the FeAl as a major coating phase.
2. At 800°C, Hf concentration <0.5 at% can be deposited with Fe₂Al₅ as a major coating phase.

Thus, 800°C was found to be a preferred temperature to get higher Al activity at the surface (Al/Fe = 2.5) as compared to 1000°C (Al/Fe=1). Whereas, 1000°C is a preferred temperature to get higher reactive element concentration in the surface coating with a compromised lower Al-activity. However, both aluminide phases are alumina formers and can form a protective Al₂O₃ scale at the surface when exposed to the corrosive environments at high temperature. To study the effect of different reactive element on the scale stability, coating parameters for pack-2 and 5 were chosen to form yttrium coatings as described in following section.

Table 5.4: Summary of HfFeAl coatings prepared with respective process parameters, Hf content and phases

Sample No.	Temperature (°C)	Time (hrs)	NH ₄ Cl (Wt%)	RE-Cl (Wt%)	RE (Wt%)	Al (Wt%)	Al ₂ O ₃ (Wt%)	REO (Wt%)	At% Hf in coating	XRD Phases
Hf1	1000	10	1	2	3	0	94	0	1.41	FeAl, HfC, HfN
Hf2	1000	8	2	1	0	5	92	0	1.59	FeAl, Hf ₃ N ₂ , HfN
Hf3	1000	8	2	0	0	5	91	1	0.44	FeAl, HfN
Hf4	800	8	3	0	1	5	90	1	0.34	Fe ₂ Al ₅
Hf5	800	8	2	0	0	5	92	1	0.15	Fe ₂ Al ₅

5.2 Y-MODIFIED IRON ALUMINIDE COATING

Based on the results from Hf co-deposition work, two pack conditions were chosen to co-deposit yttrium and aluminum in the coating, as listed in Table 5.5. For yttrium containing packs, vapor species generated are YCl , YCl_2 and YCl_3 . Figure 5.14 shows the partial pressures of vapor species responsible for yttrium deposition, as calculated from HSC Chemistry, thermochemical software package, for the two yttrium containing packs listed in Table 5.5. Similar to the Hf co-deposition results, Yttrium-pack-1 showed high partial pressures of YCl_3 in the pack which contained yttrium-chloride and ammonium chlorides as activators. On the other hand, yttrium-pack-2 with only Y_2O_3 as a source of yttrium showed lower calculated partial pressures for $AlCl$ and YCl_3 . Figure 5.15 shows the surface microstructures and elemental x-ray maps for the aluminide coating formed with yttrium-pack-1. Network like fine grained coating microstructure is evident. Small precipitates were observed at the surface, as shown in Figure 5.15(b) EDS data for the surface concentration of yttrium at various areas marked in Figure 15(b) are listed in Table 5.6. This data indicates that there was no significant difference in the Y, Fe and Al composition between the grains and the precipitate-like particles in Figures 15(a) and 15(b). Similar to the Hf-modified coatings, FeAl was observed as the major coating phase for the coatings deposited at $1000^\circ C$, as is indicated by the XRD data in Figure 5.16. Figure 5.17 shows the surface of coated sample from yttrium-pack 2 along with the elemental x-ray maps for Fe, Al and Y. Corresponding surface XRD results are shown in Figure 5.18. EDS data indicated that the Yttrium composition in the coating was in the range of 0.08-0.2 at% as shown by the spot analysis data in Table 5.7. Although EDS

spot analysis shown variation in the relative ratio of Al/Fe in the coating but XRD data indicates that the major aluminide phase formed in the yttrium-pack-2 test was Fe_2Al_5 .

After 8 hours of deposition time, the surface microstructure of yttrium-modified aluminide coating using yttrium-pack-1 looked similar to the hafnium-modified coatings with pack-1. Concentration of co-deposited yttrium in this coating was between 1-2 at% whereas, concentration of yttrium in the coating from yttrium-pack-2 test was in the range of 0.08-0.2 at%. Yttrium-Pack-1 showed the formation of low activity aluminum coating (FeAl , $\text{Al/Fe} = 1$) whereas yttrium-pack-2 conditions produced Fe_2Al_5 , ($\text{Al/Fe}=2.5$), as shown by the XRD results. Columns of iron aluminide growing outwards shows that the coating formed with an outward diffusion of Fe ions similar to the mechanism discussed in Chapter 4.

Table 5.5: Pack cementation conditions chosen to form yttrium-modified iron aluminide coatings on SA210 carbon steel

Sample	T (°C)	Time (hrs)	Pack Composition						Partial pressures of depositing species		Wt gain (mg/cm ²)
			NH ₄ Cl (Wt%)	YCl ₃ (Wt%)	Y (Wt%)	Al (Wt%)	Al ₂ O ₃ (Wt%)	Y ₂ O ₃ (Wt%)	P _{AlCl} (atm)	P _{YCl₃} (atm)	
Y1	1000	8	2	1	0	5	92	0	4.85x10 ⁻²	5.81x10 ⁻⁴	77.042
Y2	800	8	2	0	0	5	92	1	1.85x10 ⁻¹⁰	3.89x10 ⁻²⁵	26.739

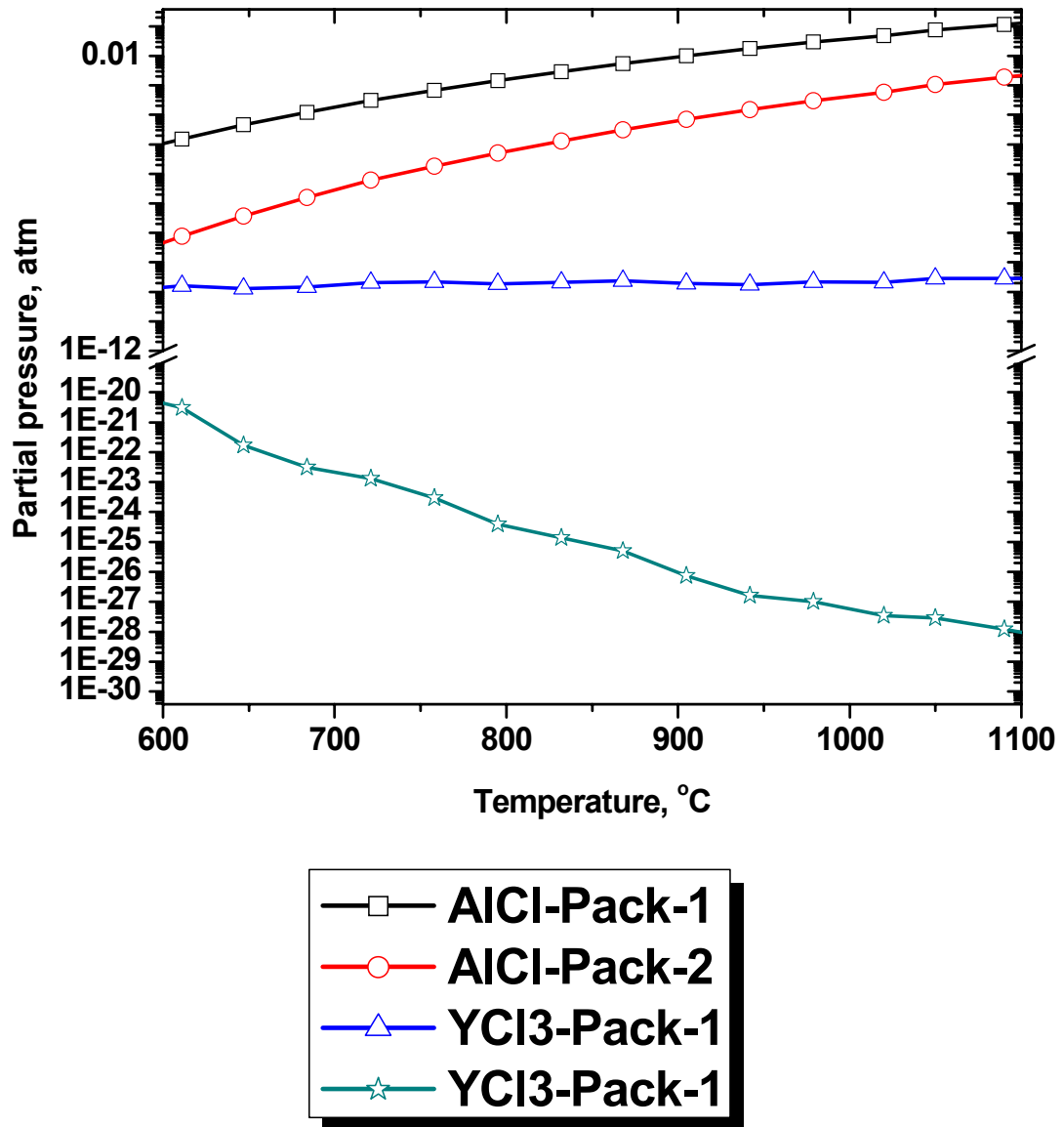


Figure 5.14: Calculated partial pressures of AlCl(g) and YCl₃(g) for the pack composition listed in Table for YFeAl coatings

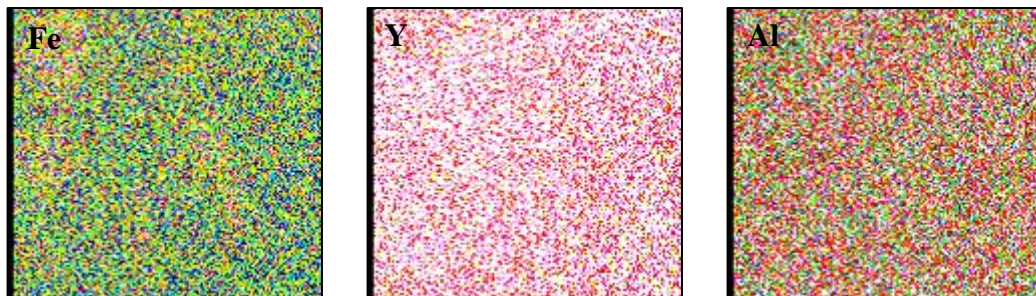
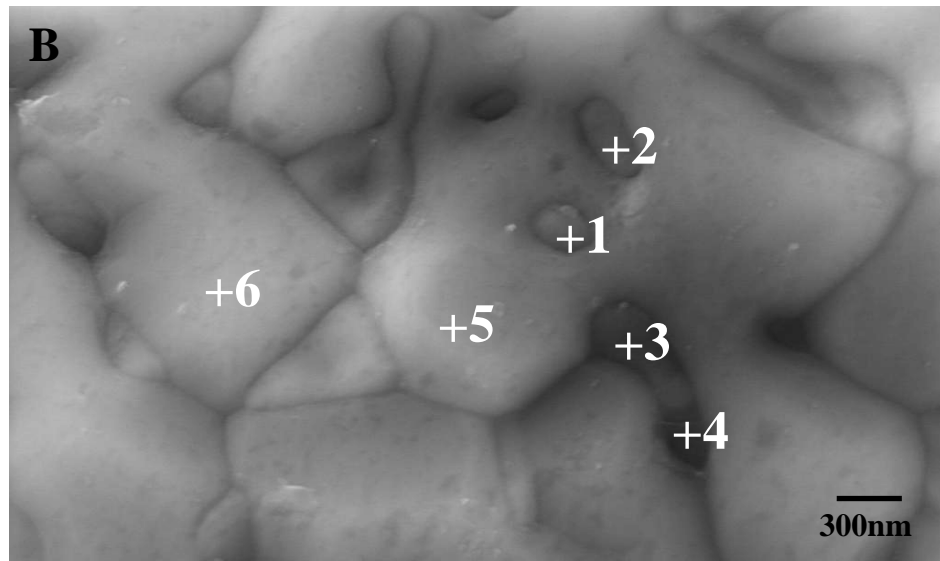
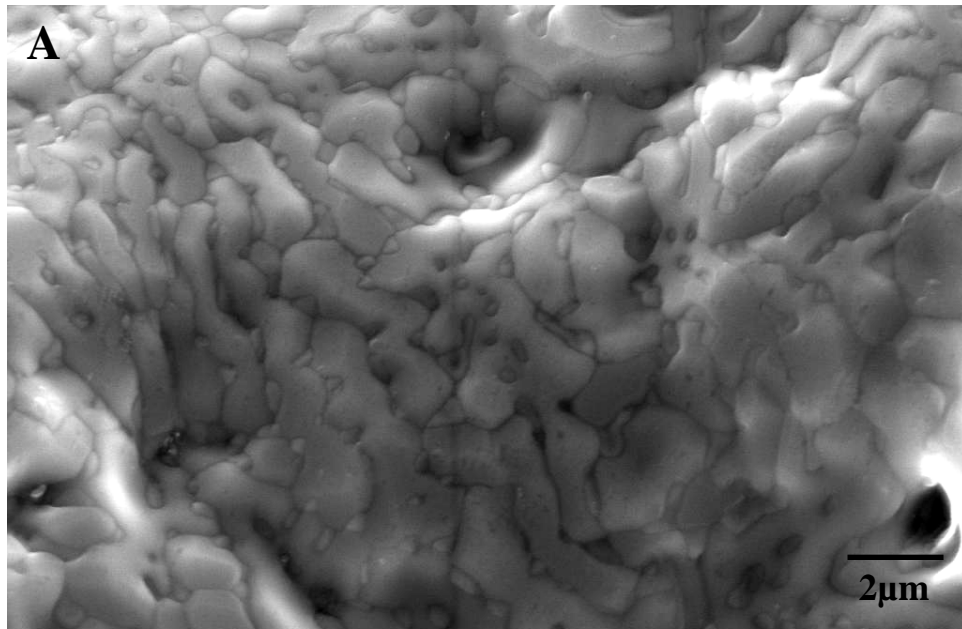


Figure 5.15: Surface SE micrograph of YFeAl coating formed by pack-1 condition listed in Table . EDS maps of Fe, Y and Al confirms co-deposition with spot analysis showing yttrium deposition in 1-2 at% range as shown in Table 5.6.

Table 5.6: Fe, Al and Y concentration in YFeAl coating shown in Figure 5.15.

Spectrum	Al	Fe	Y
Spectrum 1	57.00	41.78	1.22
Spectrum 2	56.38	42.28	1.34
Spectrum 3	60.50	38.04	1.46
Spectrum 4	57.74	41.16	1.10
Spectrum 5	56.19	42.33	1.48
Spectrum 6	46.13	52.92	1.96

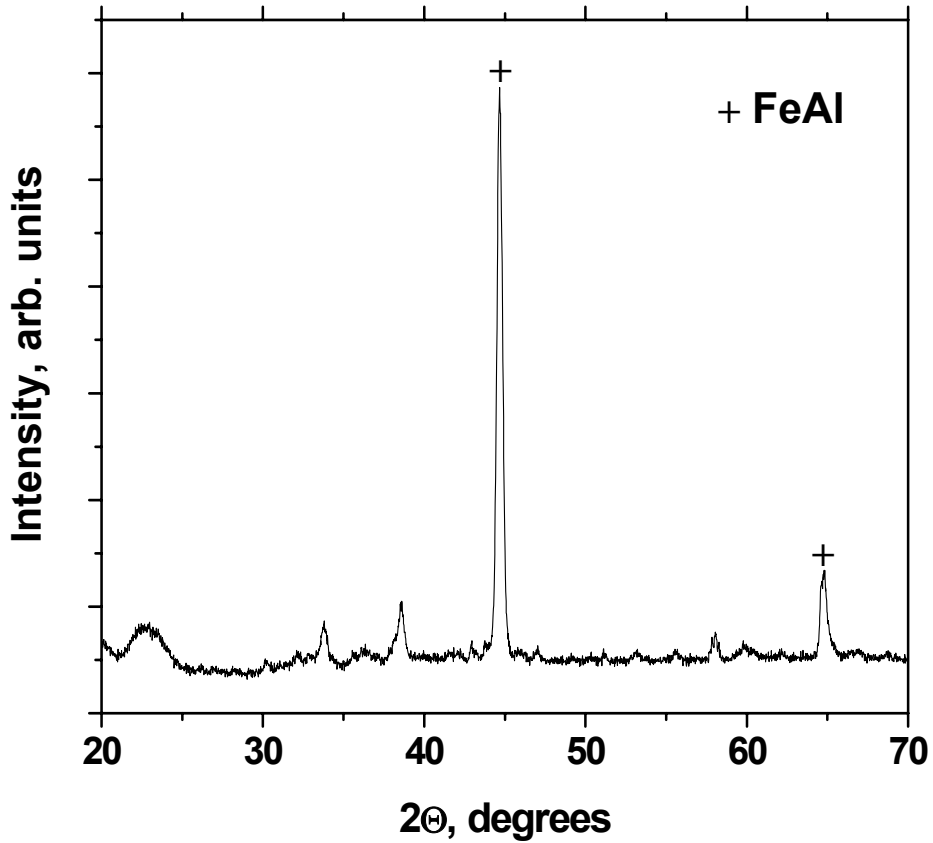


Figure 5.16: XRD pattern of YFeAl coating formed using pack condition-1 listed in Table 5.5. Major phase detected was FeAl

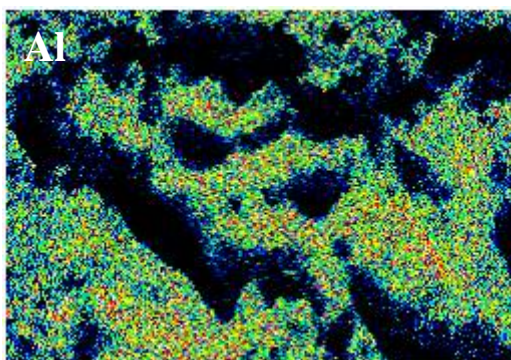
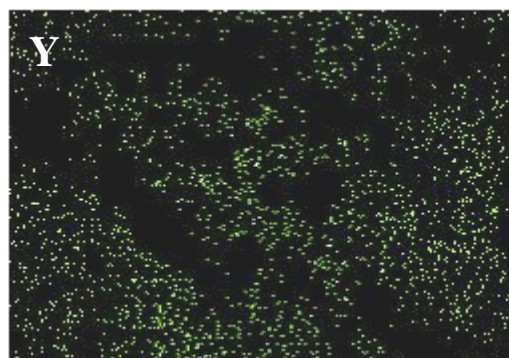
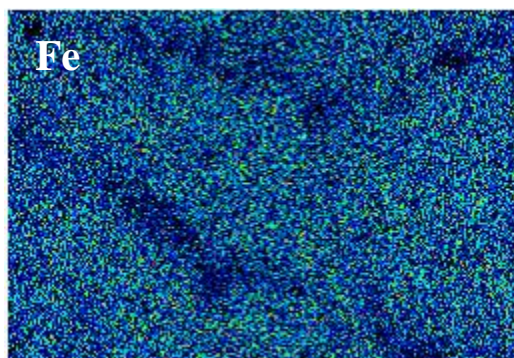
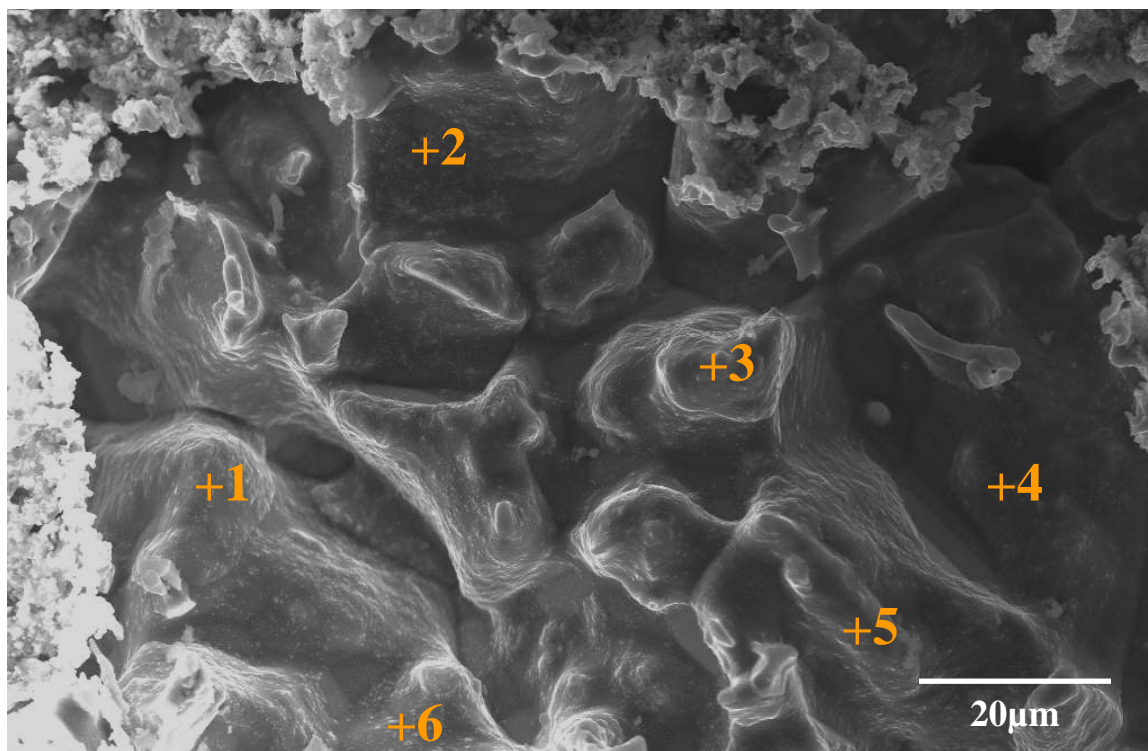


Figure 5.17: Surface SE micrograph of YFeAl coating formed by pack-2 condition listed in Table . EDS maps of Fe, Y and Al confirms co-deposition with spot analysis showing yttrium deposition in 0.08-0.2 at% range as shown in Table 5.7.

Table 5.7: Al, Fe and Y concentration in YFeAl coating prepared by pack-2 condition as shown in Figure 5.17.

Spectrum Label	Al	Fe	Y
Spectrum 1	72.07	28.01	0.08
Spectrum 2	72.99	26.87	0.14
Spectrum 3	70.86	29.26	0.12
Spectrum 4	62.66	37.39	0.06
Spectrum 5	48.91	51.14	0.05
Spectrum 6	49.61	50.23	0.16

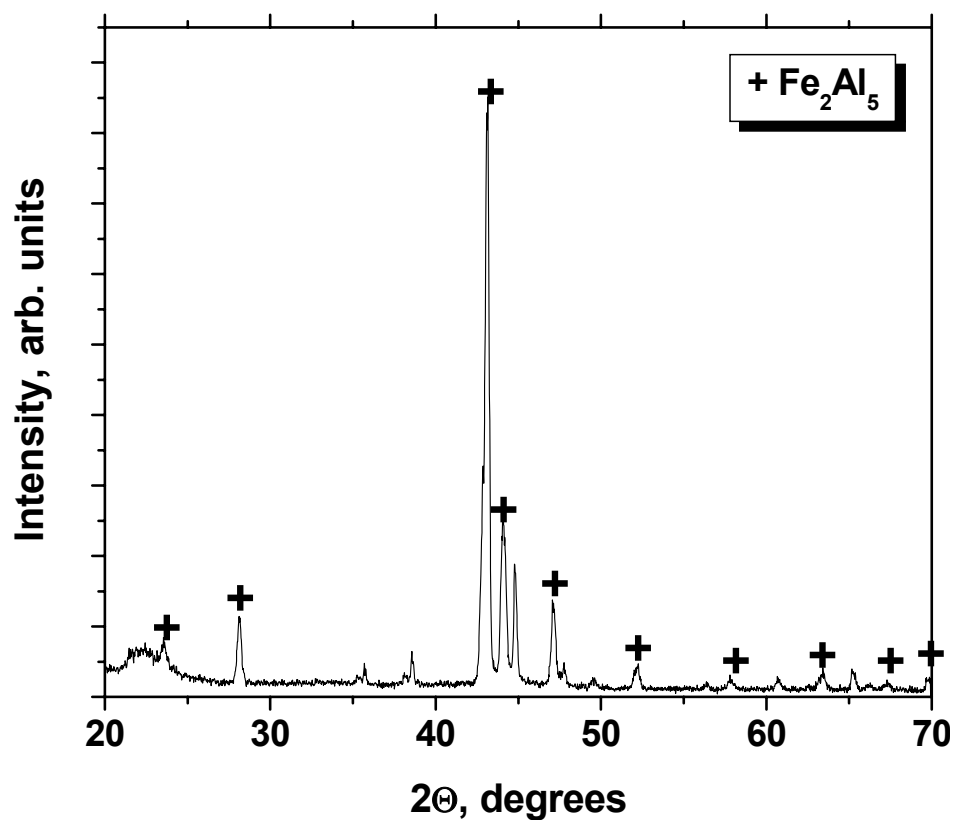


Figure 5.18: XRD pattern of YFeAl coating formed using pack condition-2 listed in Table. Major phase detected was Fe_2Al_5

5.3 OXIDATION/SULFIDATION BEHAVIOR

Four coatings were selected for further investigating the effect of reactive elements on the corrosion resistance of aluminide coatings in sulfidizing-oxidizing environments, as listed in Table 5.8. Coatings 1 and 2 had RE concentration >1 at% whereas coatings 3 and 4 had RE concentration <0.5 at%. Gaseous composition used for these tests_cycled every 12 hrs between sulfidizing ($p_{S_2} = 10^{-8}$ atm) and oxidizing ($p_{O_2} = 0.21$ atm) conditions. All RE-modified coatings were tested at 800°C. Figure 5.19 shows phase stability diagrams for the Fe-O-S, Al-O-S, Hf-O-S and Y-O-S systems at 800°C respectively. Environments used in corrosion tests are superposed on these diagrams as square dots, indicating the stable phase expected in the simulated environments. It is evident that in simulated cyclic environments, oxides are thermodynamically stable in oxidizing environment and the sulfides in the sulfidizing environment. Thus, if the partial pressures of sulfur and oxygen changes as a consequence of environmental cycling, corresponding conversion of oxides to sulfides and vice-versa will occur in corrosion scale, similar to the results for the carbon steel at 300°C discussed in chapter 3.

Table 5.8: RE modified coatings chosen for corrosion kinetics study

Sample No.	Coating type	Aluminide	At % RE in coating
Y1	Yttrium	FeAl	1.5
Hf1	Hafnium	FeAl	1.5
Y2	Yttrium	Fe ₂ Al ₅	0.3
Hf2	Hafnium	Fe ₂ Al ₅	0.4

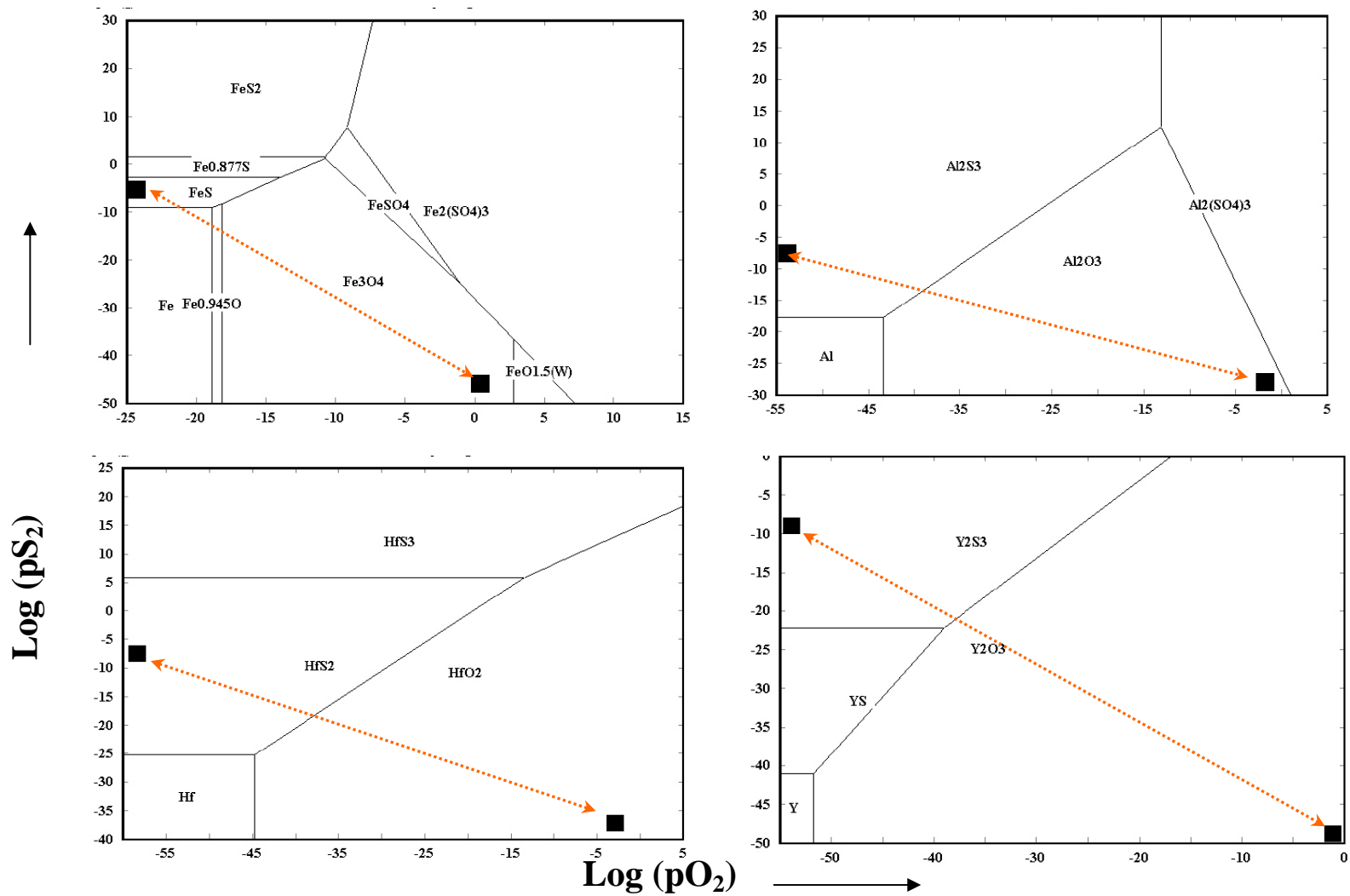


Figure 5.19: Fe-O-S, Al-O-S, Hf-O-S and Y-O-S stability diagram at 800°C . Square symbols show the simulated laboratory environments.

5.3.1 Corrosion Behavior of Unmodified Fe-Al Coatings

Figure 5.20 shows the corrosion behavior of unmodified Fe-Al coatings in fluctuating, oxidizing ($p_{O_2} = 0.21 \text{ atm}$)-sulfidizing ($p_{S_2} = 10^{-8} \text{ atm}$), environments at 800°C . It is evident from these results that the cyclic gaseous environment has a significant effect on the corrosion resistance of unmodified coatings with total mass gain of $\sim 4 \text{ mg/cm}^2$ in 100 hours exposure compared to the gain of $< 2 \text{ mg/cm}^2$ in the static sulfidizing environment. Slope of the mass change curves during different gas cycle indicates that the sample had lower corrosion rates during the oxidizing cycles, whereas sulfidizing cycle showed higher corrosion rates. Parabolic rate constants for the individual gaseous cycle, calculated from this data, are listed in Table 5.9. On changing the environment to oxidizing from sulfidizing, spallation on the order of 0.5 mg/cm^2 was observed, as shown in Figure 5.21, resulting in an increase in the oxidation/sulfidation rate with cycling. This suggests that although protective Al_2O_3 scale forms at the surface, some scale spallation can destabilize the scale, compromising its protective nature during long exposures to cyclic environments. Reactive elements are known to improve the spallation resistance of Al_2O_3 scales in oxidizing environments with thermal cycling. The primary goal of this task was to evaluate if the reactive elements are also beneficial under cyclic gaseous conditions.

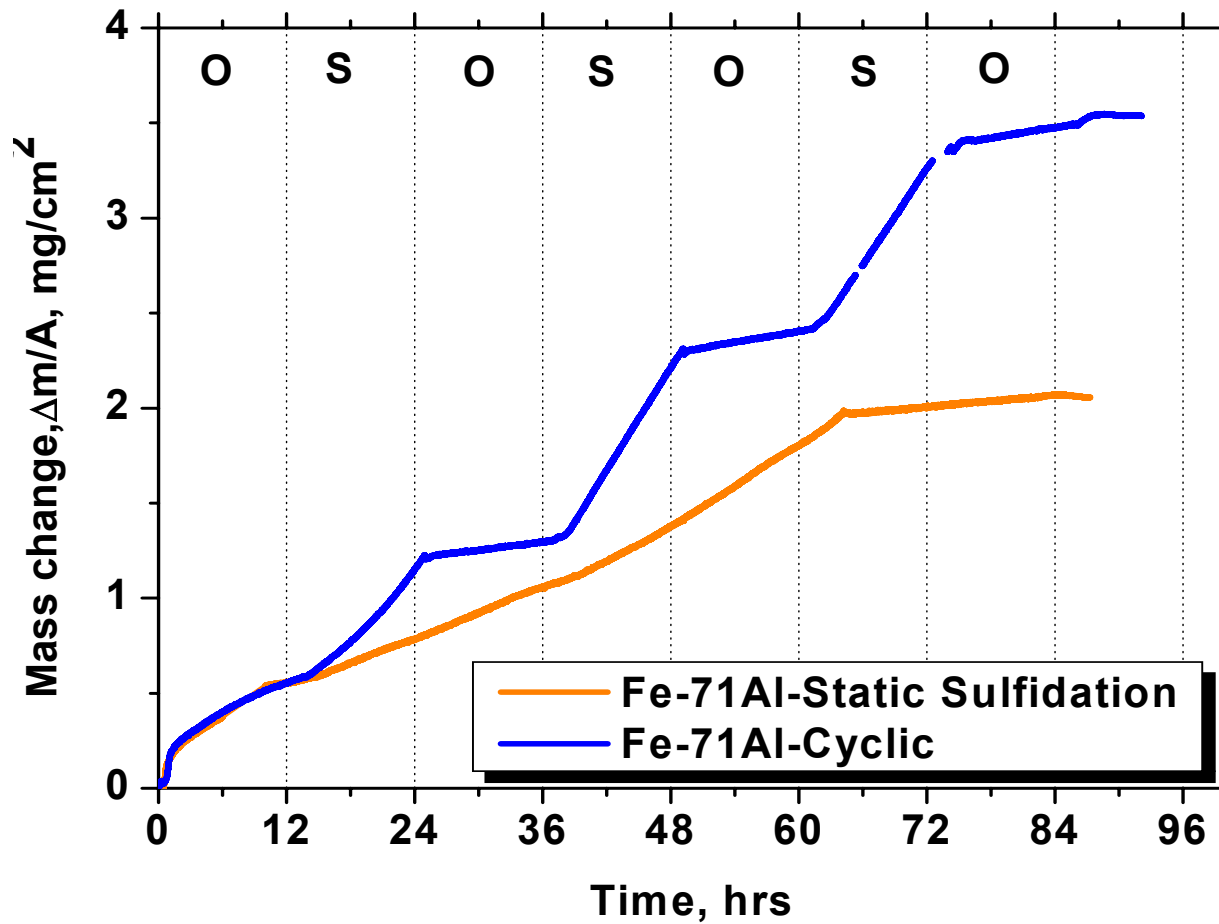


Figure 5.20: Corrosion kinetics of unmodified coatings in cycling sulfidizing –oxidizing environments:
(O) $pO_2 = 0.21$ atm, (S) $pS_2 = 10^{-8}$ atm

Fe-Al coating behavior in static sulfidizing environment has been shown to compare the effects of cyclic environments.

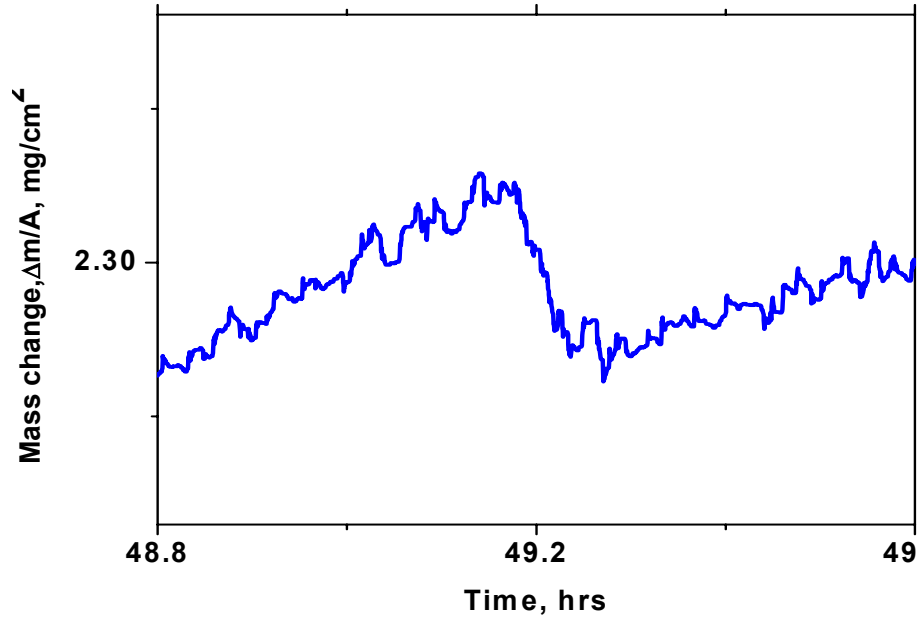


Figure 5.21: Spallation observed environmental cycling from sulfidizing-to oxidizing as shown in Figure 20.

Table 5.9: Parabolic corrosion rates for each cycle as shown in Figure 5,20 for modified coating as compared to unmodified coatings in cyclic gaseous environments:
(O) $p\text{O}_2=0.21$ atm, (S) $p\text{S}_2 = 10^{-8}$ atm

Environment	Fe-Al ($\text{mg}^2/\text{cm}^4 \cdot \text{hr}$) $\times 10^{-3}$
O	25.45
S	104.17
O	18.99
S	309.04
O	45.73
S	466.9
O	63.7

5.3.2 Corrosion performance of aluminide coatings with >1 at% RE addition

Figure 5.22 shows corrosion kinetics curves for a FeAlY coating and a unmodified Fe-Al coating under similar cyclic environmental conditions at 800°C. It is evident from these results that the yttrium doped aluminide coating (total mass gain $\sim 8 \text{ mg/cm}^2$) had lower corrosion resistance than the un-doped aluminide coating (total mass gain $\sim 3.5 \text{ mg/cm}^2$). Figures 5.23 (a)-(f) show magnified view of the kinetics curve to indicate various changes in the corrosion kinetics on changing the gas composition from oxidizing to sulfidizing, Figures (a)-(c), and from sulfidizing to oxidizing, Figures (d)-(f). Data in Table 5.10 is for the corresponding parabolic rate constants calculated from this data. Sharp mass loss of $\sim 0.4 \text{ mg/cm}^2$ was detected at the beginning of first O-to-S cycle (Figure (a)) suggesting that the scale spallation occurred during this change. For the subsequent O-to-S cycling, no spallation was observed, but the corrosion rate increased sharply, as is evident from Figures (b) and (c), and the sulfidation rate increased significantly as shown by data in Table 5.10.

Figures 5.23 (d)-(f) show the kinetic changes when the gaseous environment was changed from sulfidizing to oxidizing. On every cycle, a slight mass gain was observed at the beginning of cycle followed by a slight mass loss before reaching a steady state as shown in Figures (d)-(f).

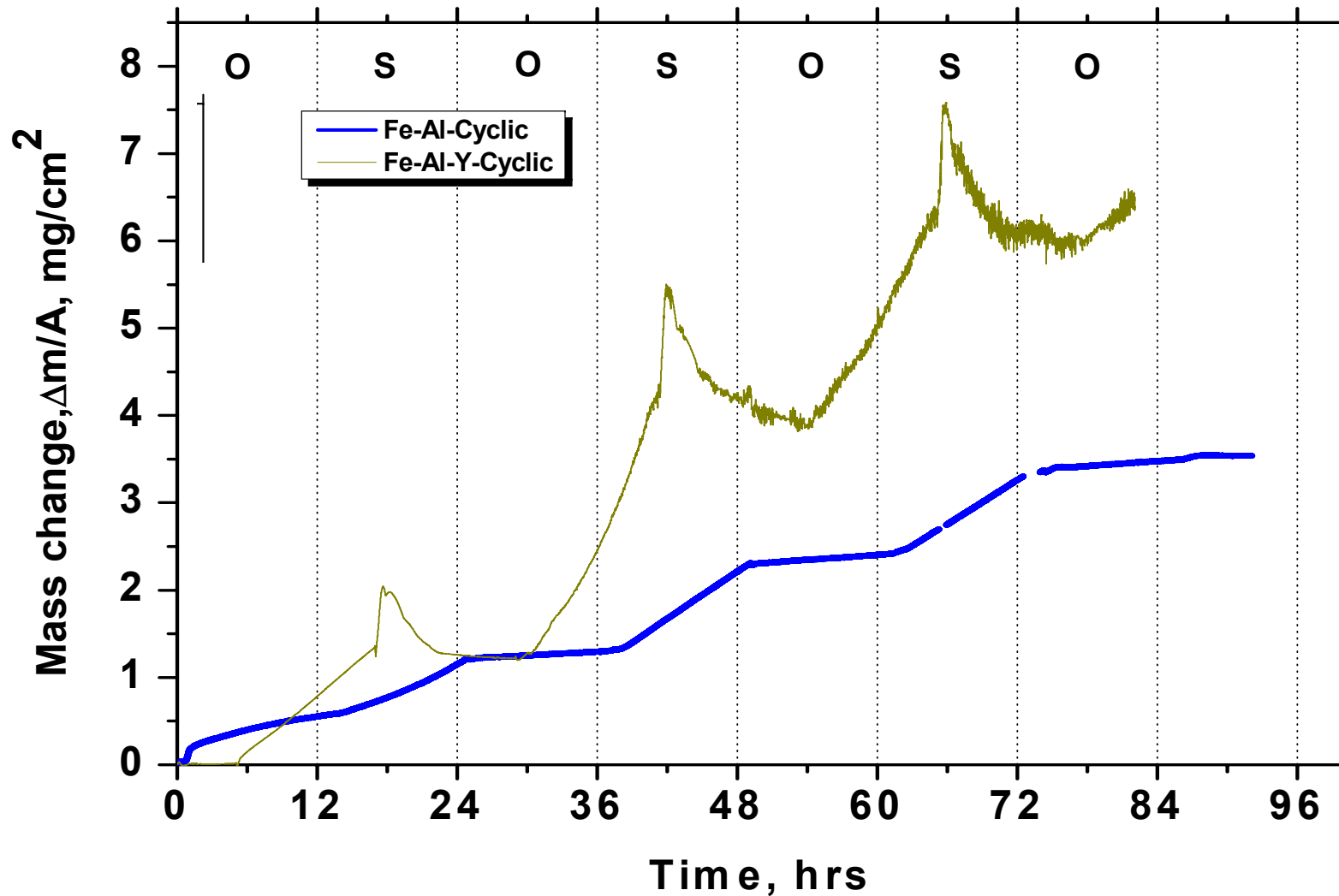


Figure 5.22: Corrosion kinetics of YFeAl coatings as compared to unmodified-Fe-Al coatings in cycling sulfidizing – oxidizing environments: (O) $p\text{O}_2 = 0.21$ atm, (S) $p\text{S}_2 = 10^{-8}$ atm

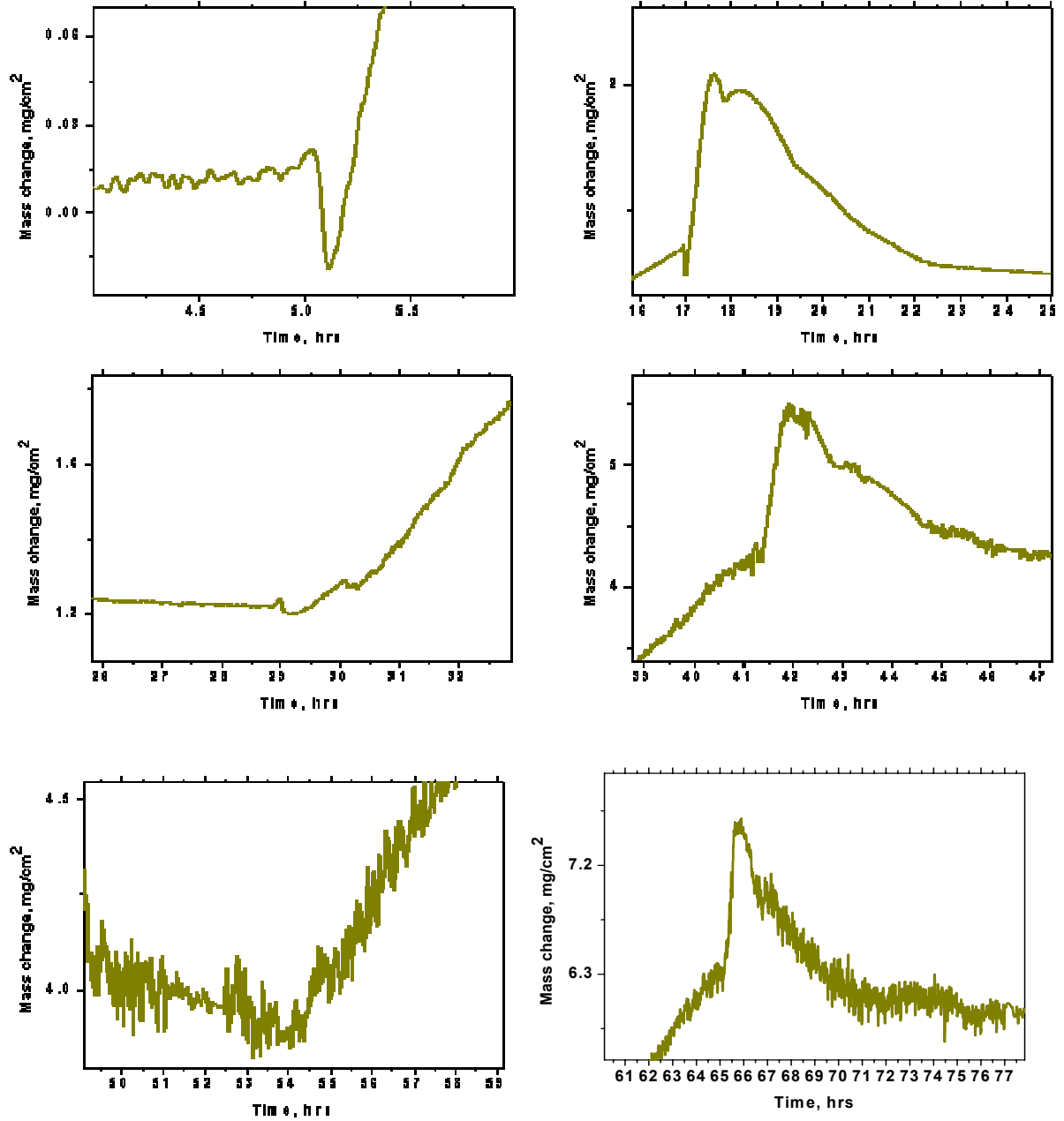


Figure 5.23: Kinetics of YFeAl coating in cyclic environments from (a)-(c) oxidizing-to-sulfidizing, (d)-(f) sulfidizing-to-oxidizing

The overall process can be described in three stages as the pO_2 increases and the pS_2 decreases:

- A mixed sulfidizing-oxidizing non-equilibrium environment exists intermittently with both oxygen and sulfur present as reacting species showing an initial mass gain.
- As the residual sulfur is consumed, mass loss is observed due to the conversion of sulfides formed during previous sulfidation to oxide.
- Once, the conversion reaction is completed at the surface, a steady state oxidation starts with the formation of protective scale and the kinetics is further governed by the diffusion of oxygen through the scale.

Parabolic rate constants for each sulfidizing and oxidizing cycle for the two RE-containing aluminide coatings are shown in Table 5.10. These values were calculated from the part of curves showing a steady state reaction.

Table 5.10: Parabolic corrosion rates for each cycle as shown in Figure 5.22 for yttrium-modified coating as compared to unmodified coatings in cyclic gaseous environments: (O) $pO_2=0.21$ atm, (S) $pS_2 = 10^{-8}$ atm

Environment	Fe-Al ($mg^2/cm^4.hr$) $\times 10^{-3}$	Y-Fe-Al ($mg^2/cm^4.hr$) $\times 10^{-3}$
O	25.45	-
S	104.17	171.02
O	18.99	-28.18
S	309.04	1083.5
O	45.73	-499.4
S	466.9	2313.37
O	63.7	-2176.48
S	-	-

Some kinetic features of modified coatings in cyclic environments are following:

- Corrosion rate increases for the subsequent sulfidation exposures suggesting a lower resistance of these coatings in sulfidizing environments compared to the oxidizing environments.
- Rates for oxidation become negative showing continuous mass loss. This is due to a combination of oxidation and conversion reaction. As oxidation rates are slower, the kinetics prominently shows the mass loss due to sulfide-to-oxide conversion and outward diffusion of sulfur back into the atmosphere. As the scale thickens, more sulfide is present in the scale, thus showing larger negative rates.

Results indicate that the oxidation reaction is much slower than the sulfidation reaction as the sulfur diffusion during sulfidation is much faster than the oxygen diffusion during oxidation. Figure 5.24 shows the surface of corrosion scale formed on 1.5% yttrium-containing aluminide coating along with the XRD pattern. Iron sulfide and iron oxide was detected on the surface along with Al_2O_3 . Figure 5.25 shows a cross-section of Y-modified coating along with EDS elemental maps showing the presence of S and Fe in the corrosion scale along with Al, O and Y. EDS spot analysis along the corrosion scale thickness is shown in Table 5.11. It is evident from the spot analysis data that the scale surface (gas/scale interface) was very rich in Yttrium with the concentration decreasing towards the scale/metal interface. Fe, Al, O and S segregation near the surface shows an outward diffusion of Fe^{+3} and Al^{+3} during the exposure. This observation is contrary to the conventional view of the effect of reactive elements on scale growth in oxidizing environments as the reactive elements were shown to provide resistance to the outward diffusion of metal cations.

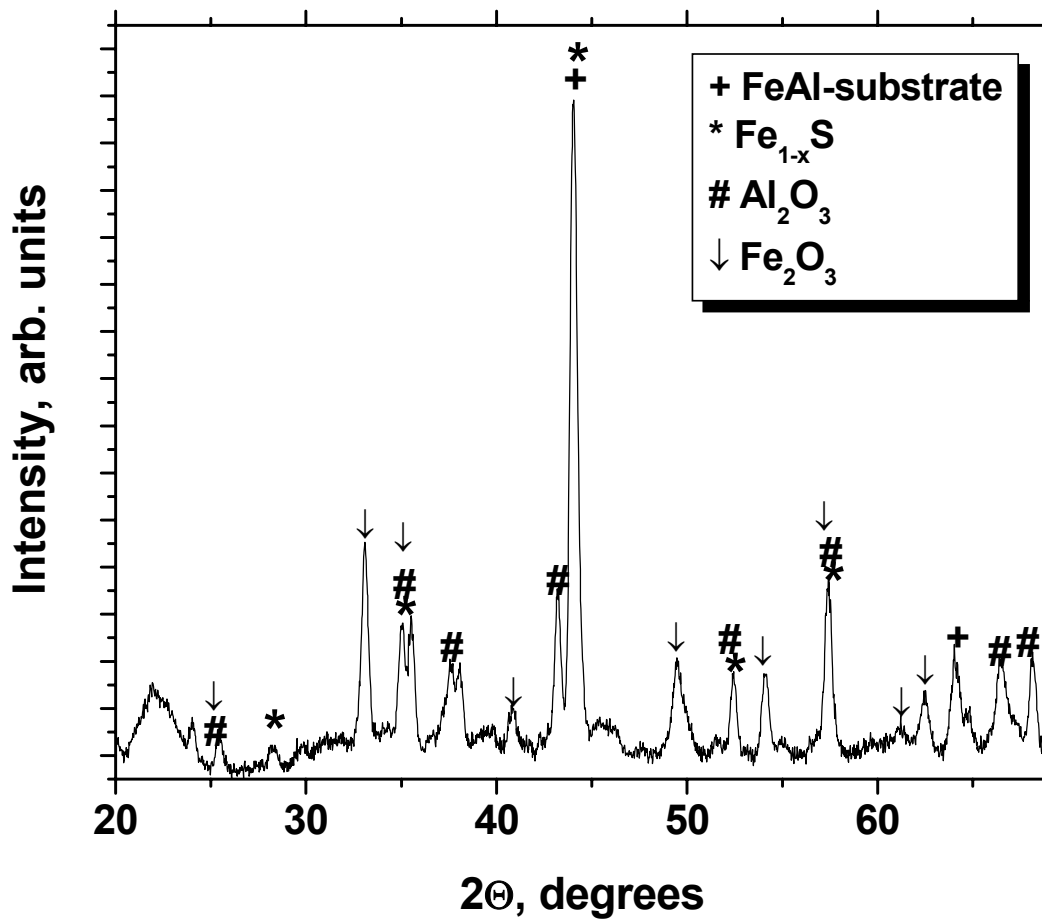
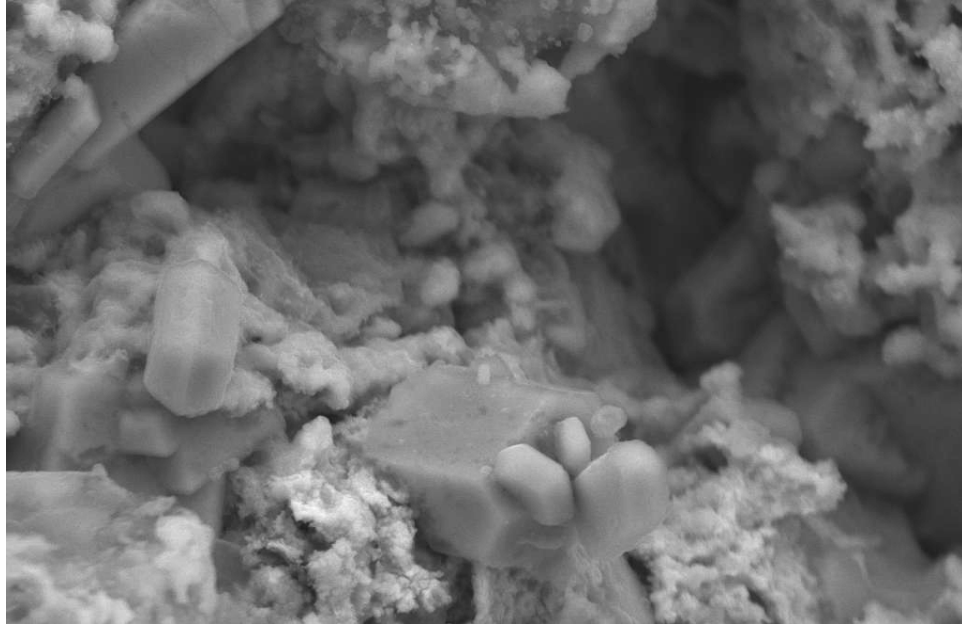


Figure 5.24: (a) Surface micrographs of scale on YFeAl coating with Y=1.5 at%. TGA curves are shown in Figures 5.22-5.23, (b) surface XRD pattern.

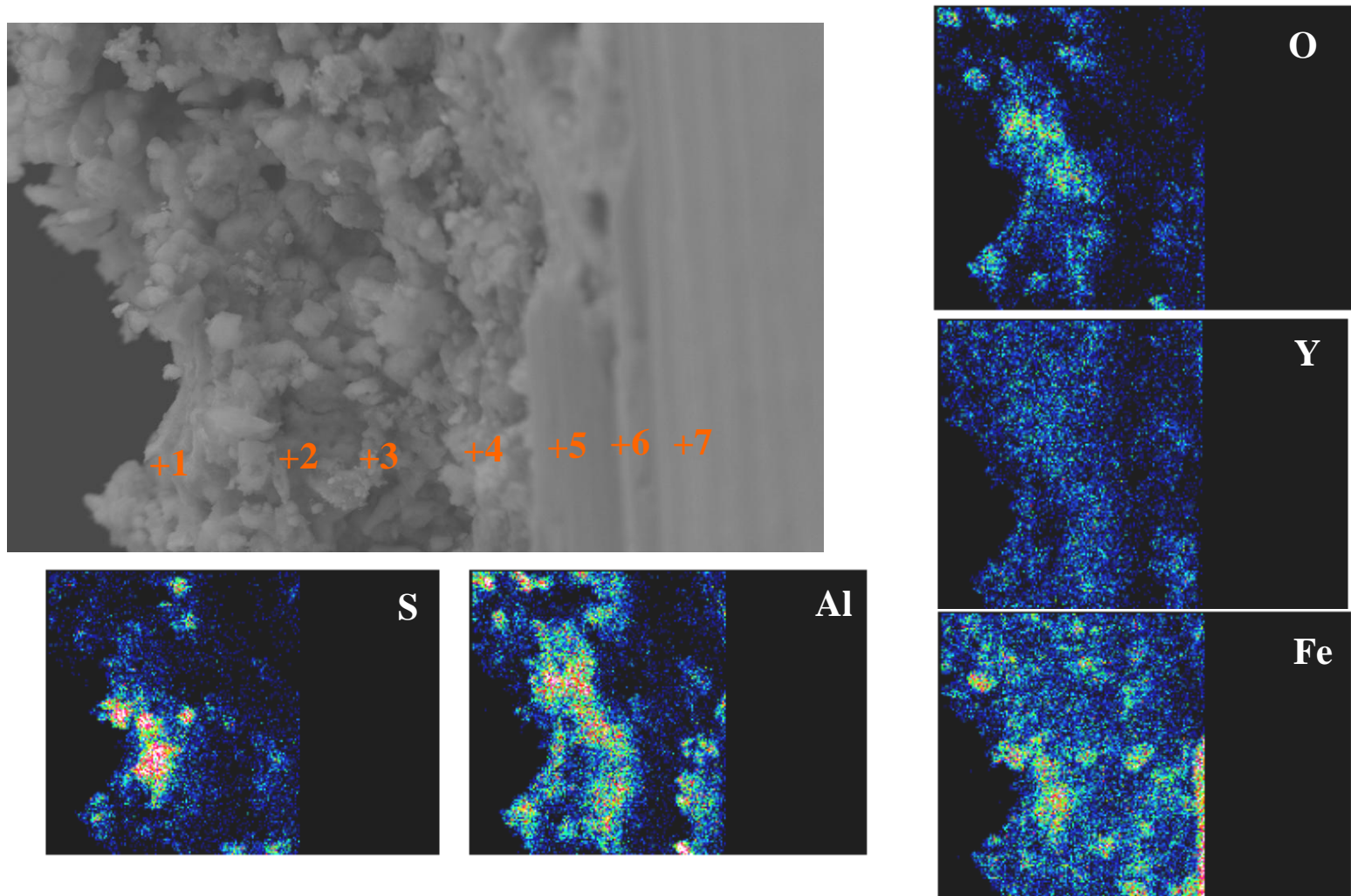


Figure 5.25: Cross-section of HfFeAl coating after exposure to cyclic sulfidizing-oxidizing environments at 800°C and EDS maps of Fe, Al, Fe, S, and O

Table 5.11: Fe, O, S, Al, and Y concentrations in scale after exposure to cyclic environments at 800°C for 100 hours as shown in Figure 5.25.

Spectrum	O	Al	S	Fe	Y
Spectrum 1	30.37	21.43	6.41	13.48	28.32
Spectrum 2	22.01	5.45	37.74	33.33	1.47
Spectrum 3	40.62	13.79	6.76	15.13	23.69
Spectrum 4	55.13	21.26	7.78	11.96	3.87
Spectrum 5	10.78	8.19	1.02	79.92	0.09
Spectrum 6	12.46	6.35	1.53	79.37	0.29
Spectrum 7	5.63	6.70	1.76	85.64	0.27

Similar reaction kinetics was observed for the HfFeAl coatings (Hf ~ 1.5 at%) as shown in Figure 5.26. Figures 5.27(a)-(c) shows the changes in corrosion kinetics on cycling from oxidizing-to-sulfidizing whereas Figure 5.27(d)-(f) shows the magnified view during periods of environmental changes from sulfidizing-to-oxidizing. Parabolic rate constants for reactions during different environmental cycles are listed in Table 5.12. Data suggests that as the environment is changed from oxidizing to sulfidizing, the corrosion rate increases sharply, as evident from a sudden increase in the slope of the mass change curve in Figures 5.27(a)-(c). On changing the environment from sulfidizing to oxidizing, a minor spallation of the order of 0.1 mg/cm^2 was observed followed by a “bump”-like feature in the kinetic curve followed by a slow mass loss, similar to the one seen for YFeAl coatings discussed earlier. Although the corrosion reaction kinetics of Y and Hf modified coatings with RE >1 at% showed similar behavior, HfFeAl showed a

better resistance to the fluctuating environments with a total mass gain of $\sim 4.5 \text{ mg/cm}^2$ as compared to the YFeAl ($\sim 8 \text{ mg/cm}^2$). Doping of higher concentration ($\sim 1.5\%$) of both REs had a detrimental effect on corrosion resistance in cyclic environments as compared to the unmodified Fe-Al coating (total mass gain $\sim 3.5 \text{ mg/cm}^2$) under equivalent conditions.

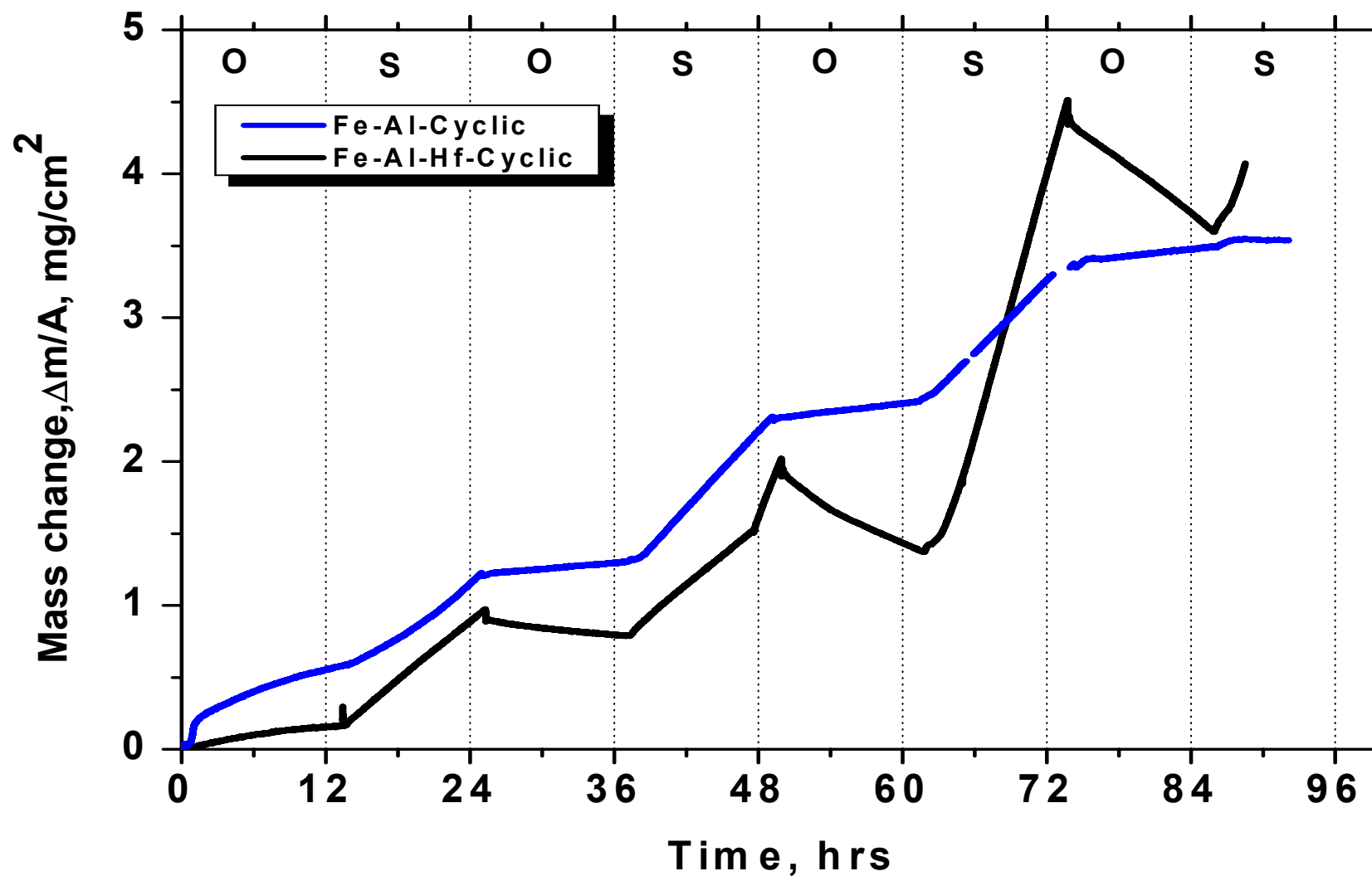


Figure 5.26: Corrosion kinetics of HfFeAl coatings as compared to unmodified-Fe-Al coatings in cycling sulfidizing –oxidizing environments: (O) $p\text{O}_2 = 0.21$ atm, (S) $p\text{S}_2 = 10^{-8}$ atm

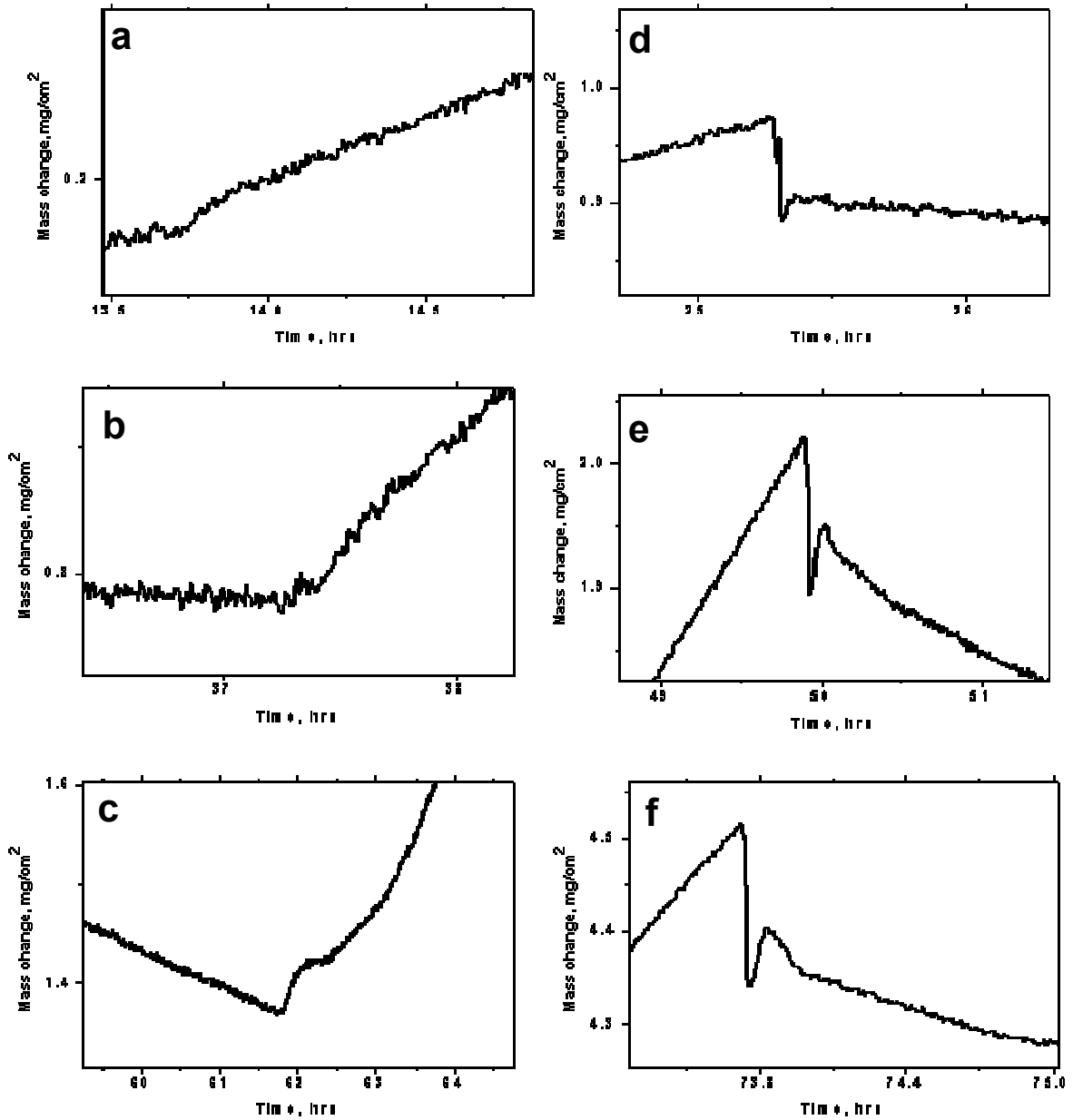


Figure 5.27: Kinetics of HfFeAl coating in cyclic environments from (a)-(c) oxidizing-to-sulfidizing, (d)-(f) sulfidizing-to-oxidizing

Table 5.12: Parabolic corrosion rates for each cycle as shown in Figure 5.26 for hafnium modified coating as compared to unmodified coatings in cyclic gaseous environments:
(O) $p_{O_2}=0.21$ atm, (S) $p_{S_2} = 10^{-8}$ atm

Environment	Fe-Al ($mg^2/cm^4.hr$) $\times 10^{-3}$	Hf-Fe-Al ($mg^2/cm^4.hr$) $\times 10^{-3}$
O	25.45	2.42
S	104.17	80.87
O	18.99	-14.62
S	309.04	146.83
O	45.73	-138.82
S	466.9	1591.9
O	63.7	-489.99
S	-	1521.45

Figure 5.28 shows the comparison of YFeAl and HfFeAl with unmodified FeAl coatings under similar cyclic environmental conditions with Table 5.13 showing the calculated parabolic rates. Corrosion resistance in cyclic environments for aluminide coatings was observed in the order:

$$FeAl > HfFeAl > YFeAl$$

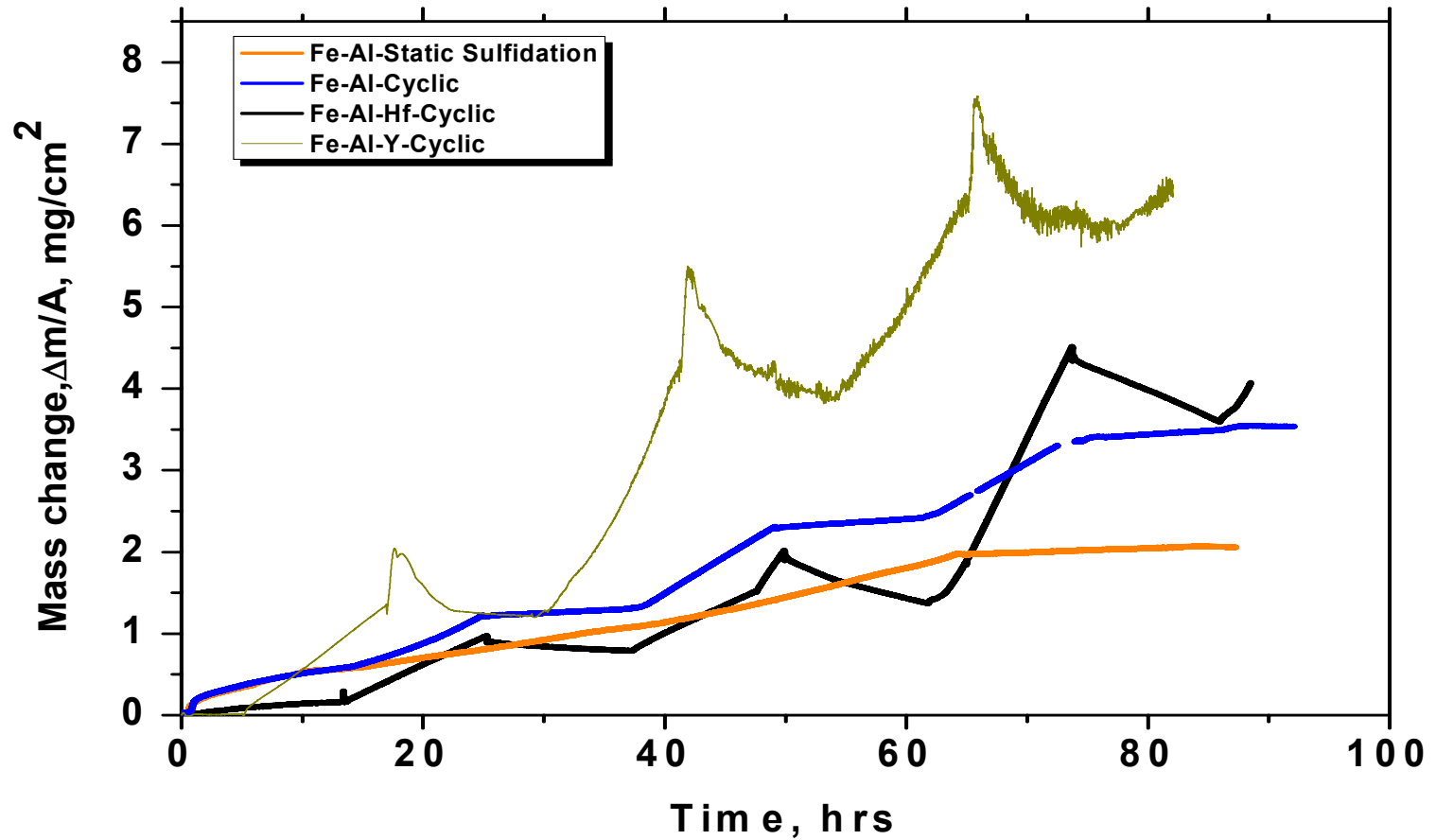


Figure 5.28: Corrosion kinetics of HfFeAl and YFeAl coatings as compared to unmodified-Fe-Al coatings in cycling sulfidizing –oxidizing environments: (O) $pO_2 = 0.21$ atm, (S) $pS_2 = 10^{-8}$ atm
 Fe-Al coating behavior in static sulfidizing environment has been shown to compare the effects of cyclic environments.

Table 5.13: Parabolic corrosion rates for each cycle as shown in Figure 5.28 for modified coating (RE>1 a%) as compared to unmodified coatings in cyclic gaseous environments:
(O) pO₂=0.21 atm, (S) pS₂ = 10⁻⁸ atm

Environment	Fe-Al (mg²/cm⁴.hr) x10⁻³	Hf-Fe-Al (mg²/cm⁴.hr) x10⁻³	Y-Fe-Al (mg²/cm⁴.hr) x10⁻³
O	25.45	2.42	-
S	104.17	80.87	171.02
O	18.99	-14.62	-28.18
S	309.04	146.83	1083.5
O	45.73	-138.82	-499.4
S	466.9	1591.9	2313.37
O	63.7	-489.99	-2176.48
S	-	1521.45	-

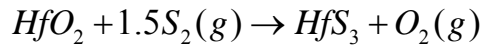
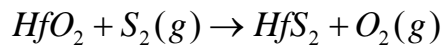
5.3.2.1 Corrosion mechanism of RE-modified Fe-Al coatings in cyclic gaseous environment

The protection provided by the Al₂O₃ scale is dependent on its performance as a diffusion barrier to the reactants. Formation of any fast diffusion path formed in the scale can compromise its protective nature. The total effective path for an outer metal ion or inward gas-anion diffusion can be considered as:

$$\eta_{eff} = \eta_{GB} + \eta_s, \quad (1)$$

where η_{GB} is the available grain boundary path and η_s is the short-circuit path through RE-sulfides. Sulfides of Fe, Hf and Y are non-stoichiometric in nature thus contain cation/anion defects such as vacancies. These vacancies can provide a short-circuit diffusion path for the metal cations and/or corrosive anions. The mechanism for corrosion behavior in a fluctuating sulfidizing-oxidizing environment has been proposed in this section with HfFeAl as an example to show different reaction stages corresponding to the observed thermogravimetric results. Vermaut et al^[129] studied the Hf-S system in the temperature range of 700-1000°C and reported that the Hf-sulfide compositions range from HfS₂-HfS₃ (i.e. HfS_{2.05}, HfS_{2.44}, HfS_{2.86}) and the concentration of defects increases at higher temperatures. For any kinetic process, the slowest step determines the effective rate of reaction. RE-sulfide provides faster diffusion due to presence of vacancies. More grain boundary path will show lower corrosion rates. On the other hand, presence of RE-sulfide in the grain boundary will increase the effective diffusion path and thus the corrosion rate. Based on above observations, following mechanism is proposed for the corrosion mechanism of RE-modified coatings (e.g. Hf) in cyclic sulfidation/oxidation environments, as shown schematically in Figure 5.29:

1. Segregation of reactive element oxides in Al_2O_3 grain boundaries has been reported^[56]. During oxidation in air, protective scale with Al_2O_3 and RE-oxide forms where the RE-oxides segregate at the Al_2O_3 grain boundaries inhibiting an outward diffusion of Fe and Al. This results in the lower corrosion rate as shown for the first oxidizing environment cycle data in Table 5.13.
2. On changing the environment to sulfidizing, S^{2-} will diffuse through the scale grain boundaries and scale.
3. On encountering, RE-oxide, it converts RE-oxide to sulfide by reactions:

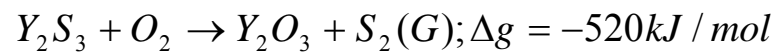
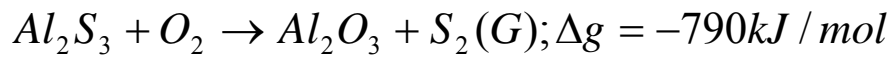
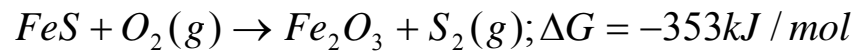


Although RE-oxides are thermodynamically stable, in presence of high sulfur and low oxygen partial pressures, the conversion reaction will happen as evident from phase stability diagram in Figure 5.19.

4. RE-sulfide being non-stoichiometric in nature, provides a short-circuit diffusion path for inward sulfur diffusion and outward metal (Fe^{+3} and Al^{+3}) diffusion causing the rate of corrosion to increase. This is evident from the presence of Al, Fe and S at scale/gas interface as shown in Figure 5.25 and was confirmed by XRD characterization of scale as shown in Figure 5.24. XRD detected Fe_2O_3 , Al_2O_3 and Fe_{1-x}S at the surface indicating an outward diffusion of Fe^{+3} through corrosion scale. Grain boundaries can provide an easy path for both outward cation and inward anion diffusion. However, the segregation of coating metals at

the scale/gas interface suggests that outward metal ion diffusion is faster through the scale than inward sulfur/oxygen diffusion.

5. On changing the environment back to oxidizing, sulfides convert back to oxide showing a mass loss in kinetic curves. Following conversion reactions may take place:



More the amount of RE in the scale, more mass loss will be observed on changing the environment from sulfidizing to oxidizing.

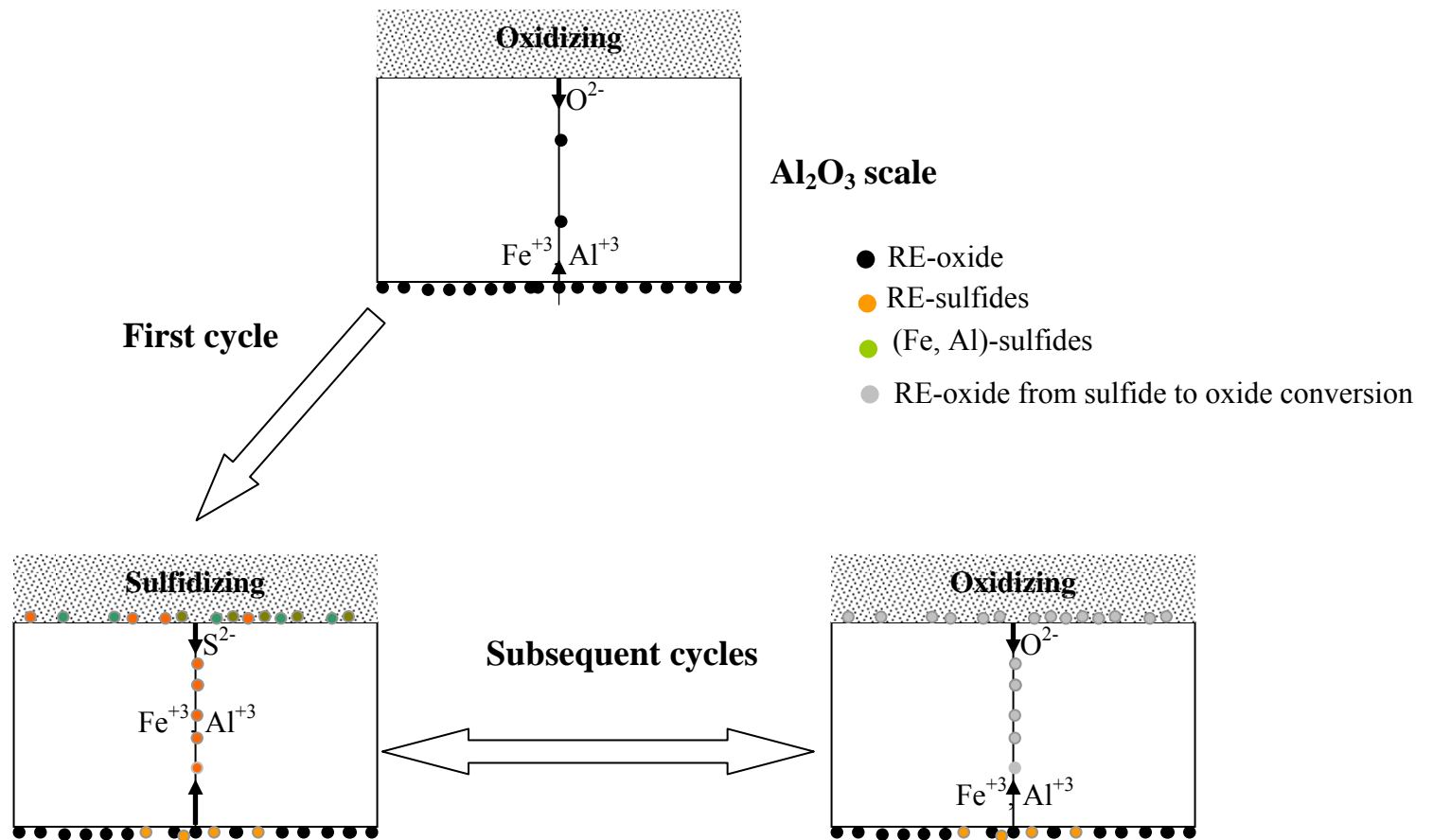


Figure 5.29: Corrosion mechanism for RE-modified Fe-Al coatings in cyclic oxidizing-sulfidizing environments

5.3.3 Corrosion performance of aluminide coatings with <0.5 at% RE addition

To evaluate the effect of RE concentration in aluminide coatings on their corrosion resistance, coating with lower RE concentrations (<0.5 at%) were prepared. Figure 5.30 shows the corrosion kinetics of YFeAl (Y~0.3at%) in cyclic environments with Figure 5.31(a)-(f) showing the magnified areas of the kinetics curve. It is evident that the lower concentration of yttrium in aluminide coating (total mass gain ~2 mg/cm²) showed a better corrosion resistance than the unmodified coating (total mass gain ~3.5mg/cm²). Also, the parabolic rates observed for low yttrium coatings were lower than the high yttrium containing coating as shown in Table 5.14. “Bump”-like kinetics feature, associated with scale spallation followed by an increased corrosion rate, was observed when gas composition was changed from oxidizing to sulfidizing. This effect was similar for the aluminide coatings with higher concentration of RE elements, as discussed in section 5.3.2. However, reduced weight of spalled scale (0.05mg/cm²) suggests a better scale adhesion for the low RE-aluminide coatings. On changing the environment from oxidizing to sulfidizing, corrosion rate increased slightly as evident from increased slope in Figures 5.31(a-c), but the change in slope was not as high as for coatings with high yttrium containing coatings (see Figure 5.23).

Figures 5.32 show the corrosion kinetics of HfFeAl (Hf ~ 0.4 at %) coating as well as an equivalent iron aluminide coating without RE elements. Overall corrosion performance for the Hf-containing aluminide was better in the cyclic environment. Figures 5.33(a)-(f) showing kinetic events during environmental cycling. Comparison of data in Figures 5.30 and 5.32 indicate that the corrosion behavior for the two aluminides was identical.

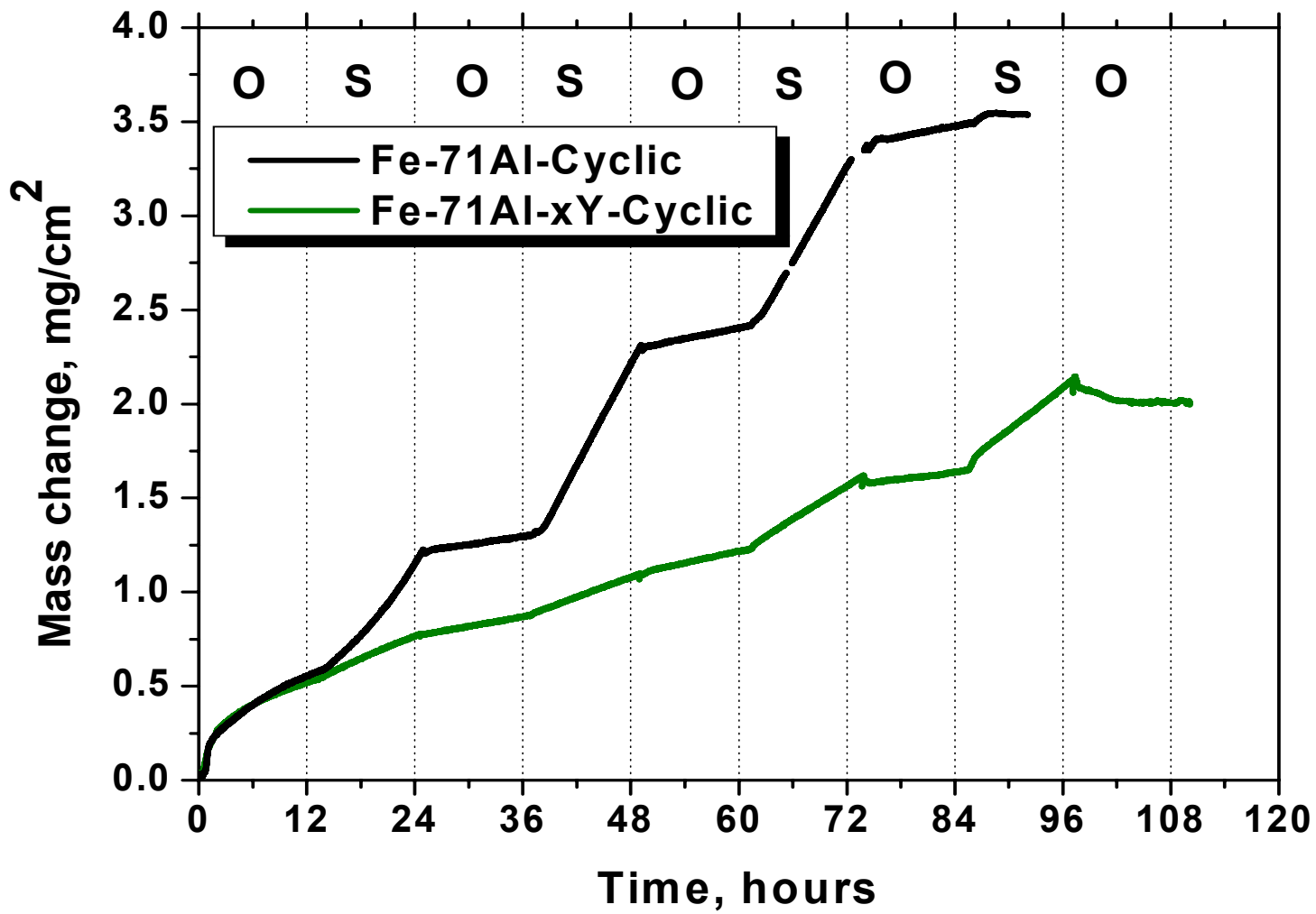


Figure 5.30: Corrosion kinetics of YFeAl coatings as compared to unmodified-Fe-Al coatings in cycling sulfidizing –oxidizing environments: (O) $pO_2 = 0.21$ atm, (S) $pS_2 = 10^{-8}$ atm

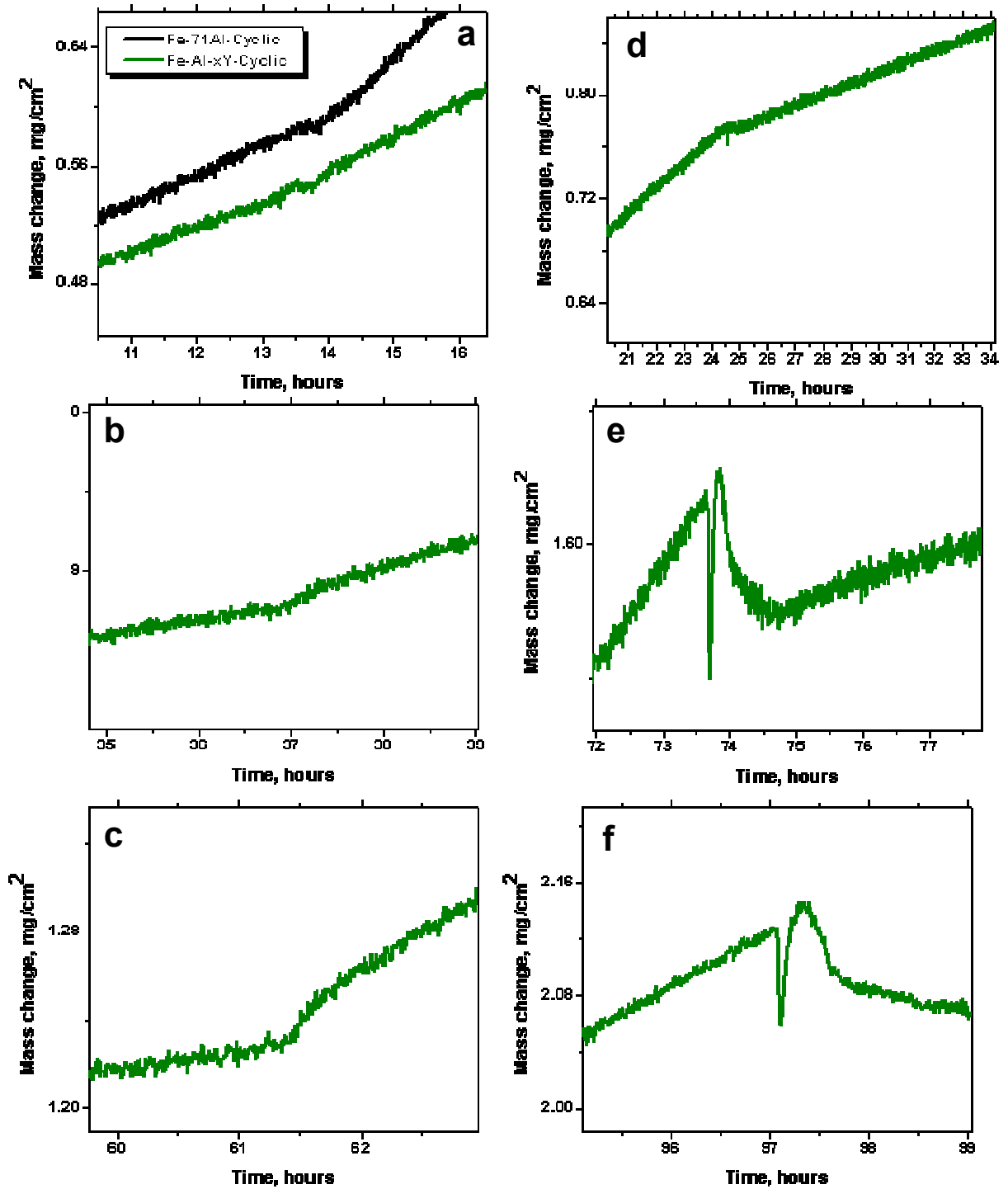


Figure 5.31: Kinetics of YFeAl coating in cyclic environments from (a)-(c) oxidizing-to-sulfidizing, (d)-(f) sulfidizing-to-oxidizing

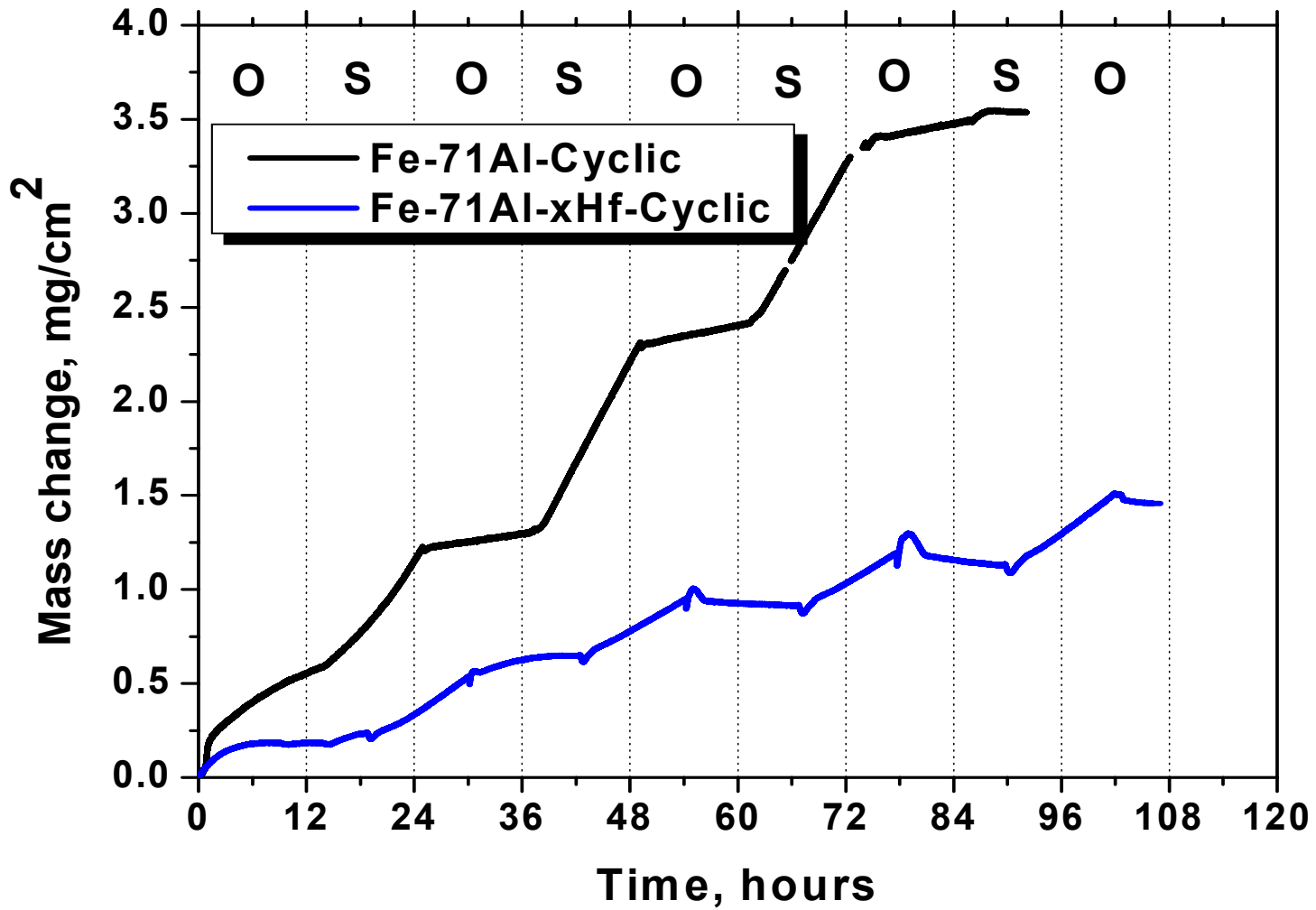


Figure 5.32: Corrosion kinetics of YFeAl coatings as compared to unmodified-Fe-Al coatings in cycling sulfidizing –oxidizing environments: (O) $p_{O_2} = 0.21$ atm, (S) $p_{S_2} = 10^{-8}$ atm

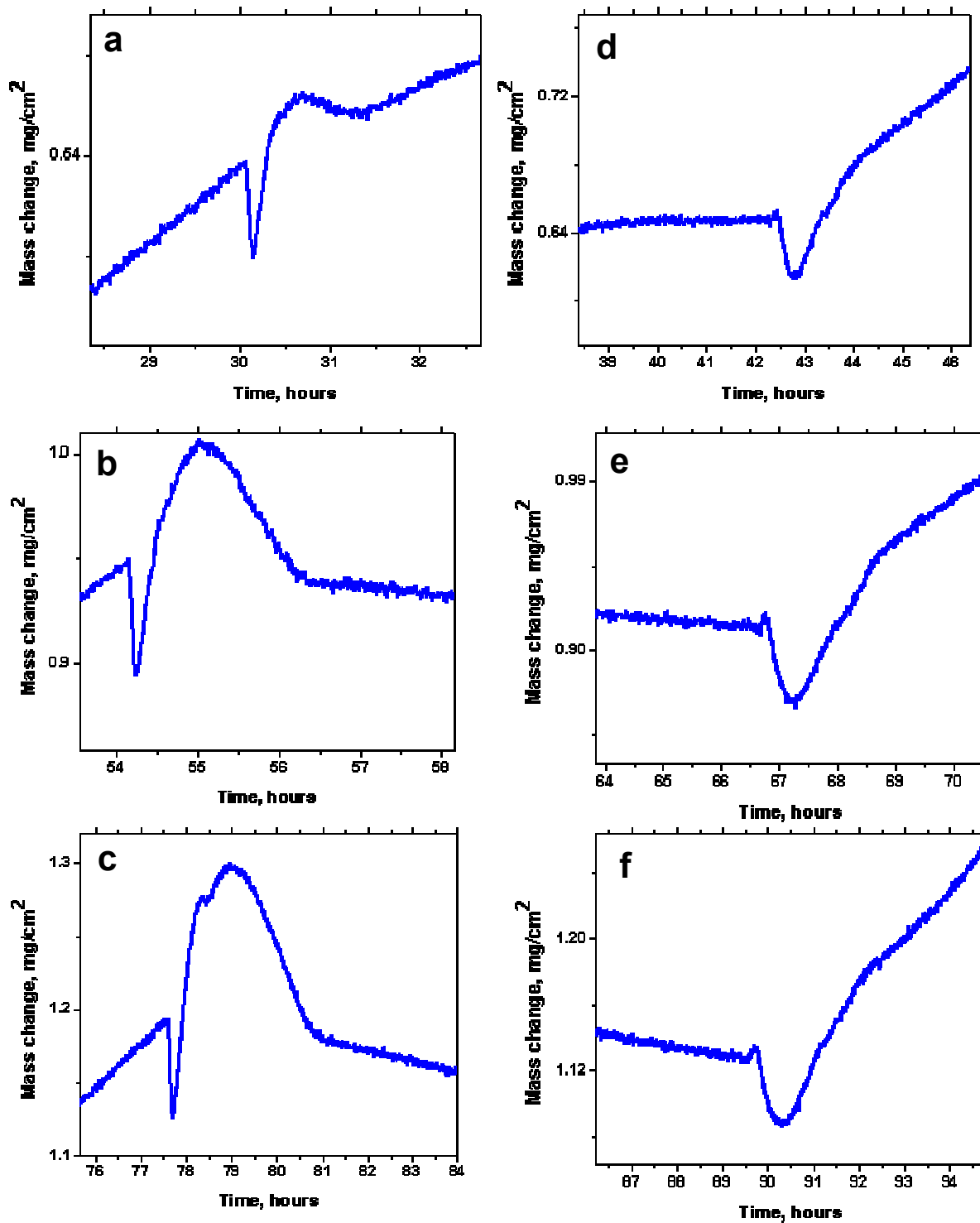


Figure 5.33: Kinetics of HfFeAl coating in cyclic environments from (a)-(c) oxidizing-to-sulfidizing, (d)-(f) sulfidizing-to-oxidizing

Table 5.14: Parabolic corrosion rates for each cycle for modified coating (RE <0.5 at%) as compared to unmodified coatings in cyclic gaseous environments:
(O) $pO_2 = 0.21$ atm, (S) $pS_2 = 10^{-8}$ atm

Environment	Fe-Al ($mg^2/cm^4 \cdot hr$) $\times 10^{-3}$	Hf-Fe-Al ($mg^2/cm^4 \cdot hr$) $\times 10^{-3}$	Y-Fe-Al ($mg^2/cm^4 \cdot hr$) $\times 10^{-3}$
O	25.45	2.87E-01	20.23
S	104.17	19.06	27.83
O	18.99	1.79	13.99
S	309.04	41.35	34.98
O	45.73	-4.28	25.32
S	466.9	52.68	85.61
O	63.7	-14.14	18.8
S	-	84.29	143.05

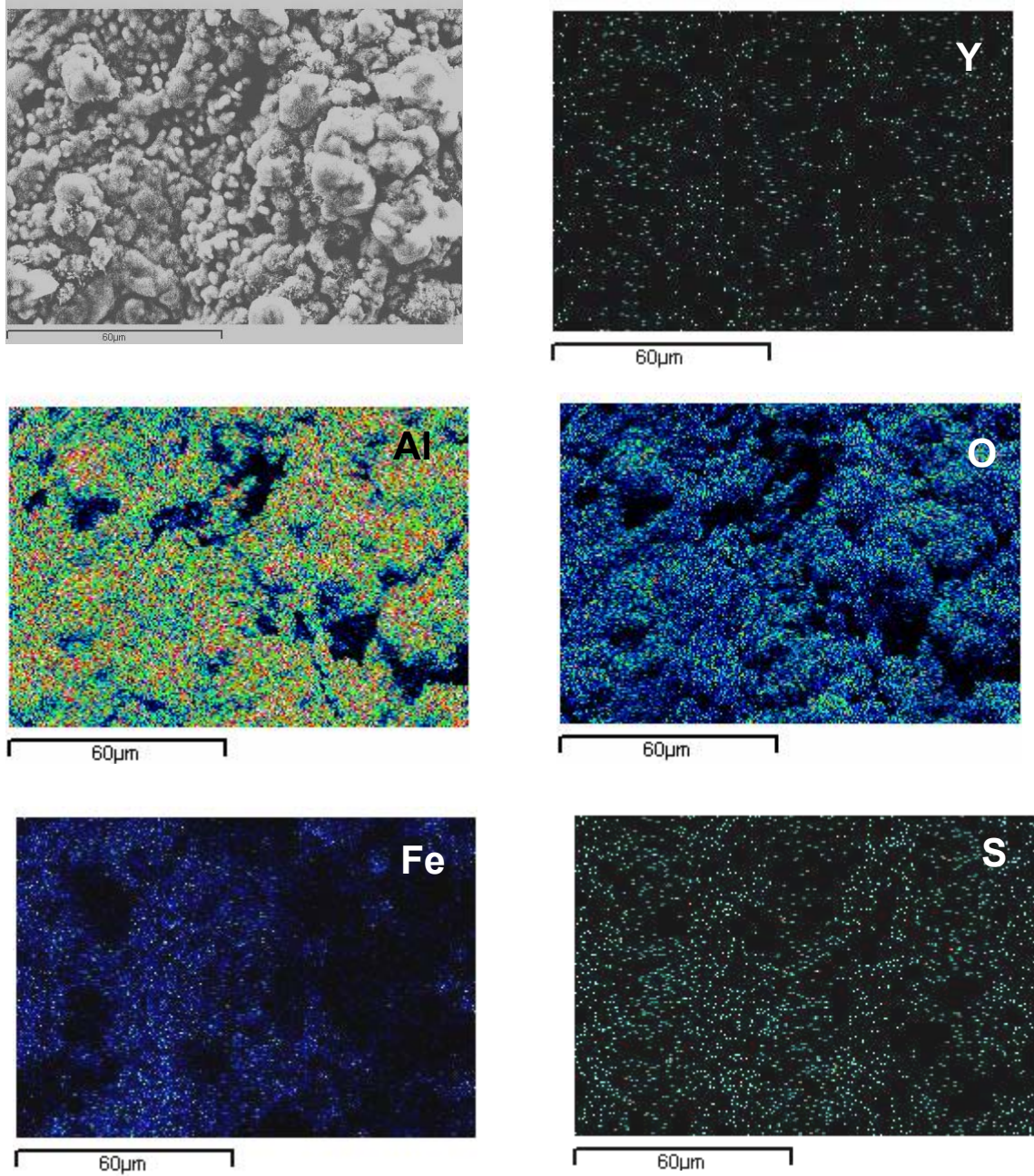


Figure 5.34: Y, Al, O, Fe and S x-ray maps of scale developed on YFeAl coating (Y~0.3 at%) after exposure to cyclic gaseous environment at 800°C for 100 hours

Figure 5.35 shows the surface of corrosion scale formed on the HfFeAl coated sample after its cyclic environment exposure at 800°C for 100hrs. Spot analysis of different scale areas, as shown in Figure 5.35 indicated that the RE concentration was ~2 at% in corrosion scale, which is more than the RE concentration in the coating. This indicates that the Hf diffused outwards through the scale, towards the surface, during corrosion.

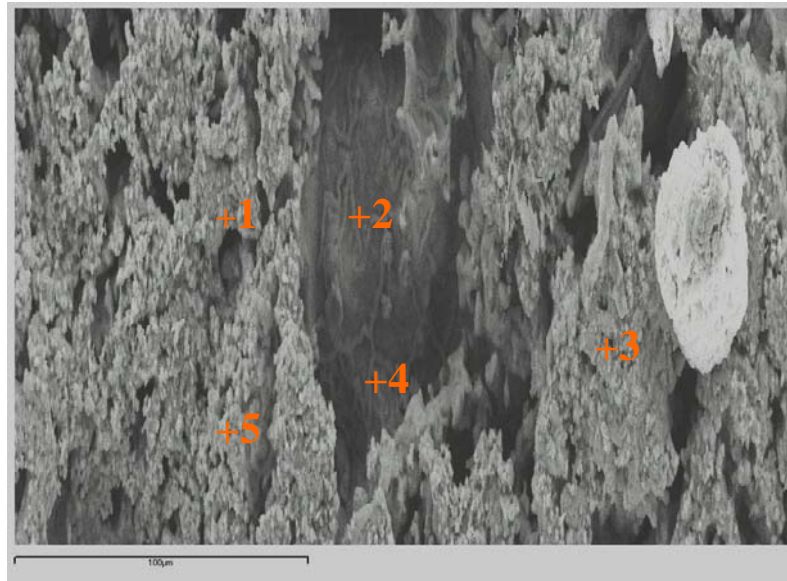


Figure 5.35: Surface micrograph of HfFeAl coating (Hf~0.4 at%) after exposure to cyclic gaseous environment at 800°C for 100 hours

Table 5.15: EDS elemental analysis for spots shown on Figure 5.35.

	O	Al	S	Fe	Hf
Spectrum 1	60.81	31.69	0.15	5.31	2.04
Spectrum 2	32.54	28.97	0.19	37.05	1.25
Spectrum 3	64.99	29.6	0.27	3.38	1.76
Spectrum 4	37.12	46.5	1.1	12.81	2.47
Spectrum 5	61.43	30.98	0.62	4.01	2.96

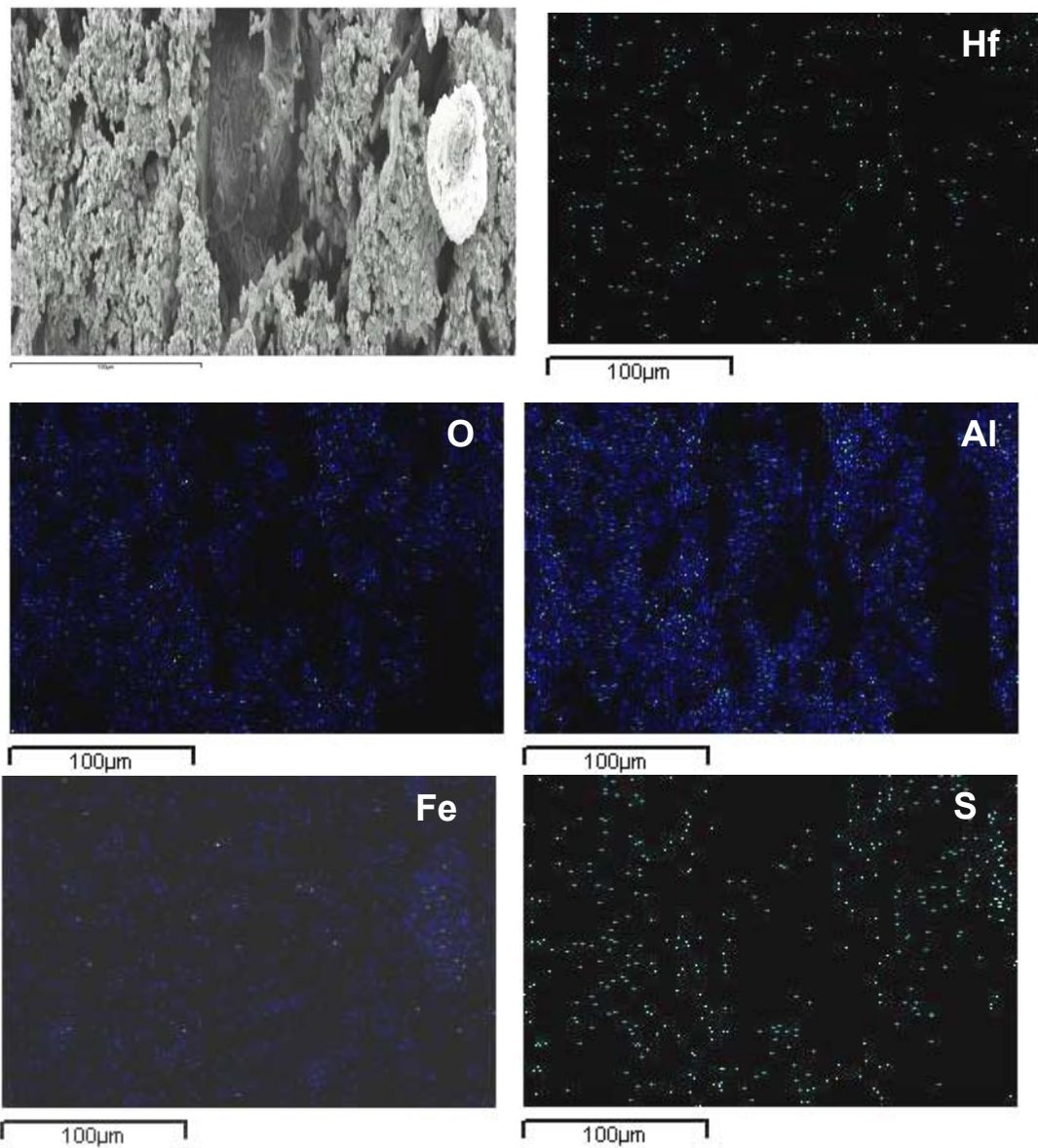


Figure 5.36:Hf, O, Al, Fe and S x-ray maps of scale developed on HfFeAl coating (Hf~0.4 at%) after exposure to cyclic gaseous environment at 800°C for 100 hours.

Corrosion behavior of FeAlHf and FeAlY coatings, with RE concentration <0.5 at%, is shown in Figure 5.37. It is evident that both the coatings showed improved behavior than unmodified aluminide coatings under similar exposure conditions.

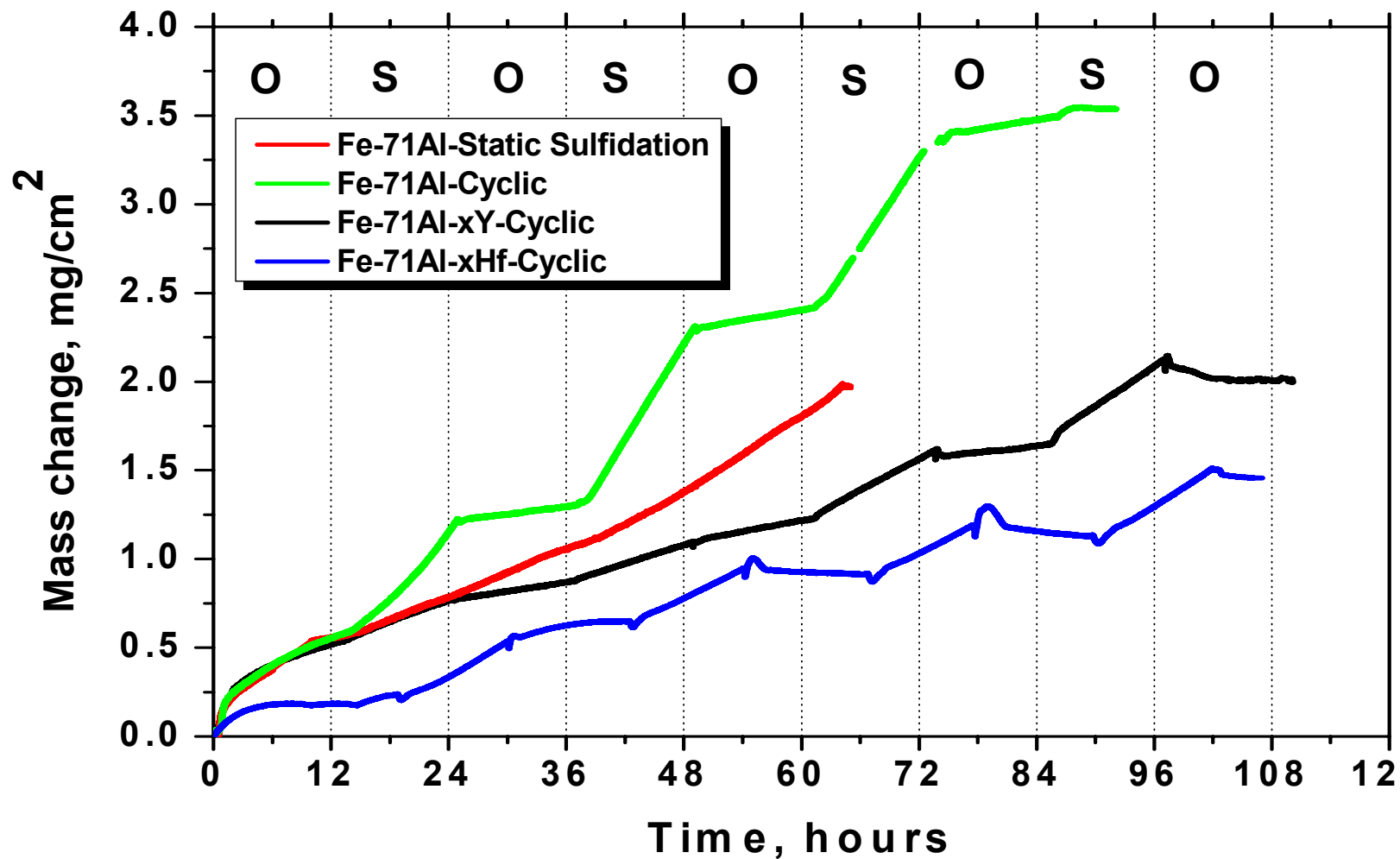


Figure 5.37: Corrosion kinetics of HfFeAl and YFeAl coatings as compared to unmodified-Fe-Al coatings in cycling sulfidizing – oxidizing environments: (O) $p_{O_2} = 0.21$ atm, (S) $p_{S_2} = 10^{-8}$ atm
 Fe-Al coating behavior in static sulfidizing environment has been shown to compare the effects of cyclic environments.

The most prominent observation of this study is the diffusion of reactive elements from the coating into the scale and their segregation at the scale/gas interface, as shown by the spot analysis data from the cross-section shown in Figure 5.25. Oxygen/sulfur potential gradient exists across the corrosion scale in the metal-scale-gas system **Error! Bookmark not defined.** which can act as the driving force for diffusion. Three different types of processes can operate during sulfidation/oxidation of reactive element modified coatings:

1. Segregation of RE at metal/scale interface to inhibit the outward diffusion of metal ions (Fe^{+3}).
2. Reactive element have high affinity towards oxygen and sulfur, which can result in an outward diffusion of RE itself through the fastest path available in scale i.e. grain-boundaries, assuming no cracks in scale.
3. Segregation of RE at scale/gas interface and reaction with environment (S_2 or O_2).

As RE cations ($\text{Hf}^{+4} \sim 0.71 \text{ \AA}$, $\text{Y}^{+3} \sim 0.9 \text{ \AA}$) are larger in size than the native cations from substrate ($\text{Fe}^{+3} \sim 0.49 \text{ \AA}$, $\text{Al}^{+3} \sim 0.535 \text{ \AA}$)^[130]. This suggests that the grain boundary diffusion of RE ions will be slower than Fe and Al ions, and thus RE ions will segregate on grain boundaries inhibiting the further diffusion after transient oxidation regime. It has been shown by Pint et al that as grain boundaries become supersaturated with RE, it ultimately nucleates RE-rich particles. The driving force for RE-diffusion is the partial pressure difference between the scale/gas interface and the grain boundaries. It was observed that at the scale/gas interface, concentration of RE is much higher than that present in the coating. But the supersaturation and precipitate nucleation may happen in this system after a certain concentration is reached and therefore may take long time. Although, tests in this study were carried out for shorter durations (100 hours) but the

results show the concentration of reactive element in scale as well as gas/scale interface. Oxides of RE (e.g. Y_2O_3) are more stable than any of its sulfides, but in the presence of high sulfur and low oxygen activity, sulfides can be more stable as shown in Figure 5.19. The adhesion of protective scale depends on the void nucleation and growth at the scale/metal interface. Results from this study and previous work have shown that voids are always present at the interface. If the voids remain small (less than half the grain size of scale), adhesion will not be compromised, but if voids grow, scale spallation can occur. Interfacial sulfur can allow these voids to grow by changing the interfacial energies. As REs inhibit the diffusion of outward metal ions, inward diffusion of corrosive gaseous anions becomes the rate determining step. This may result in an increase in the sulfur concentration at the scale/metal interface to the level where the activation energy for void nucleation is low and thus voids may start to nucleate and grow to compromise the scale adhesion, as shown by the minor scale spallation events due to environment cycling in this study. Pint et al] have reported that sulfur segregation can lower the activation energy of void formation.

Table 5.16 compares the parabolic rates for the cycling environments for RE-modified coatings studied in the present work. Also, RE-modified coatings with concentration <0.5 at% showed better behavior than unmodified coatings. The overall mass gain in 100 hours exposure was $\sim 2.1 \text{ mg/cm}^2$ and 1.5 mg/cm^2 for Y-modified coating and Hf-modified coating respectively as compared to unmodified coating $\sim 3.7 \text{ mg/cm}^2$. On the other hand, RE-modified coatings with concentration >1 at% showed detrimental behavior as discussed previously.

Table 5.16: Summary of effects of reactive element modifications on corrosion behavior of iron aluminide coatings in fluctuating sulfidizing-oxidizing environments at 800°C

Environment	Fe-Al ($\text{mg}^2/\text{cm}^4 \cdot \text{hr}$) $\times 10^{-3}$	Hf-Fe-Al		Y-Fe-Al	
		0.4 at% ($\text{mg}^2/\text{cm}^4 \cdot \text{hr}$) $\times 10^{-3}$	1.5 at% ($\text{mg}^2/\text{cm}^4 \cdot \text{hr}$) $\times 10^{-3}$	0.3 at% ($\text{mg}^2/\text{cm}^4 \cdot \text{hr}$) $\times 10^{-3}$	1.5 at% ($\text{mg}^2/\text{cm}^4 \cdot \text{hr}$) $\times 10^{-3}$
	O	25.45	2.87E-01	2.42	20.23
S	104.17	19.06	80.87	27.83	171.02
O	18.99	1.79	-14.62	13.99	-28.18
S	309.04	41.35	146.83	34.98	1083.5
O	45.73	-4.28	-138.82	25.32	-499.4
S	466.9	52.68	1591.9	85.61	2313.37
O	63.7	-14.14	-489.99	18.8	-2176.48
S	-	84.29	1521.45	143.05	-

SUMMARY

1. Hf and Y modified coatings were prepared by co-depositing RE with Al by pack cementation process. Coating parameters were optimized to get desired coating compositions.
2. Coating process at 1000°C showed higher concentration of RE co-deposition with the formation of nitrides and carbides along with the FeAl as a major coating phase.
3. Coating process at 800°C showed lower RE deposition with Fe₂Al₅ as a major coating phase.
4. Four coatings with different RE concentrations were tested for corrosion behavior in simulated cyclic sulfidizing-oxidizing environments at 800°C.
5. Coatings with higher RE content showed detrimental behavior whereas equivalent coatings with relatively lower RE content showed improved corrosion behavior in high temperature fluctuating gaseous environments.
6. A mechanism for corrosion behavior in fluctuating environments for iron aluminide coating containing RE has been proposed. The similar mechanism can also be extended to the alloys containing different amounts of RE in similar environments.

CHAPTER VI

EFFECTS OF REACTIVE ELEMENTS (Hf and Y) ON STRESS DISTRIBUTION AND SPALLATION RESISTANCE OF PROTECTIVE Al_2O_3 SCALES

INTRODUCTION

Performance of high temperature iron aluminide coatings depend on the formation and stability of the adherent, protective Al_2O_3 scale formed on the surface. It has been long recognized that significant stress levels, which are often compressive, can develop in oxide scales formed on the alloy surface at high temperatures, which in turn can lead to spallation.^[99] Thus, corrosion scale spallation, as discussed in previous chapters, remains a serious problem since it can significantly reduce the life of a coating material. Spallation behavior of Al_2O_3 scale formed during high temperature corrosion depends on the stress generation, distribution and its relaxation in the scale. Scale spallation is thermodynamically possible if the release of elastic strain energy stored in a stressed oxide scale is higher than the fracture energy of the metal-oxide interface and its relaxation during cooling. The stored elastic energy is determined by the stresses and thickness of the scale. Reactive elements have been known to improve the scale adhesion of Al_2O_3 scale if added in minor amounts^[74]. Several mechanisms have been proposed and major hypothesis include:

- (a) increased scale plasticity due to RE doping,^[131]
- (b) modification of the oxide scale growth process leading to lower growth stresses,^[132]
- (c) improved chemical bonding at the interface,^[133,134,135]

- (d) prevention of void growth by providing an alternate vacancy sink at the interface, [136,137]
- (e) mechanically anchoring the oxide scale by formation of “pegs”, [138]
- (f) RE elements acting as “getter” for alloy impurities such as sulfur to form stable compounds, preventing segregation at the oxide/metal interface which may weaken interfacial bonding. [133,134,135]

The mechanisms (a), (b) and (c) above are based on an assumption that REs decrease the stresses in the oxide scale or improve the mechanical properties of oxide scale to accommodate stresses rather than relaxing stresses through buckling and consequent debonding the interface between the scale and the metal. Extreme case of stress generation/relaxation is on cooling from the high temperature to the room temperature. Thermal cycling at 1000°C was used in this study to evaluate the effects of RE doping on corrosion scale stresses on Fe-Al coatings. Several authors^[139,140] have used X-ray diffraction method for to measure stresses in oxide scales, but this method provides the average stresses over a large scanned region and cannot distinguish difference in the stress distribution over the sample. The edges can contain higher geometric stresses whereas the plane surface may contain higher growth stresses. To study the stress distribution over the sample edge/surface and to further contribute to the understanding of reactive element effect, residual stresses were determined using photostimulated Cr⁺³ luminescence spectroscopy or Piezospectroscopy. The experimental setup and theory behind this technique has been described in chapter 2. Piezospectroscopy provides a better spatial resolution and the oxide surface can be mapped for stress measurements by mapping the selected grid area by laser beam. The goal of this work was to measure the

variation in the magnitude of stresses in the corrosion scale and how that may affect its protective behavior.

6.1 STRESS MAPPING

Stress relaxation by spallation of protective oxide layer is the most important concern during thermal cycling. Typical samples used in this study were aluminized SA210 (Fe-Al, HfFeAl and YFeAl), oxidized at 1000°C in air followed by the cooling to the room temperature every 24 hours to provide the necessary thermal shock. Stress maps were acquired after 72 hours (3 cycles), 168 hours (7 cycles) and 240 hours (10 cycles) exposure to thermal cycling test conditions, as discussed in Chapter 2. Stresses at edge and the center of sample were measured after each thermal cycle using piezospectroscopy to study the geometric and growth stress respectively. Procedures used to collect and process spectra are described in section 6.1.1.

6.1.1 Spectra processing

Spectra from each measured spot in the selected area of sample were analyzed for position of Cr⁺³ luminescence peaks. Figure 6.1 shows the typical Cr⁺³ luminescence spectrum obtained from Al₂O₃ scale. The luminescence lines recorded from an alumina scales have a mixed Gaussian–Lorentzian line shape as a result of thermal broadening and various instrumental factors^[141].

As a result, the measured line shape can be represented by:

$$\Phi(\nu) = 2A_{Ri} \left[\underbrace{\frac{G\sqrt{\ln 2}}{W_{Ri}\sqrt{\pi}} \exp\left(-4 \ln 2 \left(\frac{\nu - C_{Ri}}{W_{Ri}}\right)^2\right)}_{\text{Gaussian component}} + \underbrace{\frac{L}{\pi W_{Ri} [1 + 4(\nu - C_{Ri} / W_{Ri})^2]}}_{\text{Lorentzian component}} \right]$$

where G and L are the shape parameters describing the relative proportions of Gaussian and Lorentzian components, ν is frequency, W_{Ri} is full width at half maximum, C_{Ri} is frequency at maximum intensity, A_{Ri} . Therefore, for a homogeneously strained body, the luminescence line is unchanged in shape and merely shifted by a constant frequency, $\Delta\nu$.

6.1.2 Procedure used for peak fitting

The collected spectra were analyzed by using an automatic curve fitting procedure for the two mixed Lorentzian-Gaussian curves to determine the peak positions of R1 and R2, and the peak parameters such as height, area, shape and full width at half maximum, as are shown schematically in Figure 1. The procedure adapted for fitting the collected spectra is an iterative one. The parameter constrained was the range of L fraction: 0.4-0.7 for R2 and 0.7-0.9 for R1 based on literature data.^[142] The process was automatized to analyze the spectra collected by rastering the laser beam over the sample surface to get a stress map. Origin®^[143] was used as a curve fitting tool with a multfit add-on for automatization. Automatic initialization of parameters was performed and the software code was modified to use a series simplex and Levenberg-Marquardt non-linear peak fit iterations

[144] to get the best fit. Once the computer had found the best fit (no reduction in chi-square and $R^2 > 0.95$), the R2 peak data was converted to stress value. Figure 6.1 shows typical deconvolution of luminescence spectrum by fitting two mixed Gaussian-Lorentzian peaks. Special care was taken to include the data points with high signal-to-noise ratio to get precise estimation of stresses in scales.

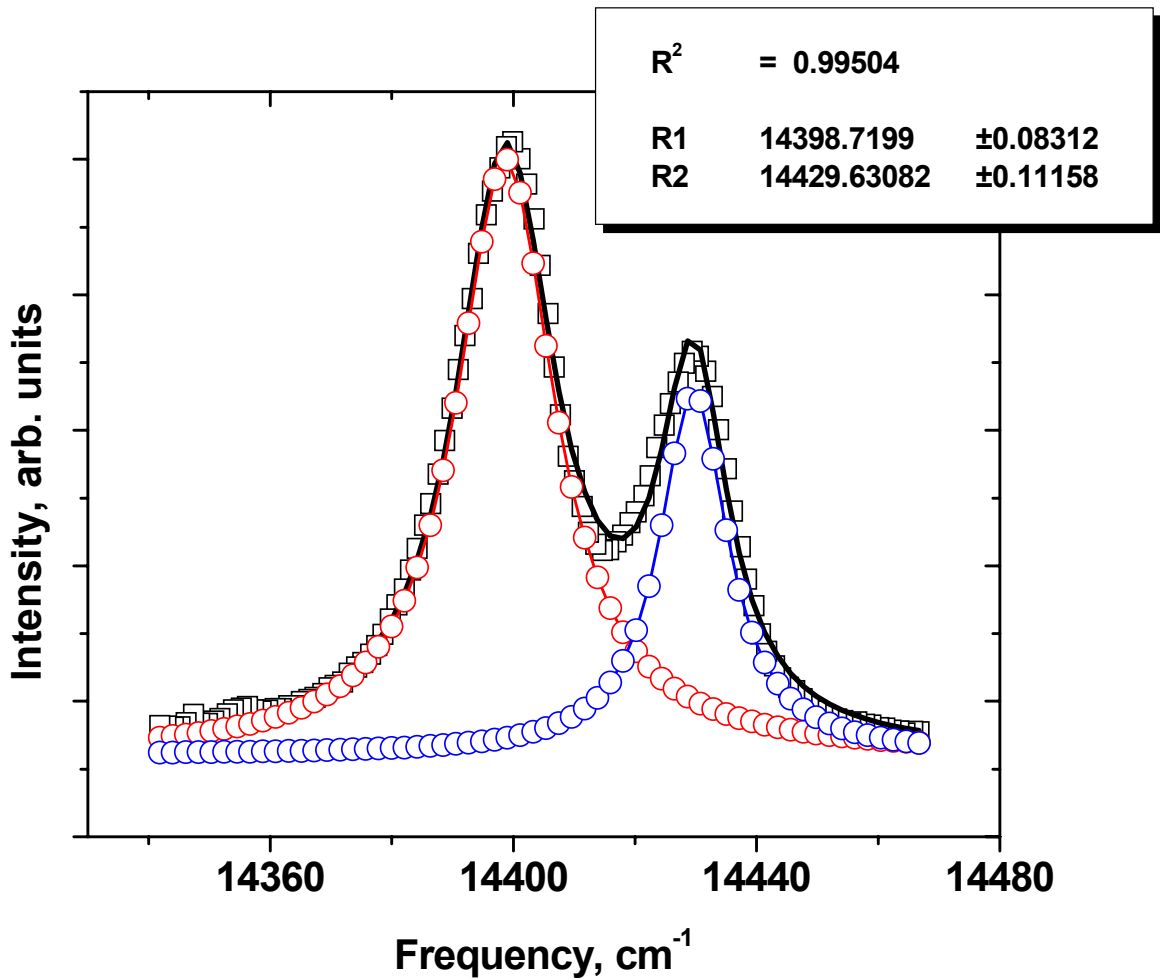


Figure 6.1: Typical luminescence spectra obtained from Al_2O_3 scales on oxidized aluminide coatings. Deconvolution of peaks was carried out as described in section 6.1.2

6.2 CYCLIC OXIDATION AT 1000°C

Aluminide coated carbons steel sample were exposed to thermal shocks by quickly removing them from the heating zone to room temperature and again exposing them to the high temperature. High cooling and reheating rates were expected to produce extreme case of thermal cycling as shown schematically in Figure 6.2. Figure 6.3 shows the mass change of uncoated SA210 in air as compared to Fe-Al, HfFeAl and YFeAl coatings. Coated samples showed a superior corrosion resistance to thermal cycling in oxidizing environment compared to the uncoated samples. Figure 6.3(b) shows the magnified view to compare oxidation kinetics of different aluminide coatings under thermal cycling conditions at 1000°C in air.

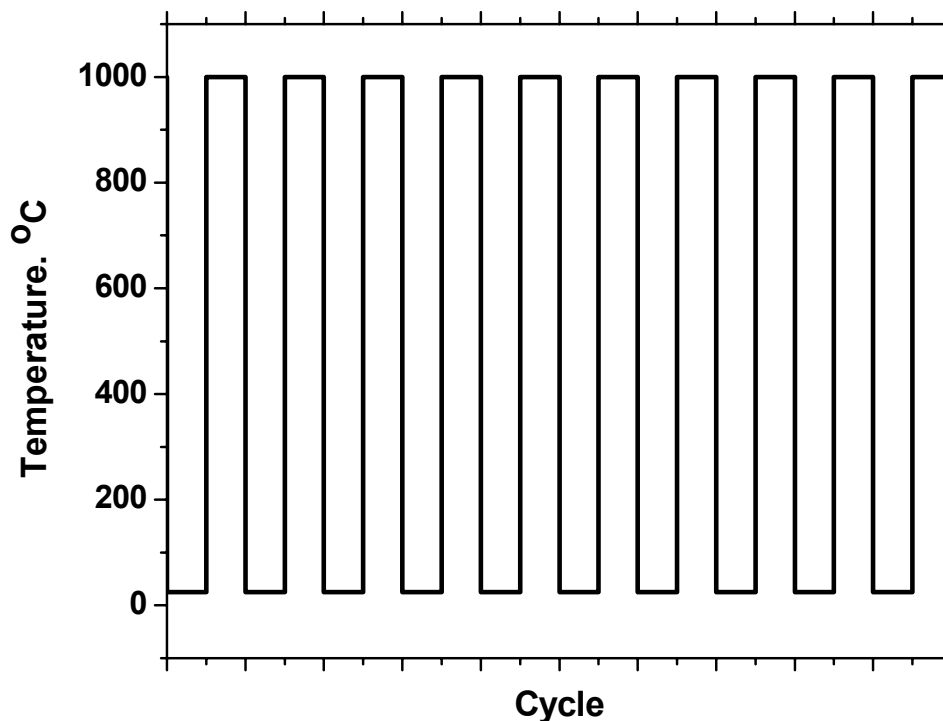


Figure 6.2: Thermal cycling expected from removing from and reinserting the samples into the heating zone. High cooling/heating rates can create tensile stresses

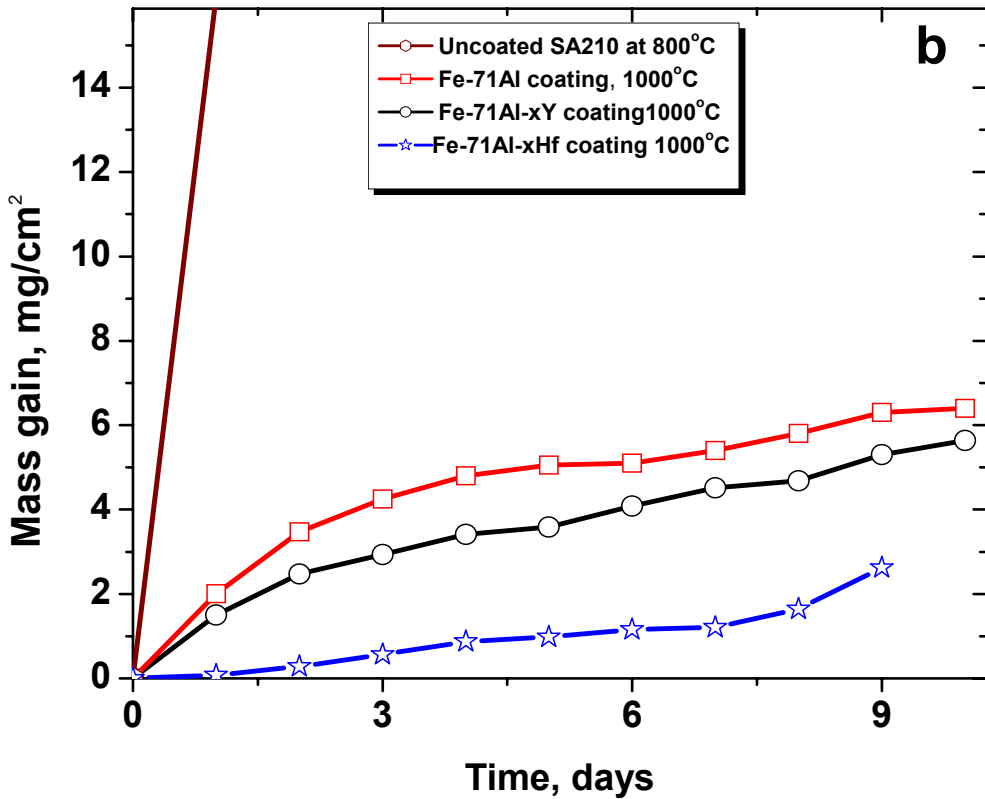
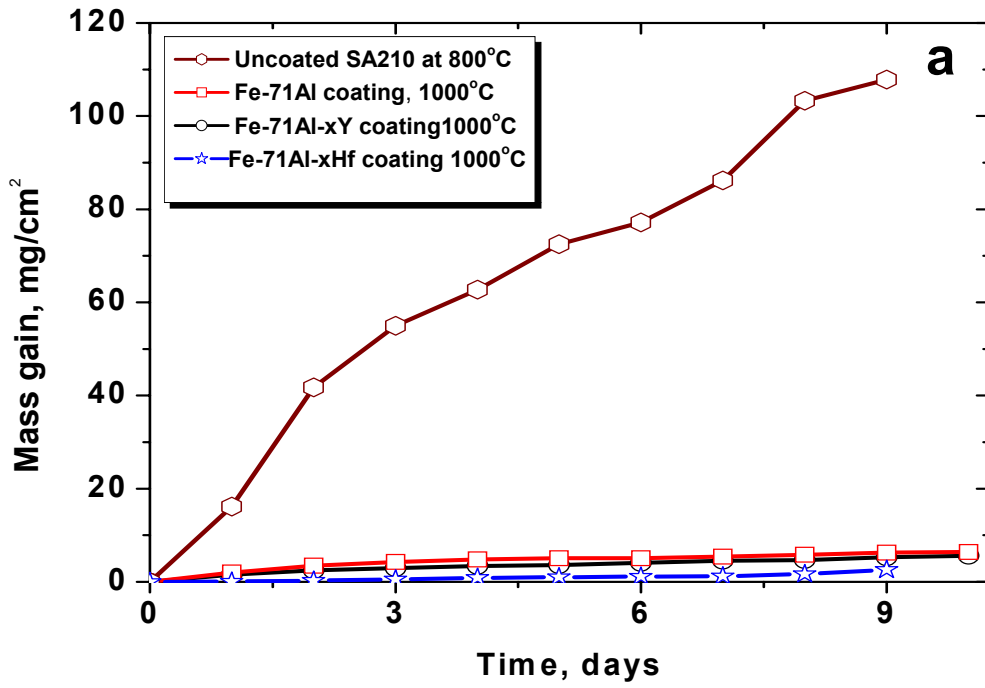


Figure 6.3: (a) Thermal cycling at 1000°C for uncoated, aluminized, Hf-modified, and Y-modified aluminide coatings in air, (b) magnified view of aluminide coatings

Uncoated SA210 showed spallation of oxide scale at sample edges and heavy cracking at planer surface after first 1 day cycle (Figure 6.4). Uncoated carbon steel sample displayed a break away behavior during subsequent exposure to thermal cycles with total mass gain of 110 mg/cm² in 240 hours (10 thermal cycles). However, all the aluminide coated steels showed an excellent behavior as compared to uncoated steel with total mass gain of ~6mg/cm² for Fe-Al, ~5 mg/cm² for Fe-Al-Y and ~ 2 mg/cm² for Fe-Al-Hf coating. As shown in Figure 6.3, yttrium additions showed slight increase in the oxidation resistance while Hf additions showed significant improvement in corrosion resistance. Parabolic rate constants calculated from data in Figure 3 for cyclic oxidation are listed in Table 6.1 which shows that the resistance to oxidation for the tested samples was in the following order:



Figures 6.5 (a) and (b) shows the surface and cross-section micrographs of fractured oxide scale after 240 hours of cyclic oxidation (i.e. 10 one day thermal shock cycles from 1000°C to and RT to 1000°C). Figure 6.5 (a) shows the presence of needle shaped alumina crystal whereas Figure 6.5 (b) clearly indicates the rumpled scale of Al₂O₃ scale indicating that the scale had debonded from the metal surface for Fe-Al coating. The scale had separated from the substrate and large convolutions developed as a result of lateral growth. It was observed that the oxide scale was extensively detached from substrate at several locations and Figure 6.5 (b) shows only a representative micrograph of those locations.

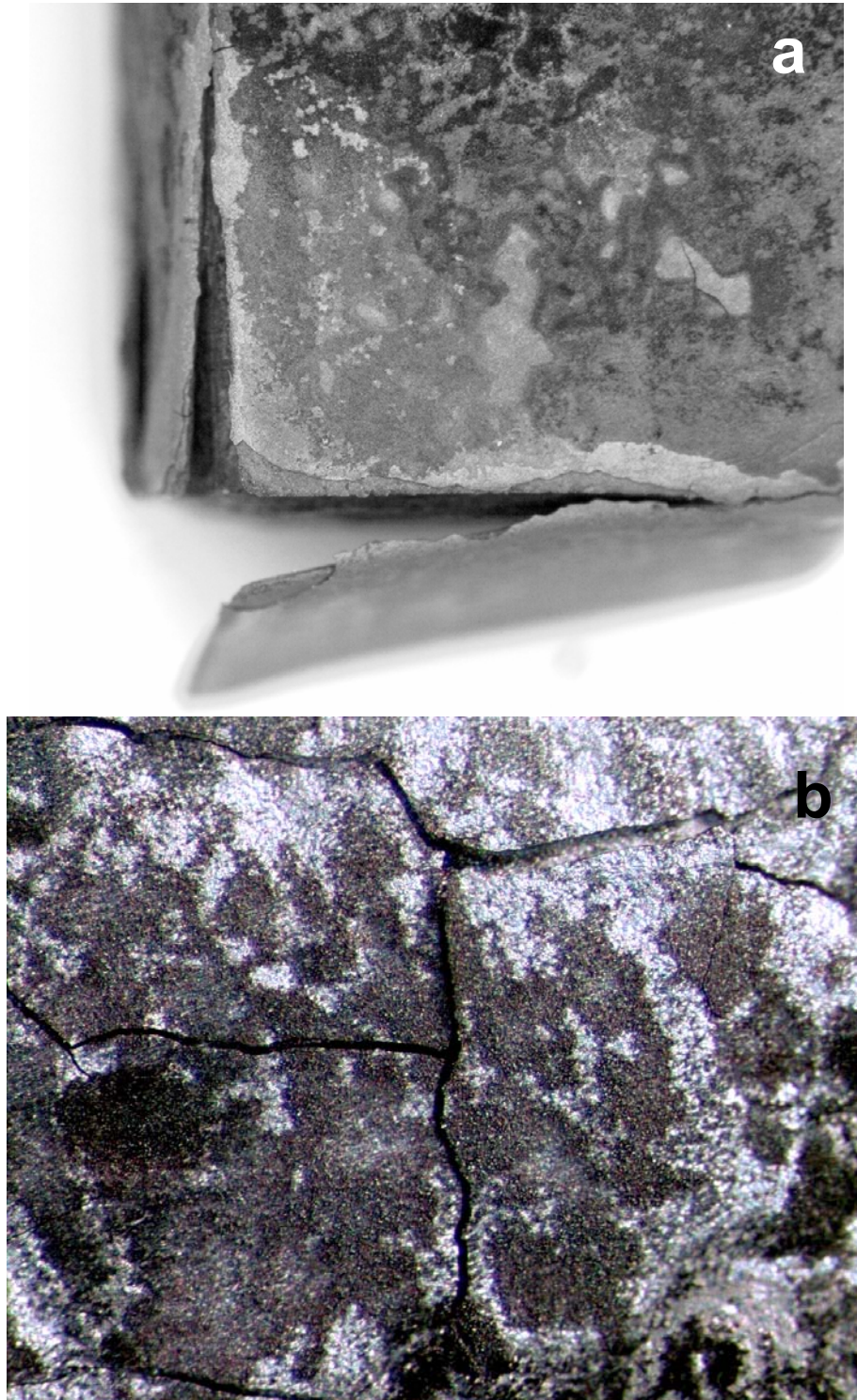


Figure 6.4: SA210 after first thermal cycle at 1000°C, (a) Spallation and detachment of Fe_3O_4 scale at edges, (b) heave cracking at the planer surface

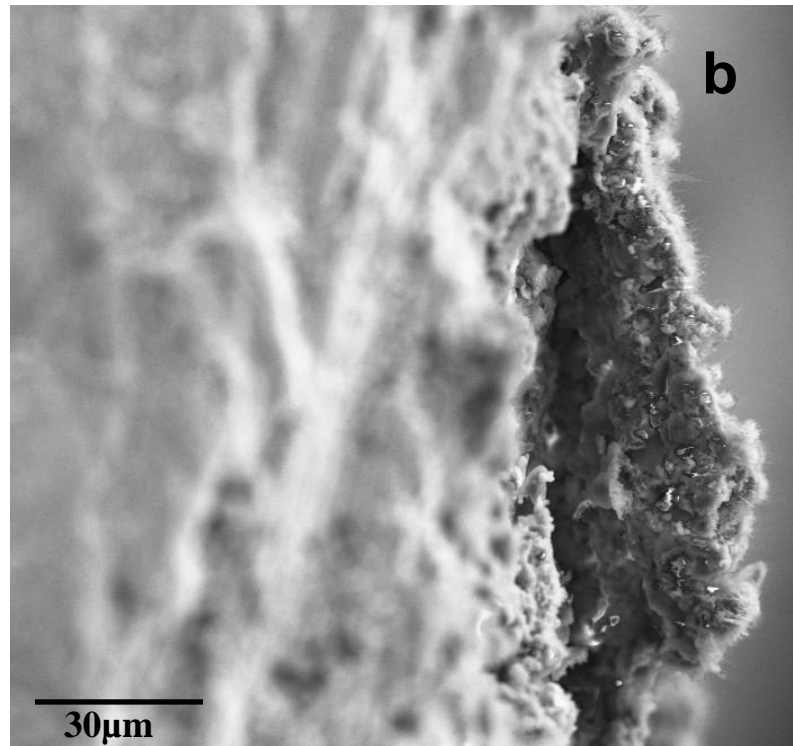


Figure 6.5: (a) Surface micrograph of unmodified Fe-Al coating after 10 one day thermal cycles from 1000°C to room temperature. (b) spalled region of scale

Table 6.1: Parabolic rate constants for oxidation of uncoated and coated samples under thermal cyclic conditions from 1000°C to room temperature every 24 hours.

Coating	K_p ($\text{mg}^2 \cdot \text{cm}^{-4} \cdot \text{day}^{-1}$)
None	1309.19
Fe-Al	3.98
Fe-Al-Y	3.07
Fe-Al-Hf	0.55

Figure 6.6 shows a surface microstructure of the scale developed after 240 hours of cyclic oxidation, where the wavy scale morphology for undoped Fe-Al coated sample suggests scale deformation due to stresses, whereas scales on Hf and Y modified coatings remained planer under cyclic oxidation conditions as shown in Figures 6.7 (a) and (b) respectively, and no spalling was observed in either case. The lack of wrinkling may be a result of low growth rate of scale or reduction in the stress relaxation levels that can deform the scale. Figures 6.8, 6.9 and 6.10 show the cross-section of alumina scale grown on Fe-Al, YFeAl and HfFeAl coatings respectively after 240 hours of thermal cycling at 1000°C. It is evident that RE doping changes the grain size of Al_2O_3 scales with Hf-modified scale with smallest grain size (<500nm) and unmodified coating with the largest grain sizes (>2 μm). This is in agreement with the previous results on the effect of reactive elements ^[137] with arguments that reactive element doping reduces the mean oxide grain size thus increasing the plasticity for better mechanical behavior of scale. The

results confirm the effect of reactive element on oxide microstructure and slow growth of oxide scale, but do not provide convincing evidence for improved scale spallation resistance which primarily depend on the local stresses in the oxide scale.

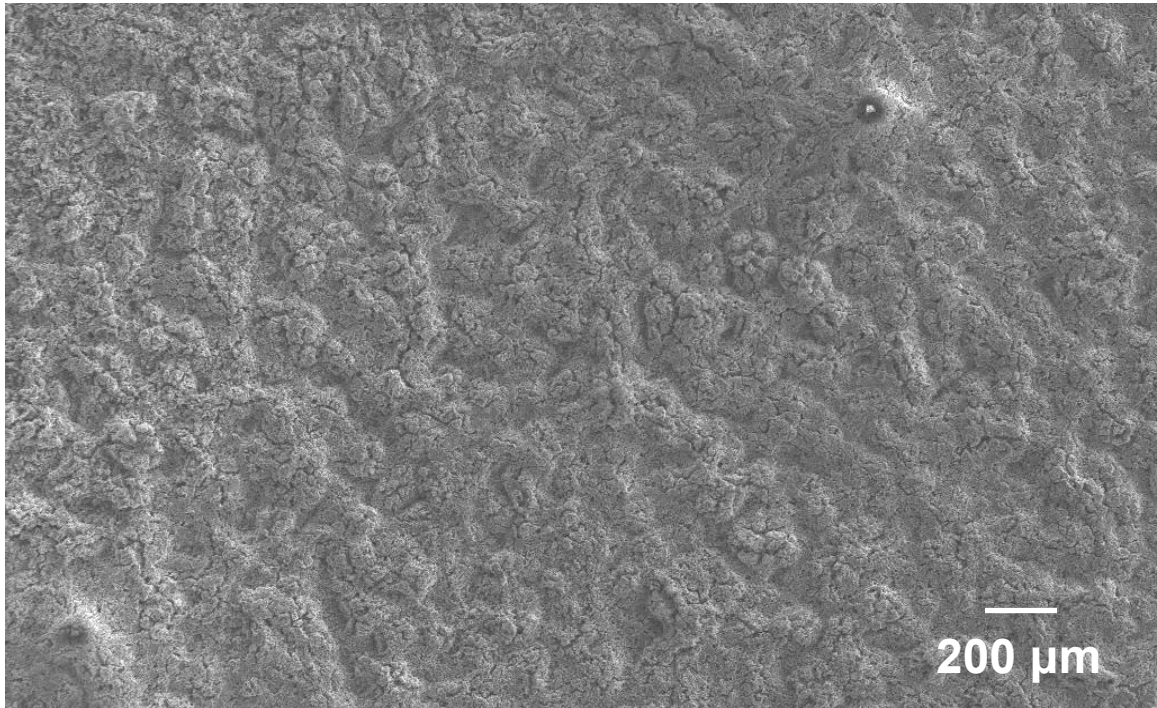


Figure 6.6: Rumpling or wavy morphology of alumina scale developed on Fe-Al coating after 240 hours of thermal cycling at 1000°C

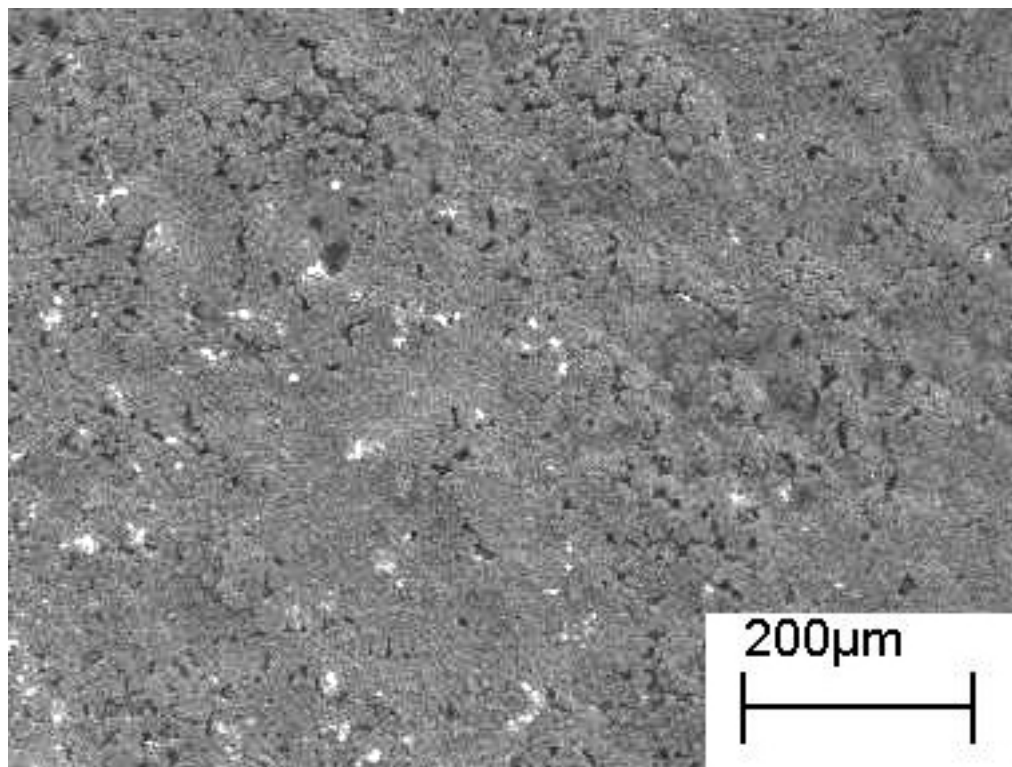
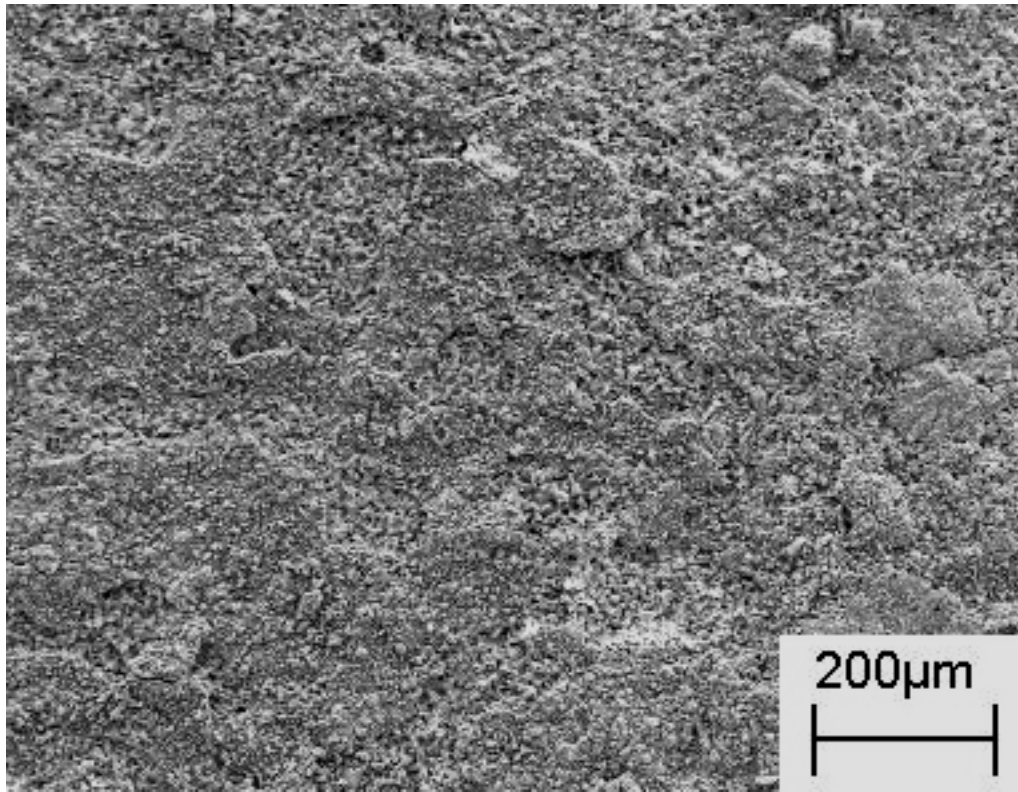


Figure 6.7: Surface morphology of scale developed after 240 hours of thermal cycling on (a) YFeAl , (b) HfFeAl

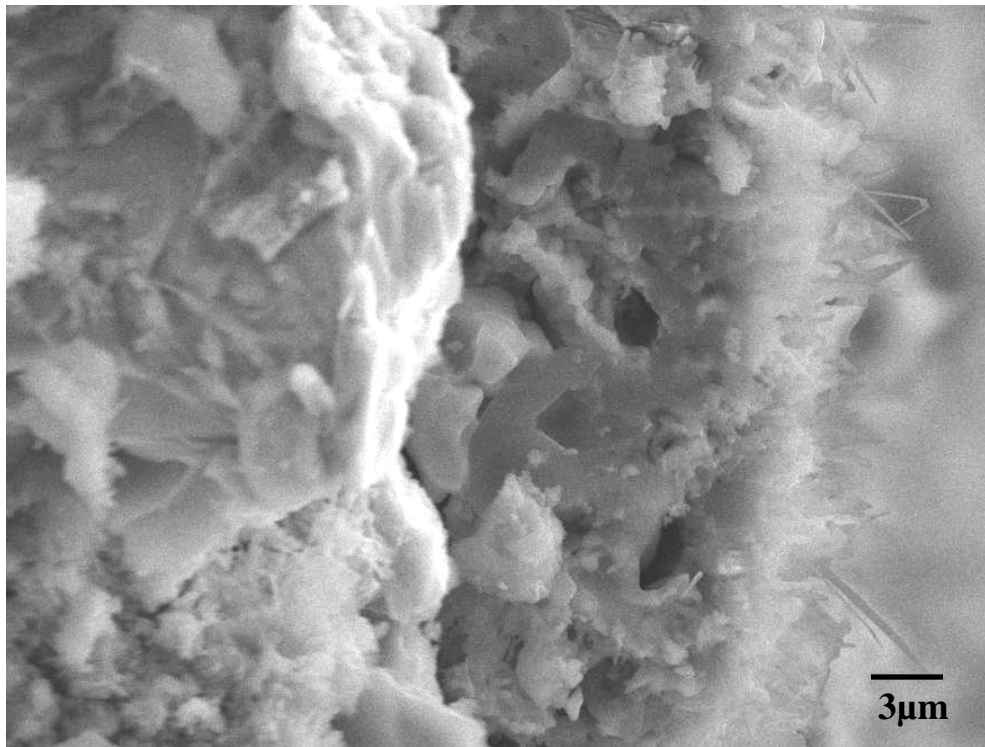


Figure 6.8: Cross-section after 10 one day thermal cycles for scale on Fe-Al coating,

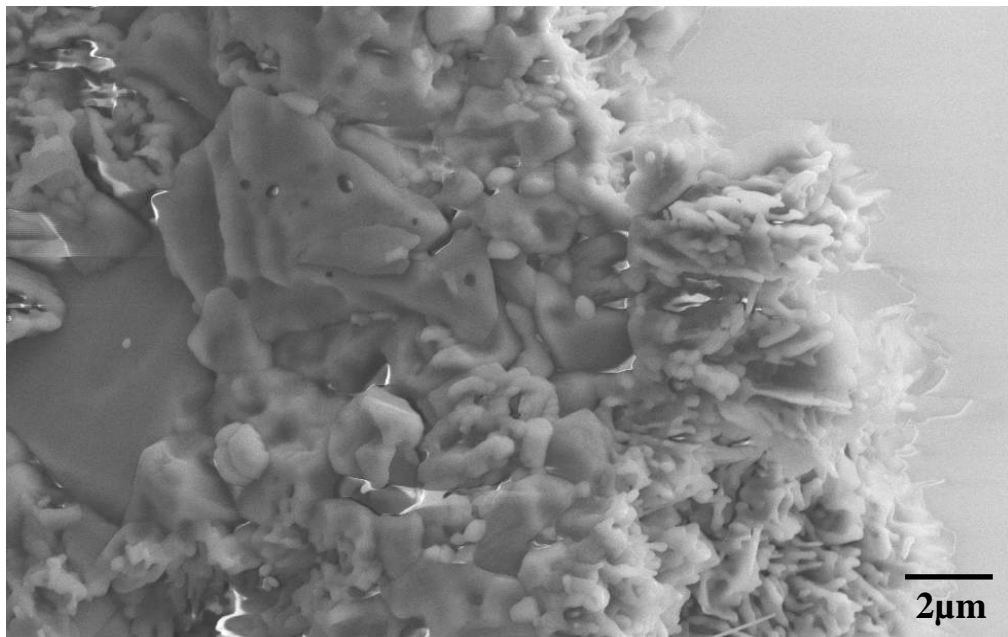


Figure 6.9: Cross-section after 10 one day thermal cycles for scale on YFeAl coating showing smaller mean grain size as compared to unmodified coating in Figure 6.8.

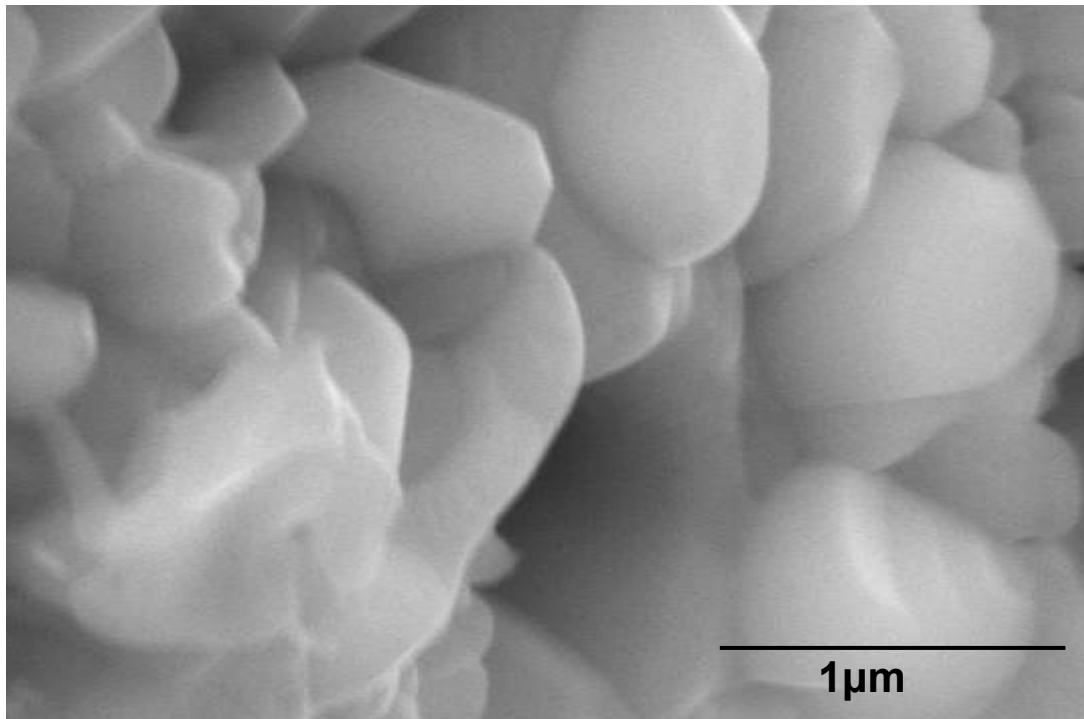
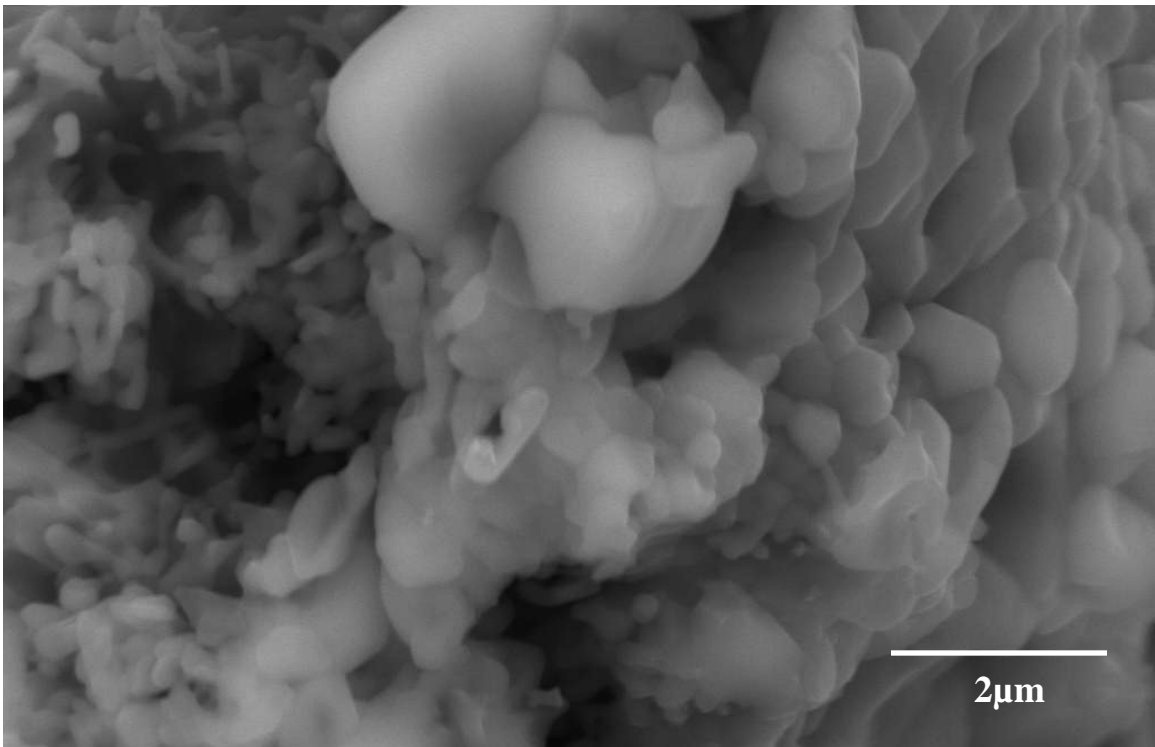


Figure 6.10: Cross-section after 10 one day thermal cycles for scale on HfFeAl coating with magnified view showing smaller grain size as compared to unmodified coating and Y-modified coating (see Figures 6.8 and 6.9).

6.3 STRESS DISTRIBUTION IN SCALES

Stress distribution on the scale, obtained from the piezpspectroscopic mapping, has been discussed in this section with two different types of maps presented here to elucidate the procedure used to measure stresses in the oxide scales:

1. 2D contour map showing the stress value at each point probed with laser spot of 30 μm .
2. 3D surface map showing the compressive stresses as “dips” and tensile stresses in the scale as “protrusions”. The surface plots can clearly show the stress variations in scale as a consequence of RE doping with higher roughness of surface being a measure of accommodation of stresses as compared to plane surface being due to relaxed/reduced stresses. Please note that “roughness” in this section refers to the stress variations and not the physical roughness of the scale surface.

A series of R-line fluorescence spectra were obtained from two sets of location using 20X objective lens. The first set of spectra was obtained near the edge of the sample and the second set was towards center of the sample on the flat part, well away from edges. The frequency shift for the Cr^{+3} fluorescence R-lines is proportional to the mean value of the normal elastic stress in the alumina averaged over the volume of probed area. Plastic stresses can accumulate during the cooling process. Thus, slow cooling from the oxidation temperature is expected to have a beneficial effect on resistance to spalling for the protective alumina films. This study was carried out at fast cooling rates by removing the sample from 1000°C to RT, thus there was possibility of introducing tensile stress in the oxide scale upon cooling and subsequent heating.

Due to the differences in the thermal expansion coefficient of corrosion scale and the substrate, stresses develop in the scale during each thermal cycle. With increasing the stress relaxation on cooling, the magnitude of the tensile stress also increases which may lead to cracking of the oxide after reheating to high temperature. Figures 6.11 and 6.12 show the stress maps of aluminized SA210 after 72 hours of oxidation (3 one day cycles) acquired at the corner and near the center of the sample respectively. Measured stress at the edge was in the range of 1GPa tensile to 6GPa compressive. A high peak of tensile stress was observed at the sample edge which corresponded to a localized bending in the oxide scale. In this area the scale surface is under similar conditions to an elastic beam in bending with the tensile stress present along the outside of the beam. Other points, where most of the stresses had been relieved, the average stresses over the probed volume were of very small magnitude. In the middle of the sample, where the edge effects are absent, the growth of oxide scale and its thickness is the primary reason for stresses present in the scale. Local growth stresses observed for aluminized SA210 varied significantly and were in the range of 1GPa tensile to 9GPa compressive as shown in Figure 6.12. Some localized sharp peaks of unreleased compressive stresses were observed on the scale surface. Stress measurements from the middle of sample, with flat surface, in Figures 6.11 and 12, show that the localized stresses were in the close vicinity of zero-stress areas suggesting that the scale can not accommodate higher stress values and relieves it by localized deformation or rumpling, as discussed in section 6.2 (Figure 6.6).

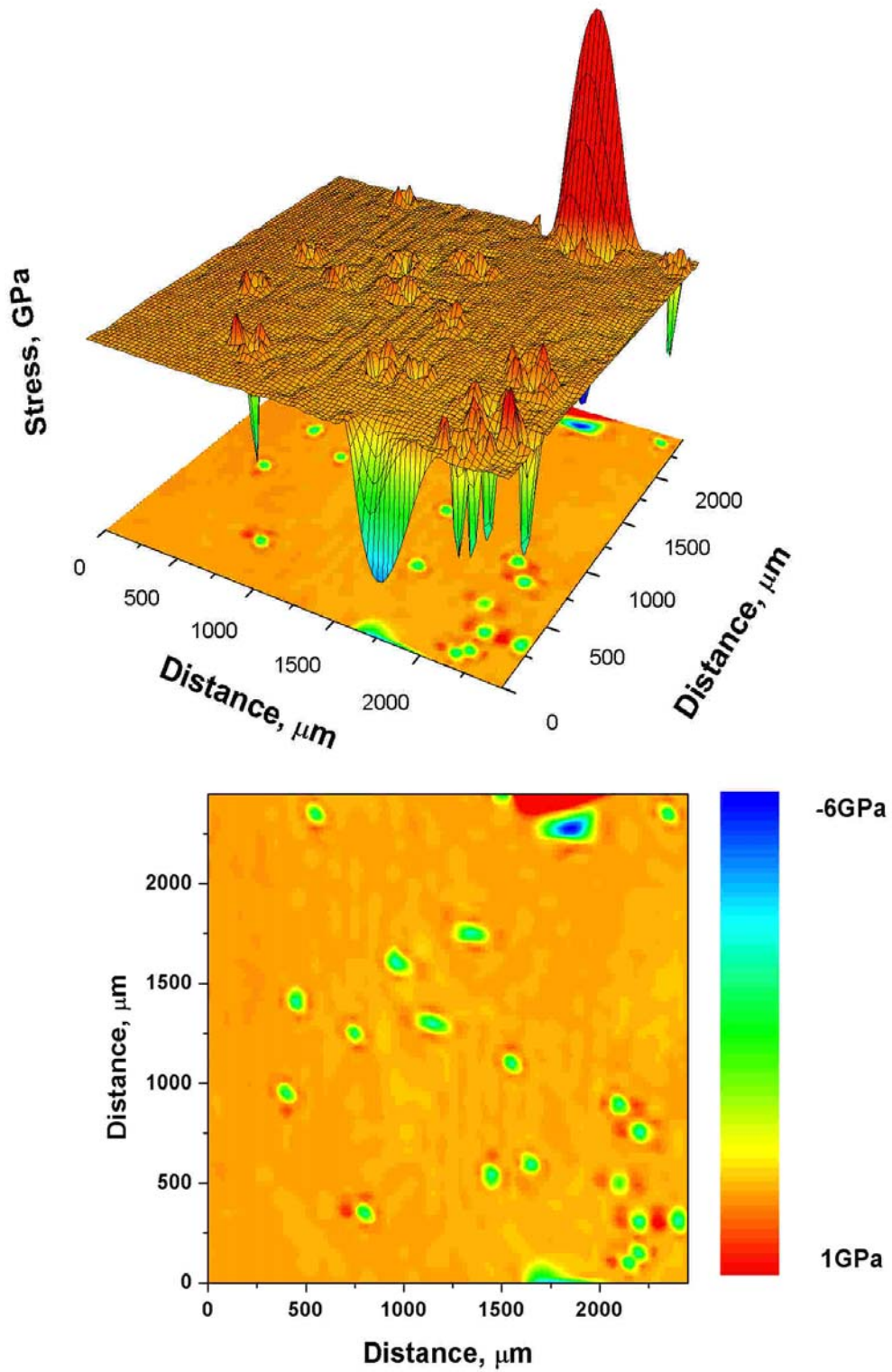


Figure 6.11: Surface and contour plots of stress maps of Fe-Al coating at the edge of sample after 72 hours of cyclic oxidation at 1000°C

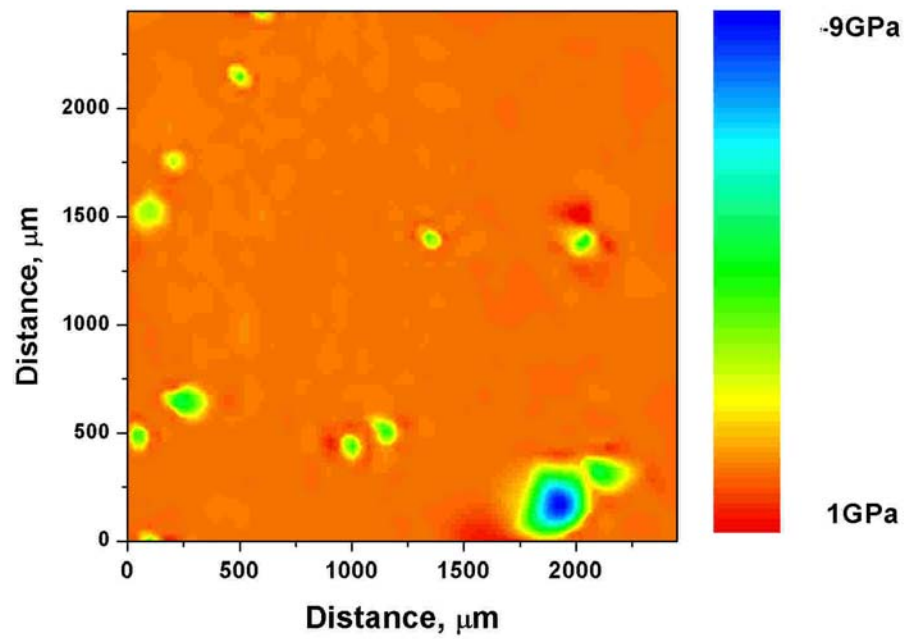
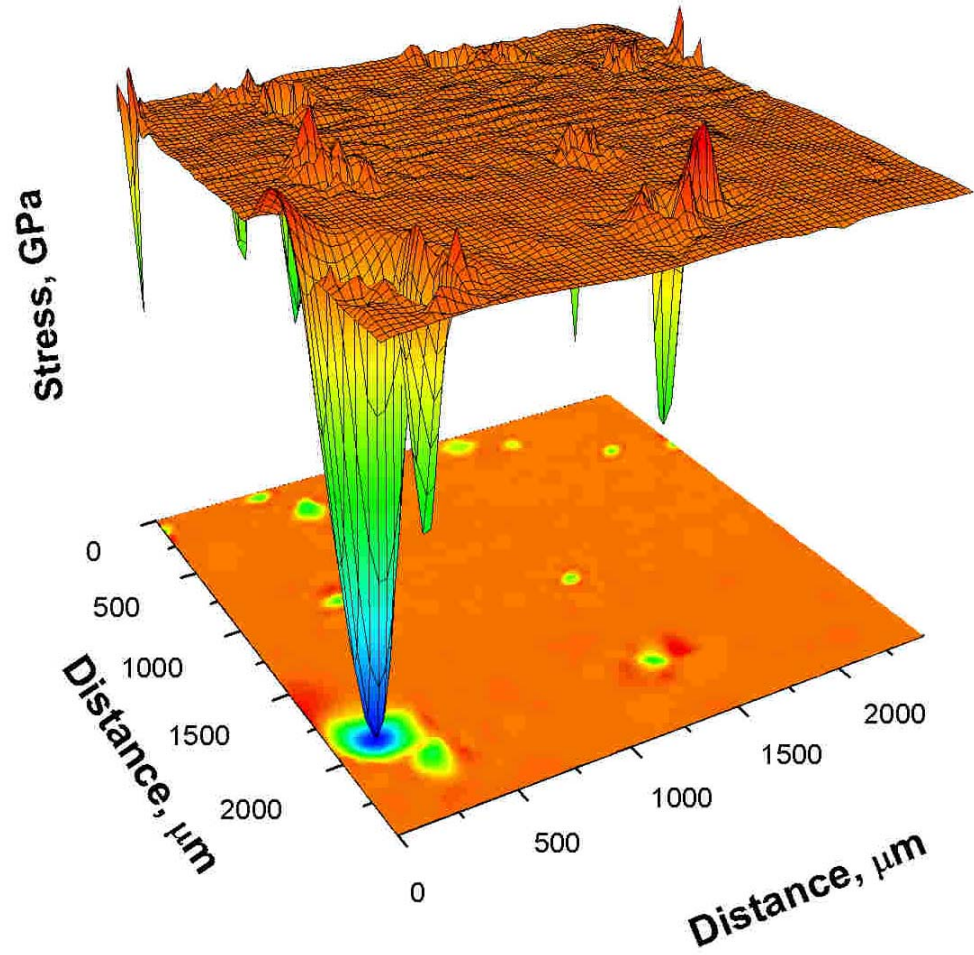


Figure 6.12: Surface and contour plots of stress maps of Fe-Al coating at the center of sample after 72 hours (3 cycles) of cyclic oxidation at 1000°C

Figures 6.13 and 6.14 show the surface and contour maps at edge and center respectively after 168 hours (seven one day cycles) of thermal cycling. Areas with high tensile stress were observed near sample edges, as discussed earlier. Localized spots with compressive stresses were also observed with the surface plot showing the low roughness indicating that the stress accommodation in the scale is low. Figures 6.15 and 6.16 show stress maps at the edge and near the middle of sample after 240 hours (ten one day cycles) of exposure. Results are similar to the results after seven day exposure. This data indicates that the average stress in the scale after thermal cycling is compressive with minimal stress accommodation.

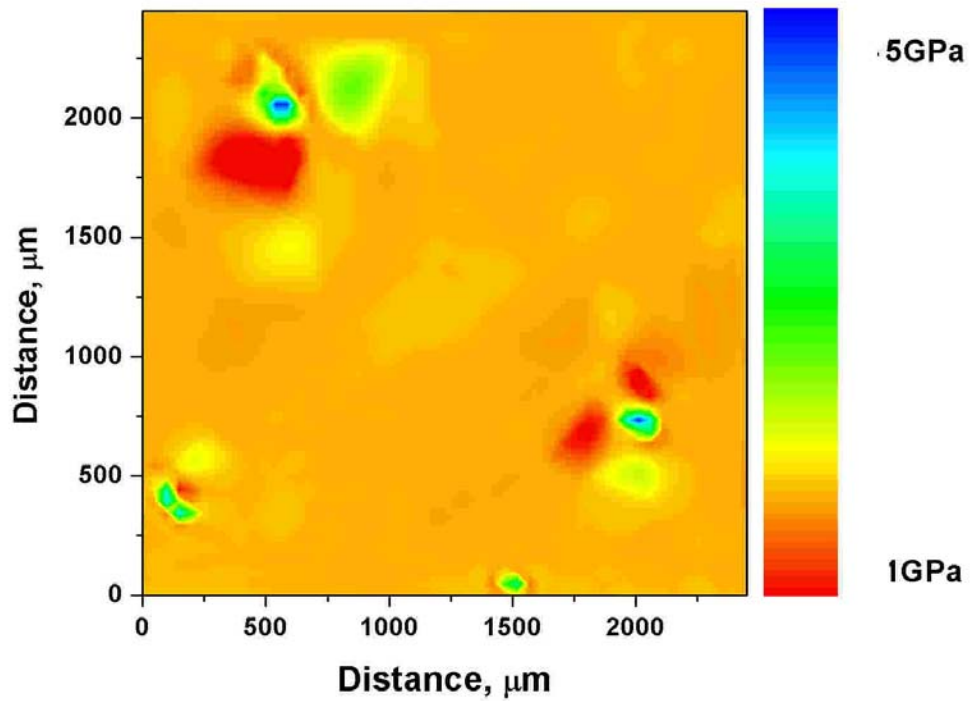
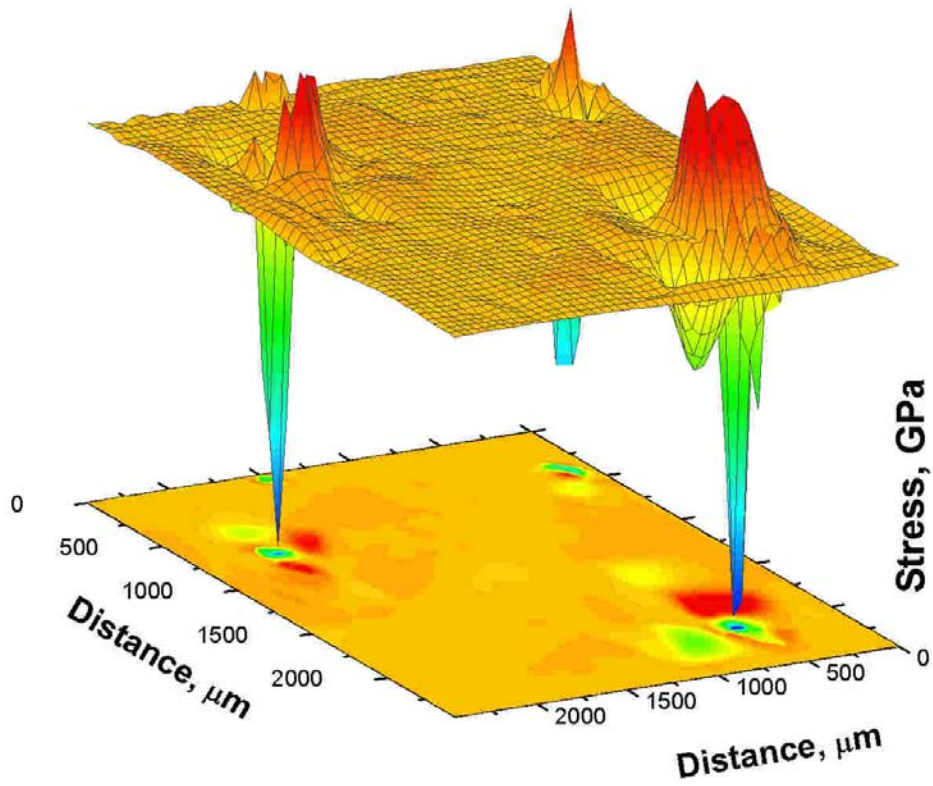


Figure 6. 13: Surface and contour plots of stress maps of Fe-Al coating at the edge of sample after 168 hours (7 cycles) of cyclic oxidation at 1000°C

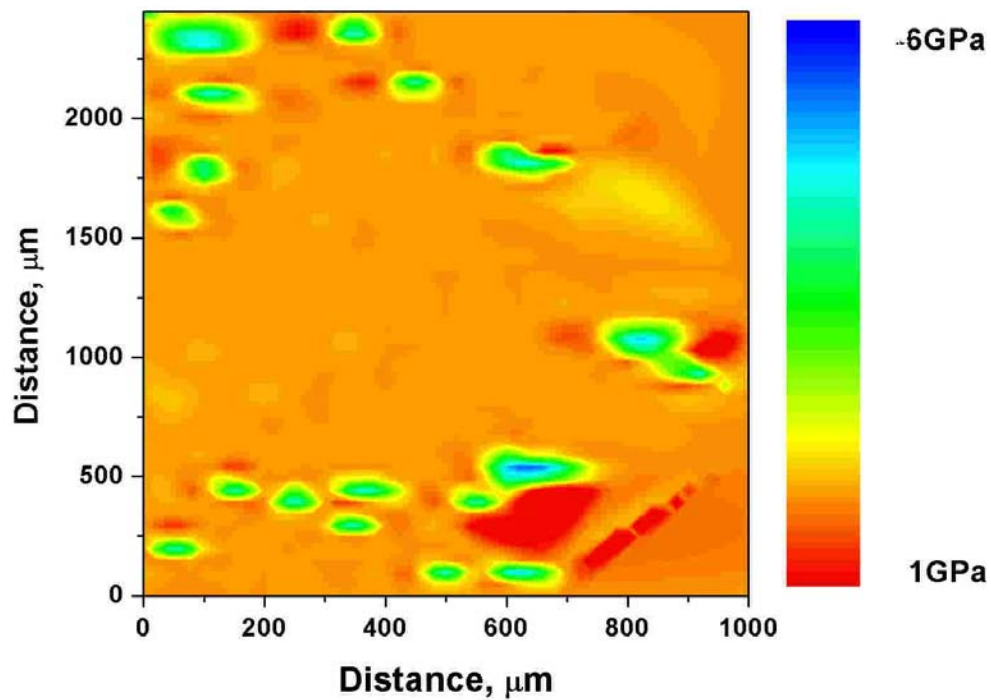
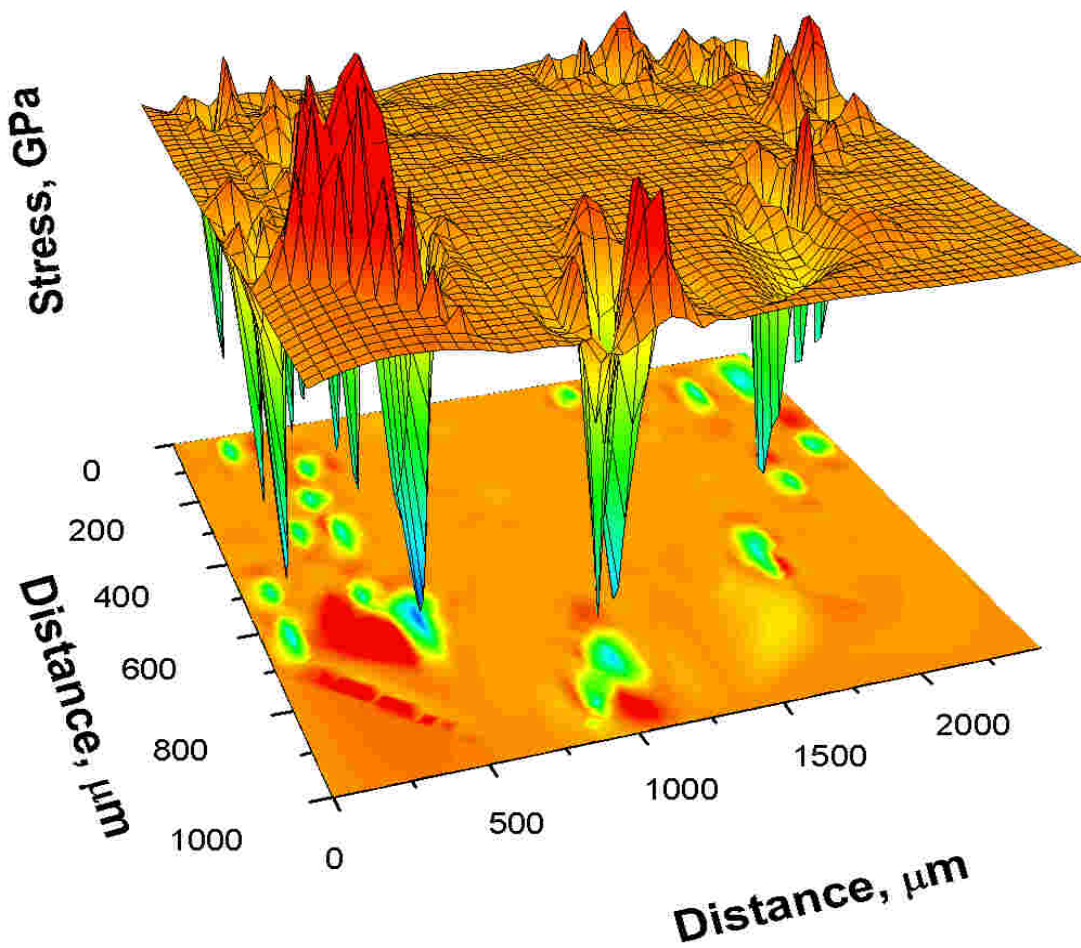


Figure 6.14: Surface and contour plots of stress maps of Fe-Al coating at the center of sample after 168 hours (7 cycles) of cyclic oxidation at 1000°C

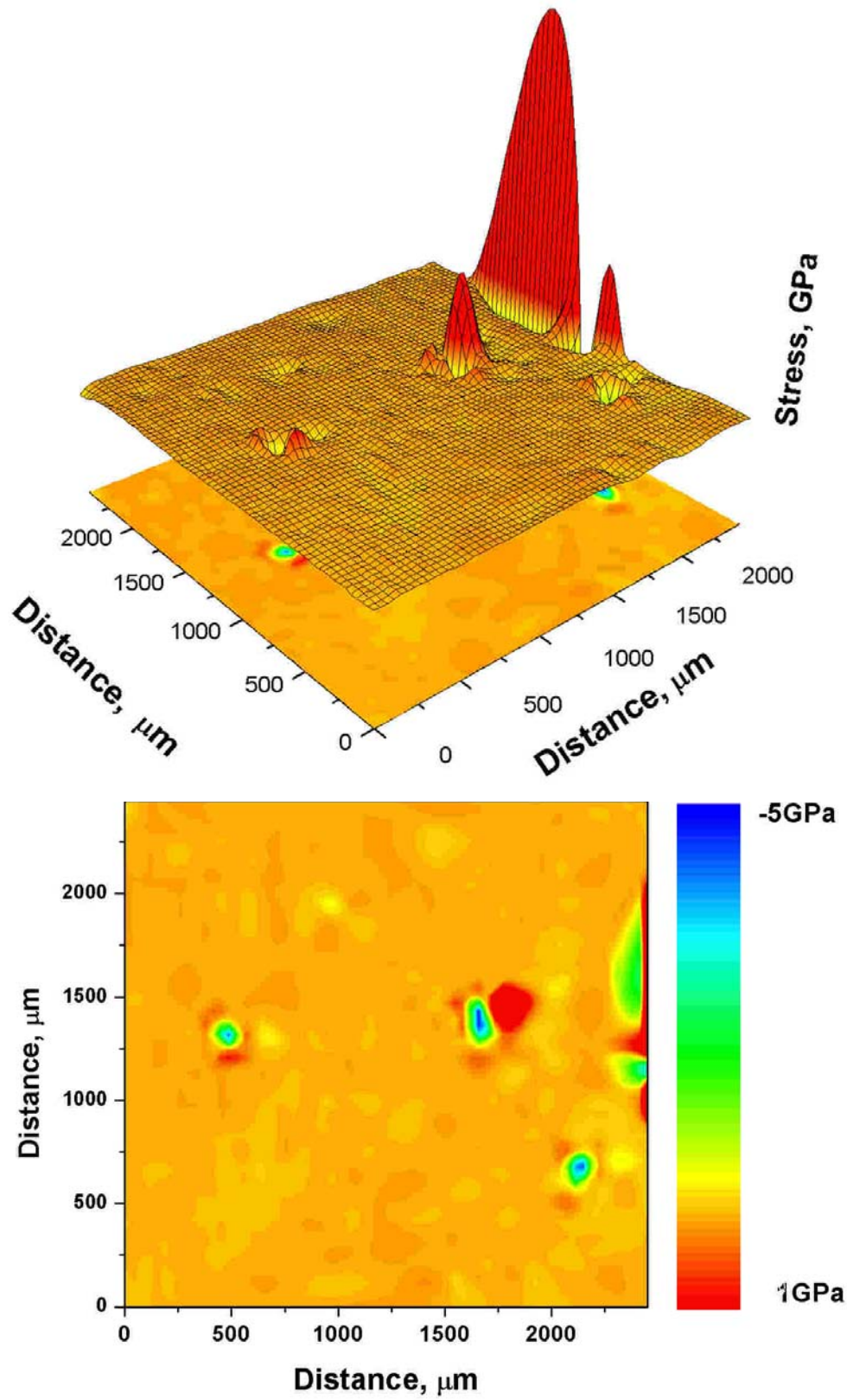


Figure 6.15: Surface and contour plots of stress maps of Fe-Al coating at the edge of sample after 240 hours (10 cycles) of cyclic oxidation at 1000°C

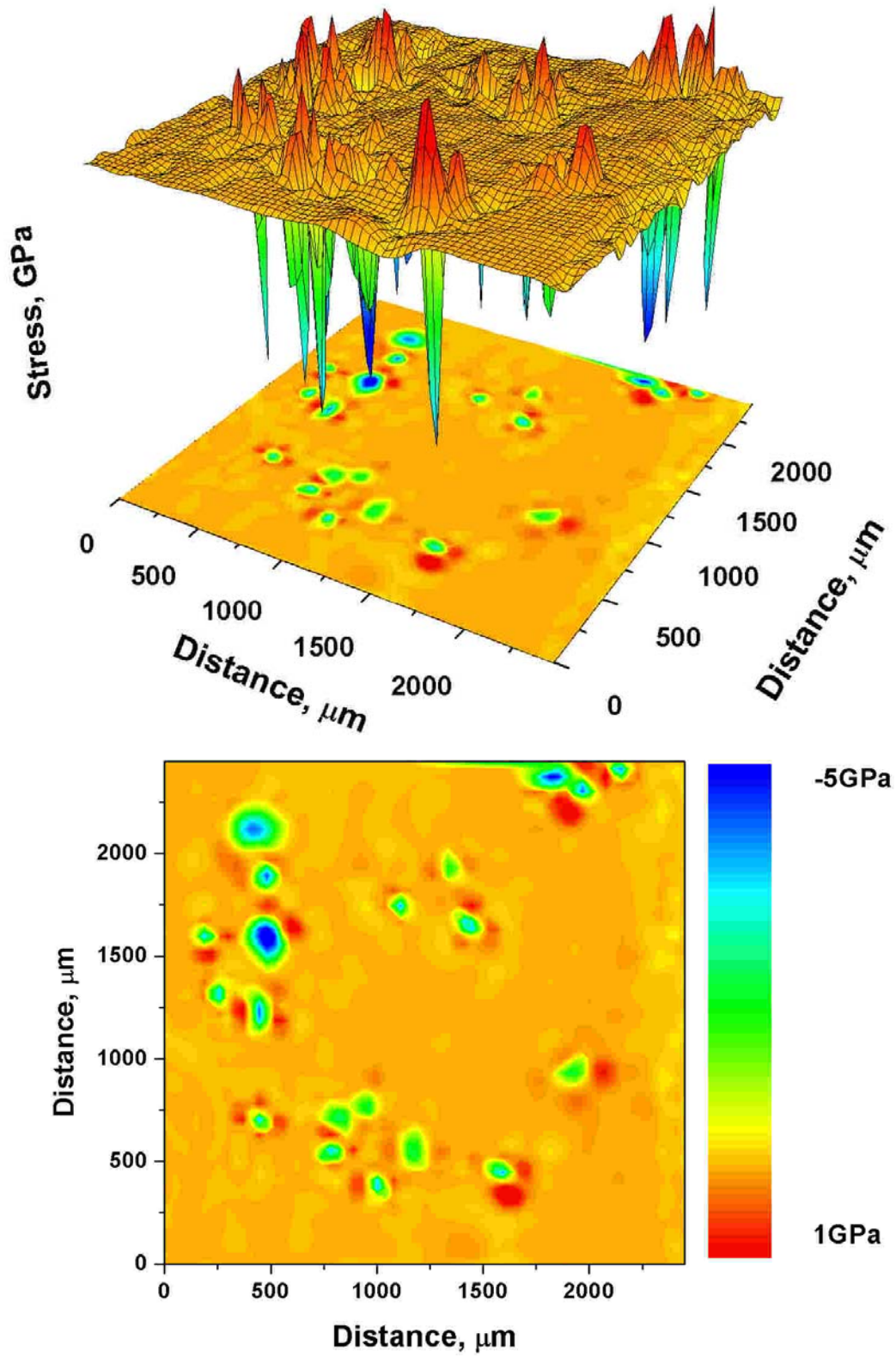


Figure 6.16: Surface and contour plots of stress maps of Fe-Al coating at the center of sample after 240 hours (10 cycles) of cyclic oxidation at 1000°C

Stresses were also measured on a HfFeAl coated sample, exposed to thermal cyclic conditions. Figures 6.17-6.22 show the corresponding stress maps at edges and middle for HfFeAl after 72 hours, 168 hours and 240 hours respectively. After 72 hours (3 one day cycles) as shown in Figures 6.17 and 6.18, there was a high variation (roughness) in the surface stress plot and contour plots. Compressive stresses in the range of 8GPa were measured, which shows that Hf addition in aluminide coatings have clearly resulted in an increase in the alumina scale's capability to hold the stresses during cooling and reheating. Edges showed more stresses than the middle of the sample as evident from data in Figures 6.17 and 18 indicating that edge/geometric stresses were almost 2GPa higher than the growth stresses measured in the middle of the sample. Thus edges resulting in higher spallation. After 168 hours (7 one day cycles) as shown in Figure 6.19 and 6.20, the roughness in the surface plots decreased but some tensile spikes were observed along with the compressive peaks suggesting that the Hf-modified alumina scale can accommodate both tensile and compressive stresses. Decrease in roughness of surface plots can be due to the growth of scale. For a thin scale, the probe scans the stresses due to interaction between scale and alloy and as the scale thickens, laser excites only the surface of scale rather than scale/alloy interface. After 240 hours (10 one day cycles), roughness decreased even more with edge of sample showing some spikes but plot at middle of sample being relatively flat (Figure 6.21 and 6.22) due to a relatively thicker scale.

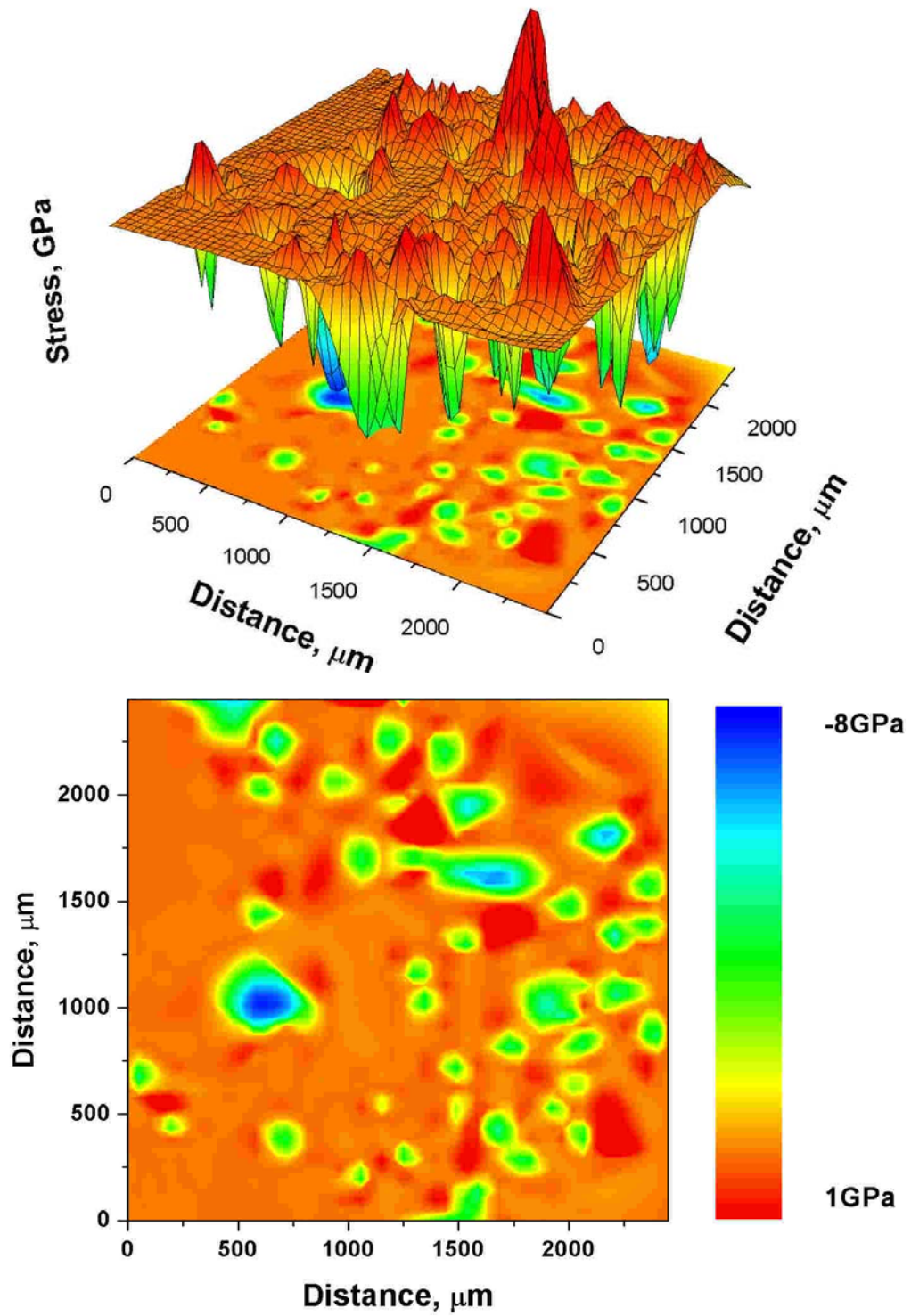


Figure 6.17: Surface and contour plots of stress maps of Hf-Fe-Al coating at the edge after 72 hours (3 cycles) of cyclic oxidation at 1000°C

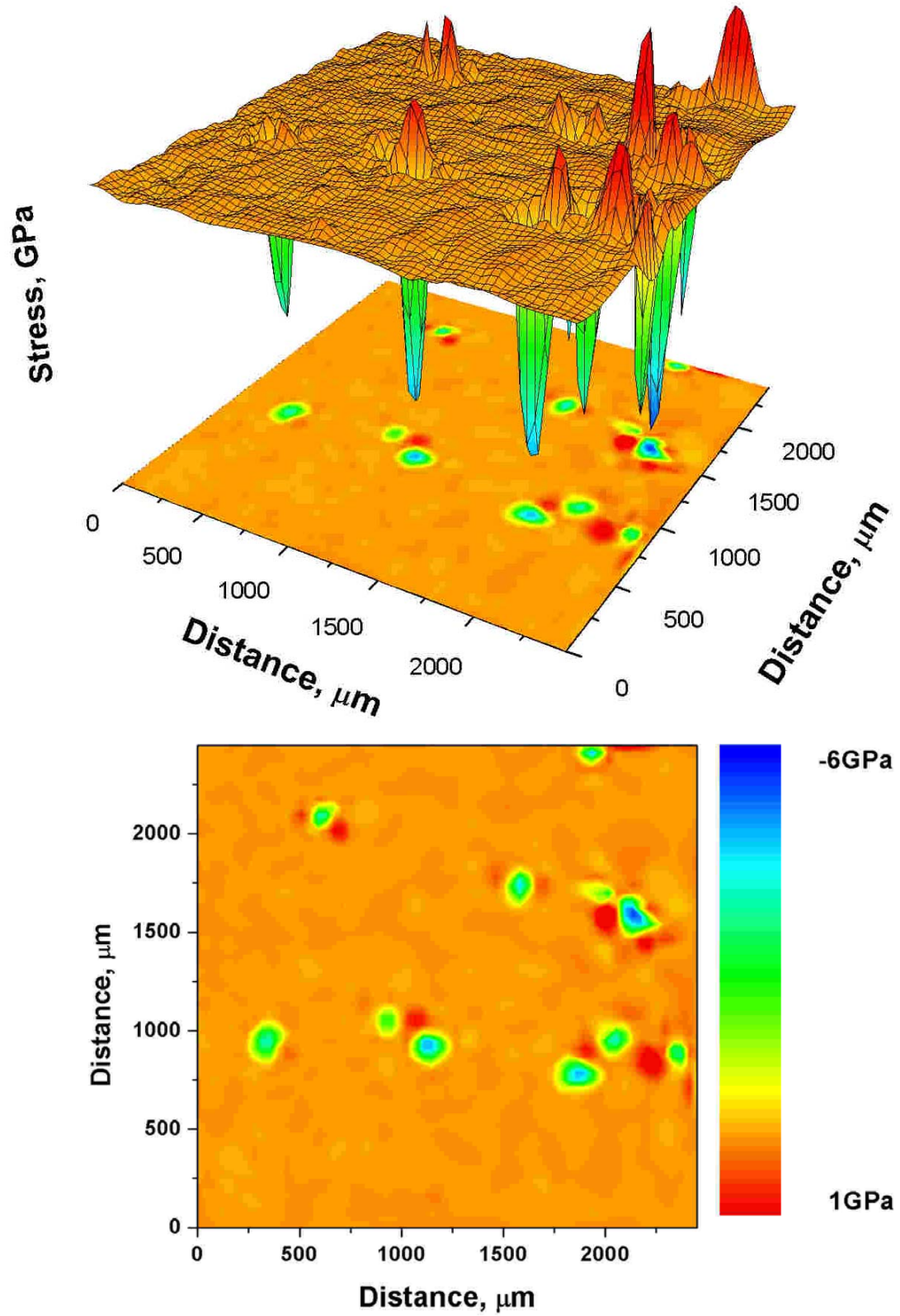


Figure 6.18: Surface and contour plots of stress maps of Hf-Fe-Al coating at the center of sample after 72 hours (3 cycles) of cyclic oxidation at 1000°C

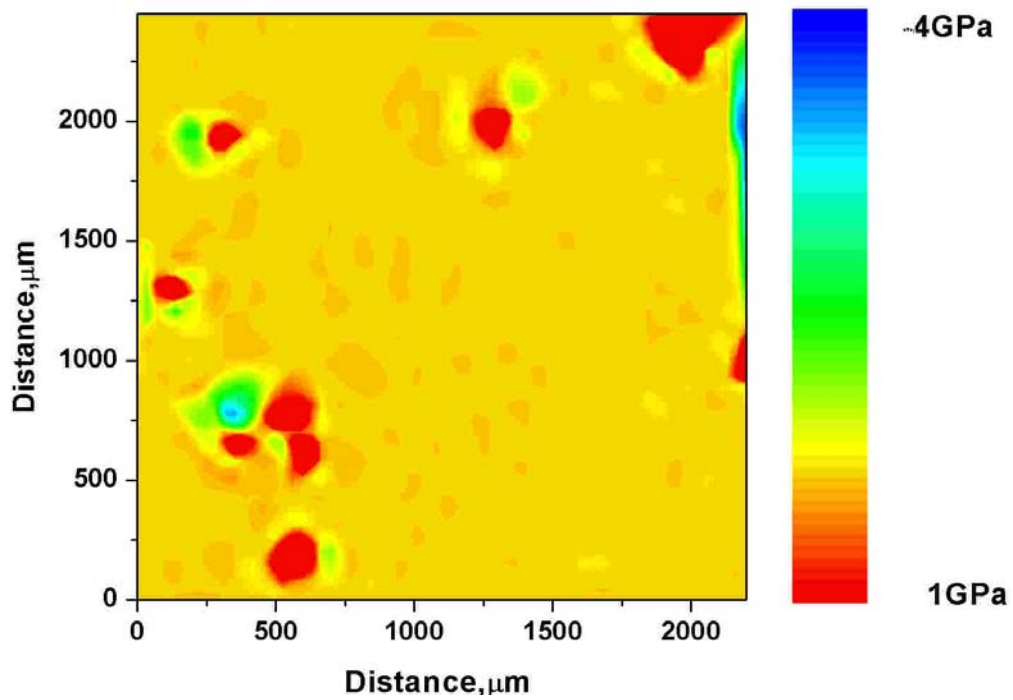
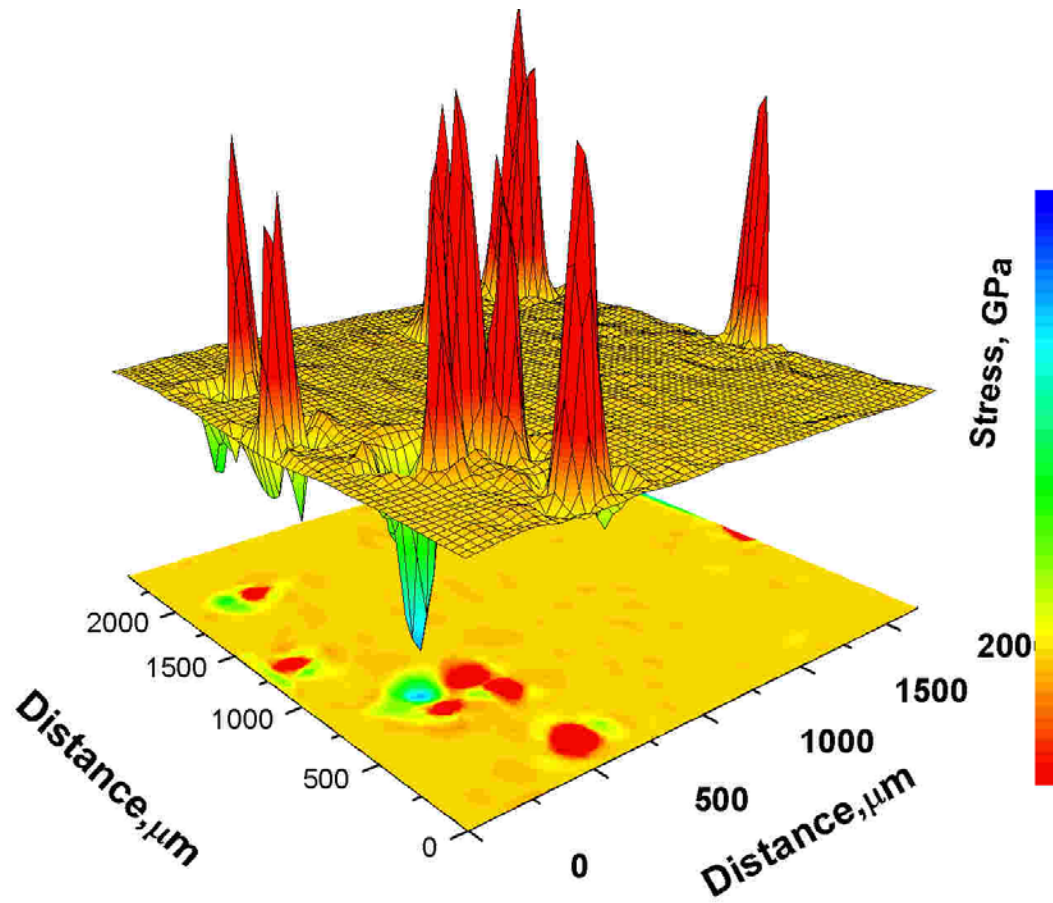


Figure 6.19: Surface and contour plots of stress maps of Hf-Fe-Al coating at the edge of sample after 168 hours (7 cycles) of cyclic oxidation at 1000°C

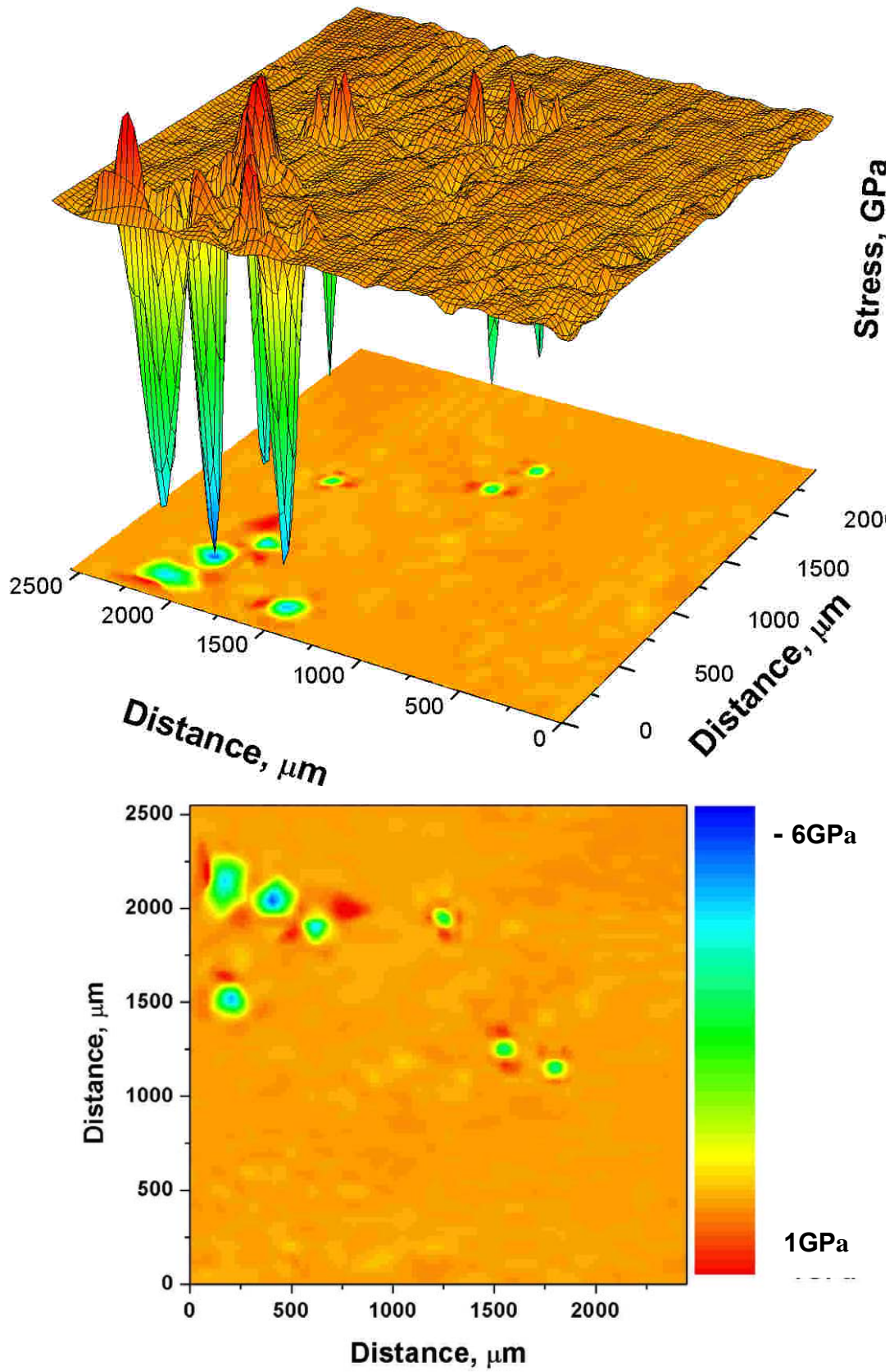


Figure 6.20: Surface and contour plots of stress maps of Hf-Fe-Al coating at the center of sample after 168 hours (7 cycles) of cyclic oxidation at 1000°C

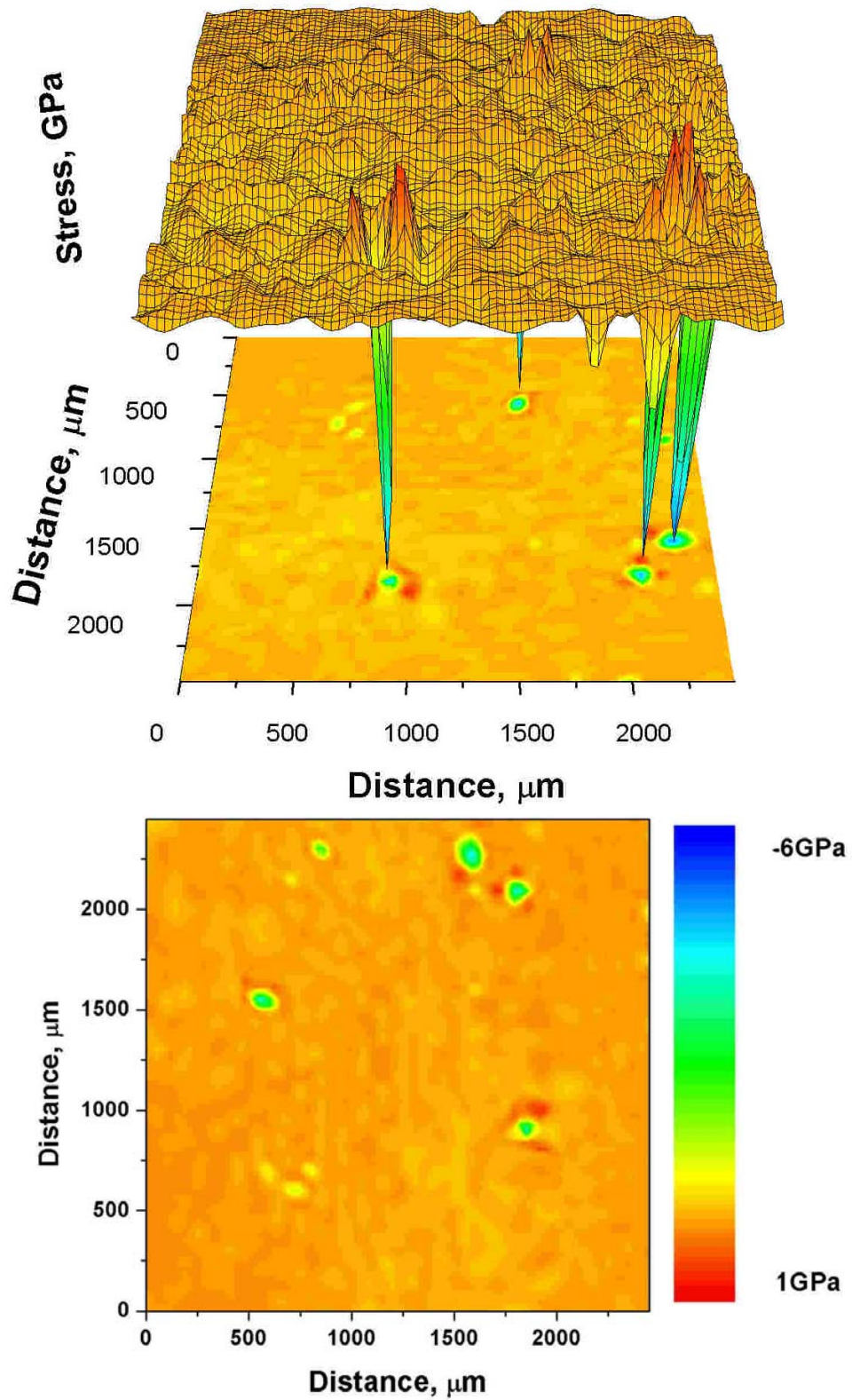


Figure 6.21: Surface and contour plots of stress maps of Hf-Fe-Al coating at the edge of sample after 240 hours (10 cycles) of cyclic oxidation at 1000°C

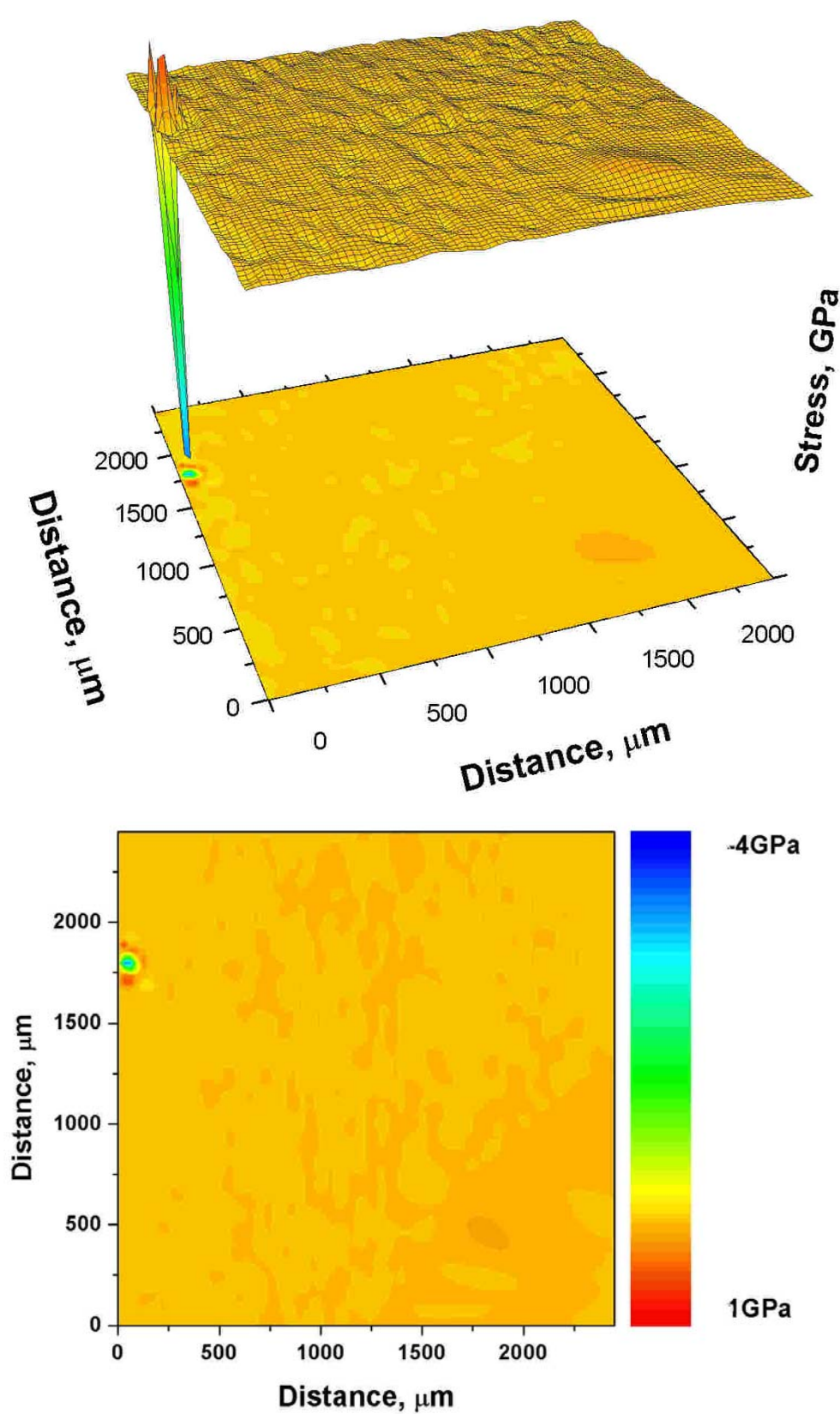


Figure 6.22: Surface and contour plots of stress maps of Hf-Fe-Al coating at the center of sample after 240 hours (10 cycles) of cyclic oxidation at 1000°C

Yttrium doped aluminide coatings showed very similar results to that observed for hafnium doped coatings. Corresponding surface and contour maps at edges and middle for YFeAl after 72 hours, 168 hours and 240 hours respectively are presented in Appendix C. Although a region of tensile stresses was observed in the middle of sample after 168 hours, weight change data did not show any large mass loss due to spallation as shown in Figure 6.3. After 240 hours of oxidation, stress maps showed some compressive peaks with surface plot being relatively flat due to thicker scales. Figure 6.23 shows the comparison of stress contour maps after 72, hours for Fe-Al, Hf-Fe-Al and Y-Fe-Al coatings respectively. It is evident that after 3 cycles, alumina scales on unmodified coatings showed no stress accumulation at edges while Hf and Y modified coatings showed excellent capability of holding stresses during thermal cycling. Middle of the sample probed for studying growth stresses showed stress accumulation range increased by 1GPa as shown in the color bar of the contour maps.

Mean stress measured over the complete grid was calculated by averaging all the measured stress points. Figures 6.24 (a) and (b) show average stresses developed in alumina scales at edges and middle of the sample as a function of thermal cycles for the unmodified, as well as Hf and Y modified coating respectively. Comparing Figures 6.24 (a) and (b), it is evident that stresses near the edge of the sample were more than twice of that at the middle, where stresses are predominately growth stresses irrespective of reactive element doping. Figure 6.24 suggests that reactive element doping can increase the capability of Al_2O_3 scale for stress accommodation. The most prominent effect of reactive element on stresses was observed after short exposure times when the scale was thin and the probed volume shows the stresses due to alloy/scale interface interaction.

However, as the scale grows thicker, the limitations in depth sensing capability of equipment makes it difficult to detect the reactive element effect. Stress mapping results from the thinner scales show that with longer exposure to thermal cycling, the scale, with RE, acquires a steadily increasing compressive stress; thus it does not achieve strain relief from plastic flow increasing the spallation resistance. Clearly, the scales can tolerate higher strain with the reactive element.

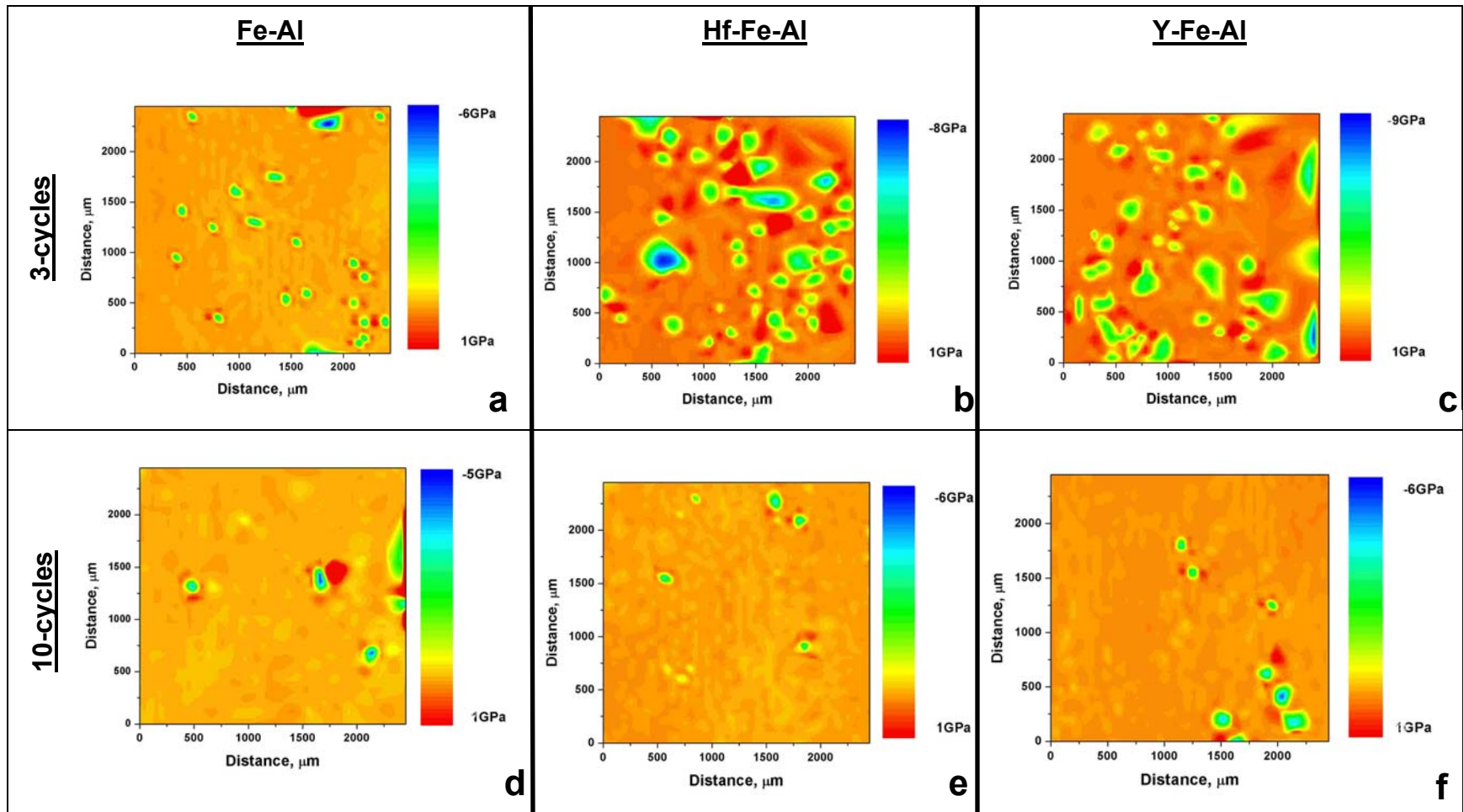


Figure 6.23: Stress distribution for FeAl , HfFeAl and YFeAl at corner grid after cyclic oxidation at 1000°C for (a) –(c) 72 hours, (d)-(f) 240 hours, respectively. Reactive element addition improves ability of scale to accommodate stresses.

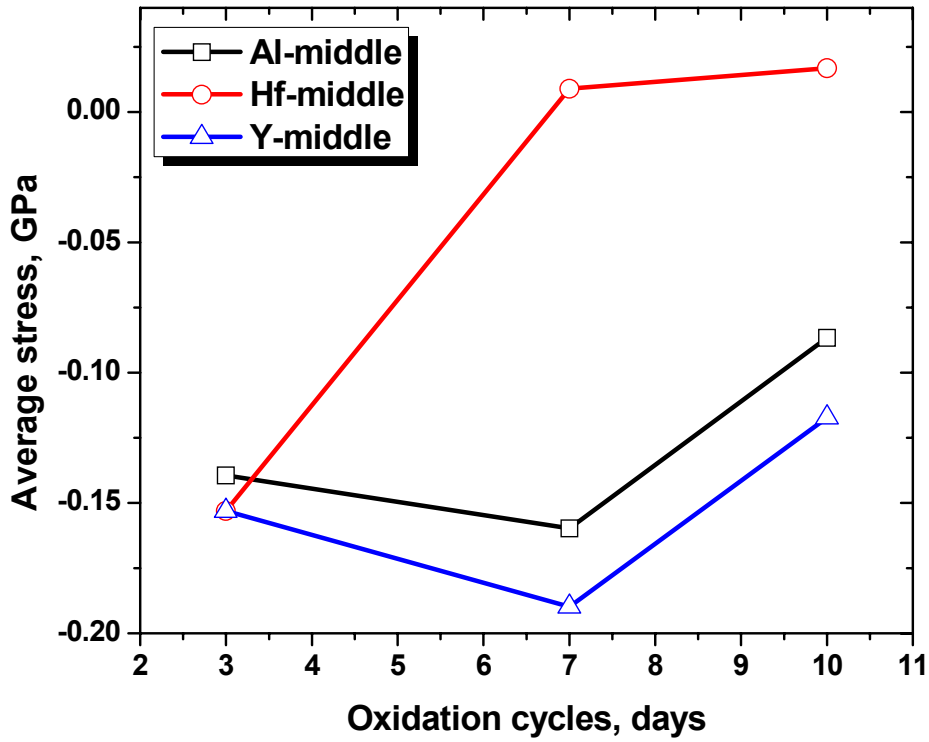
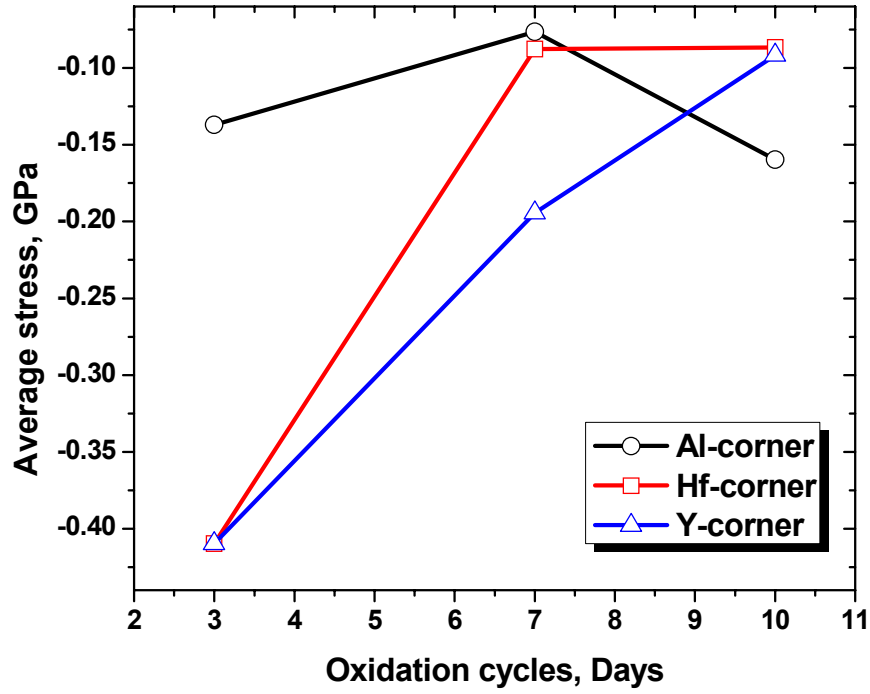


Figure 6.24: Effect of reactive element doping on average stress in alumina scales during cyclic oxidation at 1000°C: (a) at edge of sample, (b) at middle of sample

SUMMARY

1. Stresses in alumina scales were probed by photosimulated luminescence technique for samples with unmodified and Hf/Y modified iron aluminide coatings exposed to thermal cycling under oxidizing conditions.
2. RE doping in coatings showed alumina scales with smaller grain sizes as compared to unmodified coatings.
3. RE addition showed significant increase in the ability of alumina scale to accommodate the stresses and prevent stress relaxation which can lead to spallation.
4. Edges showed significantly higher stresses than planer surfaces due to geometrical effects.
5. As scale thickens, the technique was unable to show reactive element effect due to lower depth sensing capability of instrument. This can be overcome by using better optics equipped equipments such as confocal microscope.

CHAPTER VII

GENERAL CONCLUSIONS

Characterization of gaseous environments in the mid-furnace areas of a boiler have shown that gas compositions are not stable and may fluctuate frequently between oxidizing to reducing and sulfidizing, especially in areas with high corrosion rates of carbon steel tubes. Results of corrosion tests on carbon steel corrosion in fluctuating gaseous environment have shown that the fluctuating sulfidizing/oxidizing atmosphere in the mid furnace leads to an unstable layered sulfide/oxide scale formation at the surface. This resulted into scale cracking and spallation, and accelerated corrosion rate for carbon steel at 300°C. However, intermittent introduction of oxygen in sulfidizing environments resulted in adherent and protective scale with significant improvement in corrosion behavior. To further improve the corrosion behavior of carbon steel up to gasifier temperatures (800°C), chromized and aluminized coatings were prepared by pack cementation process on SA210 carbon steel. Chromizing of carbon steel showed the formation of chromium carbides and nitrides with 10-50µm thick coatings. Chromized SA210 carbon steel showed improved corrosion behavior under static sulfidizing environments ($p_{S_2} = 10^{-15}$ atm) up to 300°C, but failed at 600°C and 800°C with formation of porous chromium sulfide scale. Chromized coatings were also exposed to cyclic environments and the coating showed an excellent behavior at 300°C, as compared to the uncoated carbon steel, with the formation of adherent and protective scale.

Aluminizing was used to enrich the carbon steel surface with aluminium by formation of iron aluminide intermetallics on surface. Fe-Al pack cementation coating growth kinetics

was investigated in temperature range of 650-900°C, and 2-10 hrs of deposition time. Pack cementation coating showed an activation energy dependence on Al content of the pack, where a pack with 5 wt% Al showed E_a of 68.58 kJmol⁻¹ and with 10 wt% Al showed 93.78 kJmol⁻¹. Fe₂Al₅ coating phase showed strong {002} texture with outward growth of coating phase as columns perpendicular to the substrate surface. Formation of FeAl at 1000°C and Fe₂Al₅ at 800°C showed that the composition at surface can be controlled by changing the temperature. Mechanical properties of aluminide coatings were characterized by nanoindentation. Hardness and modulus showed strong dependence on Al content in coating. Hardness and modulus for aluminide coating was higher than carbon steel substrate. Interdiffusion zone showed intermediate values between the substrate and the coating.

Aluminide coating on carbon steel showed excellent oxidation and sulfidation resistance up to 800°C with formation of continuous protective Al₂O₃ scale under cyclic sulfidizing-oxidizing environment. Minor spallation on the order of 0.5 mg/cm² was observed for aluminide coatings in cyclic gaseous exposure. In air, corrosion rates for aluminide coated sample were low even at 1000°C. To improve the spallation resistance of alumina scales and consequent corrosion behavior in cyclic gaseous and thermal environments, Hf and Y modified coatings were prepared by co-depositing RE with Al by pack cementation process. Coating parameters were optimized to get desired coating compositions. Coating process at 1000°C showed higher concentration of RE co-deposition with the formation of nitrides and carbides along with the FeAl as a major coating phase, whereas coating process at 800°C showed lower RE deposition with Fe₂Al₅ as a major coating phase. RE modified Fe-Al coatings with different RE

concentrations were tested for corrosion behavior in simulated cyclic sulfidizing-oxidizing environments at 800°C. Coatings with higher RE content (> 1 at%) showed detrimental effect on corrosion behavior whereas equivalent coatings with relatively lower RE content (<0.5 at%) showed improved corrosion behavior in high temperature cyclic gaseous environments. A mechanism for corrosion behavior in fluctuating environments for iron aluminide coating containing RE has been proposed. The similar mechanism can also be extended to the alloys containing different amounts of RE in similar environments. RE modified and unmodified Fe-Al coatings were also tested for thermal shock resistance at 1000°C by cycling between 1000°C and room temperature in air. RE doping in coatings showed alumina scales with smaller grain sizes as compared to unmodified coatings. Oxidation resistance of coatings was found in the order:



Stresses in alumina scales were probed by photosimulated luminescence technique for samples with unmodified and Hf/Y modified iron aluminide coatings exposed to thermal cycling under oxidizing conditions. RE addition showed significant increase in the ability of alumina scale to accommodate the stresses and prevent stress relaxation which can lead to spallation. Edges showed significantly higher stresses than planer surfaces due to geometrical effects. As scale thickens, the technique was unable to show reactive element effect due to lower depth sensing capability of instrument. This can be overcome by using better optics equipped equipments such as confocal microscope.

Scientific Accomplishments

Industrial environments are generally considered non-fluctuating while testing alloys application performance. This study showed that fluctuating environments is an added failure mode with thermal cycling, and can significantly affect the lifetime of industrial equipments. Unstable industrial environments characterization showed that surface gas compositions in contact with materials can be very unstable as compared to stable bulk gaseous compositions.

Chromization/aluminization of carbon steel and kinetics of coating growth provides better understanding of the coating growth process and control over vapor deposition techniques. Effect of fluctuating environments on coatings corrosion provides better understanding for selection of materials for sulfur-oxygen containing environments. Mechanism of coatings failure mode in cyclic gaseous environments has been proposed and it has been shown that fluctuating environments can significantly induce spallation of protective scale due to formation of sulfides.

Reactive element modifications of aluminized carbon steels showed the effect of different RE concentrations in coatings with:

- High RE concentration being detrimental
- Low RE content being beneficial

Mechanism has been proposed for corrosion behavior of RE modified Fe-Al coatings in cyclic gaseous environments, which shows the conversion of RE at grain boundaries to respective sulfides leading to accelerated corrosion in sulfur containing environments. RE ability to inhibit outward metal diffusion was proved to be invalid in sulfur containing environments due to formation of grain boundary sulfides. Stresses measurements after

thermal cycling in scale showed the changes in mechanics of scale due to RE additions. This contributes to the ongoing debate of reactive element effect and further validates that the scale ability of stress accommodation is the primary reason for spallation resistance. Stress mapping through automated photoluminescence piezospectroscopy provides a fast and high spatial resolution alternative for stress measurements to XRD.

APPENDIX A

GAS COMPOSITION MEASURED IN KRAFT RECOVERY BOILER

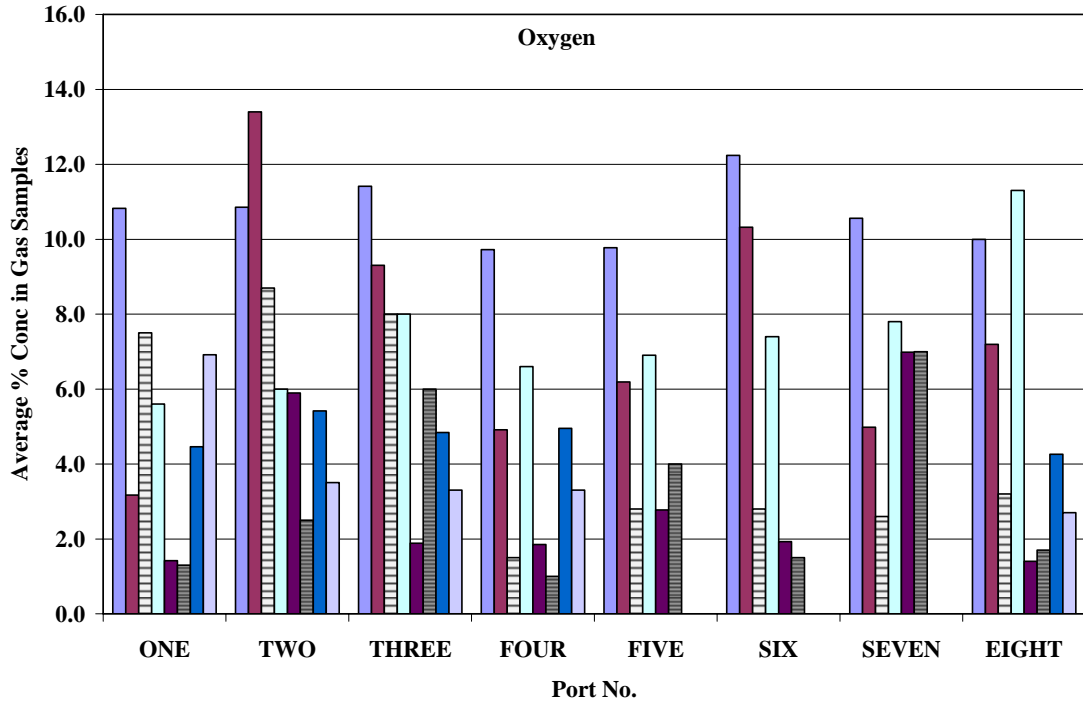


Figure A-1: Concentration of O₂ measured in kraft recovery boiler

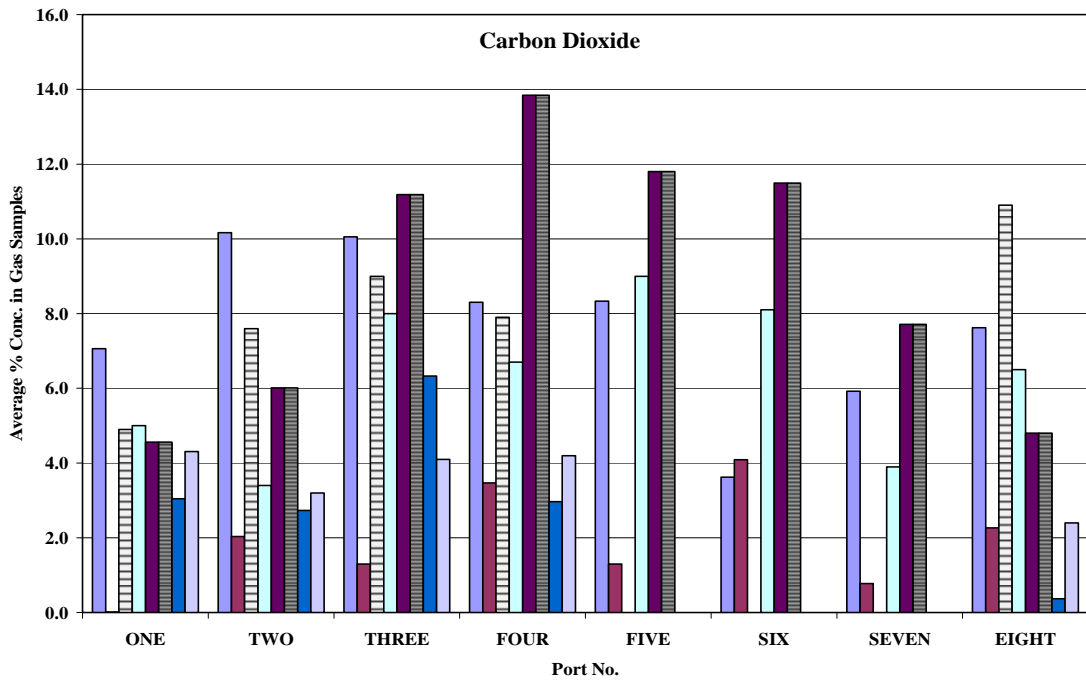


Figure A-2: Concentration of CO₂ measured in kraft recovery boiler

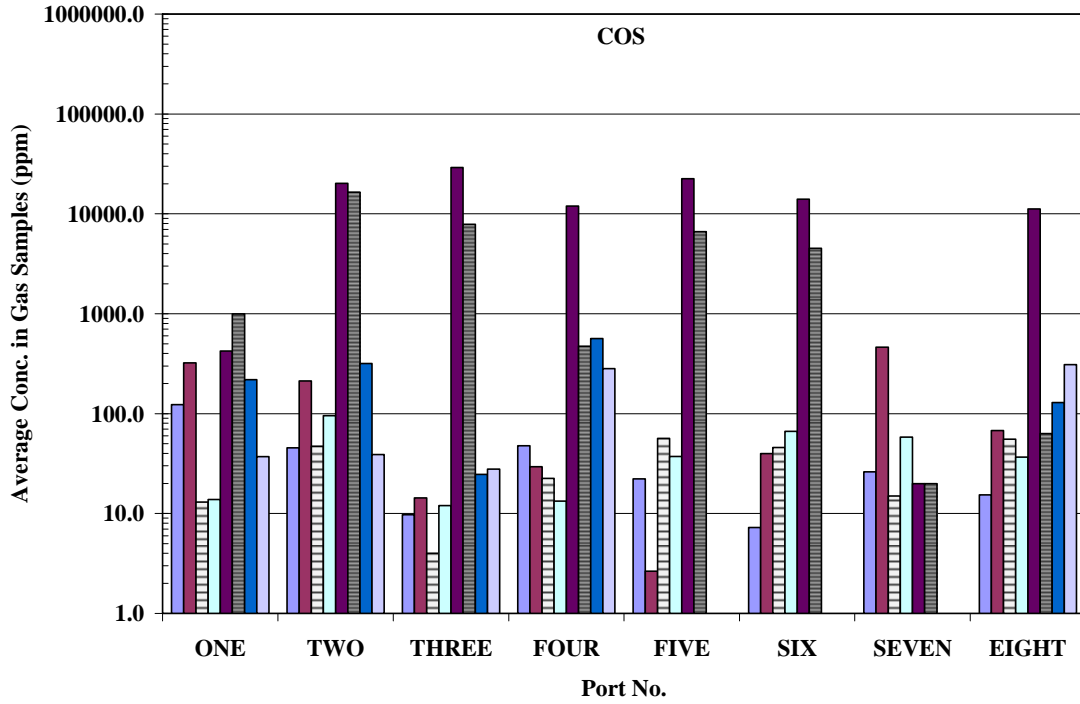


Figure A-3: Concentration of COS measured in kraft recovery boiler

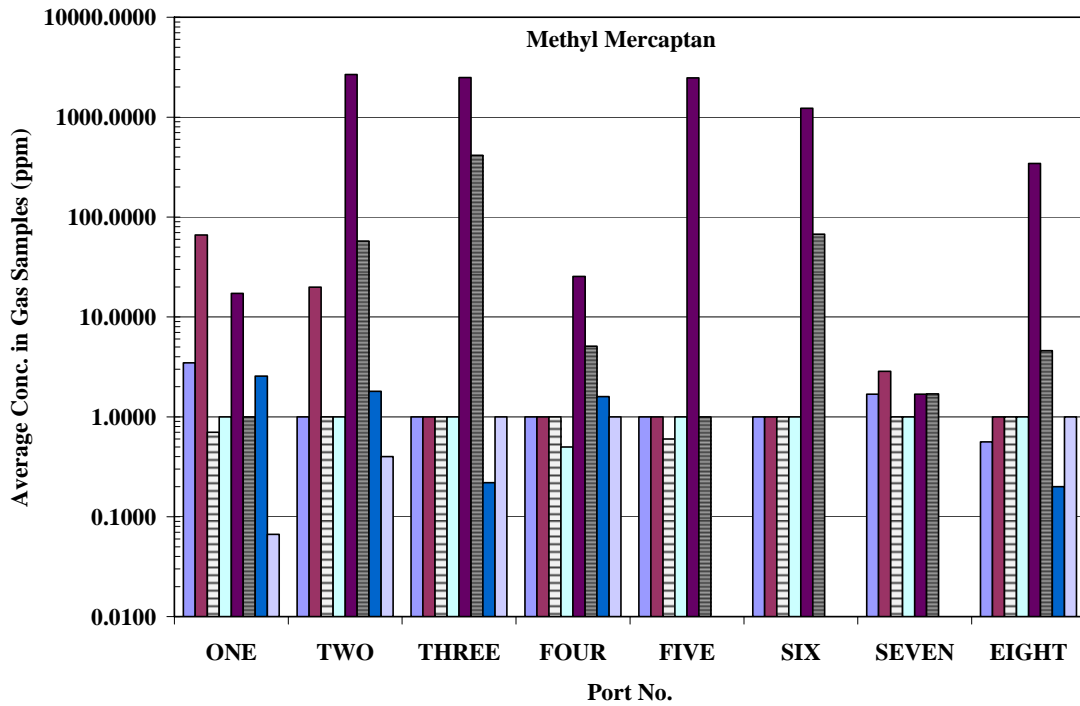


Figure A-4: Concentration of CH₃S measured in kraft recovery boiler

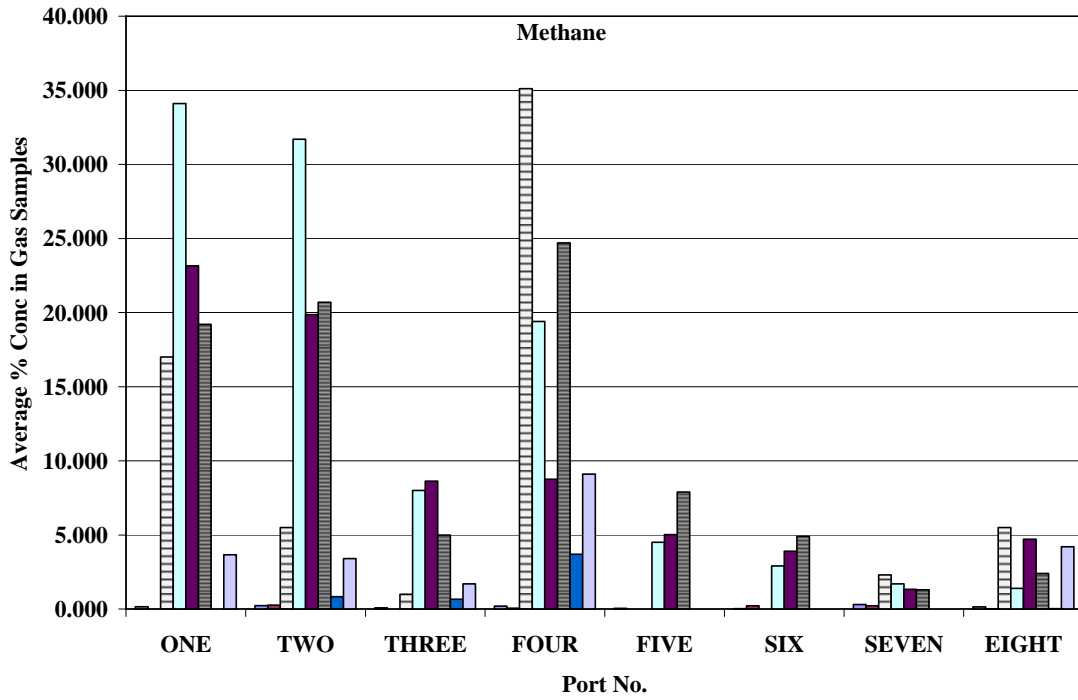


Figure A-5: Concentration of CH₄ measured in kraft recovery boiler

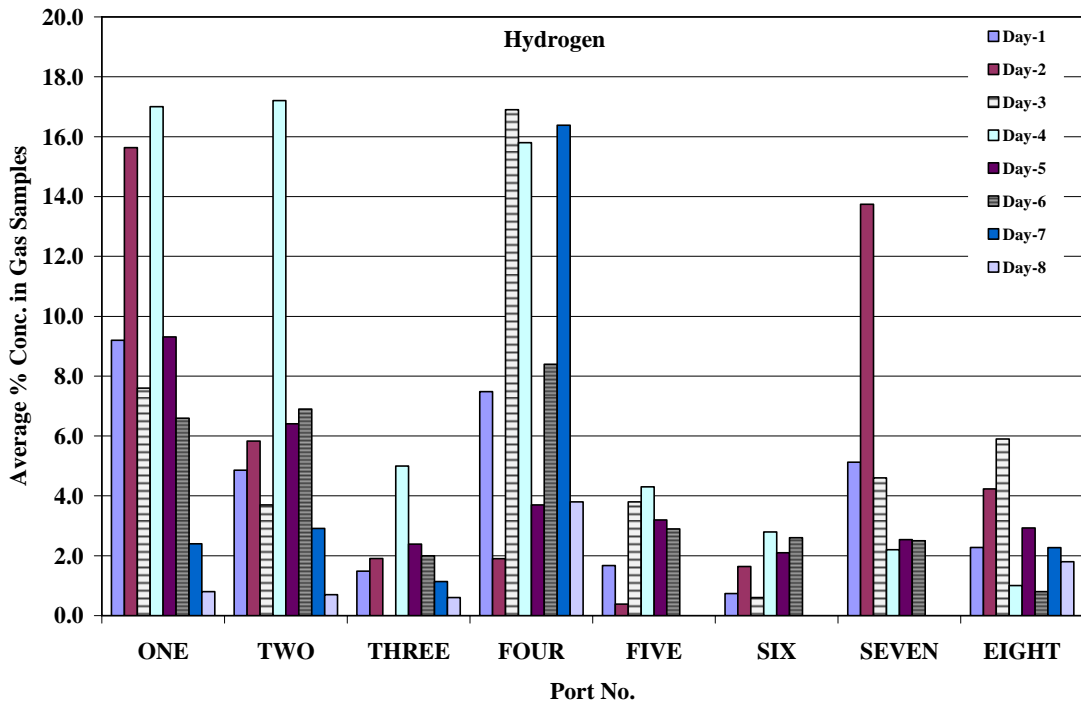


Figure A-6: Concentration of H₂ measured in kraft recovery boiler

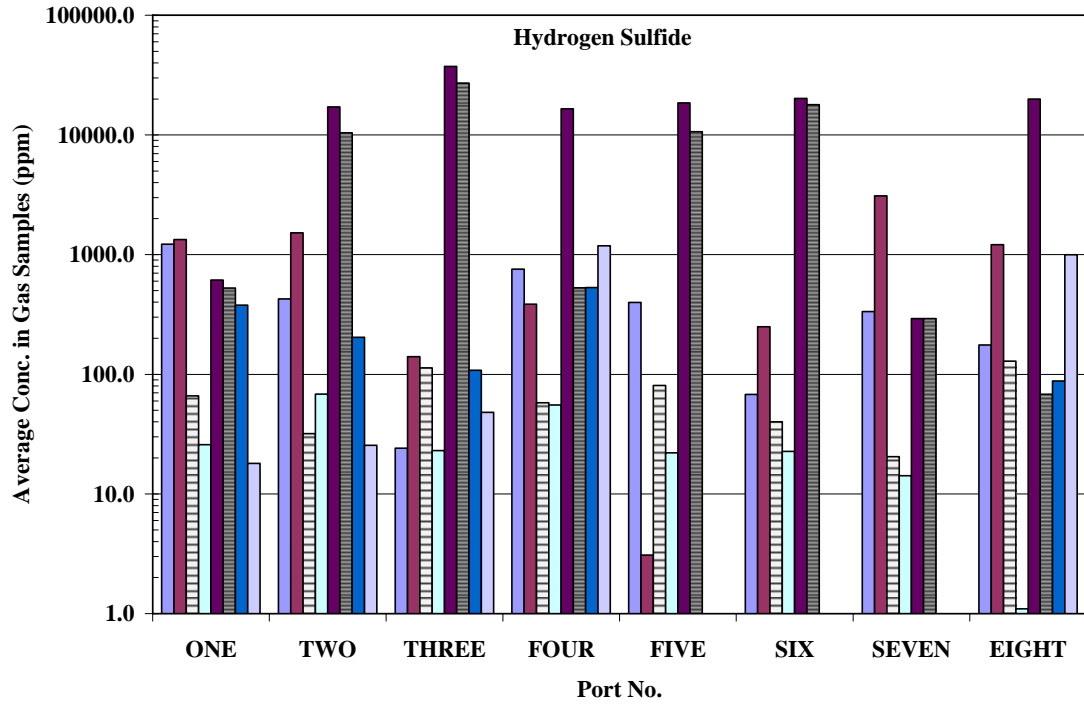


Figure A-7: Concentration of H₂S measured in kraft recovery boiler

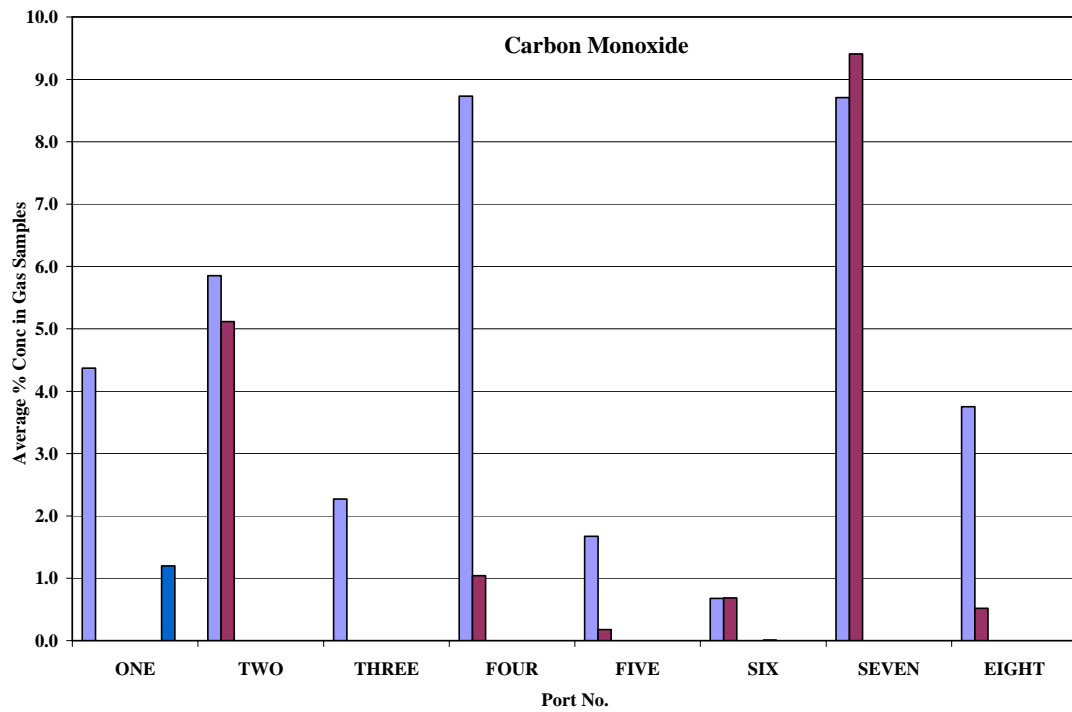


Figure A-8: Concentration of CO measured in kraft recovery boiler

APPENDIX B

ALGORITHM USED FOR EXTRACTION OF MECHANICAL PROPERTIES FROM LOAD DISPLACEMENT CURVES

APPENDIX B

There are two different types of results reported by nanoindenter:

- Hardness and modulus over a defined range
- Hardness and modulus from unload

The hardness and modulus over a defined range is based on continuous stiffness and hardness readings. The hardness and modulus from unload is based on the unloading stiffness.

Continuous measurements

Continuous stiffness measurements are accomplished by applying a small oscillation to the force signal at a relatively high frequency. The amplitude of the force oscillation is small enough that it does not affect the deformation process.

There are two methods by which the continuous stiffness can be calculated:

$$\left| \frac{P_{os}}{h(\omega)} \right| = \sqrt{\left[(S^{-1} + C_f)^{-1} + K_s - m\omega^2 \right]^2 + \omega^2 D^2}$$

Or

$$\tan(\phi) = \frac{\omega D}{(S^{-1} + C_f)^{-1} + K_s - m\omega^2}$$

C_f = load frame compliance (~1.13 m/MN)

K_s = column support spring stiffness (~ 60 N/m)

D = damping coefficient (~ 54 N s/m)

P_{os} = magnitude of force oscillation

$h(\omega)$ = magnitude of resulting displacement oscillation

ω = frequency of oscillation (69.3 Hz)

ϕ = phase angle between force and displacement signals

m = mass (~4.7 gms)

Oliver-Pharr method

The Oliver-Pharr method is based on elastic solutions by Sneddon, who derived general relationships among the load, displacement, and contact area for any punch that can be described as a solid revolution of a smooth function.

The Oliver-Pharr method builds on solutions by Doerner and Nix who suggested that unloading stiffness could be computed from a linear fit of the unloading curve. By extrapolating the linear portion of the curve to 0 load, the extrapolated depth could be used to determine contact area.

Oliver-Pharr found that unloading data is usually not linear but better described with a power law.

$$P = A(h-h_f)^m$$

The modulus from unloading is then calculated using the following equations:

$$S = \frac{dP}{dH} = \frac{2}{\sqrt{\pi}} E_r \sqrt{A} \beta$$

$$E_r = \frac{(1-\nu^2)}{E} + \frac{(1-\nu_i^2)}{E_i}$$

Where:

S = measured stiffness of the upper portion of the unloading curve

A = projected contact area

E_r = reduced modulus

b = correction factor which is 1.034 for Berkovich indenter

E and ν = Young's modulus and Poisson's ratio for specimen

E_i and ν_i = Young's modulus and Poisson's ratio for the indenter

One major advantage to the Oliver-Pharr method is that a direct measurement of the indent is not necessary. The indenter contact area can be calculated using the following equations.

The area function for a perfect Berkovich indenter is the following:

$$A(h_c) = 24.5h_c^2$$

(Other terms following the first one describe deviations in geometry due to blunting at the tip.)

$$h_c = h_{\max} - \varepsilon \frac{P_{\max}}{S}$$

Where:

P_{\max} = peak indentation load

$\varepsilon = 0.75$ for Berkovich indenter

S = unloading stiffness

h_{\max} = maximum depth of indentation

The Hardness from unloading is calculated using the following equation:

$$H = \frac{P_{\max}}{A}$$

$H = P_{\max}$ = peak indentation load A = projected area of hardness impression

This hardness definition may be different from conventional hardness definition. The observed hardness impression may be less than that at peak load if a portion of the contact area did not plastically deform.

APPENDIX C

**STRESS DISTRIBUTION FOR YFeAl COATINGS DURING THERMAL
CYCLIC OXIDATION AT 1000°C**

APPENDIX C

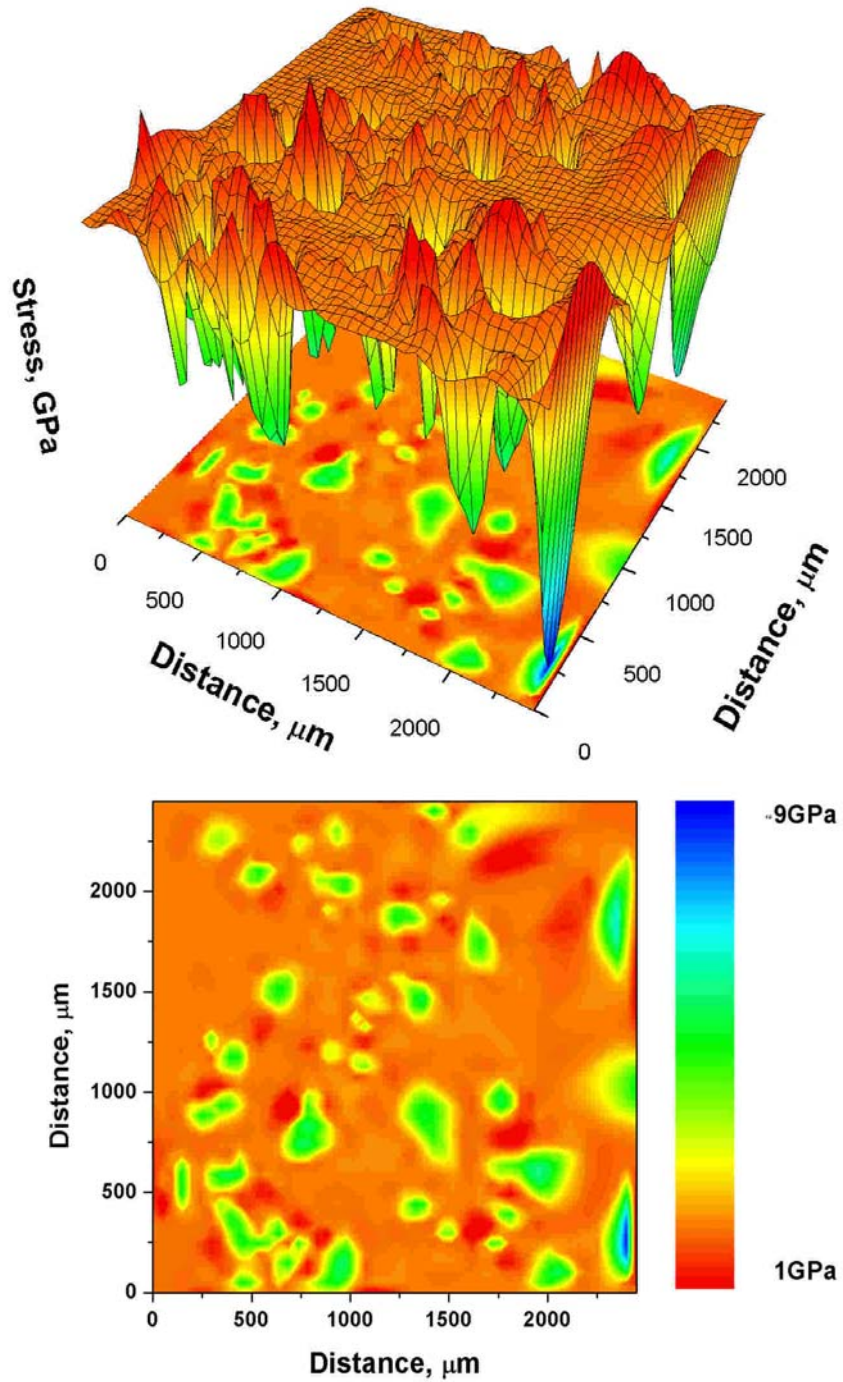


Figure C-1: Surface and contour plots of stress maps of Y-Fe-Al coating at edge of sample after 72 hours (3 cycles) of cyclic oxidation at 1000°C

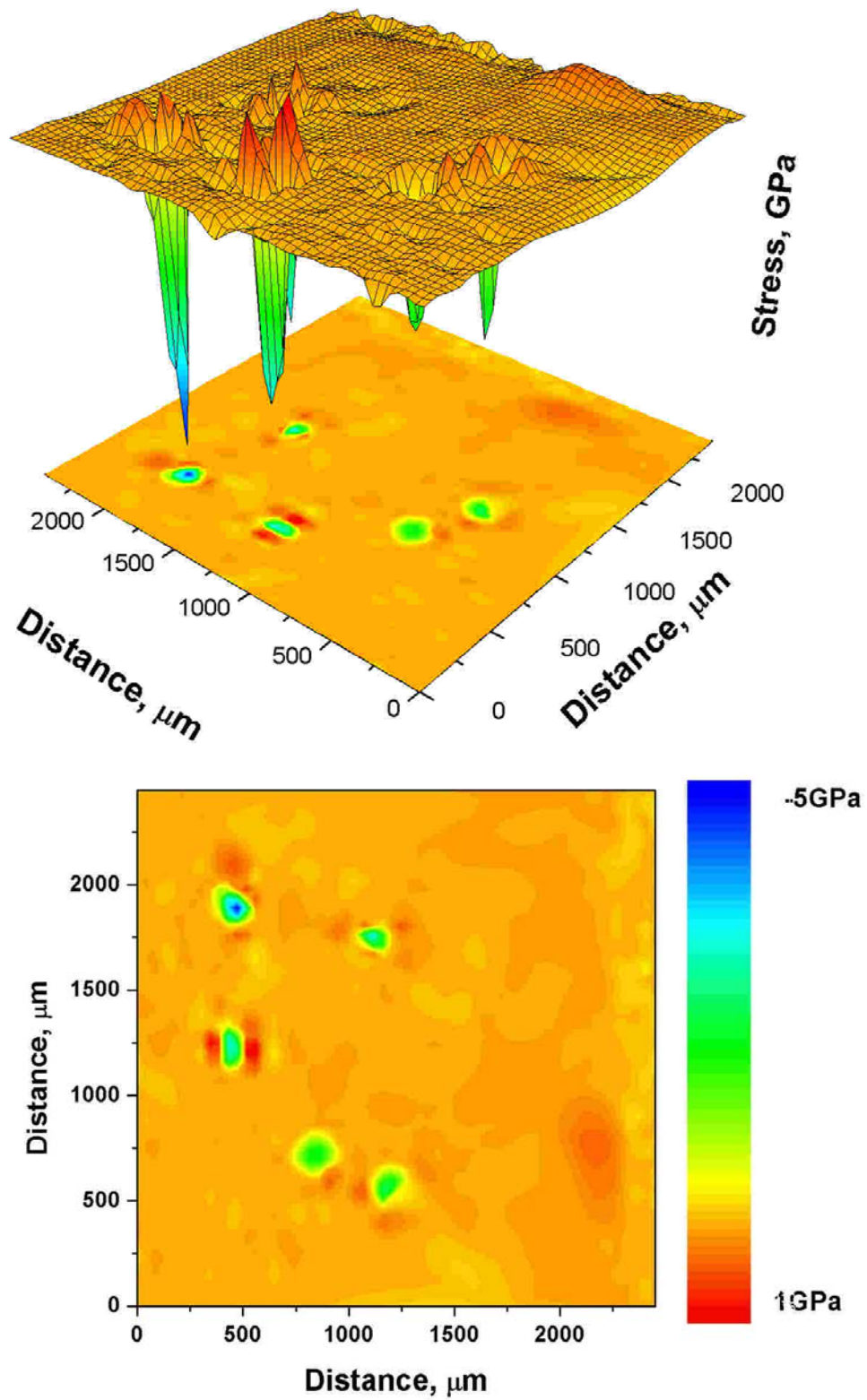


Figure C-2: Surface and contour plots of stress maps of Y-Fe-Al coating at center of sample after 72 hours (3 cycles) of cyclic oxidation at 1000°C

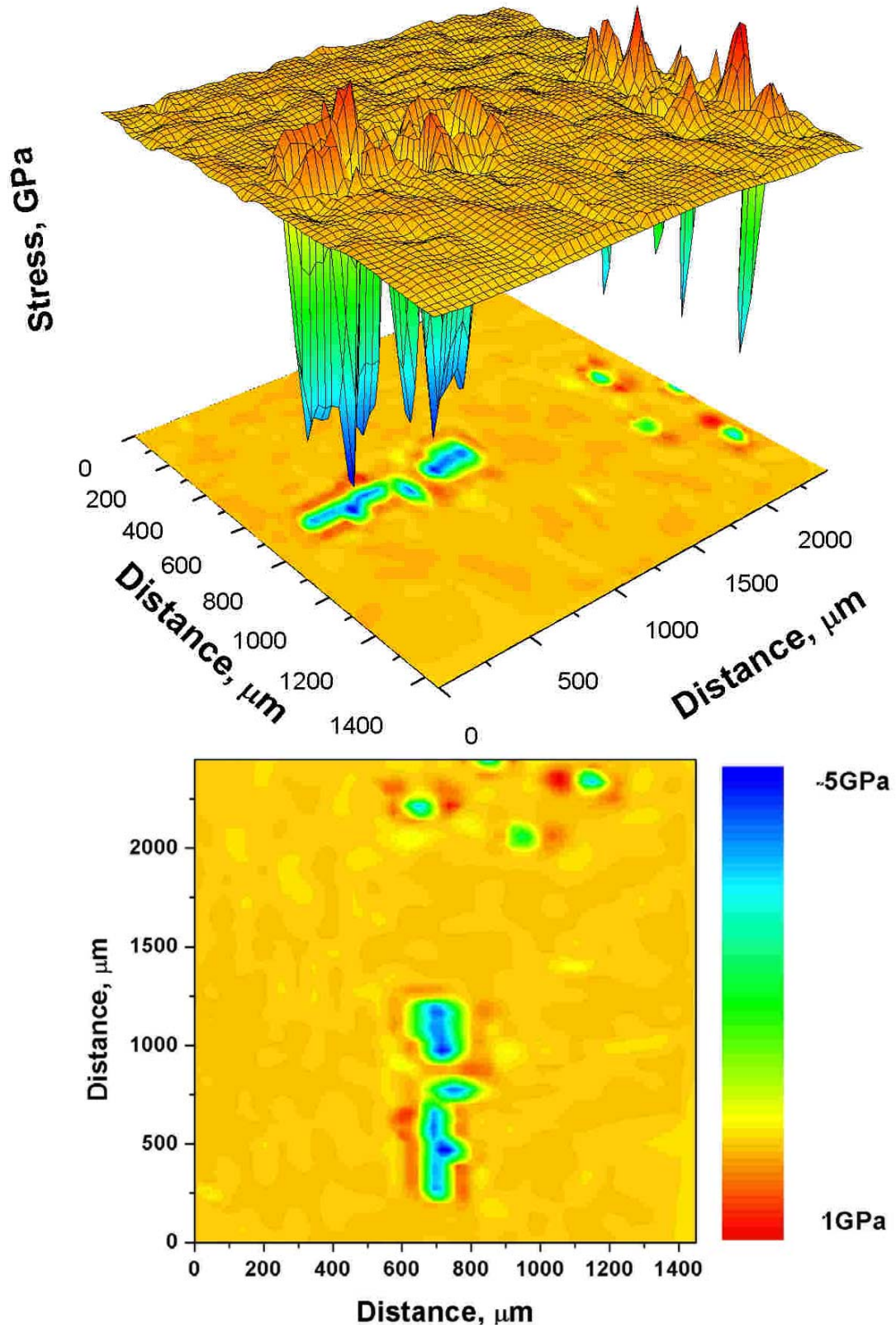


Figure C-3: Surface and contour plots of stress maps of Y-Fe-Al coating at edge of sample after 168 hours (7 cycles) of cyclic oxidation at 1000°C

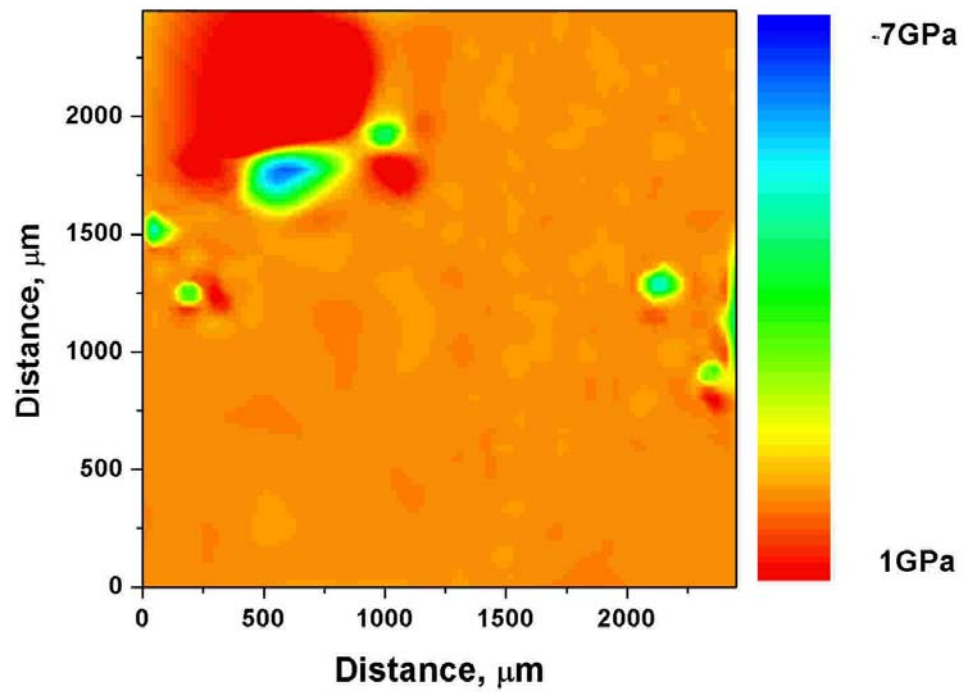
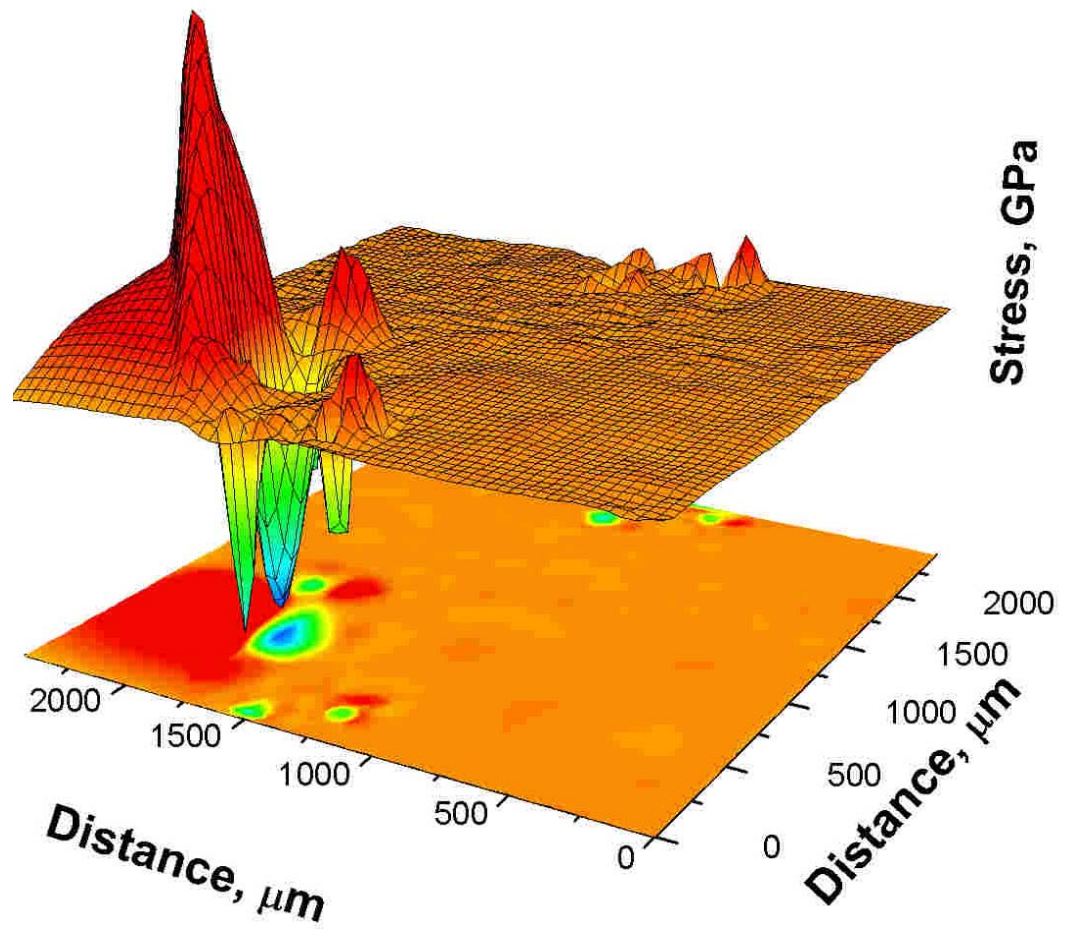


Figure C-4: Surface and contour plots of stress maps of Y-Fe-Al coating at center of sample after 168 hours (7 cycles) of cyclic oxidation at 1000°C

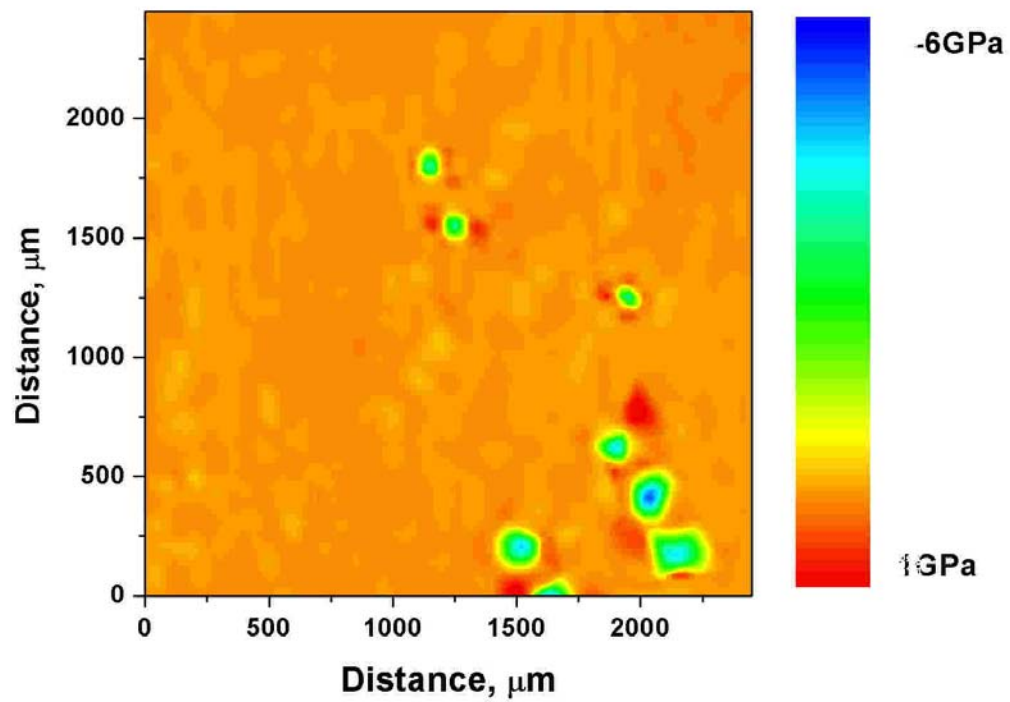
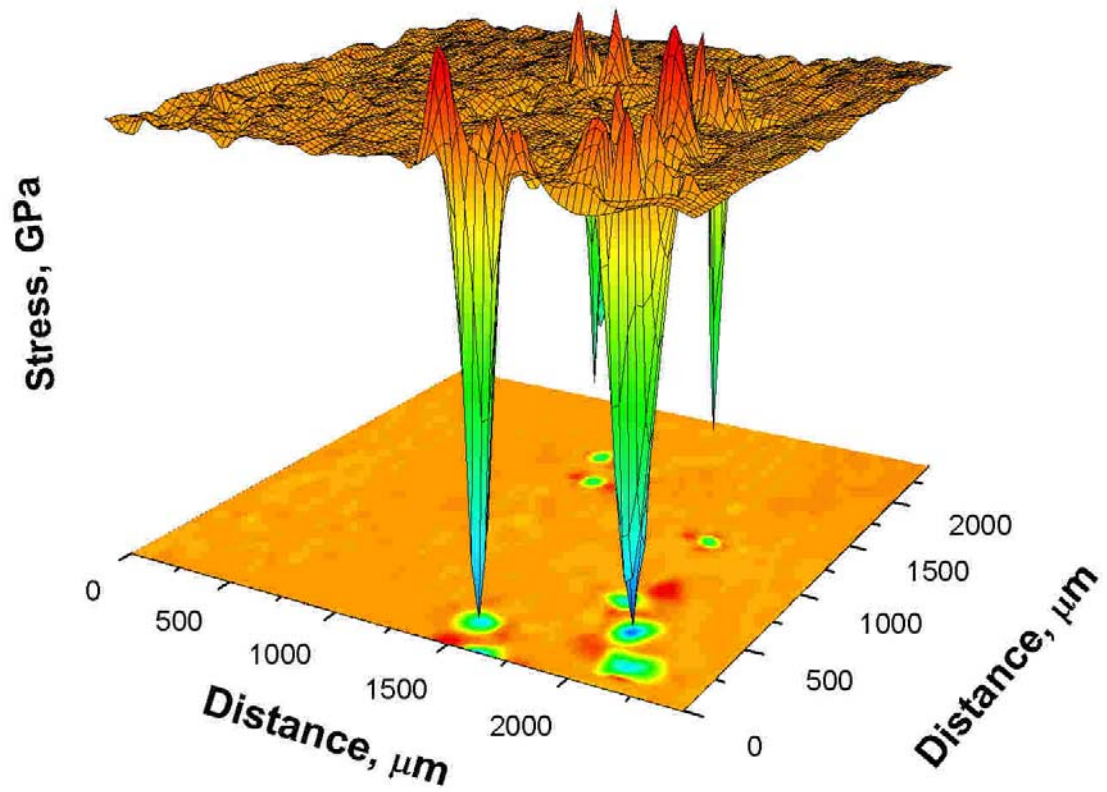


Figure C-5: Surface and contour plots of stress maps of Y-Fe-Al coating at edge of sample after 240 hours (10 cycles) of cyclic oxidation at 1000°C

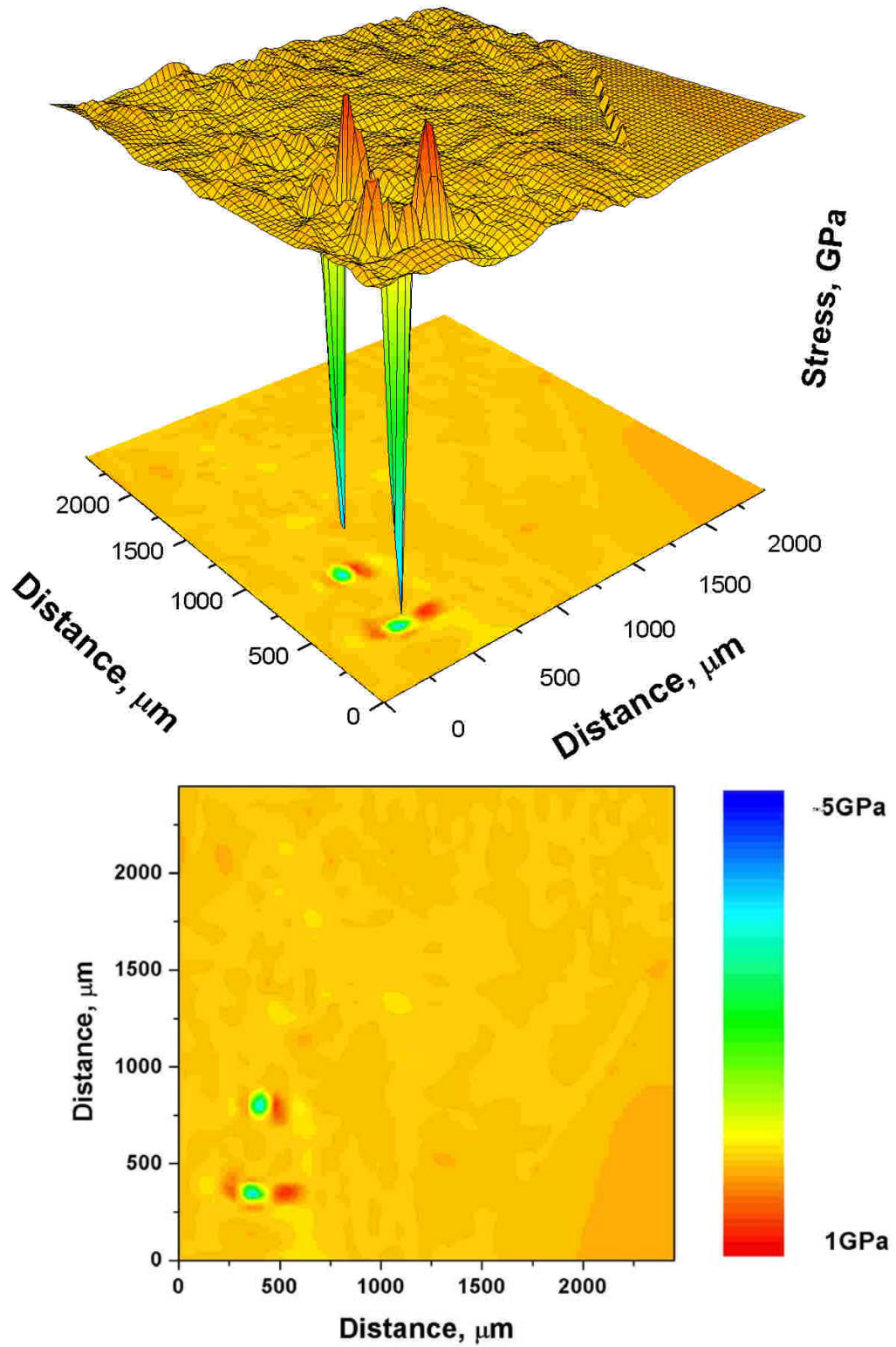


Figure C-6: Surface and contour plots of stress maps of Y-Fe-Al coating at center of sample after 240 hours (10 cycles) of cyclic oxidation at 1000°C

REFERENCES

-
- [1] V. Sricharoenchaikul, W.J. Frederick, and T.M. Grace, *Journal of Pulp and Paper Science*, vol. 23, no. 8, pp J394-J399.
- [2] H. Tran, "Recovery Boiler Corrosion", in *Kraft Recovery Boilers*, Eds. T.N. Adams, W.J. Frederick, T.M. grace, M. Hupa, K. Iisa, A.K. Jones, and H. Tran, TAPPI Press, Atlanta, GA.
- [3] J. Li and A.R.P. Van Heiningen, *TAPPI Journal*, vol. 74, no. 3, pp 237-239.
- [4] K.N. Strafford and P.K. Datta, *Materials Science and Technology*, vol. 5, no. 8, pp 765-779.
- [5] P.M. Singh, S.J. Al-Hassan, S. Stalder, and G.J. Fonder, *Proceedings of NACE Corrosion-2000*, FL, Paper no. 00237.
- [6] C.H.P. Lupis, "*Chemical Thermodynamics of Materials*", Elsevier Science Publishing Co., Inc.
- [7] L. G. Wright, Metal and Ceramics Information Center (MCIC) report, 1972.
- [8]. J. Yuan, Z. Xiao, M. Salcudean, P. M. Singh and P. Gorog, *Proceedings of 2007 International Chemical Recovery Conference*, Canada.
- [9] S. F. Chou and P. L. Daniel, *Symposium Proceedings, High Temperature Corrosion in Energy Systems*, pp 327-43.
- [10] M. Schulte and M. Schutze, *Oxidation of Metals*, vol. 51, no. 1/2, pp 55-77.
- [11] S. Osgerby, *Materials at High Temperatures*, vol. 17, no. 2, pp 307.
- [12] S. J. Al-Hassan, G. J. Fonder, and P. M. Singh, *Pulp & Paper Canada* , vol. 100, no. 10, pp 40-43.
- [13] P. M. Singh and V.R. Behrani, *Proceedings of NACE Corrosion-2005*, Paper no. 05197, Houston, TX, 2005.
- [14] P. M. Singh, J. Perdomo, and J. Mahmood, *Proceedings of the 11th International Symposium on Corrosion in the Pulp and Paper Industry*, Charleston, USA, pp 7-11.
- [15] M. Mäkipää, M. Oksa, and P. Pohjanne, *Proceedings of 10th International Symposium on Corrosion in Pulp and Paper Industry*, vol. 1, pp 73-87.

-
- [16] P. J. Ficalora and T. G. Godfrey, Oak Ridge Natl. Lab., Oak Ridge, TN, USA. Report, ORNL/TM-8734; DE83014565.
- [17] F. Gesmundo, D. J. Young, and S. K. Roy, *High Temperature Materials Processes*, vol. 8, pp 149-90.
- [18] M. F. Stroosnijder and W. J. Quadackers, *High Temperature Technology*, 4, no. 141.
- [19] J. Stringer, *High-Temperature Oxidation and Sulphidation Processes*, Ed. J.D. Embury, Pergamon Press, New York, pp 257-275.
- [20] H. J. Grabke, R. Lobnig, and P. Papaiacovou, *Selected Topics in High Temperature Chemistry: Defect Chemistry of Solids*, Eds. O. Johannesen and A. G. Andersen Elsevier, New York, pp 263-289.
- [21] P. M. Singh, S. J. Al-Hassan, S. Stalder, and G. Fonder, *TAPPI Journal*, vol. 3, no. 2, pp 21-26.
- [22] T. P. Levi, J. F. Norton, and W. T. Bakker, *Materials and Corrosion*, vol. 50, pp 405-416.
- [23] G. L. Miller and F. G. Cox, *Journal of Less-Common Metals*, vol. 2, pp 207.
- [24] Z. D. Xiang and P. K. Datta, *Journal of Materials Science*, vol. 40, pp 1959-1966.
- [25] P. F. Tortorelli and J. H. DeVan, *Materials Science and Engineering A*, 153, pp 573.
- [26] J. H. DeVan and P. F. Tortorelli, *Corrosion Science*, vol. 35, pp 1065-71.
- [27] K. Natesan and R. N. Johnson, *Heat Resistant Materials II*, K Natesan, P. Ganesan and G. Lai, Eds., pp.591-9, ASM International, Materials Park, OH.
- [28] P. F. Tortorelli and K. Natesan, *Materials Science and Engineering*, vol. A258, pp 115.
- [29] B. A. Pint, P. F. Tortorelli and I. G. Wright, *Materials at High Temperatures*, vol. 16, pp 1-13.
- [30] Z. D. Xiang and P. K. Datta, *Surface and Coating Technology*, vol. 179, no. 1, pp 95.
- [31] Z. D. Xiang, J. S. Burnell-Gray and P. K. Datta, *Journal of Materials Science*, vol. 36, pp 5673.

-
- [32] R. Mevrel, C. Duret and R. Pichoir, *Materials Science and Technology*, vol. 2, no. 3, pp 201.
- [33] G. Allison, M. W. Hawkins, *GEC revue*, 17, pp 947.
- [34] P. A. Choquet, E. R. Naylor and R. A. Rapp., *Materials science and engineering A*, A121, pp 413-418.
- [35] F. D. Geib, R. A. Rapp, *Oxidation of metals*, 40, 3/4, pp.213-228.
- [36] W. Da Costa, B. Gleeson, D. J. Young, *Journal of Electrochemical Society*, 141, 10, pp 2690-2697.
- [37] M.A. Quraishi MA, Sharma HS, *Anti corrosion methods and materials* 51, 1 (2004) p. 41.
- [38] R. A. Rapp, *Proceedings of Corrosion 89, April 17-21, Convention Center, New Orleans, Louisiana* (1989) paper 532.
- [39] W. Da Costa, B. Gleeson, D. J. Young., *Journal of Electrochemical Society*, 141, 6, (1994) p. 1464- 1471.
- [40] B. V. Cockeram, *Surface and Coating Technology*, vol. 76–77, pp 20.
- [41] T. B. Massalski, *Binary Alloys Phase Diagram*, The Materials Information Society, 2nd Ed., pp 147.
- [42] Z. D. Xiang and P. K. Datta, *Surface and Coating Technology*, vol. 184, pp 108.
- [43] B. V. Cockeram and R. A. Rapp, *Metallurgical and materials transactions A*, 26A, p. 777-791.
- [44] S. R. Levine., R. M. Caves, *Journal of the Electrochemical Society*, 121, 8, pp 1051.
- [45] R. Sivakumar, L. Seigle, *Metallurgical transactions A*, 7A (1976) p. 1073-1079
- [46] Gupta B.K., Seigle L.L., *Thin solid films*, 73 (1980) p.365-371
- [47] R. Bianco, R. A. Rapp, *Journal of the Electrochemical Society*, 140, 4 (1993) p. 1181-1190
- [48] S. C. Kung, R. A. Rapp, *Oxidation of metals*, 32, 1/2, pp 89-109
- [49] B. K. Gupta, A. K. Sarkhel, L. L. Seigle, *Thin solid films*, 39, pp 313-320

-
- [50] A. J. Hickl, R. W. Heckel, *Metallurgical transactions A*, 6A (1975) p. 431-440.
- [51] H. E. Evans, J.R. Nicholls, and S.R.J. Saunders, *Solid State Phenomenon*, vol. 41, pp 137–156 1995.
- [52] J. R. Nicholls, H.E. Evans, and S.R.J. Saunders, *Materials at High Temperatures*, vol. 14, pp 5–13, 1997.
- [53] H. E. Evans, *Materials Science and Engineering A*, vol. A120, pp 139–146, 1989.
- [54] C. Sarioglu, E. Schumann, J.R. Blachere, F.S. Pettit, and G.H. Meier, *Materials at High Temperatures*, vol. 17, pp 109–115, 2000.
- [55] E. J. Felten , F.S. Pettit, *Oxidation of Metals*, vol. 10, pp 189-223, 1976.
- [56] B. A. Pint, *Oxidation of Metals*, vol. 45, pp 1-37, 1996.
- [57] A. Strawbridge and P.Y. Hou, *Materials at High Temperatures*, vol. 12, pp 177-81, 1994.
- [58] J.A. Haynes, B.A. Pint, W.D. Porter, I.G. Wright, *Materials at High Temperatures*, vol. 21, no. 2, pp 87–94, 2004.
- [59] B.A. Pint, I.G. Wright, W.Y. Lee, Y. Zhang, K. Prüßner, and K.B. Alexander, *Materials Science and Engineering A*, vol. A245, no. 2, pp 201-11, 1998.
- [60] B. A. Pint, J. A. Haynes, K. L. More, I. G. Wright, and C. Leyens, in: *Superalloys 2000*. (Eds T. M. Pollock, R. D. Kissinger, R. R. Bowman, K. A. Green, M. McLean, S. L. Olson and J. J Schirra) TMS, Warrendale, PA, pp.629–638 (2000).
- [61] J. G. Smeggil, A.W. Funkenbusch, N.S. Bornstein, *Metallurgical Transactions A*, vol. 17A, pp 923-932, 1986.
- [62] J. L. Smialek, *Metallurgical Transactions A*, vol. 18A, pp 164-167, 1987.
- [63] H. Nagai, *Materials Science Forum*, vol. 43, pp 75-130, 1989.
- [64] T. A. Ramanarayanan, R. Ayer, R. Petkovic and D. P. Leta, *Oxiation of Metals*, vol. 29, nos. 5/6, pp 445-72, 1988.
- [65] J. Stringer, *Materials Science and Engineering A*, vol. A12, pp 129-137, 1989.
- [66] Bianco and R.A. Rapp, *Journal of Electrochemical Society*, vol. 140 pp 1191, 1993.

-
- [67] H.L. Du , J. Kipkemoi, D.N. Tsipas , P.K. Datta , *Surface and Coatings Technology*, vol. 86-87, pp 1-8, 1996.
- [68] M. J. Bennett, H. E. Bishop, P. R. Caalxer and T. Tiuson, *Materials Science and Engineering*, vol. 90, pp 177-190, 1987.
- [69] R. L. Nelson, J. D. Ramsay, and L. Woodhead, *Thin Solid Films*, vol. 81, pp 329-337, 1981.
- [70] M. J. Bennett, *Journal of Vacuum Science and Technology*, vol. B2, nos. 10-12, pp 800-805, 1984.
- [71] P. Y. Hou and J. Stringer, *Journal of Electrochemical Society*, vol. 134, pp 1836, 1987.
- [72] M. F. Stroosnijder, V. Gutrmann, T. Fransen, and J. Wit, *Oxidation of Metals*, vol. 33, pp 371-397, 1990.
- [73] J. P. Larpin, G. Aguilar, H. Buscail, and J. C. Colson, *High Temperature Oxidation and Sulphidation Processes*, Ed. J. D. Embury, pp. 337-345. Pergamon Press, Oxford, 1990.
- [74] D. P. Whittle and J. Stringer, *Philosophical Transactions of the Royal Society of London A*, vol. A295, pp 309, 1980.
- [75] A.W. Funkenbusch, J.G. Smeggil, and N.S. Bornstein, *Metallurgical Transactions A*, vol. 6A, pp 1164-66, 1985.
- [76] R. Prescott, D.F. Mitchell, M.J. Graham, and J. Doychak, *Corrosion Science*, vol. 37, pp 1341-64, 1995.
- [77] D. R. Sigler, *Oxidation of Metals*, vol. 32, pp 337, 1989.
- [78] J. L. Smialek and B.A. Pint, *Materials Science Forum*, vol. 459-466, nos. 1-2, pp 369, 2001.
- [79] J. Quadackers and L. Singheiser, *Materials Science Forum*, vol. 369, pp 77, 2001.
- [80] B. A. Pint, *Journal of American Ceramic Society*, vol. 86, pp 686, 2003.
- [81] B. A. Pint, K. L. More and I.G. Wright, *Materials at High Temperature*, vol. 20, pp 375, 2003.

-
- [82] B. A. Pint, J. A. Haynes, K. L. More, and I.G. Wright, *Proceedings of Superalloys 2004*, Eds. K. A. Green, T. M. Pollock, H. Harada, T.E. Howson, R.C. Reed, J.J. Schirra, and S. Walston, pp 597, 2004.
- [83] R. J. Hussey and M. J. Graham, *Oxidation of Metals*, vol. 45, nos. 3/4, pp 349-374, 1996.
- [84] P. Kofstad, *High Temperature Corrosion*. Elsevier Applied Science. London, pp 389-424, 1988.
- [85] P. Skeldon, J. M. Calvert and D. G. Lees, *Phil. Trans. R. Soc. London. A*, vol. 296, 545-580, 1980.
- [86] E. W. A. Young and J.H.W. De Wit, *Solid State Ionics*, vol. 16, pp 3946, 1985.
- [87] E. W. A. Young and J. H. W. De Wit, *Oxidation of Metals*, vol. 26, nos. 5/6, pp 351-361, 1986.
- [88] M.K. Loudjani, A.M. Huntz and R. Cortès, *Journal of Materials Science*, vol. 28, pp 6466-6473.
- [89] E.J. Felten, *Journal of Electrochemical Society*, vol. 108, pp 490-502, 1961.
- [90] J.K. Tien and F.S. Pettit, *Metallurgical Transactions*, vol. 3, pp 1587-1596, 1972.
- [91] F.A. Golightly, F.H. Stott and G.C. Wood, *Oxidation of Metals*, vol. 10, pp 163-175, 1976.
- [92] E. Schumann, J.C. Yang, M. Ruhle, and M.J. Graham, *Oxidation of Metals*, vol. 46, pp 37-49, 1996.
- [93] J.E. Antill and K.A. Peakall, *Journal of the Iron and Steel Institute*, vol. 205, pp 1136-1142, 1967.
- [94] J. E. McDonald and J. G. Eberhart, *Transactions of Metallurgical Society of AIME*, vol. 233, pp 512, 1965.
- [95] B. A. Pint, A. J. Garratt-Reed, and L.W. Hobbs, *Journal of American Ceramic Society*, vol. 81, pp 305, 1998.
- [96] G. Y. Kim, L. M. He, J.D. Meyer, A. Quintero, J.A. Haynes, and W.Y. Lee, *Metallurgical and Materials Transactions A*, vol. 35A, no. 11, pp 3581-93.
- [97] B. Ning, M. Shamsuzzoha, and M.L. Weaver, *Journal of Vacuum Science and Technology*, vol. A 23, no. 1, pp 44-54.

-
- [98] D.C. Tu, C.C. Lin, S.J. Liao, and J.C. Chou, *Journal of Vacuum Science and Technology*, vol. A4, no. 6, 2601-06.
- [99] J. Stringer, *Corrosion Science*, Vol. 10, pp 513.
- [100] M. Schutze, *Materials Science and Technology*, Vol. 6, pp32.
- [101] H.E. Evans and M.P. Taylor, *Surfaces and Coatings Technology*, Vol. 94-95, p 27.
- [102] B.D. Bartolo, *Optical Interactions in Solids*, (John Wiley, New York), pp193-219.
- [103] G.F. Imbusch in *Luminescence of Inorganic Solids*, ed. By B.D. Bartolo (Plenum Press, New York), pp115-130.
- [104] J. He, and D. R. Clarke, *Journal of American Ceramic Society*, 78, 1347.
- [105] Q. Ma and D. R. Clarke, *Journal of American Ceramic Society*, 76, 1433.
- [106] S. C. Moss and R. E. Newnham, *Z. Kristall.*, 120. 359.
- [107] K. Edmondson, S. Agoston and R. Ranganathan, *Am. J. Phys.*, 64, 787.
- [108] Q. Ma and D. R. Clarke, *Journal of American Ceramic Society.*, 77, 298.
- [109] V. K. Tolpygo, and D.R. Clarke, *Acta. Mater.*, 46, pp5153.
- [110] S.E. Molis and D.R. Clarke, *Journal of American Ceramic Society*, 73, pp 3189.
- [111] W.C. Oliver and G.M. Pharr, *Journal of Materials Research*, 7(6), pp 1564-83.
- [112] R. C. John, A. D. Pelton, A. L. Young, W. T. Thompson, I. G. Wright, T. M. Besmann, *Materials Research*, vol.7 no.1.
- [113] V. Behrani and P. M. Singh, *Oxidation of Metals*, Submitted.
- [114] J. W. Lee, J. G. Duh, and S. Y. Tsai, *Surfaces and Coatings Technology*, 59.
- [115] T. Narita, T. Ishikawa, K. Imai and K. Nishidat, *Oxidation of Metals*, Vol. 28, Numbers 1-2, pp17-31.
- [116] H. J. Rau, *Journal of Less-Common Metals*, 55(2), 205.

-
- [117] D. J. Young, W. W. Smeltzer, and J. S. Kirakaldy, *Journal of Electrochemical Society*, 120, 1221.
- [118] J.F. Norton, M. Maier, and W.T. Bakker, *Materials at High Temperatures*, vol. 17, no. 2, pp 327–337.
- [119] U. Burkhardt., Y. Grin, M. Ellner, *Acta Crystallographica*, B50 (1994) p. 313-316.
- [120] S. R. Levine and R. M. Caves, *Journal of Electrochemical Society*, Vol. 121, Issue 8, pp. 1051-1064.
- [121] B. Nciri and L. Vandenbucke, *Thin Solid Films*, 139, 311-324.
- [122] Z. D. Xiang and P. K. Datta, *Acta Materialia* 54, 4453-4463.
- [123] S. G. Denner, R. D. Jones, *Met. Technol. (Lond.)* 4 (3) 167.
- [124] N. A. El Mahallaway, M. A. Taha, M.A. Shady, A.R. El-Sissi, A.N. Attia, W. Reif, *Mater. Sci. Technol.* 13 (1997) 832.
- [125]. S. Huanrong, W. Wuji, D. Yi, L. Gang, *Mater. Prot.* 22 (2002) 35 (in Chinese).
- [126] C. A. C. Sequeira, C. M. G. S. Nunes, *Surface Engineering*, 3 (1987) p. 247.
- [127] M. K. Kazmanli, B. Rother, M. Urgan and C. Mitterer, *Surfaces and Coatings Technology*, 107 (1998), p. 65.
- [128]. L. Xiaodong and B. Bharat, *Thin Solid Films* 315 (1998), p. 214.
- [129] N. A. Vermaut, PhD thesis, University of Missouri-Rolla, 1964.
- [130] CRC Handbook of Chemistry and Physics.
- [131] J. E. Antill, K.A. Peakall, *J. Iron Steel Inst.*, 205 (1967) 1136.
- [132] F. A. Golightly, F.H. Stott, G.C. Wood, *Oxidation of Metals*, 10 (1976) 163.
- [133] J. E. McDonald, J. G. Eberhardt: *Trans. TMS-AIME* 233 (1965) 512.
- [134]. A. W. Funkenbusch, J. G. Smeggil, N. S. Bornstein, *Metallurgical Transactions*, 16A (1985) 1164.
- [135] J. G. Smeggil, A. W. Funkenbusch, N. S. Bornstein, *Metallurgical Transactions*, 17A (1986) 923.

-
- [136] J. Stringer, *Met. Rev.*, 11, (1966) 113.
- [137] J. K. Tien, F.S. Pettit, *Metallurgical Transactions*, 3 (1972) 1587.
- [138] E. J. Felten, *Journal of Electrochemical Society*, 108 (1961) 490.
- [139] C. Sarioglu, E. Schumann, J. R. Blachere, F.S.Pettit and G.H. Meier, *Materials at High Temperatures* 17(1) 109-115.
- [140] C. Sarioglu, M. J. Stiger, R. Ranakiraman, E. Schumann, A. Ashary, F.S.Pettit and G.H. Meier, *Materials and Corrosion* 51, 358-372.
- [141] D. M. Lipkin and D. R. Clarke, *Oxidation of Metals*, 45 3-4, (1996) 267
- [142] A. Selcuk and A. Atkinson, *Materials Science and Engineering A* 335 (2002) 147-156
- [143] OriginLab Corporation, Northampton, MA USA.
- [144] D.W. Marquardt, *J. Soc. Ind. Appl. Math.*, 11, (1963) 431.

